



AFRL-RX-WP-TR-2010-4023

DURABLE HYBRID COATINGS

Annual Performance Report (2008)

Vsevolod Balbyshev, Bret J. Chisholm, Douglas L. Schulz, Gregory J. McCarthy,
Dante Battocchi, Kerry Allahar, and Gordon P. Bierwagen

North Dakota State University

SEPTEMBER 2008
Interim Report

Approved for public release; distribution unlimited.

See additional restrictions described on inside pages

STINFO COPY

**AIR FORCE RESEARCH LABORATORY
MATERIALS AND MANUFACTURING DIRECTORATE
WRIGHT-PATTERSON AIR FORCE BASE, OH 45433-7750
AIR FORCE MATERIEL COMMAND
UNITED STATES AIR FORCE**

NOTICE AND SIGNATURE PAGE

Using Government drawings, specifications, or other data included in this document for any purpose other than Government procurement does not in any way obligate the U.S. Government. The fact that the Government formulated or supplied the drawings, specifications, or other data does not license the holder or any other person or corporation; or convey any rights or permission to manufacture, use, or sell any patented invention that may relate to them.

This report was cleared for public release by the USAF 88th Air Base Wing (88 ABW) Public Affairs Office (PAO) and is available to the general public, including foreign nationals. Copies may be obtained from the Defense Technical Information Center (DTIC) (<http://www.dtic.mil>).

AFRL-RX-WP-TR-2010-4023 HAS BEEN REVIEWED AND IS APPROVED FOR PUBLICATION IN ACCORDANCE WITH THE ASSIGNED DISTRIBUTION STATEMENT.

*/Signature//

AARON VEYDT, Program Manager
Thermal Sciences and Materials Branch
Nonmetallic Materials Division

//Signature//

NADER HENDIZADEH, Chief
Thermal Sciences and Materials Branch
Nonmetallic Materials Division

//Signature//

SHASHI K. SHARMA, Deputy Chief
Nonmetallic Materials Division
Materials and Manufacturing Directorate

This report is published in the interest of scientific and technical information exchange, and its publication does not constitute the Government's approval or disapproval of its ideas or findings.

*Disseminated copies will show “//Signature//” stamped or typed above the signature blocks.

REPORT DOCUMENTATION PAGE

*Form Approved
OMB No. 0704-0188*

The public reporting burden for this collection of information is estimated to average 1 hour per response, including the time for reviewing instructions, searching existing data sources, gathering and maintaining the data needed, and completing and reviewing the collection of information. Send comments regarding this burden estimate or any other aspect of this collection of information, including suggestions for reducing this burden, to Department of Defense, Washington Headquarters Services, Directorate for Information Operations and Reports (0704-0188), 1215 Jefferson Davis Highway, Suite 1204, Arlington, VA 22202-4302. Respondents should be aware that notwithstanding any other provision of law, no person shall be subject to any penalty for failing to comply with a collection of information if it does not display a currently valid OMB control number. **PLEASE DO NOT RETURN YOUR FORM TO THE ABOVE ADDRESS.**

1. REPORT DATE (DD-MM-YY) September 2008			2. REPORT TYPE Interim		3. DATES COVERED (From - To) 01 October 2007 – 01 September 2008		
4. TITLE AND SUBTITLE DURABLE HYBRID COATINGS Annual Performance Report (2008)			5a. CONTRACT NUMBER FA8650-04-1-5045				
			5b. GRANT NUMBER				
			5c. PROGRAM ELEMENT NUMBER 61202F				
6. AUTHOR(S) Vsevolod Balbyshev, Bret J. Chisholm, Douglas L. Schulz, and Gregory J. McCarthy (Center for Nanoscale Science and Engineering) Dante Battocchi, Kerry Allahar, and Gordon P. Bierwagen (Department of Coatings and Polymeric Materials)			5d. PROJECT NUMBER 4347				
			5e. TASK NUMBER 60				
			5f. WORK UNIT NUMBER 65100002				
7. PERFORMING ORGANIZATION NAME(S) AND ADDRESS(ES)			8. PERFORMING ORGANIZATION REPORT NUMBER				
Center for Nanoscale Science and Engineering 1805 NDSU Research Park Drive N. North Dakota State University Fargo, ND 58102		Department of Coatings and Polymeric Materials 1735 NDSU Research Park Drive N. North Dakota State University Fargo, ND 58105					
9. SPONSORING/MONITORING AGENCY NAME(S) AND ADDRESS(ES) Air Force Research Laboratory Materials and Manufacturing Directorate Wright-Patterson Air Force Base, OH 45433-7750 Air Force Materiel Command United States Air Force			10. SPONSORING/MONITORING AGENCY ACRONYM(S) AFRL/RXBT				
			11. SPONSORING/MONITORING AGENCY REPORT NUMBER(S) AFRL-RX-WP-TR-2010-4023				
12. DISTRIBUTION/AVAILABILITY STATEMENT Approved for public release; distribution unlimited.							
13. SUPPLEMENTARY NOTES PAO Case Number: 88ABW- 2010-0510; Clearance Date: 08 Feb 2010. Report contains color.							
14. ABSTRACT The overall goal of this program is to contribute to the development of the next-generation anti-corrosion and other protective coating systems for USAF aircraft. The initial emphasis was on improvements in NDSU's promising Mg-based primer, which NDSU recently licensed to the major international aircraft coatings manufacturer. Work continued over the last year on improvements in primer binder, additions to NDSU's world-class high-throughput (HT) research and development capabilities that are necessary to work with this class of coatings, and meeting additional Air Force protective coatings needs such as hard surface pretreatments to work with the binder, and development of a methodology for depot-based repair indium tin oxide aircraft canopy coatings. Progress on all areas was made over the last year, as described in papers appended to this report. A significant new effort was initiated in prognostic measurement techniques to monitor the effectiveness of the magnesium-based primers previously developed. Accomplishments over the last year included development of an embedded sensor for monitoring corrosion of metallic primers based on Mg and Mg alloys in aircraft coating systems. Research on in situ monitoring of primer degradation involves the application of an embedded sensor within the coating system followed by polling the system using various electrochemical techniques while subjecting it to ASTM standard corrosion tests, namely B117 salt fog and Prohesion. The feasibility and effectiveness of the embedded sensor electrode have been investigated. It has been demonstrated that the two-electrode sensor assembly produces consistent and reliable electrochemical data for both ex situ and in situ environments, and the data are in agreement with control experiments carried out using the conventional three-electrode electrochemical cell configuration.							
15. SUBJECT TERMS high-throughput (HT), hybrid organic-inorganic binders, dual-core polymerization mechanism, rapid-cure Mg-rich primers, embedded sensor, in situ monitoring, wire-beam electrode							
16. SECURITY CLASSIFICATION OF: a. REPORT Unclassified		17. LIMITATION OF ABSTRACT: b. ABSTRACT Unclassified		18. NUMBER OF PAGES c. THIS PAGE Unclassified	19a. NAME OF RESPONSIBLE PERSON (Monitor) Aaron Veydt		
				19b. TELEPHONE NUMBER (Include Area Code) N/A			

Acknowledgements

This material is based on research sponsored by Air Force Research Laboratory under agreement number FA8650-04-1-5045.

The views and conclusions contained herein are those of the authors and should not be interpreted as necessarily representing the official policies or endorsements, either expressed or implied, of Air Force Research Laboratory or the U.S. Government.

Distribution List

Air Force Research Laboratory

AFRL/MLBT: Aaron R. Veydt, 2Lt, USAF
Copy to: Dr. Stephen L. Szaruga
2941 P. Street, Rm 136
Wright-Patterson Air Force Base, Ohio 45433-7750

1 e-mail copy: Aaron.Veydt@wpafb.af.mil

1 e-mail copy: Steve.Szaruga@wpafb.af.mil

AFR/PKMM:L: Michael A. Cramer
Copy to: Rebecca Powers
Pam S. Strader

1 e-mail copy: Michael.Cramer@wpafb.af.mil

1 e-mail copy: Rebecca.Powers@wpafb.af.mil

1 e-mail copy: Pam.Strader@wpafb.af.mil

Office of Naval Research – Administrative Grants Officer

Sandra Thomson
ONR Seattle Regional Office
1107 NE45th Street, Suite 350
Seattle WA 98105-4631

1 e-mail copy: Sandra.Thomson@navy.mil

North Dakota State University

Dr. Gordon Bierwagen
Dr. Bret Chisholm
Dr. Séva Balbyshev
DrEng. Dante Battocchi
Dr. Kerry Allahar
Dr. Douglas Schulz
Mr. Aaron Reinholtz
Dr. Philip Boudjouk

1 e-mail copy: Gordon.Bierwagen@ndsu.edu

1 e-mail copy: Bret.Chisholm@ndsu.edu

1 e-mail copy: Seva.Balbyshev@ndsu.edu

1 e-mail copy: Dante.Battocchi@ndsu.edu

1 e-mail copy: Kerry.Allahar@ndsu.edu

1 e-mail copy: Doug.Schulz@ndsu.edu

1 e-mail copy: Aaron.Reinholtz@ndsu.edu

1 e-mail copy: Philip.Boudjouk@ndsu.edu

Contact information for inquiries

Programmatic:

Gregory McCarthy, Director CNSE
1805 NDSU Research Park Dr. N.
Fargo, ND 58102
(701) 231-7193 (voice)
(701) 231-7916 (fax)
Greg.McCarthy@ndsu.edu

Technical:

Gordon Bierwagen, Professor
Department of Coatings & Polymeric
Materials
1735 NDSU Research Park Dr. N.
Fargo, ND 58102
(701) 231-8294 (voice)
(701) 231-8439 (fax)
Gordon.Bierwagen@ndsu.edu

Financial:

Mark Lande, Asst. Dir. CNSE
Admin. and Financial Services
1805 NDSU Research Park Dr.
Fargo, ND 58102
(701) 231-5882 (voice)
(701) 231-7916 (fax)
Mark.Lande@ndsu.edu

Summary

The overall goal of this program is to contribute to the development of the next-generation anti-corrosion and other protective coating systems for USAF aircraft. The initial emphasis was on improvements in NDSU's promising Mg-based primer, which NDSU recently licensed to the major international aircraft coatings manufacturer. Work continued over the last year on improvements in primer binder, additions to NDSU's world-class high-throughput (HT) research and development capabilities that are necessary to work with this class of coatings, and meeting additional Air Force protective coatings needs such as hard surface pretreatments to work with the binder, and development of a methodology for depot-based repair indium tin oxide aircraft canopy coatings. Progress on all areas was made over the last year, as described in papers appended to this report. A significant new effort was initiated in prognostic measurement techniques to monitor the effectiveness of the magnesium-based primers previously developed. Accomplishments over the last year included development of an embedded sensor for monitoring corrosion of metallic primers based on Mg and Mg alloys in aircraft coating systems. Research on *in situ* monitoring of primer degradation involves the application of an embedded sensor within the coating system followed by polling the system using various electrochemical techniques while subjecting it to ASTM standard corrosion tests, namely B117 salt fog and Prohesion. The feasibility and effectiveness of the embedded sensor electrode have been investigated. It has been demonstrated that the two-electrode sensor assembly produces consistent and reliable electrochemical data for both *ex situ* and *in situ* environments, and the data are in agreement with control experiments carried out using the conventional three-electrode electrochemical cell configuration.

1.0 Introduction

The *goal* of this North Dakota State University (NDSU) program is to contribute to the development of the next-generation anti-corrosion and other protective coating systems for USAF aircraft. The initial emphasis of the program was on improvements in NDSU's promising Mg-based primer, which NDSU licensed several years ago to the major international aircraft coatings manufacturer. Work has continued on a number of tasks, and was initiated on a new task focused on prognostic measurement techniques to monitor the effectiveness of the magnesium-based primers previously developed, and on aircraft coatings systems in general. Near the end of the reporting period, funding for follow-on work on prognostic measurement devices and techniques to simultaneously monitor structural and corrosion characteristics of painted aircraft structural parts.

This report is organized around the Durable Hybrid Coatings program tasks:

- **Task 1.** Mg-based primer research focusing on the primer itself and its electrochemical behavior in the coating. Initiated in 2004. Research coordinated by Dr. Dante Battocchi, with Prof. Gordon Bierwagen as senior scientific advisor, and performed in the Department of Coatings and Polymeric Materials (CPM). See *Section 2*.
- **Task 2.** Hard pretreatment research that would permit depot repainting without damaging the airframe. Work led by Dr. Douglas Schulz, and performed in the NDSU Center for Nanoscale Science and Engineering (CNSE). Initiated in 2004. Progress described in *Section 4.1*.
- **Task 3.** Primer formulation optimization research, and research, development on high-throughput electrochemical methods to evaluate corrosion of coatings, plus additional work on aircraft coatings added in 2006. Work led by Drs. Bret Chisholm, and performed in the NDSU Center for Nanoscale Science and Engineering (CNSE). Progress is described in *Section 3*.
- **Task 4.** Develop indium tin oxide coatings for in-field canopy repair. Initiated in 2006. Progress is described in *Section 4.2*.
- **Task 5.** Prognostic measurement techniques to monitor the effectiveness of the magnesium-based primers previously developed. Task 5 was initiated in July 2007. Progress is described in *Section 5.0*.

In cases where a significant portion of a study has been completed, and a manuscript has been prepared or paper published, the work will only be summarized, with reference to an appended manuscript for details.

2.0 Mg-Rich Primer Update

Task 1, which is now largely complete, dealt with improvements to NDSU's magnesium-rich aircraft coating primer technology. With support from several Air Force grants, including this Cooperative Agreement, NDSU developed aircraft primers containing Mg pigments designed as an alternative to chromate-based treatments corrosion control of Al alloys, particularly the aircraft alloy 2024-T3. The anti-corrosive properties of the Mg-rich primer are based on two different mechanisms: firstly, the coating acts as a barrier; secondly, the coating acts as a cathodic protector with the pigment undergoing corrosion preferentially versus the Al substrate.

Task 1 efforts to understand and improve the primer system are now complete. The details of the main technical accomplishments of this task have been summarized in a manuscript accepted for publication in *Corrosion* journal and provided in **Appendix A**, "The Use of Mg Alloys as Pigments in Mg-rich Primers For Protecting Al Alloys," whose abstract follows:

As an alternative to toxic chromate coating, Mg-rich primers have been designed to protect Al alloys (in particular AA 2024-T3) and developed in analogy to Zn-rich primers for steel substrate. The Mg pigment present in the primer can provide cathodic protection to Al substrates and significantly deter Al alloy corrosion when damage occurs.

In order to determine how much the pigment metal alloy composition can be varied without sacrificing corrosion protection, three different primers based on magnesium alloy powders as pigments were formulated with an epoxy-polyamide polymer binder at different pigment volume concentrations (PVCs). Their behaviors were studied after cyclic exposure in Prohesion Chamber via electrochemical methods.

Testing results from Electrochemical Impedance Spectroscopy (EIS) and Scanning Electron Microscopy (SEM) showed that the metal-rich primers with Mg alloys as pigments could provide cathodic protection, and precipitates formed from oxidation of Mg alloy particles were similar to the ones found in the pure Mg-rich primer system. Furthermore, the investigation of the properties of the three alloy pigments gave a good understanding of the effects of particle shape, particle size, particle size distribution and metal alloy chemical composition.

3.0 High-Throughput Experimentation for Coatings Formulation and Optimization

3.1 Development of New High-Throughput Methods

To apply combinatorial/high-throughput methods to the development of coatings for corrosion protection, a high-throughput method for screening corrosion inhibiting characteristics of coatings was needed. A parallel electrochemical impedance spectroscopy system was designed, built, and validated. The details of this work was recently published in the *Journal of Combinatorial Chemistry* and the article is included in this report as **Appendix B**, "Combinatorial Materials Research Applied to the Development of New Surface Coatings X: A High-Throughput Electrochemical Impedance Spectroscopy Method for Screening Organic Coatings for Corrosion Inhibition," whose abstract follows.

The objective of the study was to develop a high-throughput electrochemical impedance spectroscopy (HTEIS) method for rapid and quantitative evaluation of corrosion protective coatings. A 12-element, spatially addressable electrochemical platform was designed, fabricated, and validated. This platform was interfaced to a commercial EIS instrument through an automated electronic switching unit. The HT-EIS system enables four parallel EIS measurements to be run simultaneously, which significantly reduces characterization time compared to that of serial EIS measurements using a multiplexer. The

performance of the HT-EIS system was validated using a series of model systems, including a Randles equivalent circuit, an electrochemical reaction ($\text{Ti}/\text{K}_4\text{FeCN}_6$, K_3FeCN_6), a highly uniform polymer film, and several polymer coatings. The results of the validation studies showed that the HT-EIS system enables a major reduction in characterization time and provides high quality data comparable to data obtained with conventional, single-cell EIS measurement systems.

This article was featured on the home page for the American Chemical Society for several days.

Since primers for corrosion protection typically involve the use of a corrosion inhibiting particle or pigment, a parallel high shear mixing apparatus was also needed for the combinatorial workflow. A parallel high shear mixing apparatus was designed and built. As shown in Figure 3.1-1, the six position mixing station consists of six commercially-available rotor stator homogenizers incorporated into an oscillating cup holder. The six 70 ml cups are rotated eccentrically in the holder relative to the homogenizer head. This action promotes the bulk mixing of the powders with the viscous liquid component while exposing the coarse blend to the high shear zone of the rotor stator head.

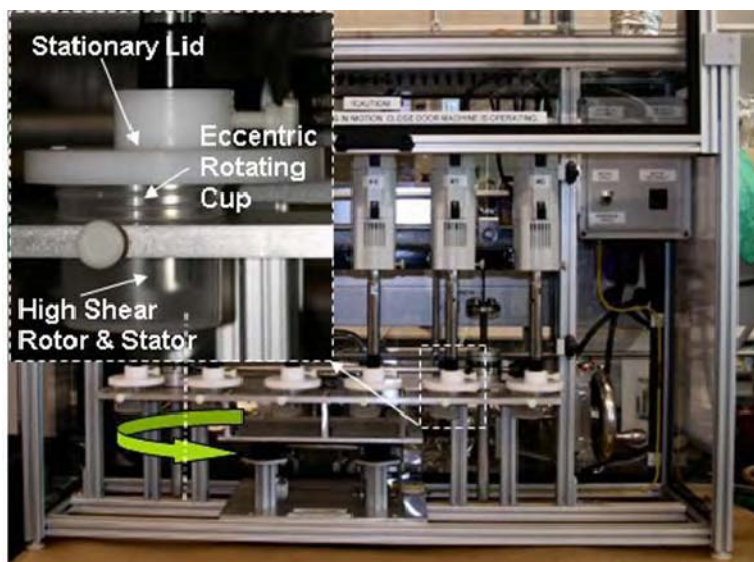


Figure 3.1-1. An image of the six station high shear mixing apparatus.

3.2 Mg-rich Primers Based on Hybrid Organic-Inorganic Binders

As discussed in the 2007 Annual Report, and in the manuscript included as **Appendix C**, “Combinatorial Materials Research Applied to the Development of New Surface Coatings XI: A Workflow for the Development of Hybrid Organic-Inorganic Coatings,” whose abstract follows.

Interest in hybrid organic-inorganic (HOI) materials has grown rapidly in the last two decades. The appeal of this broad class of materials can be attributed to the unique combinations of properties that can be achieved by combining an inorganic phase with an organic phase. HOI materials can be divided into two basic categories: homogeneous systems derived from monomers or miscible organic and inorganic components, and heterogeneous, phase-separated systems with domains ranging from angstroms to micrometers in size. The structure of the inorganic component is dependent on the interaction of many variables such as pH, water content, overall solution concentration, solvent composition, temperature, and time. Due to the complexity of HOI materials, a combinatorial/high-throughput approach to the development of novel materials is highly desired. The author's have recently developed a combinatorial workflow for the synthesis and characterization of HOI coatings.

Initial experimentation conducted with the workflow was focused on the development of primers for corrosion protection derived from a HOI binder system and magnesium particles. Both homogeneous and heterogeneous HOI binders were investigated. With just one iteration of the combinatorial workflow, heterogeneous, moisture-curable HOI binders were identified that enabled the formation of magnesium-rich primers that provided excellent corrosion protection to an aerospace aluminum alloy (Al 2024).

Mg-rich primers based on a hybrid organic-inorganic binder derived from silica nanoparticles and phenethyltrimethoxysilane gave excellent corrosion protection of Al 2024-T3. Work has continued on these coatings with particular emphasis on the silica nanoparticle functionalization process. To facilitate the synthesis of the nanoparticle-based binder system, a modification to our ChemSpeed Autoplant system was made in-house. The desire to utilize the ChemSpeed Autoplant was based on the knowledge of the high sensitivity of the sol-gel reactions used to prepare the binder systems to the reaction process conditions. The ChemSpeed Autoplant system provides accurate control over various process parameters such as temperature, reagent feed rates, stir speed, etc. The modification to the ChemSpeed Autoplant involved the fabrication of a distillation head to each reactor which would enable removal or low boiling solvent and water during processing. Figure 3.2-1 provides an image of a distillation head produced as well as a reactor module equipped with the distillation head. Currently, the system is being used to produce sols derived from colloidal silica and phenethyltrimethoxysilane and the properties of the binders as well as Mg-rich primers based on the binders are being evaluated.

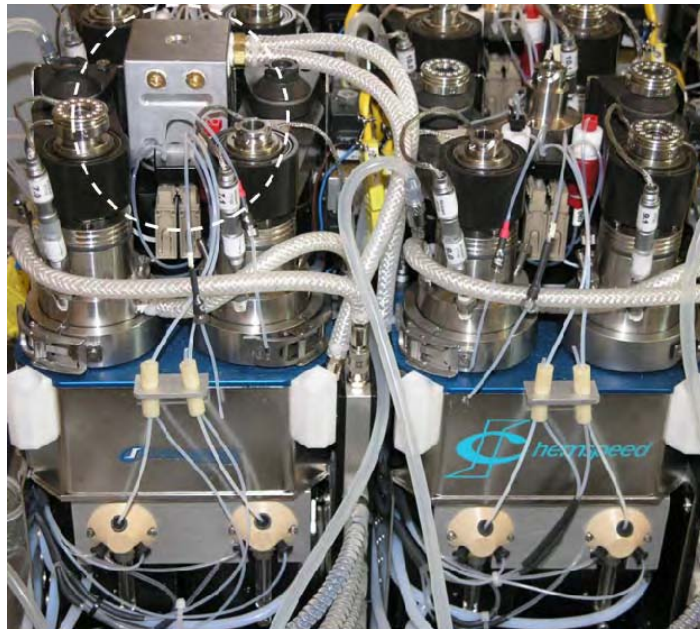


Figure 3.2-1. An image of a reactor vessel fitted with the new distillation head (highlighted circle).

3.3 Rapid-cure Mg-rich Primers Based on a Dual-Cure Polymerization Mechanism.

Based on Air Force needs for a rapid-cure coating system for aircraft that minimizes the amount of time the aircraft is out of service for repainting, work on a dual-cure binder system was initiated. The details of the work are described in a manuscript that will be published in the *Journal of Coatings Technology*. The manuscript is included as **Appendix D**, “Hybrid Organic/Inorganic Coatings Produced Using a Dual-Cure Mechanism,” whose abstract follows.

A coating precursor containing both acrylate functionality and trimethoxysilane functionality was produced by reacting bisphenol-A glycerolate diacrylate with 3-isocyanatopropyltrimethoxysilane. With this precursor, two different crosslinked networks can be produced. A polyacrylate network can be produced using a radiation-cure mechanism while a polysiloxane network can be produced by hydrolysis and condensation reactions involving the trimethoxysilane groups. The objective of the study was to determine the utility of this dual-cure system for generating rapid-cure coatings for corrosion protection. Coating properties were determined as a function of cure conditions. The results of the study showed that the formation siloxane crosslinks was significantly hindered by the crosslinked network induced by the UVcuring process. Even though the overall conversion of trimethoxysilane groups to siloxane crosslinks was relatively low, coating barrier properties were significantly enhanced and coating free volume reduced. At ambient conditions, additional crosslinking occurring through siloxane bond formation increased within the first four days after UV-curing. Beyond this period, siloxane bond formation remained unchanged as did coating properties.

4.0 Plasma Deposition of Inorganic Coatings

The application of plasmas toward thin film growth offers advantages such as denser deposits as well as growth of targeted phases at lower temperature given the additional enthalphy introduced into the system from the activated molecules.

Two different applications were evaluated for use in AFRL-relevant systems. The first related to a permanent pretreatment for aluminum that would be compatible with the NDSU Mg-rich primer (Task 2; Section 4.1). The second relates to a conductive and transparent coating that would serve as an in-field repair system for damaged polycarbonate aircraft canopies (Task 4; Section 4.2). The majority of the tasks have been completed for Section 4.1, while additional development is targeted for Section 4.2. This annual report will compile progress to date for each of these areas.

4.1 Permanent Pretreatment

The goal of this research project was the development of a permanent pretreatment layer that is (1) compatible with the Mg-rich primer and (2) resistant to the plastic-media blasting employed to strip paint at the depot. Such a thin coating would find value during repainting of aircraft as a nominally three-component system (i.e., pretreatment, primer, and topcoat) could be reduced to two components (i.e., primer and topcoat). A primary requisite for the pretreatment is that the galvanic function of the Mg-rich primer system must not be inhibited, and a layer thickness less than 100 nm would be anticipated. In addition, the layer must be durable enough to withstand media blasting and to accommodate airframe flexure. Finally, to be applied on legacy aircraft, a low deposition temperature is required to preclude ignition of combustibles.

Coatings development for this task focused on three separate efforts both at NDSU and at the facilities of industrial partners.

The first effort centered on plasma-enhanced chemical vapor deposition (*PECVD*) experiments at NDSU using trimethylsilane as a precursor gas. The results of this project were summarized in the 2007 DHC Annual report and efforts this year were aimed at publishing these results. Included as Appendix E is a manuscript entitled “Trimethylsilane-based pretreatments in a Mg-rich primer corrosion prevention system,” which has appeared in *Progress in Organic Coatings*. An abstract of this manuscript follows.

A trimethylsilane-based coating was investigated as a pretreatment for Al-2024 T3 in a novel Mg-rich

primer corrosion prevention system. SiC-based thin films were deposited onto Al substrates by plasma enhanced chemical vapor deposition (PECVD). A screening study of the pressure (P) dependence of films deposited at 350 °C showed an increase in growth rate from 0.6 to 1.9 Torr. A second screening study where P was fixed at 1.9 Torr and temperature (T) was varied from 125 to 550 °C showed decreasing growth rates with increasing temperature with an apparent transition around 300 °C. Electrochemical impedance spectroscopy (EIS) of the SiC-based films on Al-2024 after exposure to a corrosive environment (i.e., dilute Harrison solution) indicated that samples coated using SiC-based films exhibit higher low frequency impedance (i.e., 100–1000× higher) than bare Al-2024 with open circuit potential remaining 0.1V higher for the former suggesting the SiC-based films slow the corrosion process. A Mg-rich primer was coated onto the SiC on Al-2024 with the galvanic function of the system determined by EIS. As compared to SiC on Al-2024, a similar behavior for the lowfrequency impedance was observed for the Mg-rich primer-coated samples with some films exhibiting $1E + 8$ at 0.1Hz indicating a strong barrier property. Initial gas jet erosion using acrylic media indicates the Mg-rich primer coatings are removed in preference to the Si-C films—the first step toward demonstrating a permanent pretreatment. When successfully developed and optimized, the value of such a hard, protective coating is the reduction of a three-component coatings system (i.e., pretreatment, primer, and topcoat) to a two-component system (i.e., primer and topcoat). © 2008 Elsevier B.V. All rights reserved.

The second effort area related to a novel plasma spray route to thin coatings through a subaward relationship with a company, Sulzer-Metco (US), Inc. (Westbury, NY). While most plasma spray routes to coatings utilize solids as the precursor feedstock, metal-organic precursor plasma spray (*MOPPS*) is an area that we have investigated recently as a novel route to thin film materials. Very thin films are possible via MOPPS and the technology offers the possibility of forming graded structures by metering the liquid feed. To date, liquid-based precursor plasma spray efforts have utilized solutions of metal salts or dispersed colloidal particles with a limitation of these approaches related to the fact that most of the plasma energy is expended toward evaporation/combustion of the solvent which starves this process of the energy required to promote film formation.

The work from this year employed metal-organic compounds that are liquids at standard temperature-pressure conditions. In addition, these complexes contain chemical functionality that allows straightforward thermolytic transformation to targeted phases of interest. Toward that end, aluminum *sec*-butoxide ($Al(OBu)_3$) and aluminum 3,5-heptanedionate ($Al(hd)_3$) were used as precursors to alumina while triethylsilane ($HSi(C_2H_5)_3$) and titanium tetrakisdiethylamide ($Ti(N(C_2H_5)_2)_4$) were employed for studies toward silicon carbide and titanium-nitride-carbide. In all instances, the precursors contain metal-heteroatom bonds envisioned to provide atomic concentrations of the appropriate reagents at the film growth surface thus promoting phase formation (e.g., Si-C bond in triethylsilane, Ti-N bond in titanium amide, etc.). Films were deposited using a Sulzer Metco Triplex Pro-200 Plasma Spray system under various experimental conditions using Design of Experiment (DoE) principles. The composition and morphology of these films was studied as a function of application conditions. Film compositions were analyzed by glancing incidence x-ray diffraction (GXRD) and elemental determination by x-ray spectroscopy (EDS). Silicon carbide and titanium-nitride-carbide films typically exhibited a continuous morphology with reasonable adhesion (i.e., passed tape pull adhesion test) while aluminum oxide films ranged from powdery to continuous but suffered from poor adhesion. These results are the subject of an upcoming presentation at the American Vacuum Society Fall Meeting (Boston, MA Oct 19-24, 2008).

Film growth for the third effort area was realized through a subaward relationship with International Technology Center (ITC). The approach to a thin, SiC-based pretreatment layer employed by ITC encompassed a proof-of-feasibility for using overvoltage potentials in atmospheric pressure dielectric barrier discharge plasma (*APDBDP*) technology as a means of depositing hard coatings at atmospheric pressure conditions without the use of secondary gases like helium to sustain the glow discharge. The

hard coating of interest was a SiC based film from a precursor gas mixture of 2% trimethylsilane ($\text{SiH}(\text{CH}_3)_3$) in a balance of molecular nitrogen (N_2).

The results of this work are summarized in a Final Report from ITC to NDSU (see **Appendix F**). SiC films produced by ITC are presently being shipped to NDSU for characterization. It is anticipated that these results will be the subject of a future publication in a peer-reviewed journal.

4.2 Deposition of Transparent Conductive Indium and Tin Oxides by Atmospheric Pressure Plasma Jet – Toward In-field Aircraft Canopy Repair

Transparent conductive oxides (TCOs) have found broad application over the past few decades in photovoltaics, flat panel displays, and other electronic applications. Traditionally, TCO deposition has been performed at moderate temperature using vacuum-based growth systems which is not readily applicable to deposition on inexpensive polymer substrates (e.g., Mylar) nor roll-to-roll manufacturing. The aim of this project is to develop an atmospheric pressure plasma deposition system to deposit a transparent conducting oxide (TCO) layer that is (1) highly transparent and (2) shows good conductivity. This coating would have application in the field repair of aircraft canopies where TCO layers are used to reduce the buildup of static charge. Currently, damaged canopies are repaired with conductive epoxy, or replaced entirely. The conductive epoxy repair results in a reduction in pilot visibility and therefore is only appropriate for limited areas of the canopy. Complete canopy replacement results in the need to maintain inventory of expensive, bulky components at airbases around the world, an expensive and logically challenging task. The proposed coating solution could be housed in equipment roughly the size of a file cabinet, with relatively reasonable cost and high portability. The following materials properties are the metrics to establish initial proof-of-concept and represent the immediate goal of this project:

- Sheet Resistance of $10 \Omega/\text{square}$ or less;
- Optical transmittance $> 80\%$ at 550 nm ; and,
- Coating durability that meets MIL-C-48497.

Efforts this year were related to screening metal beta-diketonate complexes to both indium oxide and tin oxide thin films. For InO_x films, $\text{In}(\text{acac})_3$ was observed to yield good films using our atmospheric pressure plasma jet (APPJ) system. The results of this screening study were reported at the *2008 International Conference on Metallurgical Coatings and Thin Films* (ICMCTF) and are the subject of an article in *Surface and Coatings Technology* (see draft proof with corrections attached as **Appendix G**), whose abstract follows.

Indium (III) beta-diketonate complexes were employed as the solid precursor sources in the atmospheric-pressure plasma chemical vapor deposition of indium oxide films using He carrier gas, O_2 reactant gas and growth temperatures from 25 to 250°C . Ellipsometry and X-ray reflectivity showed that the films varied in thicknesses from 40 to 70 nm over the 30 cm^2 deposition growth area for a 12 min duty cycle. The as-deposited films exhibit transmittance in excess of 90% over the visible spectrum while maintaining resistivity on the order of $10^{-2} \Omega \text{ cm}$. Improved electrical properties (i.e., $\rho \text{b} 10^{-3} \Omega \text{ cm}$) were observed after thermal treatment ($T \sim 200^\circ\text{C}$) in a controlled gas ambient tube furnace. © 2008 Elsevier B.V. All rights reserved.

Two tin (III) beta-diketonate complexes were screened during this year's effort and it was found that $\text{Sn}(\text{hexafluoroacetylacetone})_2$ ($\text{Sn}(\text{hfa})_2$) had characteristics that did not yield a desirable vapor pressure. Toward that end, the $\text{Sn}(\text{hfa})_2$ precursor exhibited very little sublimation at atmospheric pressure at room temperature which led to the requirement that the precursor be heated. Upon slowly raising the precursor temperature, very little flux was noted in the carrier gas stream. While heating to a high enough temperature did result in sublimation, the temperature difference between no flux and an overwhelming amount of precursor in the gas stream was less than 10 degrees. Thus, efforts to utilize $\text{Sn}(\text{hfa})_2$ as a

precursor were abandoned given the engineering challenges associated with this physical characteristic. It was found that Sn(trifluoroacetylacetone)₂ (Sn(tfa)₂) possesses atmospheric-pressure sublimation characteristics that afford good materials transport. Sn(tfa)₂ was synthesized in-house and was twice sublimed prior to experimentation. The results of the proof-of-concept study for Sn(tfa)₂ will be the subject of an upcoming Materials Research Society Presentation at the Fall 2008 Meeting in Boston.

Finally, the APPJ system was reconfigured this year to allow the use of two solid-source precursors at the same time. The growth of In-Sn-O films from In(acac)₃ and Sn(tfa)₂ will be the subject of next year's research with the majority of the program funding used to support the efforts of graduate and undergraduate students who will grow the films and characterize the materials.

5.0 Coating Prognostics

In new task this year (Task 5), NDSU investigated the application of embedded electrochemical sensors for magnesium-rich primers. Unlike conventional electrochemical sensors that monitor the metal substrate itself and provide no information about the coating, the NDSU *in situ* corrosion sensors are embedded between the primer and the topcoat and thus are suitable for monitoring the corrosion protection afforded by the metal-rich primer. As an added advantage, the embedded sensor electrodes are shielded from the environment by the topcoat, which prolongs the electrode life as well as reduces the noise associated with measurements. Moreover, electrochemical measurements of the primer and primer/metal interface can be carried out without being masked by high resistant topcoats.

5.1 Embedded Sensor Approach for Monitoring Cathodic Protections of AA2024-T3 by a Mg-Rich Primer

Mg-rich primers are an alternate for Cr-rich primers that are currently used by the Air Force for the protection of aluminum structures. The magnesium pigments provide cathodic protection for the less active aluminum substrates and also provide a barrier type protection as the products from the Mg dissolution insulate the substrate from the environment. The cathodic protection is comparable to Zn-rich primers for steel substrates. Electrochemical impedance spectroscopic characterization of a Mg-rich primer and a standard Air Force urethane topcoat/Mg-rich primer system, both on AA 2024-T3 substrates, were investigated. The systems were exposed to constant immersion in dilute Harrison's solution, and embedded electrodes between the topcoat and primer were used to access the behavior of the Mg primer/substrate system while beneath the topcoat. Experimental results demonstrated the cathodic protection of the bare Mg-rich primer and the primer beneath a topcoat. Analysis of the EIS data by a Voigt element model was done to compare the behaviors of the bare primer and the primer beneath the topcoat. Interpretation of the data is intended to highlight the evolution of the electrochemical properties of the primer and topcoat/primer systems as the cathodic protection is reduced during the consumption of the Mg-rich pigments.

The time dependent electrochemical behavior of a Mg-rich primer and a topcoat/primer system on AA 2024-T3 was monitored using EIS experimentation. The open circuit potential values monitored over time for both systems indicated the change from a mixed potential value to a value consistent with the substrate. This demonstrated the loss of the cathodic protection. The topcoat extended the time of cathodic protection of the primer. Conventional monitoring of cathodic protection for active pigment coatings by monitoring Eoc in a three-electrode setup is not practical for field monitoring. The feasibility of monitoring the cathodic protection of a primer beneath a topcoat using EIS data acquired with an embedded sensor between the topcoat and primer has been demonstrated. EIS data associated with the primer and topcoat/primer systems and analyzed using a 12 element Voigt model indicate that the resistance value associated with the largest time constant tracked the loss of cathodic protection of both

primer-only and topcoated systems better than the low frequency modulus parameter. The approach of using an embedded sensor for tracking cathodic protection presented here is being developed for the field monitoring of Mg-rich primers beneath topcoats.

For detailed description of this experiment, refer to the manuscript accepted for publication in Proceedings of the Eurocorr 2008, the European Corrosion Congress, September 7-11, 2008, Edinburgh, UK, and included in **Appendix I**, “In Situ Monitoring of a Mg-Rich Primer Beneath a Topcoat Exposed to Prohesion Conditions.”

5.2 In Situ Monitoring of a Mg-Rich Primer beneath a Topcoat Exposed to Prohesion Environment

Mg-rich primers have been proven to be an adequate alternative for chromate-based coatings [Nanna, 2004] for the protection of aluminum alloys from corrosion. Its protection behavior was attributed to a combination of cathodic and barrier protection [Battocchi 2006 (1 and 2)], similar to the protection behavior associate with Zn-rich primers on steel substrates.

The performance of a Mg-rich primer on aluminum 2024-T3 under Prohesion[®] exposure (ASTM G85) has been monitored using an embedded sensor placed at the surface of the primer and below the topcoat. This accelerated weathering cycle is an alternative of wet and dry cycles to simulate outdoor weather exposure.

Electrochemical impedance spectroscopy (EIS) and electrochemical noise methods (ENM) experiments were conducted to monitor the performances and the electrochemical properties of the system beneath the topcoat. The data analysis demonstrates that the sensor is able to detect change in the barrier property of the topcoat in response to the exposure conditions and the activation of the active pigments in the primer in presence of the electrolyte.

The Mg-rich primer and polyurethane clear topcoat system were applied onto the AA2024-T3 substrate and the platinum sensor was embedded between the primer and the topcoat. Afterwards, the coated substrate was put into the standardized Prohesion[®] chamber to simulate weathering conditions in an aggressive manner to induce accelerated coating failure. The acquisition of EIS and ENM data from embedded sensor in-situ monitoring during the Prohesion[®] dry and wet steps demonstrated the coating behavior evolution. In this study, it was found that both EIS and ENM in-situ monitoring could be conducted under either dry or wet Prohesion[®] steps with the embedded sensors. Under the dry step, the coatings were sensitive to temperature changing, while in the wet step, the resistance values were more scattered due to the moisture accumulation on the coating surface. Both the temperature and humidity variation related coating property changes in Prohesion[®] chamber were *in situ* monitored by the embedded sensors. It was found that the coating degraded continuously with Prohesion exposure time shown by a continuous decrease both in low frequency impedance $|Z|_{0.05\text{ Hz}}$ and noise resistance R_n .

For detailed description of this experiment, refer to **Appendix I**, “In Situ Monitoring of a Mg-Rich Primer Beneath a Topcoat Exposed to Prohesion Conditions.”

5.3 Wire-Beam Electrode Studies

Aluminum alloys are particularly sensitive to localized attacks, and non-uniform electrochemical conditions are frequent on a coated surface. For a more complete interpretation of the events occurring under a coating on this type of substrate, a set of area-dependent information is necessary. For this purpose, the wire-beam electrode (WBE) has been constructed and is currently under testing at NDSU

[Battocchi 2005]. The principle of this type of electrode is subdividing a metal plate into many small parts, and measuring the electrochemical properties of each part by means of individual sensors [Wu 1995]. The schematic of the wire-beam electrode used in this research effort is shown in Figure 5.3-1. Here, the surface of the WBE is divided into 100 individual electrodes made of AA2024-T3 wire and represented by circles in Fig. 5.3-1 (b). The electrodes are then coated with Mg-rich primer, and the sensor is then applied over the primer. The WBE arrangement shown in Fig. 5.3-1 is the actual electrode layout used in this experiment. Green circles indicate the individual wires that were used to collect electrochemical information, and the embedded electrode is show in the position it is found within the actual WBE assembly.

In this WBE setup described above, one wire at a time can be activated, thus creating an electrochemical cell between the sensor electrode, acting as a Reference/Counter Electrode pair (RE/CE), and this particular wire of the working electrode array. By switching between individual WE wires or combinations of several wires, we were be able to poll the entire area monitored by the SE for electrochemical activity. The Gamry PCI4-300 potentiostat PC card is connected to the auto-switch transmission board shown in Figure 5.3-2. The auto switch accomplishes the task of switching electrodes, which can be a tedious procedure.

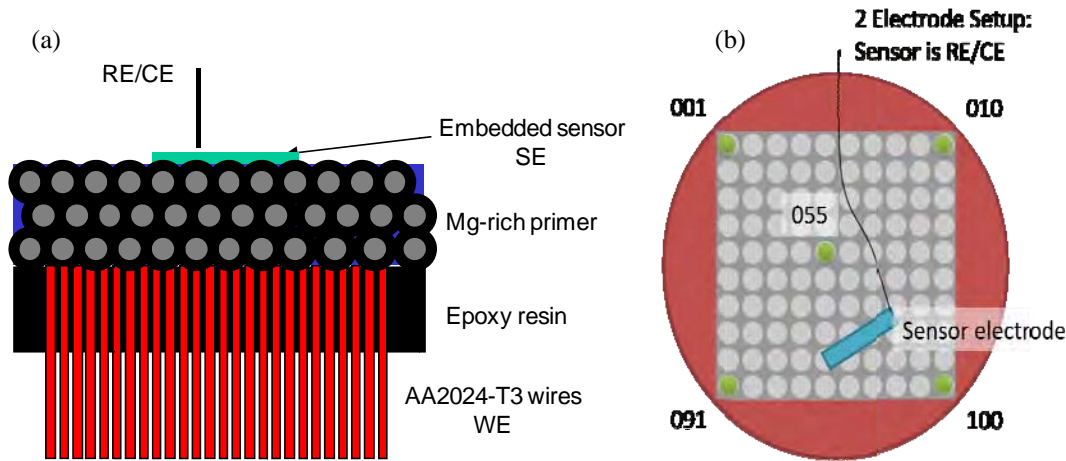


Figure 5.3-1 Schematic of the wire-beam electrode: (a) side and (b) top views.

In order to design a successful electrochemical sensor, it is imperative to understand how the geometry and dimensions of the sensor electrode influence its ability to detect small signals as a function of its separation from the substrate (WE). Therefore, several working electrode (wires) located at various distances from the sensor electrode were selected. These are marked with green circles on the diagram (b) in Figure 5.3-1.

The wires in locations shown in Fig. 5.3-1 (b) acted as working electrodes in a series of electrochemical impedance spectroscopy (EIS) experiments. EIS were collected using both the two- and three-electrode setup. The conventional three-electrode setup utilizes a reference (RE) and a counter electrode (CE) to apply the ac potential to the cell and measure the current. In the modified 2-electrode setup, the sensor electrode acts as both the reference and the counter electrode. Such simplified setup is more conducive to miniaturization, as it uses fewer parts, yet a reliable E_{oc} reading may not be possible. The goal of this experiment is to demonstrate the feasibility of using the two-electrode approach to EIS data acquisition for embedded sensor applications.

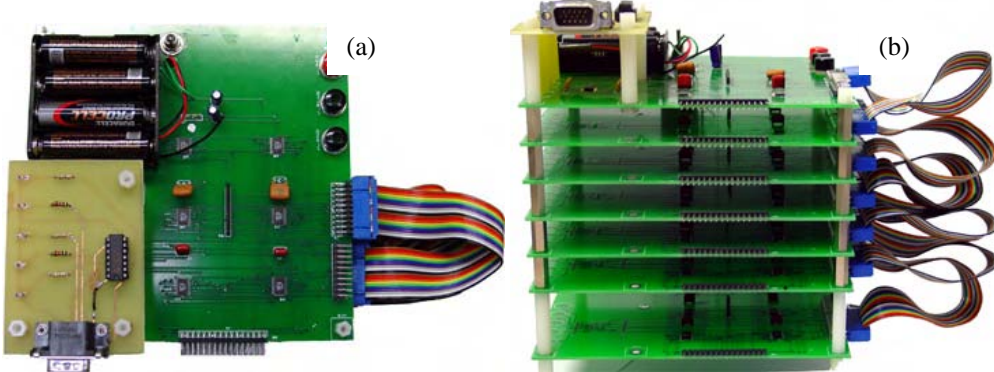


Figure 5.3-2 Wire-Beam Electrode Auto Switch: (a) top and (b) side views.

Figures 5.3-3 through 5.3-7 show the comparison of EIS impedance modulus spectra for the 5 working electrodes in positions 001, 010, 055, 091, and 100 in both 2- and 3-electrode EIS experiments at different immersion times. For simplicity, we show results for 2 and 4 weeks of constant immersion in dilute Harrison's solution (0.35 wt% $(\text{NH}_4)_2\text{SO}_4$ and 0.05wt% NaCl in water).

It can be seen that there are no difference in the measured impedance modulus between the data collected with either electrode configuration.

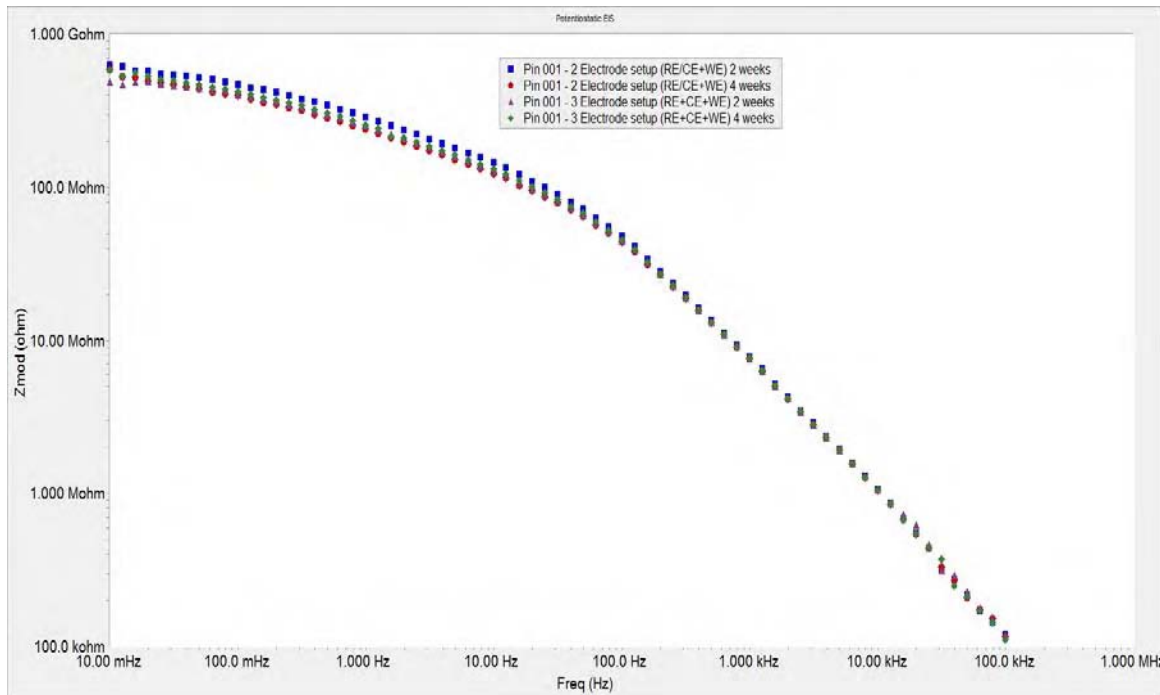


Figure 5.3-3. EIS for the WBE experiment on Wire 001: impedance modulus spectra collected in a 2- and 3-electrode setup.

The low-frequency (10 mHz) impedance modulus ($|Z|$) values follow the geometry of the electrode arrangement. The highest $|Z|$ values were observed for wires 001 and 010 that are located the farthest from the sensor electrode, on the order of $5-6 \times 10^8$ Ohm and 1×10^9 Ohm, respectively. The lowest values were observed for the two electrodes that are located closest to the sensor, namely 091 and 100, with modulus values on the order of 2×10^7 Ohm and 6×10^7 Ohm, respectively. This observation is explained by the fact that resistance is distance dependent, and larger separation between the sensor acting as a CE/RE pair and the working electrode (WBE wire) results in smaller currents flowing between the sensor and the wire.

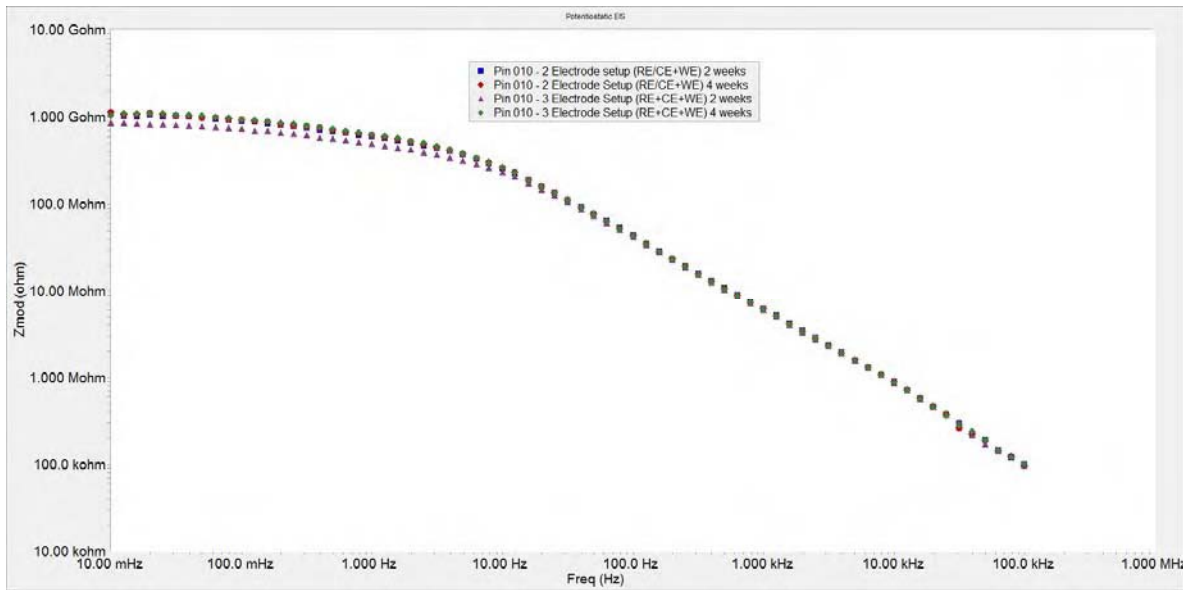


Figure 5.3-4. EIS for the WBE experiment on Wire 010: impedance modulus spectra collected in a 2- and 3-electrode setup.

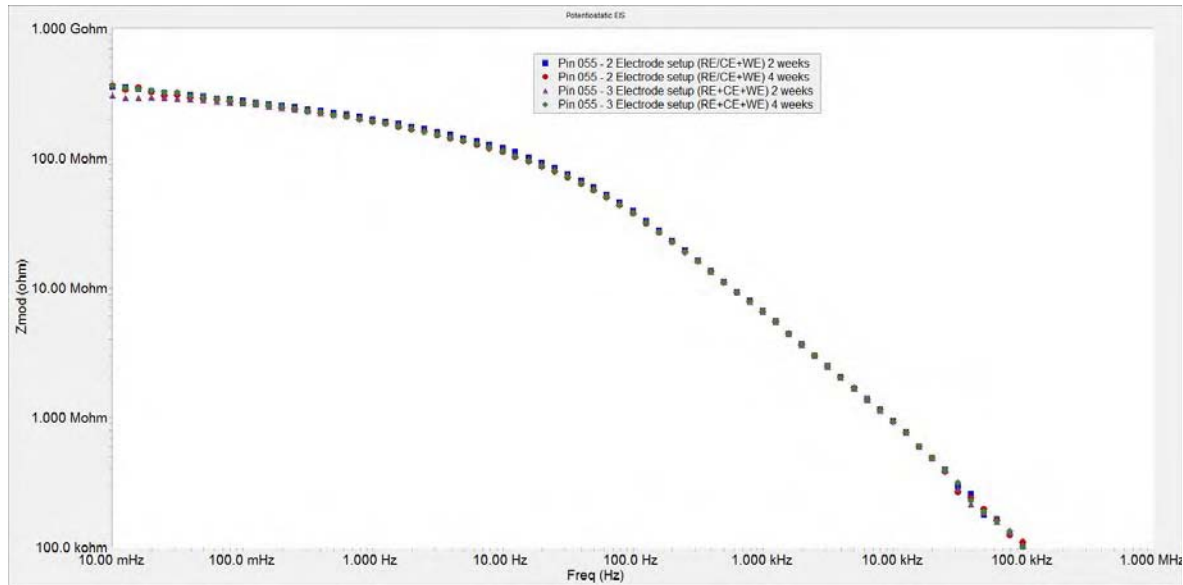


Figure 5.3-5. EIS for the WBE experiment on Wire 055: impedance modulus spectra collected in a 2- and 3-electrode setup.

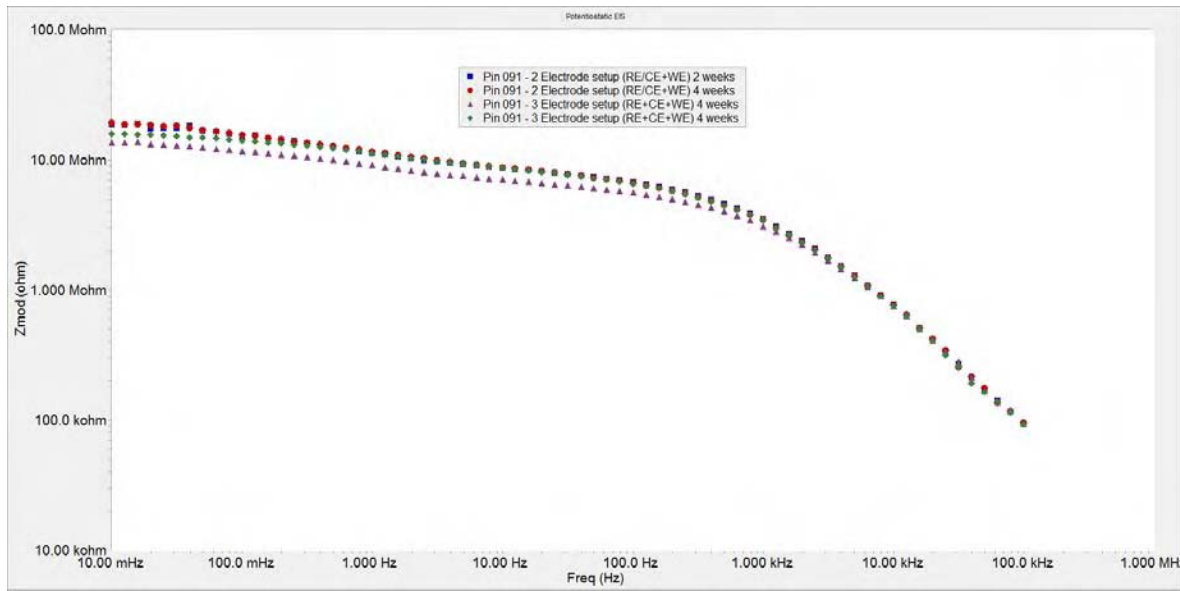


Figure 5.3-6. EIS for the WBE experiment on Wire 091: impedance modulus spectra collected in a 2- and 3-electrode setup.

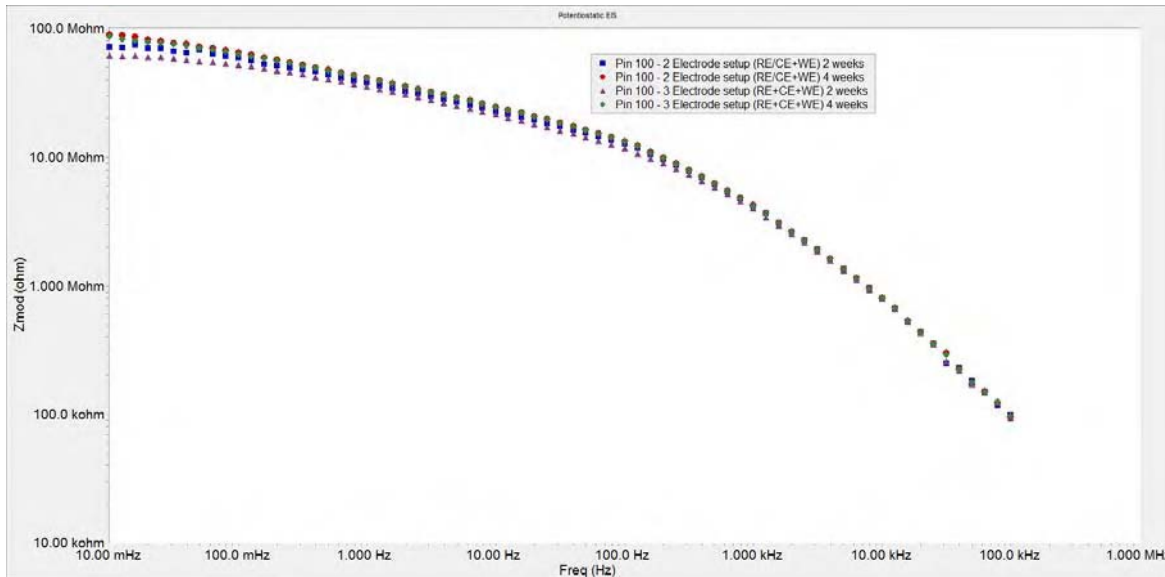


Figure 5.3-7. EIS for the WBE experiment on Wire 100: impedance modulus spectra collected in a 2- and 3-electrode setup.

The impedance modulus spectra for all 5 wire locations at 4 weeks of constant immersion are presented in Figure 5.3-8, along with the spectrum of a 3-electrode setup with all 5 wires connected simultaneously. The low-frequency (10 mHz) modulus values indicate that when all five pins are acting as one working electrode, the resulting impedance is lower than the lowest value. This suggests the linearity of the WBE

array, as the addition of more wires to the working electrode creates more conductive pathways for the current, thus lowering the overall impedance of the electrochemical cell.

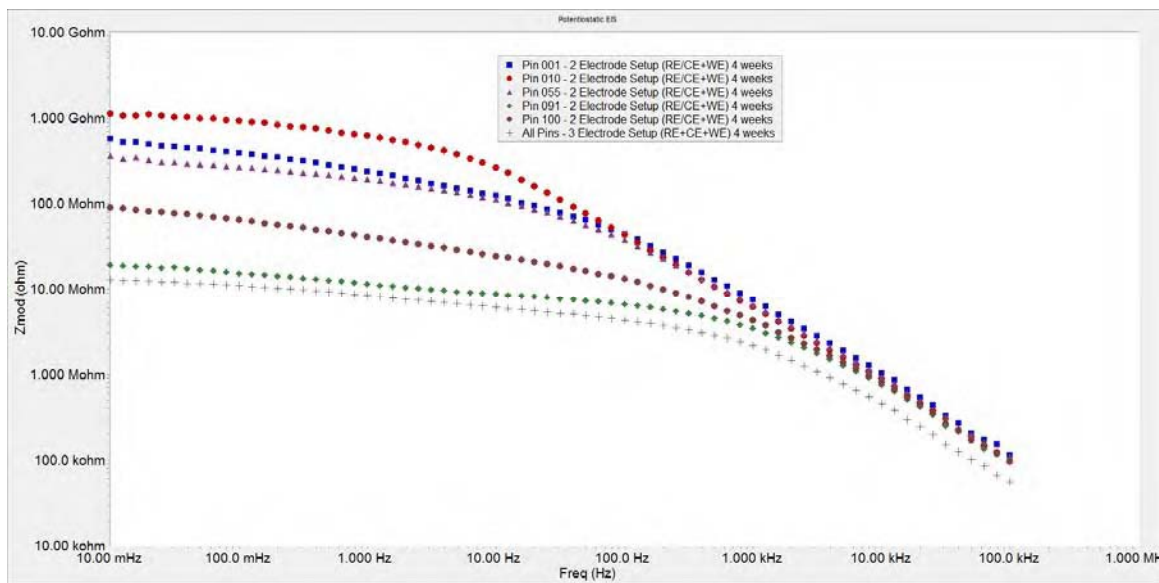


Figure 5.3-8. EIS for the WBE experiment: impedance modulus spectra collected in a 2E setup on individual wires and in a 3E setup for all wires.

By conducting a series of wire-beam experiments, we have shown that the electrochemical response of the sensor electrode acting as a combination reference/counter electrode is identical to the electrochemical response measured by separate reference and counter electrodes. The impedance modulus measured by the sensor electrode applied over Mg-rich primer is found to be the function of separation between the sensor and the electrochemically active site on the substrate. At the same time, the impedance response is strongly influenced by the most electroactive site in the system, or by the site and the closest proximity to the sensor. For all practical purposes, it is this lowest value of impedance modulus measured by the embedded sensor that is going to determine the overall level of corrosion protection afforded by the Mg-rich primer.

5.4 Real time monitoring of an Air Force topcoat/Mg-rich primer system in B117 exposure by embedded electrodes

The protection of metallic structures by organic coatings has traditionally been by virtue of a physical barrier, reducing the transport of water, ions, and oxygen from the environment to the substrate. Organic coatings are also used as repositories for corrosion inhibitors that passivate the substrate, and metallic particulates, that provide cathodic protection. Of the latter, Zn-rich primers are universally used for the protection of steel substrates with the zinc particles being sacrificially consumed while providing a mixed potential that mitigates the corrosion of the steel. Mg-rich primers have been developed for the protection of aluminum substrates, with a similar protection mechanism as that of Zn-rich primers. Real time monitoring of a Mg-rich primer on an AA2024-T3 substrate, beneath a standard Air Force topcoat, is currently being conducted where coatings are subjected to B117 exposure. Monitoring is accomplished using embedded electrodes placed between the primer and topcoat. Electrochemical impedance spectroscopy and electrochemical noise method experiments are carried out to assess the performance of the primer in the aggressive salt spray environment. *In situ* results will be compared with results of *ex situ*

electrochemical experiments. Results associated with configurations that do and do not include the substrate will demonstrate the applicability of the embedded electrodes for real-time monitoring.

The results of this research will be presented at the 2009 NACE Corrosion Conference and Expo in Atlanta, GA.

References for Section 5.0

D. Battocchi, J. He, G.P. Bierwagen, and D.E. Tallman, *Emulation and study of the corrosion behavior of Al alloy 2024-T3 using a wire beam electrode (WBE) in conjunction with scanning vibrating electrode technique (SVET)*, *Corrosion Science*, **2005**, 47(5), 1165-1176.

C. L. Wu, X. J. Zhou, Y. J. Tan; *Progress in Organic Coatings*, **1995**, 25, 379-389.

M. E. Nanna and G. P. Bierwagen, *J. Coating technol. Res.* 2004, 1, 69.

D. Battocchi, A. M. Simoes, D. E. Tallman and G. P. Bierwagen, *Corr. Sci.* 2006, 48, 1292.

D. Battocchi, A. M. Simoes, D. E. Tallman and G. P. Bierwagen, *Corr. Sci.* 2006, 48, 2226.

6.0 Program Management

The Durable Hybrid Coatings program has the following management structure:

- Technical Manager for Department of Coatings and Polymeric Materials activities: Dante Battocchi, Research Assistant Professor, Department of Coatings and Polymeric Materials.
- Technical Manager for Center for Nanoscale Science and Engineering activities: Dr. Bret J. Chisholm, Senior Research Scientist, Center for Nanoscale Science and Engineering.
- Technical Manager for inorganic hard coatings Studies: Dr. Douglas L. Schulz, Senior Research Scientist, Center for Nanoscale Science and Engineering.
- Senior Scientific Advisor: Dr. Gordon Bierwagen, Professor, Department of Coatings and Polymeric Materials. [PI of record]
- Dr. Vsevolod “Séva” Balbyshev, Research Scientist, Center for Nanoscale Science and Engineering, coordinates new work on aircraft health prognostics.
- Program Manager and management POC for AFRL: Dr. Gregory J. McCarthy, Director, Center for Nanoscale Science and Engineering.

Additional senior research staff include:

- Dr. Kerry N. Allahar, Research Assistant Professor, Department of Coatings and Polymeric Materials.
- Dr. Jie “Jim” He, Research Associate, Center for Nanoscale Science and Engineering.
- Mr. James Bahr, Senior Research Engineer, Center for Nanoscale Science and Engineering.
- Mr. Robert Sailer, Research Engineer, Center for Nanoscale Science and Engineering.

Three Graduate Research Assistants and seven Undergraduate Research Assistants worked on this program during the past year.

The Durable Hybrid Coatings program at AFRL was initiated in July 2004, and with the supplement for new work added in 2008, the end date is now May 2011. An Annual Progress Report is due each September, with a Final Report due after the close of the program.

The following table summarizes expenditures on the program through September 2007.

Durable Hybrid Coatings
Cooperative Agreement FA8650-04-1-5045
July 2004 to May 2011
Annual Report for Period ending August 30, 2008

	July-04 to Sept-07	Oct-07 to Aug-08	Total Expenditures	Budget	Balance
Personnel	\$879,344	\$514,278	\$1,393,622	\$2,314,743	\$921,121
Direct Operating Costs	\$119,863	\$389,220	\$509,083	\$649,062	\$139,979
Subcontracts	\$120,368	\$34,716	\$155,084	\$162,247	\$7,163
Capital Equipment	\$426,859	\$1,323	\$428,182	\$561,529	\$133,347
Indirect (F&A) Costs	\$519,930	\$303,132	\$823,062	\$1,282,219	\$459,157
Total	\$2,066,364	\$1,242,669	\$3,309,033	\$4,969,800	\$1,660,767

The Use of Mg Alloys as Pigments in Mg-rich Primers For Protecting Al Alloys

Hong Xu¹, Dante Battocchi^{1, 2}, Dennis E. Tallman¹ and Gordon P. Bierwagen^{1, 2}

¹*Coatings and Polymeric Materials Department*

²*Center for Surface Protection*

North Dakota State University

**1735 NDSU Research Park Drive
Fargo, ND, USA, 58105**

Abstract:

As an alternative to toxic Chromate coating, Mg-rich primers have been designed to protect Al alloys (in particular AA 2024 T3) and developed in analogy to Zn-rich primers for steel substrate. The Mg pigment present in the primer can provide cathodic protection to Al substrates and significantly deter Al alloy corrosion when damage occurs.¹

In order to determine how much the pigment metal alloy composition can be varied without sacrificing corrosion protection, three different primers based on magnesium alloy powders as pigments were formulated with an epoxy-polyamide polymer binder at different pigment volume concentrations (PVCs). Their behaviours were studied after cyclic exposure in Prohesion Chamber via electrochemical methods.

Testing results from Electrochemical Impedance Spectroscopy (EIS) and Scanning Electron Microscopy (SEM) showed that the metal-rich primers with Mg alloys as pigments could provide cathodic protection, and precipitates formed from oxidation of Mg alloy particles were similar to the ones found in the pure Mg-rich primer system. Furthermore, the investigation of the properties of the three alloy pigments gave a good understanding of the effects of particle shape, particle size, particle size distribution and metal alloy chemical composition.

Introduction:

Aluminum alloys, especially AA2024 T3, are widely used in the aerospace industry because of their high strength and stiffness combined with low density. However, Al alloys are very sensitive to corrosion environments due to their high copper content. Currently, chromate pre-treatment and chromate primer coatings are used to protect aluminum alloys from corrosive attacks.² However, with increasing environmental concerns, toxic chromate based coatings (including chromate pigments and chromate metal pretreatments) need to be replaced from coating systems and stringent regulations on their use are due to be enforced by the governments.

In analogy to the Zinc-rich primer coatings that keep steel from corrosion through cathodic protection, a promising alternative, Mg-rich primer coatings, were designed, examined and developed by M. E. Nanna, D. Battocchi and G. P. Bierwagen at NDSU.³⁻⁶ By using pure magnesium pigment, which is more active than aluminum alloy substrate, Mg-rich primers were formulated around the Critical Pigment Volume Concentration (CPVC) to make sure there are good electrical conductivities among pigment particles and between pigment and substrate. The AA2024 T3 panels coated by the Mg-rich primer combined with a topcoat successfully passed 5000 hours of Prohesion exposure and exhibited excellent corrosion protection for aluminum alloy. Furthermore, various electrochemical techniques, such as electrochemical impedance spectroscopy (EIS), scanning vibrating electrode technique (SVET) and scanning electrochemical microscopy (SECM), were used to assess global or local corrosion protection mechanisms of the Mg-rich primer. It was proved that Mg-rich primer could provide good cathodic protection to AA 2024 T3 when damage occurred^{1, 7, 8} and, further, present certain barrier₁

protection ascribed to corrosion products.

Mg alloys, which contain different elements at various concentrations, show better mechanical properties than pure Mg. However, the corrosion resistance of Mg alloys are significantly affected by the added elements as well as alloys' micro morphology.^{9, 10} For example, trace amounts of iron or copper can increase Mg alloys' corrosion rate dramatically; however, addition of zinc or manganese in large amount can decrease the corrosion rate of Mg alloys. Therefore, it could be expected that by using Mg alloy pigments in place of pure Mg particles in Mg-rich primer system, different corrosion resistance performances of Mg-rich primers would be observed due to the effects of the Mg alloy pigments. Optimistically, we are interested in finding some suitable Mg alloy pigments for the Mg-rich primer system based on their various anti-corrosion behaviours. In this very initial work, we evaluate how much we can vary the pigment composition from pure magnesium in the Mg-rich primer system, as well as the effects of particle size and particle shape on the properties of the primer, without losing the protective behaviour.

Thus, three different Mg alloy particles as pigments were chosen for the first investigation. They were AM60, AZ91B and LNR91, which had different Al contents of 5%, 8.5% and 50%, respectively; in addition, they had dissimilar particle shape, particle size, particle size distribution (PSD) and oil absorption. Different metal rich primers were formulated by using the above three magnesium alloys as pigments in an epoxy-polyamide polymer matrix at different PVCs.

Electrochemical Impedance Spectroscopy (EIS) is a fast and useful method widely applied in monitoring and evaluating the performance of organic coatings, especially the corrosion protection abilities. In our study, EIS was used to characterize the electrochemical performances of different Mg alloy pigmented primers before or after certain exposure time. Scanning Electron Microscopy (SEM) was used to identify the shapes of the different Mg alloy pigments and the surface morphology of exposed Mg alloy pigmented primers. The measurement of particle size and PSD of the magnesium alloy pigments provided information useful for understanding their effects on primer behaviour.

2. Experimental:

2.1. Property measurements of Mg alloy pigments:

Particle size and PSD of pigments were measured by using Accusizer 780 optical particle sizer (Lab Recyclers Inc., Gaithersburg, MD, USA), which is a single particle optical sensing (SPOS) method. The magnesium alloy particles suspended by acetone passed through a "photozone" one by one; meanwhile, the signal (a pulse) was recorded when an individual particle obscured the photozone with a certain area that is related to the mean diameter of the particle. The particle size distribution was obtained by comparing the single signal strength with a standard calibration curve.

Oil absorption of pigments was tested according to ASTM D281 by using the Spatula Rub-Out method. Linseed oil was added to a certain quantity of pigments drop by drop, and the pigments and Linseed oil were mixed thoroughly with the spatula. When the spatula could hold all pigments together, the end point was reached. Oil absorption was expressed as gram of oil per 100 grams of pigment. Theoretical CPVC was calculated from the Oil absorption and pigment density.¹¹

2.2. Experimental flow:

A flow chart for the experimental procedures used in our studies is presented in Figure 1. All the AA2024 T3 panels supplied by Q Panel Lab products (Cleveland, OH, USA) were polished by 220 grit and 600 grit sand papers to remove the oxide layer and finally rinsed by hexane. The Mg alloys granulates were supplied by Reade (READE Advanced Materials, East Providence, Rhode Island, USA)

An epoxy-polyamide organic coating system, which has been used in Zn-rich primers for a number of years, was used as the polymer binder in magnesium alloy rich primer to provide good adhesion between primer and substrate, as well as certain barrier property. The Mg alloy primer paints were formulated at different PVCs but about CPVC in order to obtain good electrical conductivity among pigments and between pigment and metal substrate. Methyl Ethyl Ketone was used as solvent to give appropriate viscosity for spray application.

Formulated primers were applied on the panel surfaces by air spray. Eight different individual²

panels were prepared for each type of system. Primer coatings were cured at room temperature for two days and the thickness of dry primers was around 150 µm.

Four panels of each type were topcoated by 03-GY-321 topcoat (supplied by DEFT INC, Irvine, CA, USA) and cured at room temperature for two days. The thickness of dried topcoats was around 100 µm.

All the cured non-topcoated and topcoated test panels were put into a Prohesion chamber for accelerated exposure tests according to ASTM-G85-A5, which consists of one-hour fog cycle of Diluted Harrison's Solution (DHS) fog (0.05% sodium chloride and 0.35% ammonium sulphate) at 25°C and one-hour dry-off cycle at 35°C. Once a week, the test panels were removed from the Prohesion chamber for electrochemical testing (EIS) and returned to chamber when the testing was concluded.

2.3. Thermal analysis:

A TMA 2940 Thermomechanical Analyzer (TA Instruments Inc, New Castle, DE, USA) was used to detect the existence of primer film's post-curing. The procedure consisted of two test cycles: in the first test cycle, a free film sample of primer was equilibrated at 0°C, heated at a ramp rate of 5°C per minute to 140°C; after the same sample was cooled down and equilibrated at 0°C, then the second test cycle with same conditions was run.

2.4. EIS measurement setup:

A test panel was clamped to a glass cell with a 7.06 cm² exposure area and used as the working electrode; a saturated calomel electrode (SCE) was used as the reference electrode and a Pt mesh as the counter electrode; DHS was the working electrolyte. All the EIS data were collected through a frequency range from 10⁵ Hz to 0.01Hz by using a Gamry PCL4-300 in potentiostatic mode (Gamry Instruments, Inc. Warminster, PA, USA).

Experimental CPVCs of magnesium alloy rich primers were determined by measuring impedance at low frequency with changing pigment volume concentration (PVC).

2.5. SEM measurement:

Scanning electron microscope (SEM) surface images of primers were taken by using a JEOL JSM-6300 (JEOL Ltd., Tokyo, Japan) with 15KeV acceleration voltage, at X3000 magnification for the 715 hours exposed samples.

3. Results and discussions:

3.1. Properties of Magnesium alloy pigments:

The data of particle size, PSD, oil absorption, density and chemical composition for the three magnesium alloy pigments, AM60, AZ91B and LNR91 are listed in Table 1.

We can see that the three magnesium alloy pigments have large particle size (above 60 µm); also they showed different shapes: AM60 has a plate-like shape with a smooth edge, AZ91B has a chip-like shape and LNR91 has a cubic-like shape with a sharp edge. The oil absorption of LNR91 is the lowest, which indicates LNR91 pigments have smaller surface area or smoother surface. Although the mean particle size of LNR91 is smaller in comparison with the other two pigments, its PSD exhibited much broader range. Furthermore, LNR91 has the highest Al composition within the three.

3.2. CPVC of magnesium alloy primers:

The predicted CPVCs for the three primers were estimated by the procedures outlined in the paper of Bierwagen et al.¹¹

The estimated CPVCs of the three magnesium alloy pigments are listed on Table 2.

The experimental CPVCs of magnesium alloy rich primers were determined by measuring the change in impedance at low frequency with change in pigment volume concentration.^{12, 13} With increasing PVC of a coating, the impedance of the coating decreases, because there is less polymeric binder to fill the voids between pigment particles, resulting in a more porous coating. The plots of impedance at 0.01Hz versus PVC are shown in Figure 2. The ranges of CPVC of the three different Mg alloy primers are listed in Table 2.

It can be seen that the experimental CPVC are much lower than the estimated CPVC. A possible³

reason may relate to the pigment packing. First, all particle sizes of the three magnesium pigments are above 60 micron, and the thicknesses of primer coating films were around 150 micron. Thus, in comparison with the thickness of coating film, the sizes of all the three magnesium pigments were too big to obtain good packing efficiency. Second, from the SEM images of pigments, we can see that the shape of pigment particle and particle size are not well controlled, and these may affect the pigment packing. Furthermore, some difficulties in the coating application processes, such as non uniform film thickness, also can result in pigment packing problems.

3.3. Open Circuit Potential (OCP) change with exposure time (*Mg alloy primer coated panels without topcoat*):

Figure 3 shows changes with exposure time in the OCP of Mg alloy primer coated AA 2024 T3 panels (without topcoat). The data for a single panel of each sample set is reported since each is representative of the trend shown by the entire sample set.

It can be seen that the OCP of panels increased with exposure time but fell mostly within a potential range that was higher than the OCP of pure Mg (about -1.60 V) but lower than the OCP of bare AA2024 T3 substrate (-0.60V). This mixed potential range indicated that the Mg alloy pigments could provide cathodic protection to Al alloy substrate.² Furthermore, at 0 hour exposure time, all the Mg alloy primer coated panels with different PVC had low OCP, between -1.50 V and -1.20 V, which might be due to the high content of Mg in fresh primer films. With the increasing exposure time, the OCP increased, indicating the consumption of the active pigments. Among the primers, the OCP of the AM60 primer coated panels exhibited the lowest rate of increase and remained in a low OCP range for the longest time. This might be due to its highest Mg content and plate shape of its pigments. When the OCP of the panels reached the OCP of the bare substrate, the primers no longer provided sacrificial protection to the Al alloy substrate.

In addition, the OCP change also reflected the effects of PVC on primers. For the LNR91 primer coated panels, the OCP of the lowest PVC (35%) primer increased much more slowly; in contrast, the OCP of the highest PVC (50%) primer reached -0.60V very quickly. This might due to the lower barrier protection provided by polymer binder when PVC was higher than CPVC, where the electrolyte could easily penetrate into the coating film and speed up the corrosion of Mg pigments.

3.4. Mg alloy primer coated panels without topcoat (Impedances at 0.01Hz change with exposure time):

In general, the impedance at low frequency is related to the sum of polarization resistance (R_p), pore resistance (R_{pore}) and solution resistance (R_s),¹⁴ especially when some defects, such as pores, are present in the coating system. In fact, the non top-coated Mg alloy pigmented primer system was very porous due to the existence of the Mg alloy pigments. In addition, from the Bode magnitude and phase diagrams of an AM60 31% PVC primer coated panel shown in Figure 4 A and B, it can be seen that the impedance at low frequency (0.01Hz) decreased with exposure time. Meanwhile, the phase angle at low frequency (0.01Hz) was about -10 degrees in the first 100 hours exposure and increased to -40 degrees until 506 hours exposure; after 600 hours exposure, the phase angle dropped to -20 degrees. Figure 4 C and D show the Bode magnitude and phase diagrams of the different Mg alloy primer coated panels, along with an unpigmented (clear) primer coated panel (black lines). After 550 hours exposure, the phase angles of the panel with a clear coating and panels coated with primers having higher PVC(such as AZ91B at 36%PVC and LNR91 at 50% PVC) were all less than -10 degree at low frequency, while the other panels were between -20 degree and -40 degree. That the phase angle was not 0 degree at low frequency indicates that the capacitance in the primer system also contributed to the impedance at low frequency, but we can assume that the change of the impedance at low frequency (0.01Hz) reflects primarily the alteration of the coating resistance because the range of the phase angles at low frequency didn't vary significantly and the phase angles decreased further with the increasing exposure time. The plots of impedance at 0.01Hz for the panels coated with Mg alloy primers versus exposure time are shown in Figure 5. We can see that, with exposure time increasing, the impedance at low frequency slowly decreased. This may be due to the decrease of the pore resistance and the polarization resistance (solution resistance is normally very low and can be ignored). When the electrolyte penetrated the coating film through the porous paths and reached the interface between the coating and the substrate, the pore resistance decreased. On the other hand, with the presence of the electrolyte and the electrochemically active species, the under-film corrosion was initiated and caused the decrease of polarization resistance.

Sometimes, a sharp increase in impedance at low frequency could be observed, especially during the first 24 hours. This phenomenon could be due to the post-curing of primer films. Figure 6 shows the results of thermal mechanical analysis (TMA) of the ambient cured or 60°C oven cured Mg alloy primers. It can be seen that, with increasing temperature, the primer film with ambient curing exhibited much larger dimensional changes (156.16 μm) than the one oven cured at 60°C (87.59 μm), which meant the ambient cured primer film had much bigger volume shrinkage than the one oven cured at 60°C. In addition, a second TMA cycle of either the ambient cured or the 60°C oven cured primer film showed no additional shrinkage after being exposed at high temperature. These TMA data indicate that the ambient cured primer film had lower degree of cure than the 60°C oven cured primer film,^{15, 16} and the high temperature exposure (higher than 125°C) resulted in more fully cured primers. Thus, it was possible for the primers to continue to crosslink further in the Prohesion chamber.

Figure 7 shows a SEM surface image of Mg alloy primer after 715 hours exposure. The Mg precipitates were observed around the Mg alloy pigment. The morphology of the Mg precipitate was very similar to that observed previously in the exposed primer containing pure Mg powder pigment, where the formation of the Mg precipitate was found to affect the impedance of the primer film and the film barrier properties.^{6, 8} The confirmation of the actual chemical composition of the precipitate as well as its effects on barrier protection are currently being studied.

3.5. Mg alloy primers coated panels with topcoat (OCPs change with exposure time):

Mg alloy rich primer was designed to be used with a topcoat in field application. Thus, the effects of the topcoat on the Mg alloy primers were studied to understand the anti-corrosion behaviour and the possible lifetime of the whole aerospace coating system exposed to an electrolyte. The OCP changes with exposure time are shown in Figure 8. At 0 hour exposure, the OCPs were generally low; with increasing exposure time, the OCPs slowly increased. These results indicate that, even when covered by a layer of topcoat, the Mg alloy primers still exhibited good cathodic protection to AA 2024 T3 substrates, suggesting that the barrier protection provided by topcoat didn't retard the cathodic protective function of primers.

The effect of PVC on OCP change by topcoated primers was different from that observed with the non-topcoated primers. In Figure 8, it can be seen that, when covered by the topcoat, the panels with higher PVC(such as AM60 at PVC 34% and AZ91B at PVC 38%) had the lower OCPs combined with a slower increase in OCP than the ones containing AM60 at PVC 31% and AZ91B at PVC 36%. This is attributed to the topcoat providing barrier protection for the porous primer and reducing the oxidation rate of the Mg pigments.

3.6. Mg alloy primers coated panels with topcoat (Impedances at 0.01Hz change with exposure time):

Figure 9 shows the impedance at low frequency as a function of exposure time for the topcoated Mg alloy primer panels. In general, the impedance of these panels followed a trend with respect to pigment composition very similar to that observed with the non-topcoated Mg alloy primers. However, the topcoated panels showed less variation in impedance with exposure time than non-topcoated ones, with the sharp increases and/or decreases observed in Figure 5 no longer observed in Figure 9. This is hypothesised that the effect of the epoxy-polyamide binder in the primer may be masked by the presence of the topcoat and the topcoat mainly contributes to the barrier protection of this aerospace coating system. The effects of the pigments though manifested in cathodic protection, is possibly delayed as the topcoat presents the initial barrier protection for the substrate. The lifetime of the coating can be significantly extended when the inherent barrier property of the topcoat is combined with the excellent topcoat compatibility with the primer binder.

Conclusions:

Similar to the pure magnesium pigment, the magnesium alloy pigments formulated in primer coatings can provide cathodic protection for Al alloy substrates. EIS results showed that the metal-rich primers with the Mg alloys as pigments had the mixed potentials between the OCPs of Mg alloys and the bare Al 2024 T3, which indicated the Mg alloy pigments provided sacrificial protection to the Al alloy substrates. The changes in impedance at low frequency with exposure time for the non-topcoated samples indicated that the electrolyte penetrated the coating films and reached the interface between the primer coating and the substrate,⁵

eventually initiating under-film corrosion. Similar observations were made with the topcoated samples although this penetration process was retarded by the good barrier protection of topcoat. Scanning electron microscopy (SEM) showed the existence of Mg precipitates. Furthermore, the investigation of the properties of the three alloys gave a good understanding of the effects of the particle size, the particle shape and the chemical composition on the particle packing efficiency, CPVC and electrochemical behaviour of the primer system, suggesting that pigments with smaller particle size and better controlled shape would result in a better primer system.

Acknowledgements

This research work was supported by Air Force funding (grant# FA8650-04-1-5045). The authors thank Scott Payne (Microscopy Lab, USDA/NDSU) for the SEM and EDS measurements.

References:

1. Battocchi, D.; Simoes, A. M.; Tallman, D. E.; Bierwagen, G. P., *Corrosion Science* **2006**, 48, 1292-1306.
2. Knudsen, O. O.; Steinsmo, U.; Bjordal, M., *Progress in Organic Coatings* **2005**, 54, 224-229.
3. Nanna, M. E.; Bierwagen, G. P., *JCT Research* **2004**, 1, 69-80.
4. Bierwagen, G. P.; Nanna, M. E.; Battocchi, D. Magnesium rich coatings and coating systems. 2004-US33089
2005051551, 20041007., 2005.
5. Bierwagen, G.; Tallman, D.; Nanna, M.; Battocchi, D.; Stamness, A.; Gelling, V. J., *Polymer Preprints (American Chemical Society, Division of Polymer Chemistry)* **2004**, 45, 144-145.
6. Bierwagen, G.; Battocchi, D.; Simoes, A.; Stamness, A.; Tallman, D., *Progress in Organic Coatings* **2007**, 59, 172-178.
7. Battocchi, D.; Simoes, A. M.; Tallman, D. E.; Bierwagen, G. P., *Corrosion Science* **2006**, 48, 2226-2240.
8. Simoes, A. M.; Battocchi, D.; Tallman, D. E.; Bierwagen, G. P., *Corrosion Science* **2007**, 49, 3838-3849.
9. B.A.Shaw, *ASM Hand book* **2003**, 13A, 692-696.
10. G.Song; A.L.Bowles; D.H.StJohn, *Materials Science and Engineering A* **2004**, 366, 74-86.
11. G.P.Bierwagen; R.S.Fishman; Storsved, T.; Johnson, J., *Prog. Organic Coatings* **1999**, 35, 1-10.
12. Lobnig, R. E.; Villalba, W.; Goll, K.; Vogelsang, J.; Winkels, I.; Schmidt, R.; Zanger, P.; Soetemann, J., *Progress in Organic Coatings* **2006**, 55, 363-374.
13. Asbeck, W. K., *JCT CoatingsTech* **2005**, 2, 64-66.
14. Loveday, D.; Peterson, P.; Rodgers, B., *JCT Coatings Tech* **2004**, October, 88-93.
15. Skrovanek, D. J., *Progress in Organic Coatings* **1990**, 18, 89-101.
16. Skrovanek, D. J.; Schoff, C. K., *Progress in Organic Coatings* **1988**, 16, 135-63.

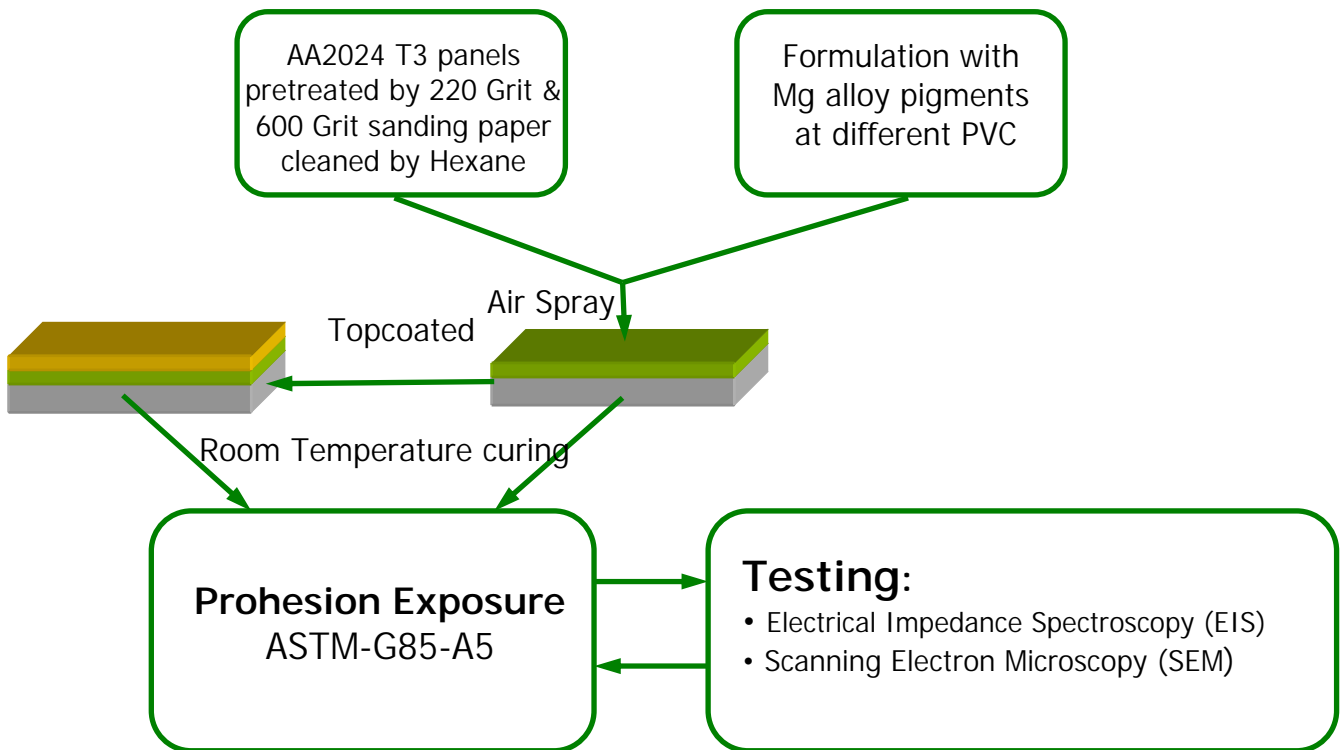


Figure1. Flow of Experiments

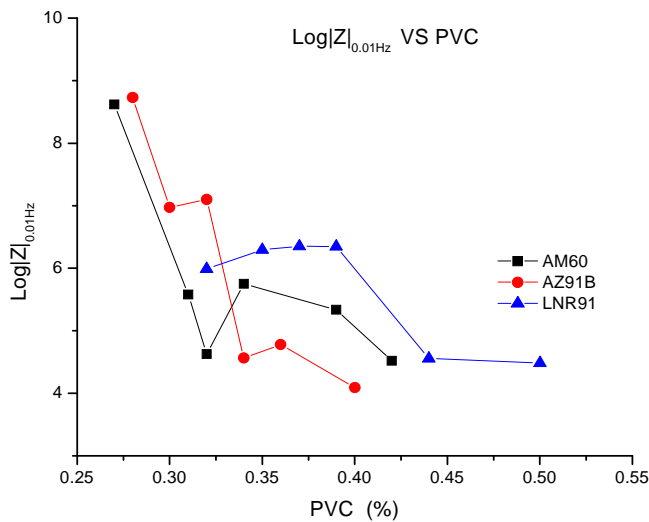


Figure 2. Impedances at 0.01Hz change with PVC of primers

Table 1: Properties of three magnesium alloy pigments

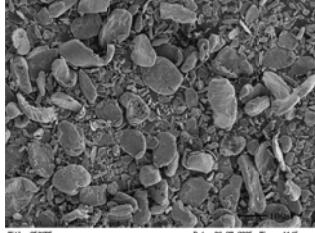
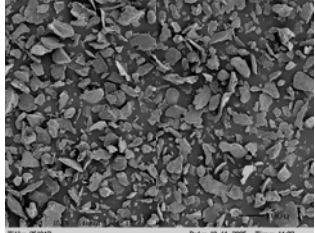
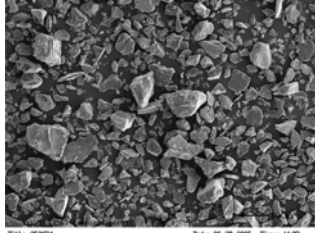
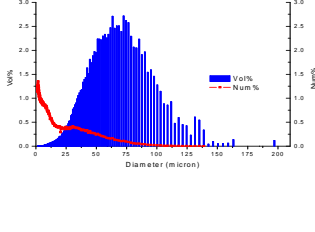
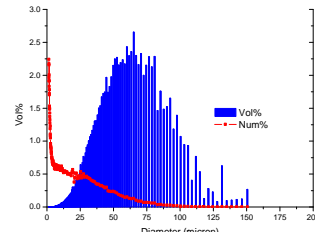
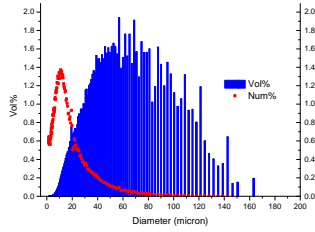
Mg Alloy Pigment	AM60	AZ91B	LNR91			
Particle Shape (SEM)						
Composition (wt%)	Al 5%, Mg 95%	Al 9.5%, Mg 90.5%	Al 50%, Mg 50%			
Oil absorption	61.53 g/100g pigment	68.30 g/100g pigment	33.45 g/100g pigment			
Density (g/cm³)	1.80	1.81	2.22			
Particle Size Plot						
Particle Size	By Vol. (μm)	By Num. (μm)	By Vol. (μm)	By Num. (μm)	By Vol. (μm)	By Num. (μm)
Mean Diameter	63.00	10.66	58.96	10.36	56.21	11.23
Mode Diameter	63.46	1.95	74.61	1.66	87.72	11.59
Median Diameter	60.12	5.02	55.45	4.16	49.78	8.39

Table 2: Theoretical and experimental CPVCs of three Mg alloy pigments

Mg Alloy Pigment	AM 60	AZ91B	LNR91
Theoretical CPVC	46%	43%	56%
Experimental CPVC	31% < CPVC < 34%	31% < CPVC < 34%	39% < CPVC < 44%

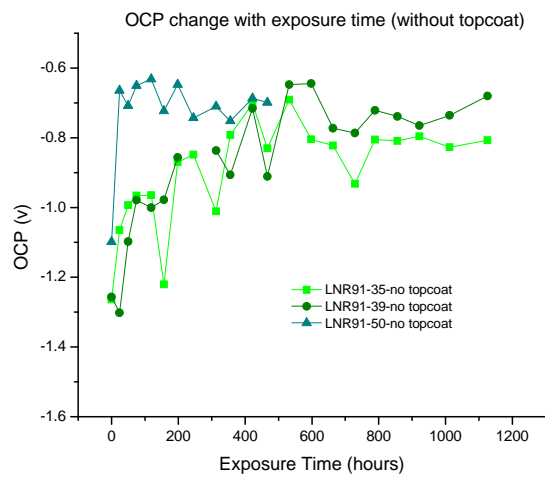
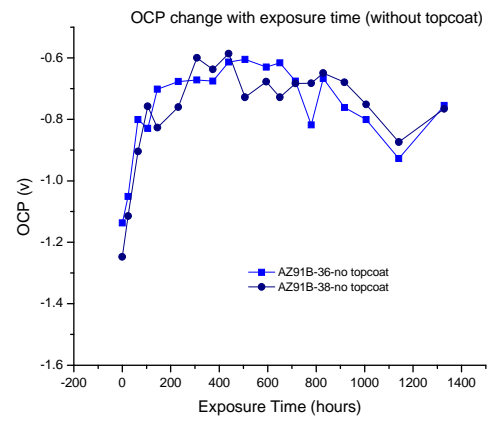
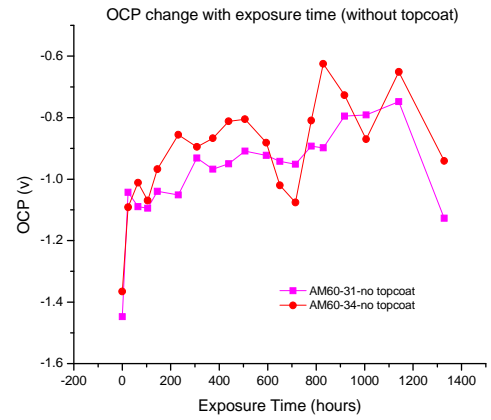


Figure 3: OCP of Mg alloy primer coated panels (without topcoat) change with exposure time

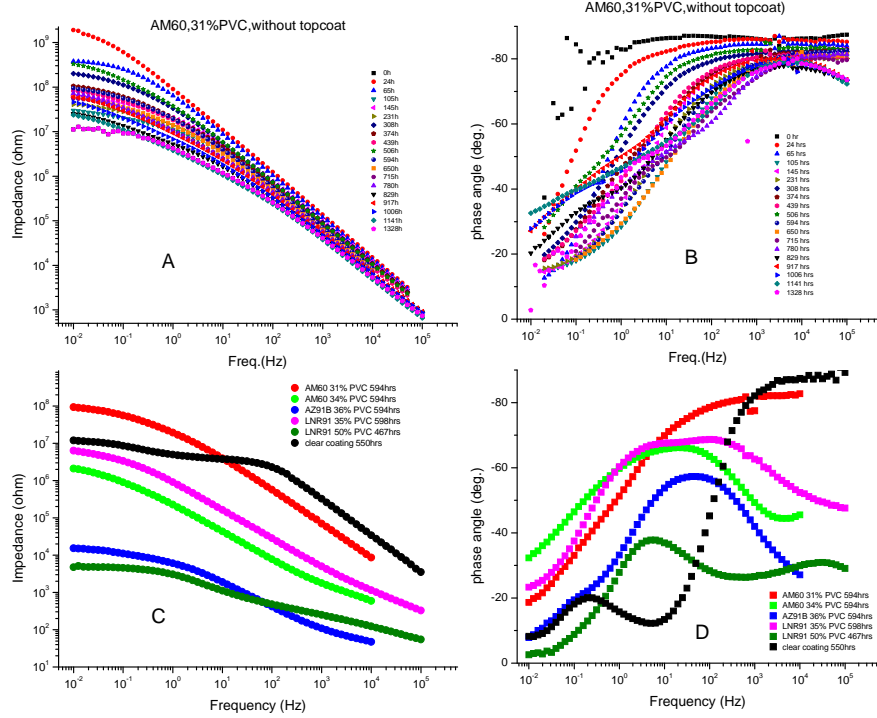


Figure 4: Impedance spectra of Mg alloy primers coated panels. (A)(B) Bode magnitude and phase diagrams, respectively, for a AM60 31% PVC primer coated panel after different exposure times. (C)(D) Bode magnitude and phase diagrams, respectively, for different primers coated panels and clear coating panel after about 600hrs exposure.

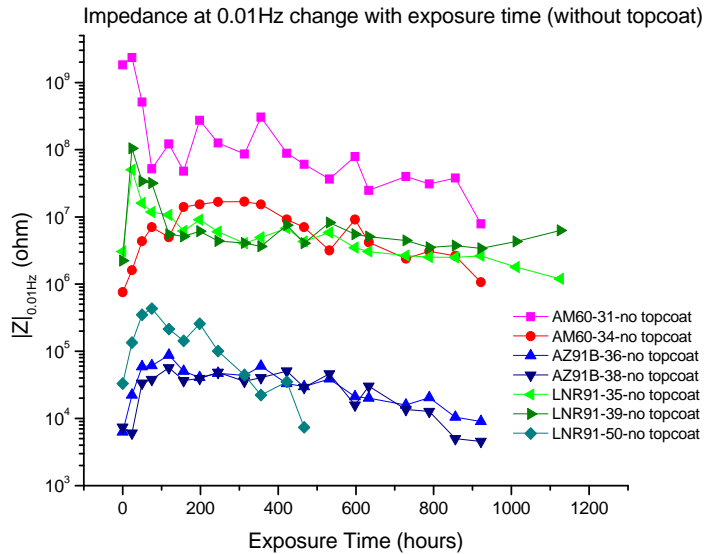


Figure 5: Impedance at low frequency of Mg alloy primer coated panels (without topcoat) as a function of exposure time

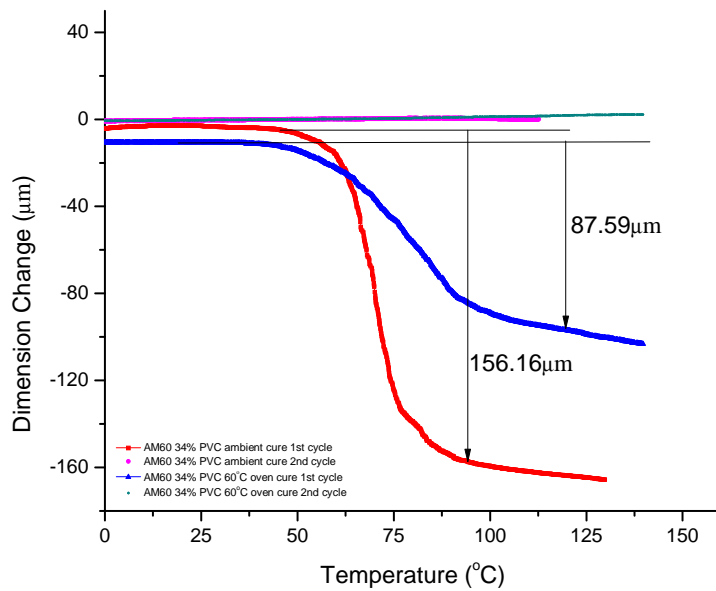


Figure 6: TMA plots of ambient cured or 60 $^{\circ}\text{C}$ oven cured Mg alloy primer films

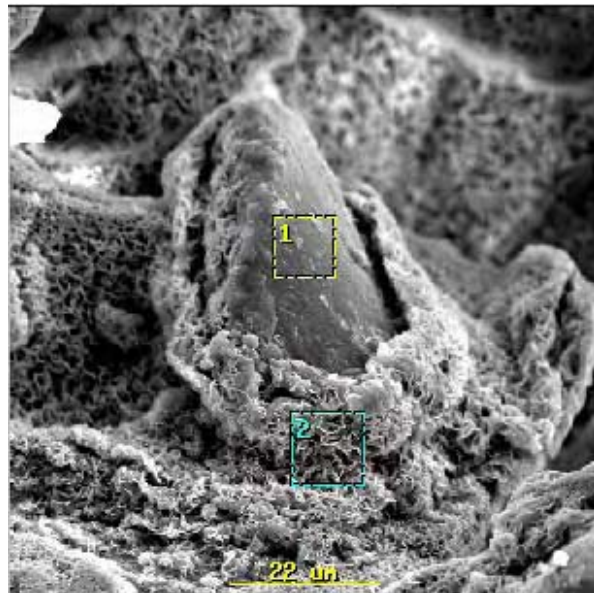


Figure 7: SEM surface image of AM60 primer coated panel (34% PVC, 715 hours exposure)
Area 1) Mg alloy pigment; Area 2) Structure of Mg precipitate

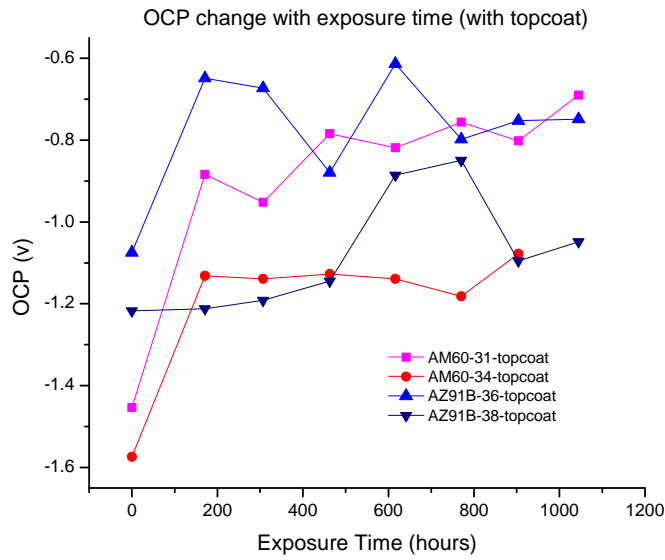


Figure 8: OCPs of Mg alloy primer coated panels (with topcoat) change with exposure time

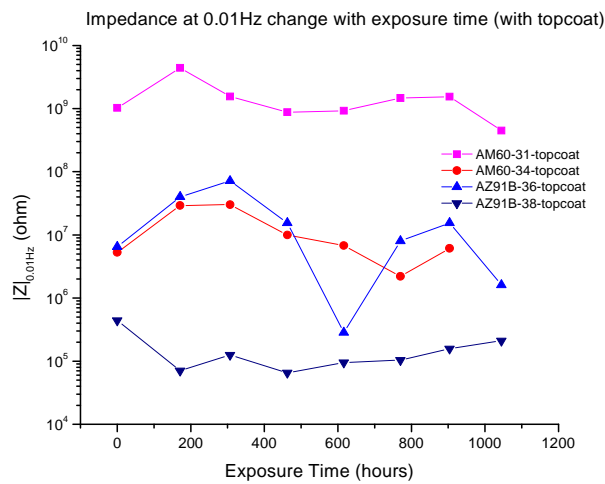


Figure 9: Impedance at 0.01Hz of Mg alloy primer coated panels (with topcoat) as a function of exposure time

Combinatorial Materials Research Applied to the Development of New Surface Coatings X: A High-Throughput Electrochemical Impedance Spectroscopy Method for Screening Organic Coatings for Corrosion Inhibition

Jie He,^{*†} James Bahr,[†] Bret J. Chisholm,^{†,‡} Jun Li,[‡] Zhigang Chen,[†] Séva N. Balbyshev,[†] Verena Bonitz,[‡] and Gordon P. Bierwagen[‡]

Center for Nanoscale Science and Engineering, North Dakota State University, 1805 Research Park Drive, Fargo North Dakota 58102, and, Department of Coatings and Polymeric Materials, North Dakota State University, 1735 Research Park Drive, Fargo North Dakota 58102

Received March 17, 2008

The objective of the study was to develop a high-throughput electrochemical impedance spectroscopy (HT-EIS) method for rapid and quantitative evaluation of corrosion protective coatings. A 12-element, spatially addressable electrochemical platform was designed, fabricated, and validated. This platform was interfaced to a commercial EIS instrument through an automated electronic switching unit. The HT-EIS system enables four parallel EIS measurements to be run simultaneously, which significantly reduces characterization time compared to that of serial EIS measurements using a multiplexer. The performance of the HT-EIS system was validated using a series of model systems, including a Randles equivalent circuit, an electrochemical reaction ($\text{Ti}/\text{K}_4\text{FeCN}_6, \text{K}_3\text{FeCN}_6$), a highly uniform polymer film, and several polymer coatings. The results of the validation studies showed that the HT-EIS system enables a major reduction in characterization time and provides high quality data comparable to data obtained with conventional, single-cell EIS measurement systems.

Introduction

Historically, the use of organic coatings has proven to be the most economical and effective method for reduction of metal corrosion. It has been reported that at least one-half of all costs for corrosion protection is related to the application and maintenance of organic surface coatings.^{1,2} In recent decades, a variety of high performance coatings, such as lead-, chromate-, and tin-containing coatings, have been or will be banned as a result of stricter environmental, health, and safety regulations. Consequently, novel, environmentally benign corrosion protective coatings are needed.

Electrochemical impedance spectroscopy (EIS) has proven to be one of the most useful tools for characterizing organic coatings designed for corrosion control.^{3–5} The utility of EIS arises from the electrochemical nature of the corrosion process and the relative ease of application in either a laboratory or field setting. Unlike traditional exposure methods for characterization of corrosion protection, such as ASTM B117 salt spray exposure⁶ or Prohesion exposure,⁷ EIS provides quantitative data in a relatively short period of time. In addition, the nondestructive nature of EIS enables repeated measurements on the same specimen, making it possible to monitor coating performance as a function of exposure time.

In recent years, the combinatorial methodology originally developed within the pharmaceutical industry has been successfully applied to coating research and development as a means to reduce the time and cost for new coating development.^{8–12} High-throughput (HT) methods for preparing, depositing, curing, and testing many key properties of surface coatings have been previously described. For example, a combinatorial workflow for the development of protective coatings for plastic substrates has been described in detail by Chisholm et al.,⁹ while a complete combinatorial workflow for the development of new marine coatings has been described by Webster et al.¹³ A key component of a combinatorial workflow for the development of new organic coatings for corrosion control is the generation of a HT method for assessment of corrosion protection. Despite the existence of a few HT electrochemical methods reported for electrosynthesis^{14,15} and screening of electrocatalysts, sensors, and batteries,^{16–18} no electrochemical methods have been reported for screening of corrosion protective coatings. This document describes the design, fabrication, and validation of a HT method for assessing the corrosion protection of coatings using EIS. The device is referred to throughout this document as a HT-EIS system.

Experimental Section

Materials. Panels (20 cm × 10 cm × 1 mm) of the aluminum alloy AA 2024-T3 were obtained from Q-panel Laboratory Products (Westlake, OH). Prior to use, the panels

^{*} To whom correspondence should be addressed. E-mail: jie.he@ndsu.edu.

[†] Center for Nanoscale Science and Engineering.

[‡] Department of Coatings and Polymeric Materials.

were sandblasted to remove the oxide layer and then cleaned with hexane. Panels ($20\text{ cm} \times 10\text{ cm} \times 1\text{ mm}$) of titanium were obtained from McMaster-Carr (Elmhurst, IL). A Tedlar film was obtained from DuPont (Wilmington, DE), and the film thickness was $51\text{ }\mu\text{m}$. A silver-containing epoxy coating (Circuitworks 7100) was obtained from ITW Chemtronics (Kennesaw, GA). An epoxy adhesive, QUIK-CURE was obtained from BSI (Atascadero, CA). A two-component, chromate-based primer coating, MIL-PRF-23377J, and a two-component polyurethane topcoat, MIL-PRF-85285D, were obtained from Deft, Inc. (Irvine, CA). An epoxy resin, Epon 1001-CX-75, and an amine-functional cross-linker, Epicure 3140, were obtained from Resolution Performance Products (Houston, TX). A modified fumed silica, Aerosil R974, was obtained from Degussa GmbH (Düsseldorf, Germany). Magnesium (Mg) particles, Eckagranules PK31 and Eckagranules PK51, were obtained from Ecka GmbH (Fürth, Germany). Methyl isobutyl ketone (MIBK), hexane, xylene, K_4FeCN_6 , K_3FeCN_6 , HF, HNO_3 , and NaCl were obtained from Sigma-Aldrich Company. All chemicals were used as received from the supplier.

A Mg-rich primer coating was prepared as follows: 67 g of Epon 1001-CX-75 was dissolved in a solvent mixture composed of 45 g of MIBK and 20 g of xylene. Next, 1 g of Aerosil R974 and 95 g of a 52/48 v/v mixture of Eckagranules PK31 and Eckagranules PK51 were added to the mixture using high-shear mixing. Just prior to application of the coating to a substrate, 9.5 g of Epicure 3140 was added with stirring.

Instrumentation. For measurements made using the HT-EIS system, four femtostats of a Gamry MultiEchem 8 Electrochemical Workstation and Gamry Framework software were used to acquire impedance spectra as a function of frequency; 10 mV rms voltages vs open circuit potential were applied as the excitation signal and impedance was measured using 10 points/per decade.

For measurements made using a conventional, single-cell EIS system, sections of poly(vinyl chloride) (PVC) tubing with an inner cross-sectional area of 5 cm^2 were adhered with QUIK-CURE adhesive to the surface of sample specimens. After the adhesive was fully cured, 10 mL of electrolyte solution was poured in the open end of the tubing to create the electrolyte reservoir. Then, an Ag/AgCl reference electrode and a Pt mesh counterelectrode were placed into the solution, and the separation distance between the sample specimen and the counterelectrode was adjusted to 1.5 cm. The single cell was connected directly to a Gamry femtostat within the same Gamry MultiEchem 8 Electrochemical Workstation used for measurements with the HT-EIS system. All data fitting described in this document was conducted using Zview software from Scribner Associates.

Randles Circuit Calibration and Open-Lead Experiment. The Randles equivalent circuit¹⁹ is one of the simplest and most common circuit models for EIS measurements. Thus, four equivalent Randles circuits (Gamry, Inc.) were used for circuit calibration experiments (Figure 1). Each circuit was connected through its respective electronic switch to its respective cell in the 12-well assembly of the HT-EIS system, and the EIS experiments were run simultaneously.

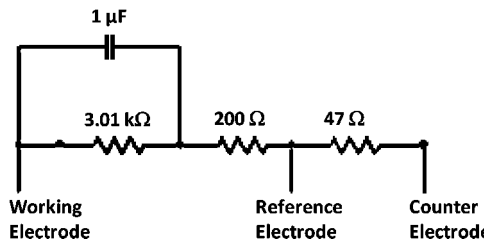


Figure 1. Schematic of the Randles circuit provided by Gamry.

The input impedance of the HT-EIS apparatus was evaluated using a series of open-lead experiments and a previously described procedure.²⁰ Briefly, the electrode cables for four cells corresponding to a row of cells within the HT-EIS system were connected to Randles circuits to define the open circuit potential ($0 \pm 3\text{ mV}$). Then, the experiments were paused; the Randles circuits were removed from the electrode cables, and EIS spectra were recorded simultaneously under an open-lead condition.

Validation Experiment Based on the Redox Couple

$\text{K}_4\text{FeCN}_6/\text{K}_3\text{FeCN}_6$. Titanium panels were degreased in acetone, rinsed with distilled water, and then placed in an acid pickling solution (an aqueous solution containing 14 wt % HNO_3 and 1 wt % HF) for 1–3 min until the surface was uniformly white. The panels were then washed with distilled water three times and allowed to air dry.²¹ The pretreated titanium substrates were used as working electrodes, and an equal molar (5/5 mM) solution of the redox couple, $\text{K}_4\text{FeCN}_6/\text{K}_3\text{FeCN}_6$, in 0.5 M aqueous KClO_4 was used as the electrolyte. The frequency range used was 10^4 –0.01 Hz.

Validation Experiments Utilizing a Uniform Polymer Film.

Following a procedure previously described,²² pieces of Tedlar film were coated uniformly with a thin layer of silver-containing epoxy adhesive, and the films were adhered to specimens of AA 2024-T3 to establish a conductive bond between the film and the metal. The AA 2024-T3 specimens laminated with Tedlar film were used as working electrodes for the HT-EIS validation experiment. The electrolyte used in this experiment was 3% NaCl. The frequency range was 10^4 –0.01 Hz.

Validation Experiments Utilizing Polymer Coatings.

Coatings were applied by spraying coating formulations onto AA 2024-T3 panels using a high-volume/low-pressure spray gun.²³ Coating specimens consisting of a single coating were allowed to cure for at least one week at room temperature before they were tested, and the coating thickness was $\sim 50 \pm 10\text{ }\mu\text{m}$ for all specimens. For the coating system consisting of the Mg-rich primer and polyurethane topcoat, the Mg-rich primer was allowed to cure for one week before the polyurethane topcoat was applied. The average film thickness for specimens based on this coating system was approximately $100 \pm 10\text{ }\mu\text{m}$. The electrolyte for EIS experiments was dilute Harrison's solution (an aqueous solution comprising 0.35% $(\text{NH}_4)_2\text{SO}_4$ and 0.05% NaCl). The frequency range used was 10^4 –0.1 Hz.

Results and Discussion

HT-EIS Apparatus. The basic components of the HT-EIS apparatus are illustrated in Figure 2. An automated

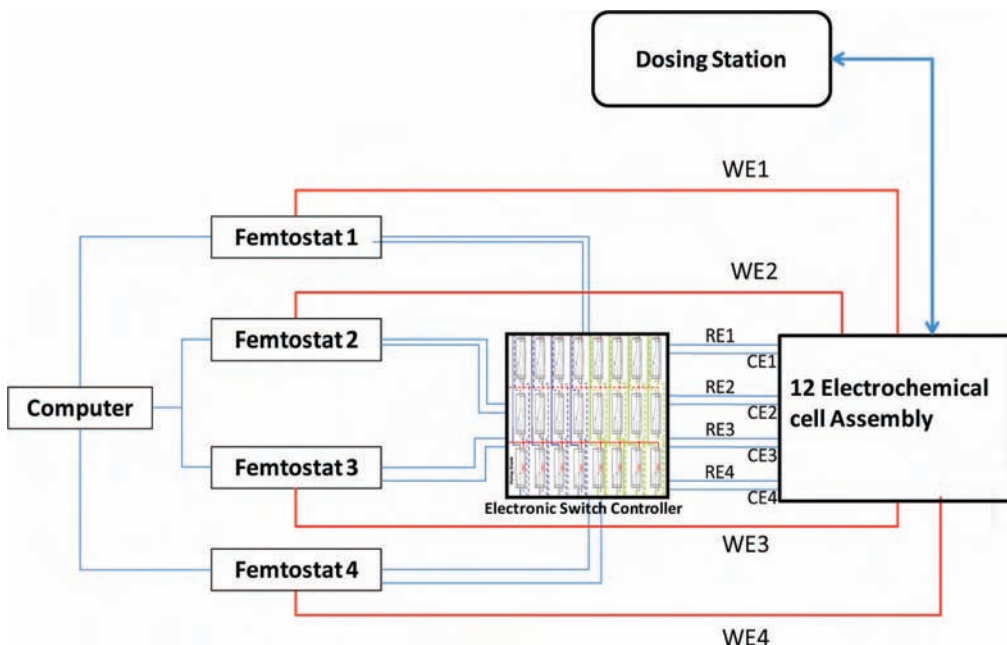


Figure 2. Schematic illustrating the basic components of the HT-EIS system.

electronic switch controller and a 12-unit array of electrochemical cells were fabricated and interfaced with each other. Four femtostats of a Gamry MultiEchem 8 Electrochemical Workstation are connected to the electronic switching system so that four electrochemical measurements can be run simultaneously. The electrochemical measurements are controlled by a computer with Gamry Framework software. A fluid-dosing station is used to control electrolyte delivery and extraction within each cell of the 12-cell electrode assembly.

As shown in Figure 3A, the working electrodes of the 12-cell electrode array are formed using a 20 cm × 10 cm × 0.16 cm piece of metal substrate machined to create four 10 cm × 3.5 cm × 0.16 cm tabs. The tabs can be simultaneously coated using a parallel dip coating process, illustrated in Figure 4, to produce an array of four coatings. The coating array is then bonded to a 20 cm × 10 cm × 0.32 cm PVC backing plate using an epoxy adhesive. After the substrate is securely adhered to the PVC plate, the four tabs are electrically isolated from one another by cutting the top spine holding them together. As illustrated in Figure 3C, the four circular positions in row A are used for the first set of EIS measurements, followed by row B and then row C.

Images illustrating assembly of the HT-EIS system are shown in Figure 5. The four-tab coating array assembly (Figure 3C) is placed into a recessed area of a nylon block (Figure 5A) designed for precisely positioning the array assembly. A second nylon block is then fastened to the uncoated edge of the coating array assembly using four metal screws. In addition to holding the coating array in place, the four metal screws are used as connection posts for working electrode cables. A digital voltmeter is used to ensure good electrical contact is established between the working electrodes and metal screws. Next, a 6.4 mm thick rubber gasket with 12 circular holes (2.54 cm in diameter) is positioned on top of the coating array assembly using the alignment posts (Figure 5B) to create a water-tight seal for the electrolyte reservoirs. A 4 mm thick nylon block possessing

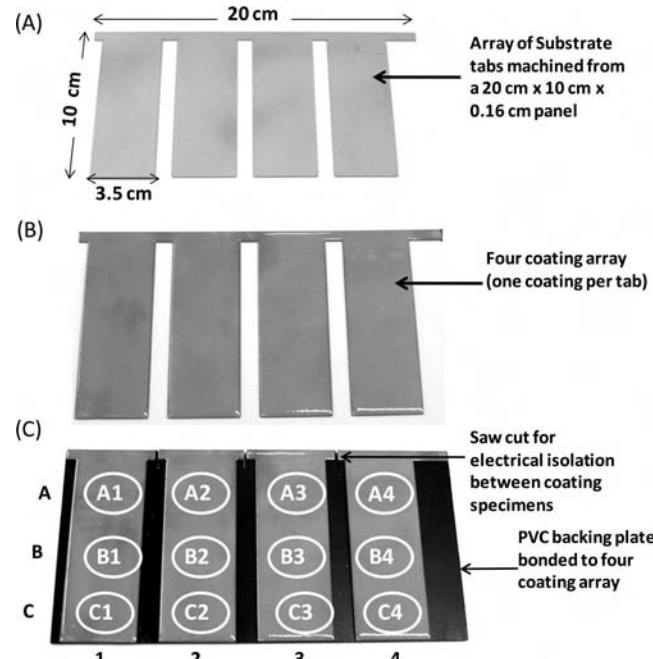


Figure 3. Images showing the four coating array assembly used for the HT-EIS system: the array of substrate tabs machined from a standard panel (A), the four coating array produced by coating each substrate tab (B), and the coating array assembly required for the HT-EIS system (C).

an analogous configuration to the rubber gasket is then placed on top of the rubber gasket and firmly held in place using three stainless steel toggle clamps (Figure 5C) to create 12 electrolyte reservoirs on the surface of the coatings (3 reservoirs per coating). The use of the rubber gasket in conjunction with the clamping device has been shown to eliminate electrolyte leakage. Finally, as shown in Figure 5D, an electrode array assembly is placed on the top of the 12-well assembly to create 12 complete electrochemical cells.

Figure 6 illustrates an individual cell setup within the HT-EIS system. Each cell contains a working electrode (substrate), a Ag/AgCl reference electrode (RE), and a Pt counter

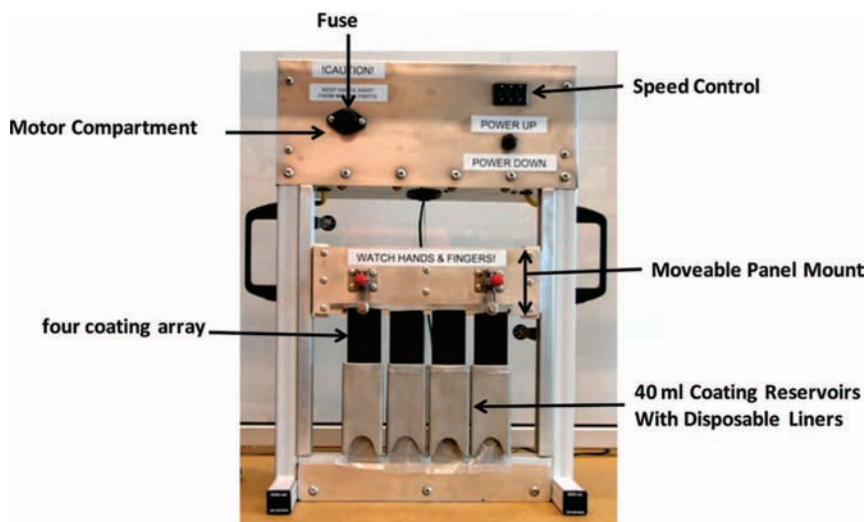


Figure 4. Image of a parallel dip-coater designed for creating a four-tab coating array.

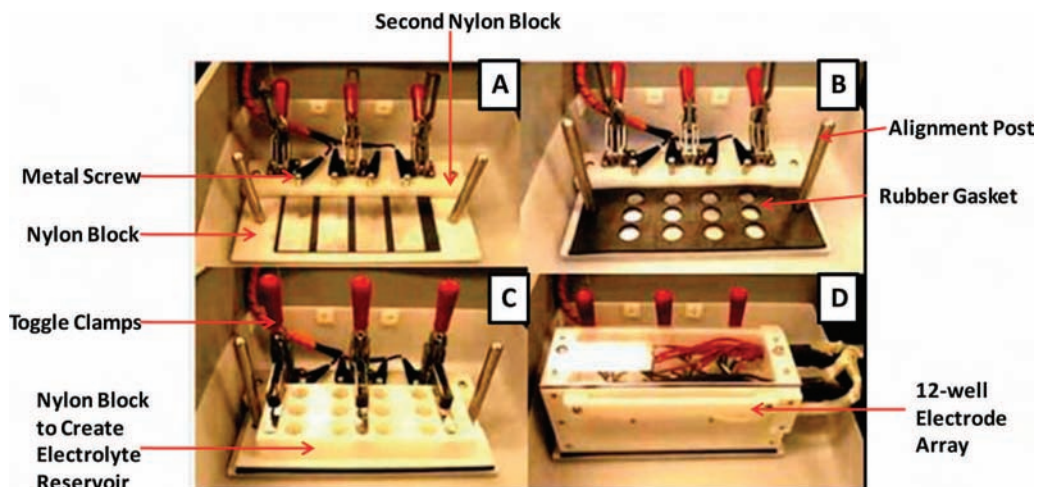


Figure 5. Image displaying the components of the 12-well electrochemical cell assembly: placement of the four coating array assembly (A), placement of the rubber gasket (B), placement and clamping of the nylon block to create the 12-well array of electrolyte reservoirs (C), and placement of the array of electrodes to produce the fully assembled 12-well array of electrochemical cells (D).

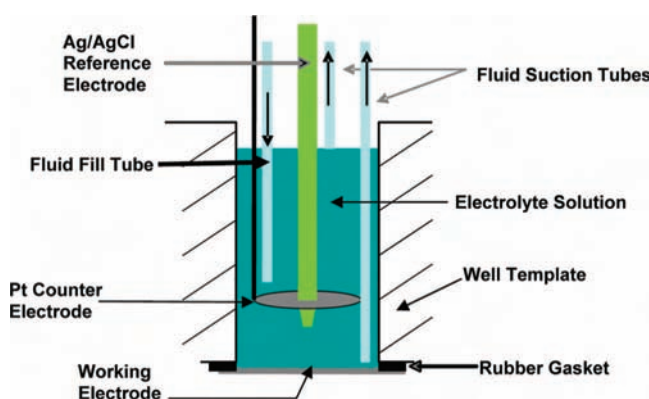


Figure 6. Schematic of an individual cell setup within the HT-EIS system.

electrode (CE). The circular Pt mesh CE (1.2 cm in diameter) was placed about 1.5 cm above the coated metal substrate to form a parallel-planar arrangement with the working electrode. A 5 mm hole was made in the center of the Pt mesh CE to allow insertion of the tip of the reference electrode. The separation distance between the working electrode and RE was adjusted to about 1 cm. To control exposure time of the test specimen to the electrolyte solution,

a fluid delivery and extraction system was also incorporated into each cell setup. Electrolyte (10 mL) can be automatically delivered to or extracted from cells simultaneously. The time required to assemble the HT-EIS system starting from placement of the coating array assembly is less than 5 min.

The electronic switch control circuit, shown schematically in Figure 6, was created to perform electrode connection/disconnection operations when changing rows during an experiment. This circuit allows for electrochemical measurements to be conducted simultaneously in groups of four without operator intervention. Row selection is controlled through the control software using the two-channel transistor-transistor logic (TTL) output available on the femtostat. A pair of four-pole mechanical relays is used to convert the two output channels to a four-state binary code decimal allowing for up to four measurement combinations. Two field-effect transistors are used to match the impedance between the relay coils and the TTL outputs. A high quality, shielded coaxial cable is used for all of the signal wiring, and the entire unit is housed in an electro-magnetic interference shielded cabinet. A highly insulated reed relay (Coto Technology, Inc.) is used for the on/off switching of REs

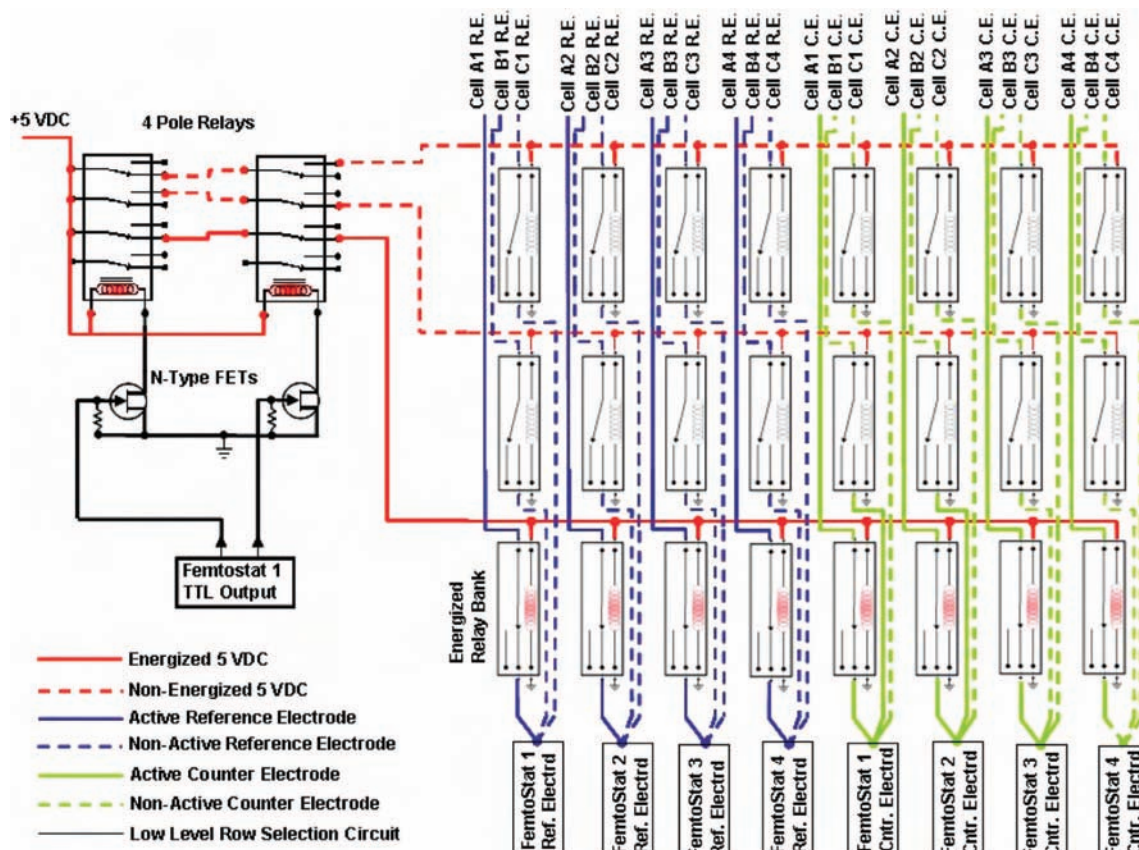


Figure 7. Schematic diagram of the electronic switch control circuit created to perform electrode connection/disconnection operations when changing rows during an experiment. This circuit allows for electrochemical measurements to be conducted simultaneously in groups of four without operator intervention.

and CEs. The working electrodes were simply wired directly to the femtostat input.

Validation of the HT-EIS System. Randles Equivalent Circuit Calibration and Open-Lead Experiment. To test the performance of the HT-EIS system, especially the compatibility of the electronic switching system with the commercial Gamry potentiostat, four identical Randles circuits were used for calibration (Figure 1). Because the EIS spectrum generated from the circuits has a known response, any deviation from the response indicates an issue with instrument operation. Figure 8A displays the 12 Bode plots generated from the respective cells within the HT-EIS system. The 12 plots overlap and the relative standard deviation was less than 0.3% over the entire frequency range, showing very good between-cell reproducibility. The 12 HT-EIS spectra were compared with a theoretical Bode plot, which was calculated using the circuit model and input parameters displayed in Figure 1. As shown in Figure 8B, an excellent correlation ($R^2 = 1$) between the theoretical result and the 12 HT-EIS spectra was obtained indicating that the HT-EIS system can generate highly accurate data over this impedance range.

Open-lead EIS experiments were conducted to evaluate the practical impedance limit of the HT-EIS system such as maximum measurable impedance and lowest measurable capacitance. For this experiment, four cells of the same row of the 12-well electrode array were measured simultaneously and the resulting 12 EIS spectra were numerically simulated using a parallel RC equivalent circuit. The open lead EIS

for the Gamry potentiostats (without using the HT-EIS system) were also conducted as a control experiment. As shown in Figure 9, the maximum measurable impedance for the commercial potentiostat was on the order of $3 \times 10^{12} \Omega$, and the lowest measurable capacitance was about $3.0 \pm 1 \text{ pF}$. In contrast, the maximum impedance recorded with the HT-EIS system was about $3 \times 10^{11} \Omega$, 1 order of magnitude lower than that obtained from the potentiostat. The corresponding lowest capacitance was $30 \pm 1.2 \text{ pF}$, which is 1 order of magnitude higher than that obtained from the potentiostat. The lower input impedance of the HT-EIS system was caused by the additional circuitry associated with the electronic switching system and cell cabling associated with the parallel multiplexer, making the DC background current larger than the measured AC signal at extremely high impedance. The test for the minimum impedance limit of the HT-EIS system was not conducted since it is not of interest for coating research.

Validation Experiment Based on the Redox Couple $\text{K}_4\text{FeCN}_6/\text{K}_3\text{FeCN}_6$. A titanium substrate in a redox couple solution, $\text{K}_4\text{FeCN}_6/\text{K}_3\text{FeCN}_6$, was used as a model system to validate the performance of the 12-well array of the HT-EIS system. There were several reasons for choosing this model system for instrument validation. First, titanium, which is a relatively inert metal, generally exhibits good chemical and electrochemical stability when immersed in an electrolyte.²⁴ Second, neither K_4FeCN_6 nor K_3FeCN_6 show significant adsorption on to titanium surfaces²⁵ which enables

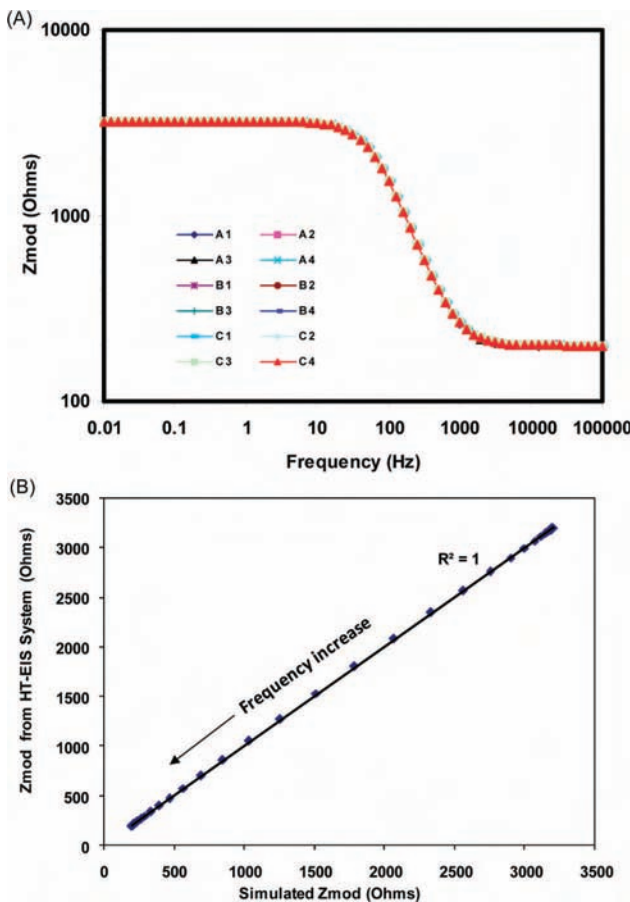


Figure 8. Bode plots generated from each of the 12 electrochemical cells within the HT-EIS system using identical Randles circuits (A). The correlation between impedance modulus generated using the HT-EIS system and the theoretical response obtained using the circuit model and input parameters (B).

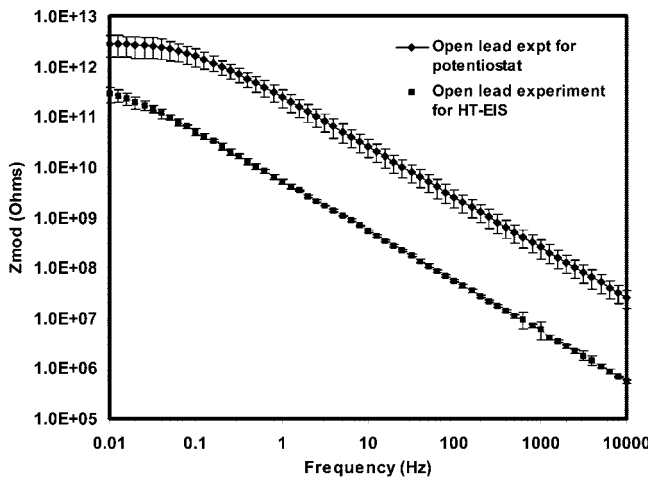


Figure 9. Bode plots obtained from an open lead experiment for the Gamry potentiostat and HT-EIS system.

higher reproducibility for EIS measurements. Further, titanium is physically robust, relatively inexpensive, and easy to handle.

For the validation experiment, a four-tab array (Figure 3A) was machined from a titanium panel. The open circuit potential (OCP) of the metal in the $\text{K}_4\text{FeCN}_6/\text{K}_3\text{FeCN}_6$ electrolyte reached steady state in a few seconds generating a relatively stable value at 0.22 ± 0.02 V vs the Ag/AgCl RE. The OCPs for the four cells comprising a single row of

the HT-EIS system were recorded simultaneously and EIS experiments were conducted. As shown in Figure 10A, the 12 Bode plots generated from the experiment were essentially the same, indicating equivalence of each of the 12 electrochemical cells. These results were also compared with results obtained using a conventional, single-cell EIS setup. A good linear correlation ($R^2 = 0.99$) was found over the entire frequency range (Figure 10B) suggesting that the HT-EIS system can provide the same level of data accuracy as a conventional, single-cell EIS setup. The EIS data for both experimental arrangements were fitted using the following equivalent circuit model:



where R1, R2, and CPE are solution resistance, charge transfer resistance, and a constant phase element, respectively. The CPE is used to simulate the surface capacitance effect that compensates for surface heterogeneity in the system. The values obtained for these parameters are listed in Table 1. No significant difference was found between the values obtained with the conventional, single-cell EIS and the values obtained with the HT-EIS system.

Validation Experiments Utilizing a Uniform Polymer Film. In practice, coatings for corrosion protection typically involve high impedances, in the range of 10^9 Ω or higher. Thus, the performance of the HT-EIS system needed to be evaluated further in this high impedance range. Recently, Bierwagen et al.²² proposed a method for calibrating a potentiostat that involved the use of a commercially available polymer film possessing uniform thickness and little or no film defects. The method is relatively simple, low-cost, and, more importantly, capable of providing highly reproducible results in the high impedance range.

As a result, a Tedlar film of uniform thickness was adhered to AA 2024-T3 and EIS measurements made. As shown in Figure 11A, Bode plots obtained using the HT-EIS system for this film were characteristic of a high-performance coating with very low permeability. The film behaved like a capacitor, generating a straight-line Bode plot with a slope of about -1 and very high impedance (more than 10^{10} Ω) at low frequency.²² The relative standard deviation (RSD) with respect to the variation in impedance generated from the 12 cells of the HT-EIS system was determined to be 12–19% which was somewhat higher than the 7–15% RSD obtained using 12 replicate measurements made with a conventional, single-cell EIS setup. As shown in Figure 11B, the average impedance values obtained using the HT-EIS system were compared with those obtained using a conventional, single-cell EIS and a good linear correlation ($R^2 = 0.99$) was found between the two set-ups. This results shows that the HT-EIS system is capable of characterizing materials possessing a high, low-frequency impedance. In addition, a CPE circuit model was used to simulate the results generated from the HT-EIS system, and the film capacitance was determined to be 0.64 ± 0.12 nF. From the capacitance, the dielectric constant of the film was calculated and determined

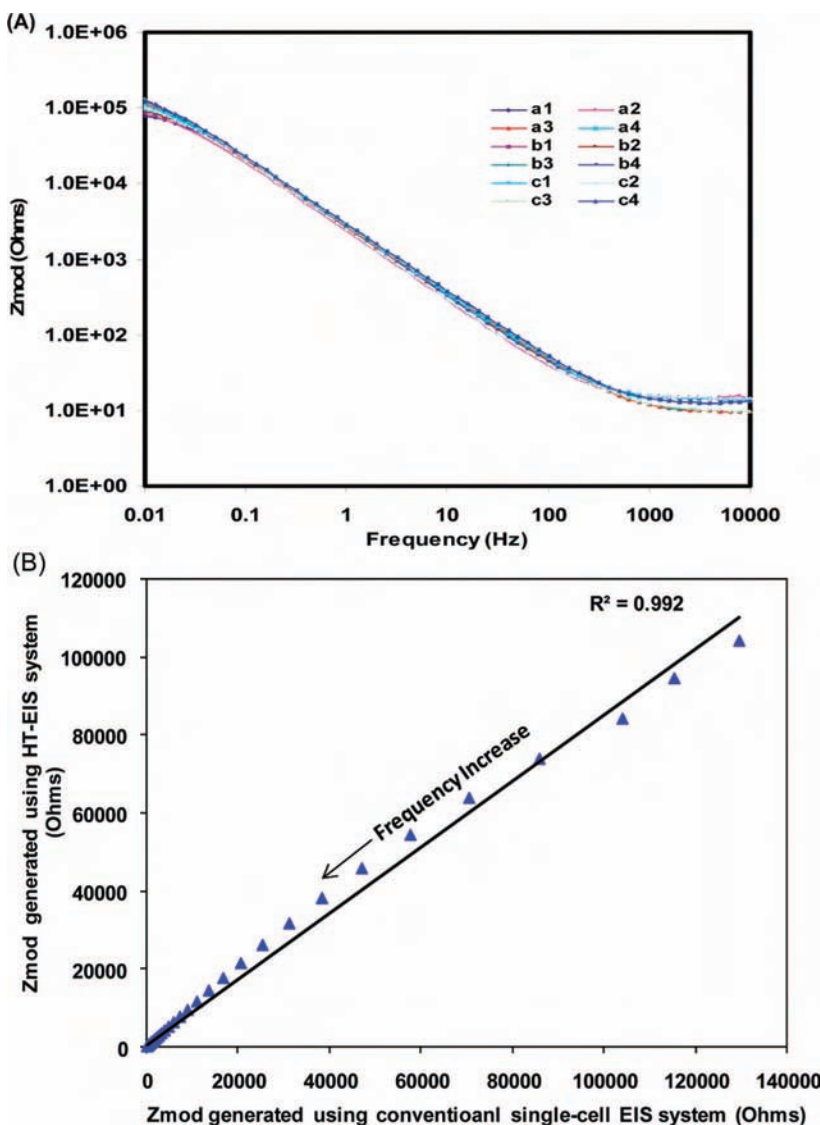


Figure 10. Bode plots generated for the $\text{K}_4\text{FeCN}_6/\text{K}_3\text{FeCN}_6$ redox couple using the HT-EIS system (A). A correlation between impedance moduli generated using the HT-EIS system and those generated with a conventional single-cell EIS setup (B).

Table 1. Electrochemical Parameters Calculated for the Redox Couple $\text{K}_4\text{FeCN}_6/\text{K}_3\text{FeCN}_6$ Using Both the HT-EIS System and a Conventional Single-Cell EIS System

	R_1 (Ω)	$R_2 \times 10^5$ (Ω)	capacitance ($\times 10^{-6}$ F)
single-cell EIS	12.1 ± 2.1	1.31 ± 0.19	73.7 ± 1.6
HT-EIS	11.8 ± 3.8	1.04 ± 0.18	78.5 ± 2.79

to be 7.3.²² This dielectric constant was within the 5–8 range provided in the technical data sheet for the film.

Validation Experiments Utilizing Polymer Coatings. To test the feasibility of the HT-EIS system for characterization of organic coating systems, a commercial polyurethane coating was applied to the four-tab array derived from a panel of AA 2024-T3. After the panels were cured, scribes were made on all specimens in row C of the array. EIS measurements were performed using all 12 positions of the four specimen array. As shown in Figure 12, the low-frequency impedance obtained for the 8 replicate unscripted samples (rows A and B of the four tab array) varied in the range of 10^6 – 10^7 Ω , and the coating capacitance ranged between 5.28 and 21.6 nF. These parameters were obtained by fitting the data to a parallel R (CPE) equivalent circuit model. This level

of variation was higher than that obtained from the model film validation experiment which may be caused by variations in coating thickness and the presence of film defects.

For the scribed positions (row C of the four tab array), the low-frequency impedance values were 2 orders of magnitude lower than for the unscripted positions. The EIS measurements on the four scribed positions produced similar and, in some cases, overlapping spectra. Variations in the manually produced scribes most likely contributed to the variation observed in the Bode plots of the scribed positions.

In addition to using the three positions of a coated specimen for obtaining replicate EIS data, the HT-EIS system can be used to conduct different electrochemical measurements on the same coating specimen to obtain a wide range of information. To illustrate, four different coatings were prepared and applied to AA 2024-T3 using the array format (Figure 13A). The coatings prepared included a chromate-containing epoxy primer (Cr-epoxy), a Mg-rich epoxy primer, a polyurethane primer (MIL-PRF-85285D), and a coating system labeled as Mg/PUR, which is composed of a Mg-rich epoxy primer and a polyurethane topcoat (MIL-PRF-

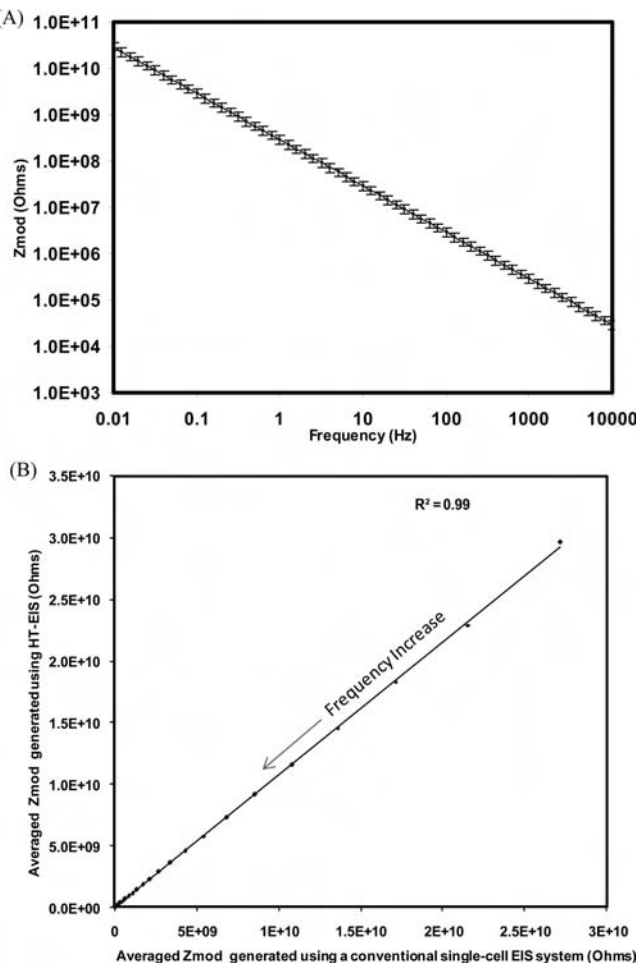


Figure 11. Bode plots for Tedlar film laminated to Al 2024-T3 generated using the HT-EIS system (A). A correlation between impedance moduli generated using the HT-EIS system and those generated with a conventional single-cell EIS setup (B).

85285D). In the top row of the array (row A in Figure 13A), EIS experiments were performed to determine the barrier properties of the coatings. In the middle positions of the array (row B in Figure 13A), linear polarization experiments were conducted to obtain electrochemical parameters such as corrosion current and corrosion potential. Scribes were made in the bottom positions of the coating array (row C in Figure 13A), and EIS was used to characterize the metal-coating interaction in the electrolyte. Utilization of multiple experiments per coating specimen enabled the generation of a plethora of information with the HT-EIS system. For example, the data obtained from the experiment provide the following information:

1. On the basis of Bode plots (Figure 13B) generated using EIS experiments at row A of the coating array, the Cr-epoxy coating was shown to possess the highest low-frequency impedance value ($3 \times 10^7 \Omega$), followed by the top-coated Mg-rich primer, the polyurethane primer, and the Mg-rich primer. The high impedance at low-frequency range for the Cr-epoxy sample (A1) is the result of the known inhibitive properties of chromate pigments by virtue of passivating the metal surface and enhancing or stabilizing the oxide layer at the metal surface. The low impedance value of the Mg-rich primer is attributed to the electrically conductive nature of the coating. The reason that the low frequency impedance

for the topcoated Mg-rich primer is higher than that for the polyurethane primer may be caused by the film thickness difference between the two forms of coatings. On the other hand, the shape and profile of the Bode plots at higher frequency range (typically from 10 to 10^4 Hz) indicate the capacitive behavior of these coatings. Qualitatively, the capacitances (C) for the four samples can be ranked in the following order: $C_{\text{Mg-richprimer}} > C_{\text{Mg/PUR}} > C_{\text{polyurethane}} > C_{\text{Cr-epoxy}}$. The higher capacitance value suggests the higher content of water ingressing into the coating. The high capacitance for the Mg containing coatings may be attributed to the relative hydrophilic nature of the coating.

2. Corrosion currents measured using linear polarization experiments (Figure 13C) at row B of the coating array showed that the relative ranking of corrosion current was $I_{\text{Cr-epoxy}} < I_{\text{Mg/PUR}} \leq I_{\text{polyurethane}} < I_{\text{Mg-richprimer}}$. It is found that a significant current drop exists between Mg-rich primer and the rest of coatings, which is because the Mg-rich primer offers higher electrical conductivity than the other coatings. The corrosion current ranking was inversely correlated with the low frequency impedance ranking obtained from the EIS measurement at row A of the coating array (Figure 13B). The corrosion potential (-1.2 V vs reference) measured for the Mg-rich primer (Figure 13C) was significantly lower than those for the other coatings and consistent with a mixed potential between Mg and AA 2024-T3. This result, in conjunction with the low impedance (Figure 13B) and high corrosion current observed for the Mg-rich primer, indicates galvanic coupling between Mg particles in the Mg-rich primer and the AA 2024-T3 substrate.

3. Comparing Figure 13B to Figure 13D, one can see that the introduction of a scribe into the Mg-rich primer-coated sample did not result in a significant reduction in impedance. This result indicates that the primer provides corrosion protection mainly through electrochemical interaction with the substrate. In contrast, the low-frequency impedance for the rest of the coatings decreased significantly after the introduction of the scribes. It is interesting to note that the impedance value for the Cr-epoxy (C1) was still the highest of the four coatings even after introduction of the scratch, the effect of which may be the result of the healing effect established either by the inhibitive pigments leached from the coating²⁶⁻³¹ or by a resistive corrosion product produced by the inhibitive pigments.^{32,33} Since looking for corrosion protection mechanisms of these particular coatings is not the main concern of the study, the subject will not be explored in further detail here.

Conclusions

A HT-EIS system based on a four-coating array was developed that enables 12 electrochemical measurements to be made with a minimum of manual intervention. In addition, the system allows for quick assembly when compared to the setup of an equivalent number of single-cell EIS assemblies. It was estimated that the HT-EIS system enables at least a 4-fold reduction in setup time compared to the use of conventional EIS equipment.

System validation experiments comparing results obtained with the HT-EIS system to results obtained using a single-

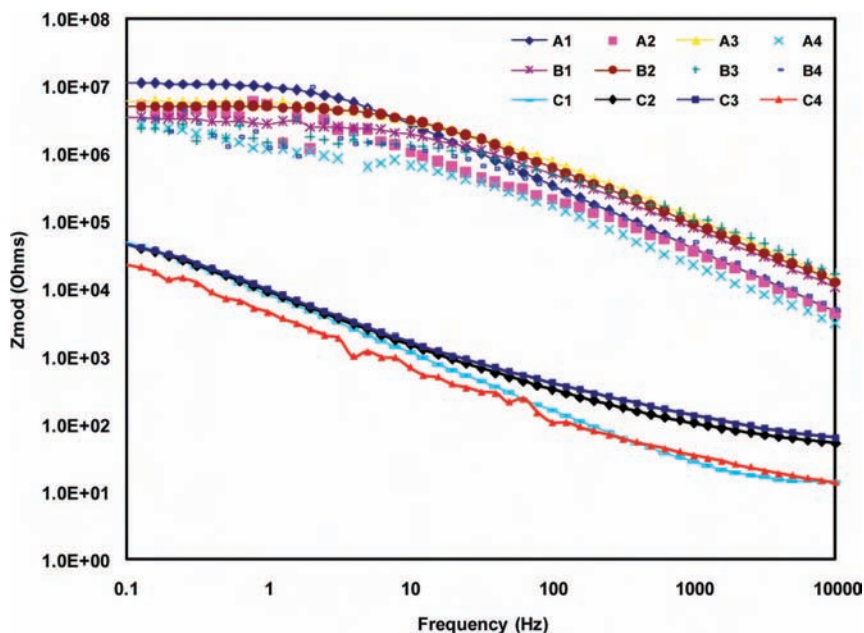


Figure 12. Bode plots for a polyurethane coating on Al 2024-T3 generated using the HT-EIS system. Positions A1–A4 and B1–B4 were not scribed, while positions C1–C4 were scribed prior to making measurements.

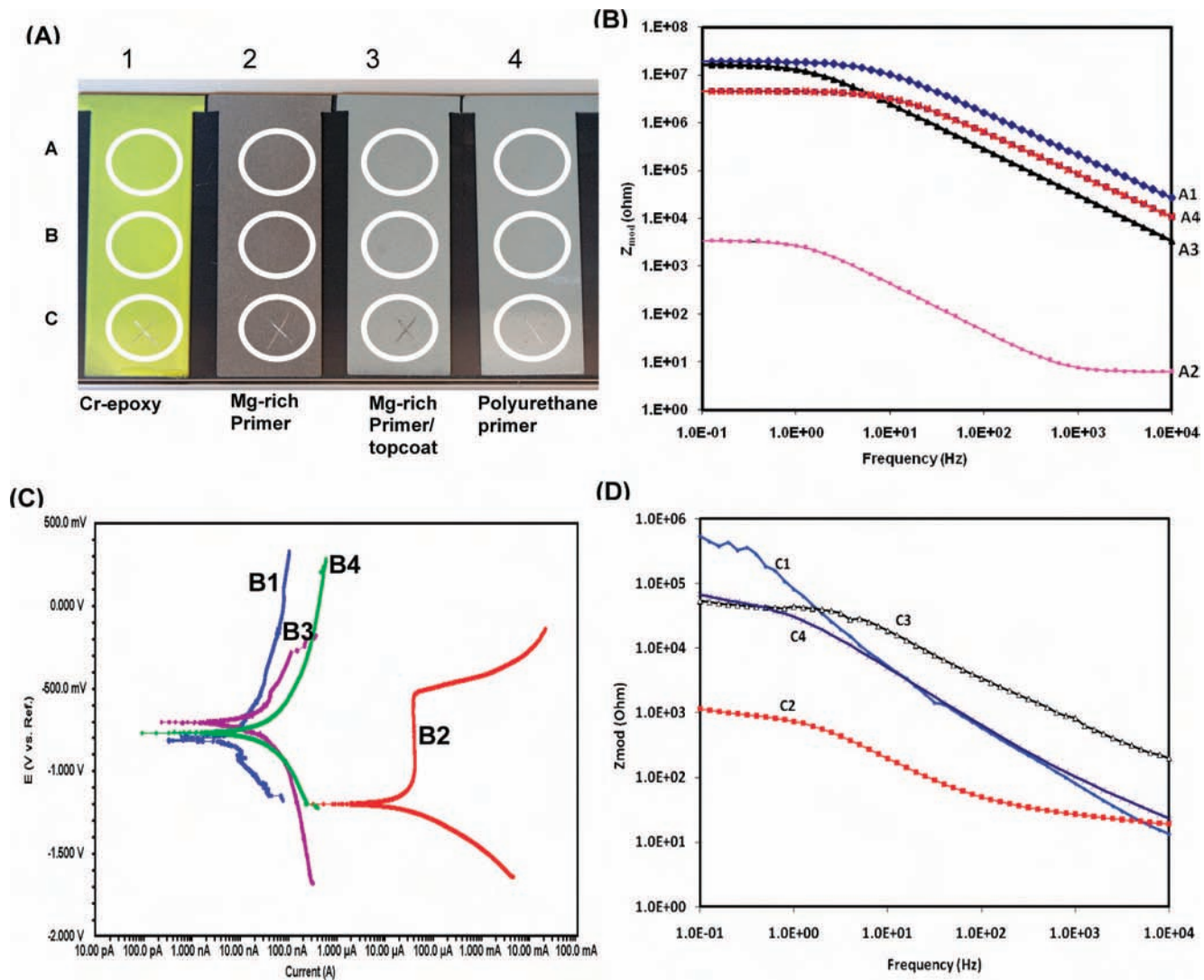


Figure 13. An illustration of the utility of using the HT-EIS system to conduct a variety of electrochemical measurements on the same sample specimen: an image of the four coating array assembly (A), Bode plots generated using row A of the coating array (B), linear polarization measurements using row B of the coating array (C), and Bode plots generated using row C of the coating array (D).

cell EIS assembly indicated that high quality data can be obtained using the HT-EIS system. The maximum impedance and the lowest capacitance that can be measured using the HT-EIS system was determined to be $3 \times 10^{11} \Omega$ and $30 \pm 1.2 \text{ pF}$, respectively. The HT-EIS system is currently being used within a full combinatorial workflow designed to enhance the rate of organic coating development.^{13,34} The throughput of the system could be further improved by increasing the density of the microelectrode array (e.g., 24-electrode array) and by developing more efficient software to facilitate library design and data analysis.

Acknowledgment. The authors gratefully acknowledge financial support from the Air Force Research Laboratory under Grant FA8650-04-1-5045.

References and Notes

- (1) *Corrosion Cost and Preventive Strategies in the United States*; CC Technologies Laboratories: Dublin, OH 2001.
- (2) Wranglen, G. *An Introduction to Corrosion and Protection of Metals*; Institute for Metallurgy: Stockholm, Sweden, 1972.
- (3) Grundmeier, G.; Schmidt, W.; Stratmann, M. *Electrochim. Acta* **2000**, *45*, 2515–2533.
- (4) Rammelt, U.; Reinhard, G. *Prog. Org. Coat.* **1992**, *21*, 205–226.
- (5) Van Westing, E. P. M.; Ferrari, G. M.; De Wit, J. H. W. *Electrochim. Acta* **1994**, *39*, 969–973.
- (6) *Standard Practice for Operating Salt Spray (Fog) Apparatus*; ASTM B117–97; ASTM International: West Conshohocken, PA, 1996.
- (7) *Standard Practice for Cyclic Salt Fog/UV Exposure of Painted Metal*; ASTM D5894–96; ASTM International: West Conshohocken, PA, 1996.
- (8) Cawse, J. N.; Olson, D.; Chisholm, B. J.; Brennan, M.; Sun, T.; Flanagan, W.; Akhave, J.; Mehrabi, A.; Saunders, D. *Prog. Org. Coat.* **2003**, *47*, 128–135.
- (9) Chisholm, B.; Potyrailo, R.; Cawse, J.; Shaffer, R.; Brennan, M.; Molaison, C.; Whisenhunt, D.; Flanagan, B.; Olson, D.; Akhave, J.; Saunders, D.; Mehrabi, A.; Licon, M. *Prog. Org. Coat.* **2002**, *45*, 313–321.
- (10) Chisholm, B.; Potyrailo, R.; Shaffer, R.; Cawse, J.; Brennan, M.; Molaison, C. *Progress in Organic Coatings* **2003**, *48*, 219–226.
- (11) Chisholm, B.; Potyrailo, R.; Shaffer, R.; Cawse, J.; Brennan, M.; Molaison, C. *Prog. Org. Coat.* **2003**, *47*, 112–119.
- (12) Chisholm, B. J.; Potyrailo, R. A.; Cawse, J. N.; Shaffer, R. E.; Brennan, M.; Molaison, C. A. *Prog. Org. Coat.* **2003**, *47*, 120–127.
- (13) Webster, D. C.; Chisholm, B. J.; Stafslien, S. J. *Biofouling* **2007**, *23*, 179–192.
- (14) Jayaraman, S.; Baeck, S.-H.; Jaramillo, T. F.; Kleiman-Shwarscstein, A.; McFarland, E. W. *Rev. Sci. Instrum.* **2005**, *76*, 1–5.
- (15) Baeck, S. H.; Jaramillo, T. F.; Brandli, C.; McFarland, E. W. *J. Comb. Chem.* **2002**, *4*, 563–568.
- (16) Guerin, S.; Hayden, B. E.; Lee, C. E.; Mormiche, C.; Owen, J. R.; Russell, A. E.; Theobald, B.; Thompsett, D. *J. Comb. Chem.* **2004**, *6*, 149–158.
- (17) Fleischauer, M. D.; Hatchard, T. D.; Rockwell, G. P.; Topple, J. M.; Trussler, S.; Jericho, S. K.; Jericho, M. H.; Dahn, J. R. *J. Electrochem. Soc.* **2003**, *150*, A1465–A1469.
- (18) Reddington, E.; Sapienza, A.; Gurau, B.; Viswanathan, R.; Sarangapani, S.; Smotkin, E. S.; Mallouk, T. E. *Science* **1998**, *280*, 1735–1737.
- (19) Randles, J. E. *Discuss. Faraday Soc.* **1947**, *1*, 11.
- (20) Loveday, D.; Peterson, P.; Rodgers, B. *JCT Coat. Technol.* **2004**, *1*, 46–52.
- (21) *Standard Guide for Descaling and Cleaning Titanium and Titanium Alloy Surfaces*; ASTM B 600–91; ASTM International, Inc.: West Conshohocken, PA, 1991.
- (22) Bonitz, V. S.; Hinderliter, B. R.; Bierwagen, G. P. *Electrochim. Acta* **2006**, *51*, 3558–3565.
- (23) Fact Sheet: High Volume Low Pressure Spray Equipment; Wisconsin Department of Natural Resources, 1993.
- (24) Hurlen, T.; Wilhelmsen, W. *Electrochim. Acta* **1986**, *31*, 1139–1146.
- (25) Hurlen, T.; Wilhelmsen, W. *Electrochim. Acta* **1988**, *33*, 1729–1733.
- (26) Suda, A. *Hyomen Kagaku* **2001**, *22*, 136–143.
- (27) Zhao, J.; McCreery, R. L.; Frankel, G. S.; Allen, F. *Abstr. Pap.—Am. Chem. Soc.* **2000**, *220th*, ANYL-163.
- (28) Ramsey, J. D.; McCreery, R. L. *J. Electrochem. Soc.* **1999**, *146*, 4076–4081.
- (29) Zhao, J.; Frankel, G.; McCreery, R. L. *J. Electrochem. Soc.* **1998**, *145*, 2258–2264.
- (30) Suda, A.; Asari, M. *Zairyo to Kankyo* **1997**, *46*, 95–102.
- (31) Lu, Y.; Ren, Y.; Ying, H.; Wu, J.; Zhang, P.; Meng, H. *Proc. Int. Conf. Surf. Sci. Eng.* **1995**, 205–208.
- (32) Lohrengel, M. M. *Mater. Sci. Eng., R: Rep.* **1993**, *R11*, 243–294.
- (33) Schmitt, G.; Schultze, J. W.; Fassbender, F.; Buss, G.; Luth, H.; Schoning, M. *J. Electrochim. Acta* **1999**, *44*, 3865–3883.
- (34) Chisholm, B. J.; Webster, D. C. *J. Coat. Technol. Res.* **2007**, *4*, 1–12.

CC8000458

Editorial Manager(tm) for Journal of Coatings Technology and Research
Manuscript Draft

Manuscript Number:

Title: Combinatorial Materials Research Applied to the Development of New Surface Coatings XI:
A Workflow for the Development of Hybrid Organic-Inorganic Coatings

Article Type: Original Research

Keywords: hybrid organic-inorganic; coating; magnesium; corrosion; combinatorial; high-throughput;
sol-gel; surface functionalization; silica

Corresponding Author: Bret J Chisholm,

Corresponding Author's Institution: North Dakota State University

First Author: Bret J Chisholm

Order of Authors: Bret J Chisholm; Missy Berry; James Bahr; Jie He; Seva Balbyshev; Gordon P
Bierwagen

Combinatorial Materials Research Applied to the Development of New Surface Coatings XI: A Workflow for the Development of Hybrid Organic-Inorganic

Coatings

Bret J. Chisholm,^{1,2} Missy Berry,¹ James Bahr,¹ Jie He,¹ Jun Li,² Seva Balbyshев,¹ and Gordon P. Bierwagen²*

¹The Center for Nanoscale Science and Engineering

²Department of Coatings and Polymeric Materials

North Dakota State University

1805 Research Park Drive

Fargo, ND 58102

Abstract

Interest in hybrid organic-inorganic (HOI) materials has grown rapidly in the last two decades. The appeal of this broad class of materials can be attributed to the unique combinations of properties that can be achieved by combining an inorganic phase with an organic phase. HOI materials can be divided into two basic categories: homogeneous systems derived from monomers or miscible organic and inorganic components, and heterogeneous, phase-separated systems with domains ranging from angstroms to micrometers in size. The structure of the inorganic component is dependent on the

interaction of many variables such as pH, water content, overall solution concentration, solvent composition, temperature, and time. Due to the complexity of HOI materials, a combinatorial/high-throughput approach to the development of novel materials is highly desired. The author's have recently developed a combinatorial workflow for the synthesis and characterization of HOI coatings. Initial experimentation conducted with the workflow was focused on the development of primers for corrosion protection derived from a HOI binder system and magnesium particles. Both homogeneous and heterogeneous HOI binders were investigated. With just one iteration of the combinatorial workflow, heterogeneous, moisture-curable HOI binders were identified that enabled the formation of magnesium-rich primers that provided excellent corrosion protection to an aerospace aluminum alloy (Al 2024).

*To Whom Correspondence Should be Addressed

Bret.Chisholm@ndsu.edu

1
2
3
4
5
6
7
8
9 **Introduction**
10
11
12
13
14
15
16
17
18
19
20
21
22
23
24
25
26
27
28
29
30
31
32
33
34

In the past two decades, research in the area of hybrid organic-inorganic (HOI) materials has exploded both in industry and academia. To illustrate this point, Loy¹ noted that the number of patents and publications containing the term “hybrid organic-inorganic” increased from fewer than five in 1985 to over 528 in the year 2000, including 85 patents. The interest in this broad class of materials can be attributed to the unique combinations of properties that can be achieved by combining an inorganic phase with an organic phase. HOI materials can be divided into two basic categories: homogeneous systems derived from monomers or miscible organic and inorganic components, and heterogeneous, phase-separated systems with domains ranging from angstroms to micrometers in size. Thus, the definition of HOI materials excludes polymeric compositions containing inorganic fillers or fibers, such as polymer composites.

The most common method for producing HOI materials is the sol-gel process, which is a solution method.² With this process, the inorganic phase is produced by hydrolysis and condensation of metal alkoxides. Many of the advantageous properties of HOI materials can be attributed to the sol-gel process which often results in the formation of a very fine inorganic phase, often interconnected three-dimensionally, within an organic polymer. A tremendous number of variables, most of which strongly influence material properties, are involved in a sol-gel process. These variables include metal-alkoxide composition and/or organometal-alkoxide composition (Si, Al, Ti, Zr, as well as their mixtures that result in co-condensed mixed metal-oxides, and organogroup chemical composition), alkoxide concentration, water:alkoxide ratio, pH, temperature, and solvent

composition. While other additional factors can be considered, the combination of the most basic variables that are listed above constitute a huge multidimensional compositional space. The complexity of the chemistry involved in a sol-gel process coupled with the high sensitivity of the compositional variables to material composition makes the prediction of material properties based on first principles very difficult. As a result, an extensive amount of experimentation is typically required to develop a HOI material with a desirable set of material properties. Based on these considerations, the application of combinatorial/high-throughput methods to the development of HOI materials appeared to be a very worthwhile endeavor.

The author's and their colleagues have created an extensive combinatorial workflow for the development of new polymers and coatings for applications such as environmentally-friendly marine coatings and coatings for corrosion protection.³⁻⁶ This document describes more recent efforts to create a combinatorial workflow for the development of HOI coatings designed to provide corrosion protection to aluminum alloys. The primary function of the combinatorial workflow was to develop a HOI binder system for magnesium (Mg) particles for the production of high performance primers for the protection of aluminum alloys from corrosion.^{7,8}

The rationale for an investigation of HOI binders for Mg-rich coatings came from prior work conducted on the development of zinc (Zn)-rich coatings for the protection of steel substrates via a cathodic protection mechanism in which the Zn serves as a sacrificial anode.⁹ Two general classes of Zn-rich coatings have been commercialized which are distinguished by their binder chemistry. The two general classes are two-component, epoxy-based Zn-rich coatings and Zn-silicate coatings. The Zn-silicate

1
2
3
4 primers are based on a silicate binder system derived from alkoxy silanes using a sol-gel
5 process in which curing occurs at ambient temperature through silanol condensation. In
6 general, it has been found that Zn-silicate primers provide longer service-life compared to
7 epoxy-based Zn-rich primers.⁹
8
9

10 Since Mg has a higher oxidation potential than aluminum (Al), Mg particles can
11 serve as a sacrificial anode to provide cathodic protection to Al substrates in analogy to
12 the protection of steel substrates with Zn particles.^{7,8} Mg-rich primers for the protection
13 of aluminum alloys based on organic binder systems have been previously investigated
14 and found to provide very good corrosion protection.⁷ This document describes initial
15 efforts to develop Mg-rich primers based on HOI binders using a combinatorial approach.
16
17
18
19
20
21
22
23
24
25
26
27
28
29
30

31 Experimental

32
33
34
35

36 *Materials.* All reagents were used as received. Methyltrimethoxysilane (MeTMS),
37 ureidopropyltrimethoxysilane (UpTMS), 3-aminopropyltrimethoxysilane (ApTMS),
38 diethylphosphatoethyltriethoxysilane (DTES), phenethyltrimethoxysilane (PhEtTMS), (3-
39 glycidoxypropyl)trimethoxysilane (GpTMS), and 2-(3,4-
40 epoxycyclohexyl)ethyltrimethoxysilane (CyTMS) were all purchased from Gelest
41 Incorporated. Glacial acetic acid, propylene glycol monomethyl ether (PMA),
42 tetrabutylammonium fluoride (1.0 M in tetrahydrofuran), and tetraethoxysilane (TEOS)
43 were purchased from Sigma Aldrich Company. Water was purified via reverse osmosis.
44 Isopropyl alcohol (IPA) was manufactured by Burdick & Jackson and purchased from
45 VWR International. Colloidal silica (Snowtex-O) was purchased from Nissan Chemical.
46
47
48
49
50
51
52
53
54
55
56
57
58
59
60
61
62
63
64

1
2
3
4 Magnesium powder was obtained from Ecka Granules and had an average particle size of
5 25 microns. AntiTerra 204, a wetting agent, was obtained from BYK Chemie. Bentone
6
7 38, an anti-settling agent, was obtained from Elementis Specialties. Aerosil R812, a
8 viscosity modifier, was obtained from Degussa. Mica 325WG was obtained from
9 Georgia Industrial Minerals Inc. The substrate used for corrosion testing was Al 2024-T3
10
11 obtained from Q-Panel. The polyurethane topcoat used together with experimental Mg-
12 rich primer compositions was MIL-PRF-85285C obtained from Deft Chemical Coatings.
13
14 Salt water used for corrosion screening by immersion testing was 3 weight percent
15 sodium chloride in water purified by reverse osmosis.
16
17
18
19
20
21
22
23
24

25 Sols used to produce homogeneous HOI coatings were synthesized as follows:
26 IPA, water, acetic acid, TEOS, and trialkoxysilane were added sequentially to an 8-mL
27 scintillation vial, containing a stir bar, using the liquid handling robot. The solutions
28 were allowed to stir overnight at room temperature. Detailed formulations for all of the
29 homogeneous sols prepared are provided in Appendices 1 and 2.
30
31
32
33
34
35
36
37

38 Sols used to produce heterogeneous HOI coatings were synthesized as follows:
39 IPA, colloidal silica, and trialkoxysilane were added sequentially to an 8-mL scintillation
40 vial, containing a stir bar, using a liquid handling robot. The solutions were allowed to
41 reflux for a total of 2 or 24 hours. In the cases where tetrabutylammonium fluoride
42 (TBAF) was used, it was added after the first hour of reflux. Detailed formulations for all
43 of the heterogeneous sols prepared are provided in Appendix 3.
44
45
46
47
48
49
50
51
52

53 Mg-rich primers based on HOI binders were prepared using the formulation
54 shown in Table I. This formulation provides a primer composition comprised of 80
55
56
57
58
59
60
61
62
63
64
65

1
2
3
4 weight percent Mg particles. The solids content of the HOI solutions or colloidal
5 dispersions were adjusted with PMA to be 10 % by weight.
6
7

8
9 *Instrumentation and Software.* A Symyx® Discovery Tools™ liquid handling
10 robot was used for producing arrays of sols while a Tecan® Freedom EVO liquid
11 handling robot was used to cast sols into stamped aluminum arrays. Library Studio® was
12 used to design all experiments run with the automated robots. The instruments were run
13 using either an Impressionist® procedure or Epoch® protocol. Solvents were removed
14 from samples using a Genevac® EZ-2 parallel evaporator. Salt spray corrosion testing
15 was done in a Q-FOG cyclic corrosion tester (model SSP, 1100 liter capacity) according
16 to ASTM method B117. Electrochemical impedance spectroscopy (EIS) measurements
17 were taken with a potentiostat from Gamry Instruments. The software used was Gamry
18 Framework (version 4.35). Data analysis was accomplished using Gamry EChem
19 Analyst (version 1.35).
20
21

22 *Methods.* The combinatorial workflow implemented for developing HOI binders
23 for Mg-rich primers for corrosion protection was based on a tiered material screening
24 process as illustrated in Figure 1. Sols were prepared robotically using the Symyx liquid
25 handling robot. The compositions used to produce the sols are shown in Appendices 1-3.
26 After having prepared the sols, their stability was evaluated 24 hours later.
27
28

29 Sols that produced homogenous solutions or homogenous, stable, colloidal
30 dispersions were robotically cast into embossed wells of the four inch by eight inch
31 aluminum panels shown in Figure 2 using the Tecan® Freedom EVO liquid handling
32 robot. Each well was 2.5 cm by 3.8 cm and approximately 1.0 mm deep, and 750 µL of
33 solution was pipetted into a well. The array of solutions were then placed in a low flow,
34
35
36
37
38
39
40
41
42
43
44
45
46
47
48
49
50
51
52
53
54
55
56
57
58
59
60
61
62
63
64
65

1
2
3
4 vented cabinet to allow for solvent evaporation and curing at ambient conditions for 24
5 hours. After the 24 hour period for solvent evaporation and curing, film formation and
6 curing characteristics were rapidly accessed using visual and physical observation.
7 Compositions that produced tack-free films that had no visible signs of cracking were
8 taken through a second solution processing step in which PMA was added to a given sol
9 at a weight equivalent to a factor of 1.75 relative to the total weight of solids and the
10 mixture solvent stripped using the parallel rotary evaporator to largely remove the lower
11 boiling solvents, IPA and water, rendering the HOI material in PMA. After this solution
12 processing step, stability of the sols was assessed using visual observation and only those
13 sols that displayed good stability were carried forward to secondary screening.

14 Secondary screening consisted of the preparation of larger volumes of the sols
15 selected from primary screening using two Radley® carousel reactors and manual
16 solution preparation. The solvent exchange process for each sol was done using a
17 conventional rotary evaporator using a temperature of 60°C and pressure of
18 approximately 5 mm Hg. With these larger volume sols, tabs machined from a standard
19 4 inch by 8 inch aluminum panel, as shown in Figure 3, were dip coated using the parallel
20 dip coater such that each tab contained a different coating composition. The dip coated
21 coatings were then allowed to cure and the barrier properties of the coatings characterized
22 using salt water immersion as a screen. The compositions that showed the best barrier
23 properties were used for formulation experiments involving the use of Mg particles for
24 cathodic protection. Traditional, manual methods of experimentation were used for Mg-
25 rich primer formulation experiments.

1
2
3
4
5
6
7
8
9 **Results and Discussion**
10
11
12
13
14
15
16
17
18
19
20
21
22
23
24
25
26
27
28
29
30

General Aspects of the Combinatorial Workflow. The combinatorial workflow created to develop new HOI Mg-rich primers for corrosion protection of aluminum alloys is shown schematically in Figure 1. The workflow was based on a tiered screening process in which initial screening involved the synthesis and characterization of sols produced from hydrolysis and condensation reactions of alkoxy silane functional monomers in solution. The results of the initial screening resulted in the identification of sols that displayed both solution stability and cured that films that were tack-free and free of macroscopic cracks. Only those compositions that showed these desirable characteristics were selected for further experimentation.

The next step in the tiered process involved exchange of water and low boiling alcohols (IPA and methanol) present in the sols with the higher boiling solvent, PMA. This process was required to largely remove water from the materials to further drive condensation reactions and minimize water induced oxidation of Mg particles during Mg-primer formulation. After completing the solvent exchange, solution stability was again screened since some of the previously stable solutions may have gelled or formed a precipitate. Those compositions that produced stable solutions or colloidal dispersions after undergoing the solvent exchange process were carried forward for further screening referred to as “secondary” screening.

Secondary screening involved scale-up of solution volumes to 50 mls, dip coating on to the aluminum alloy substrate of interest, curing at ambient conditions, and measuring relative corrosion protection using partial immersion of coated specimens in

1
2
3
4 salt water. Those compositions showing the best corrosion resistance based on visual
5 observation were selected for use in Mg-rich primer formulation experiments in which
6 the HOI solutions were utilized as the coating binder material.
7
8
9
10
11
12
13

14 *Experiments Involving the Development of Mg-rich Primers Based on a Homogeneous*
15 *HOI Binder System.* Initial high throughput experiments for the development of HOI-
16 based Mg-rich primers were focused on binders based on a homogenous HOI network
17 derived from trialkoxysilanes and tetraethoxysilane (TEOS) using a sol-gel process,
18 shown schematically in Figure 4. The experimental design utilized for the first screening
19 experiment was based on variations in trialkoxysilane composition, molar ratio of
20 trialkoxysilane to TEOS, and molar ratio of water to alkoxy silane functional groups.
21 Figure 5 provides the chemical structure of the trialkoxysilanes investigated while Figure
22
23
24
25
26
27
28
29
30
31
32
33
34
35
36
37
38
39
40
41
42
43
44
45
46
47
48
49
50
51
52
53
54
55
56
57
58
59
60
61
62
63
64
65

The rationale for the selection of the amino-, ureido-, and phosphonato-functional trialkoxysilanes was based on the need for relatively polar or reactive functional groups in order to provide for good adhesion of the primer to the substrate and good wetting and adhesion of the topcoat to the primer. Methyltrimethoxysilane (MeTMS) was included to serve primarily as a negative control to determine the effect of a relatively nonpolar, nonreactive organic functional group on coating performance.

Figure 7 displays the results obtained with regard to solution stability and cured film characteristics. As previously discussed, solution stability was simply characterized by visual observation. Figure 8 displays representative images of sols that were produced

1
2
3
4 during the experiment. It can be seen that, for this experiment, solution stability was
5 easily characterized using visual observation.
6
7

8 From Figure 7, some general trends between the responses and chemical
9 composition can be readily discerned. Most notable, all of the sols derived from ApTMS
10 were unstable and resulted in the formation of a precipitate or gel. This result was not
11 completely unexpected since the addition of ApTMS to the acidic IPA/water/TEOS
12 mixture increased pH from approximately 3 to approximately 10 causing a rapid increase
13 in condensation rate.² For sols based on UpTMS, most of the sols were unstable, with the
14 exception of two sols derived from the highest water/alkoxysilane ratio and a molar
15 excess of UpTMS to TEOS. These two sols all produced cured films that were both tack-
16 free and free of visible cracks.
17
18

19 For sols based on MeTMS, two trends were apparent. First, sols containing the
20 highest level of water tended to be unstable while those containing lower water levels
21 provided stable sols. For a sol-gel process, water/alkoxysilane ratio strongly influences
22 structure of organosilicate oligomers. Use of an excess of water to alkoxysilane groups
23 tends to produce spherical particles whereas more linear structures are produced when
24 alkoxysilane groups are in molar excess to water.²
25
26

27 The second trend observed involved the effect of TEOS/MeTMS molar ratio on
28 cured film characteristics. For coatings prepared using a molar excess of MeTMS to
29 TEOS, cured films were obtained that were tack-free after 24 hours and had no visible
30 signs of cracks, while coatings prepared using a stoichiometric ratio of MeTMS to TEOS
31 or a molar excess of TEOS produced cured films that had visible cracks. An increased
32 tendency for cracking with a relative decrease in MeTMS/TEOS ratio is consistent with
33
34

1
2
3
4 expectations since crosslink density and, thus, shrinkage during cure would increase with
5 decreasing MeTMS/TEOS ratio.
6
7

8 All of the sols produced using DTES were stable; however, most of the coatings
9 were insufficiently cured after 24 hours at ambient conditions as indicated by their tacky
10 surface. Only coatings produced using an excess of TEOS relative to DTES showed
11 sufficient cure after 24 hours. This result may be due to the fact that DTES, unlike the
12 other trialkoxysilanes, is a triethoxysilane. It is well known that ethoxysilanes hydrolyze
13 slower than methoxysilanes.² The slower hydrolysis rate associated with ethoxysilanes
14 may ultimately result in a reduction in cure rate if significant concentrations of
15 ethoxysilane groups are still present in the sol at the time of coating application.
16
17

18 Since many of the coatings based on MeTMS cracked while many based on
19 DTES were tacky and under-cured in 24 hours, primary screening was extended to
20 include coatings based on blends of MeTMS and DTES as the organosilane component.
21 The experimental design for this follow-up experiment is shown schematically in Figure
22 9. All 50 of the sols displayed good solution stability. As shown in Figure 10,
23 approximately 70 % of the compositions produced crack-free and tack-free films. These
24 compositions were carried forward to the solvent exchange process. All of the PMA-
25 based sols were stable and, thus, all of these compositions were carried forward to
26 secondary screening.
27
28

29 As indicated in Figure 10, five coating compositions were identified using salt
30 water immersion screening as being the best with respect to providing a promising barrier
31 coating for inhibiting corrosion. Figure 11 displays representative images of both a good
32
33

1
2
3
4 and a poor performing coating with respect to salt water immersion testing. These five
5 compositions were used for Mg-rich coating formulation experiments.
6
7

8 Four of the five binder compositions identified using high-throughput screening
9 were successfully utilized to produce Mg-rich primers that displayed good solution
10 stability. Corrosion protection of topcoated samples prepared using Mg-rich primers
11 derived from the four promising HOI binder candidates was assessed using B117 salt
12 spray in conjunction with electrochemical impedance spectroscopy. Figure 12 displays
13 Bode plots of the four samples of interest both before after 2,500 hours of B117 salt spray
14 exposure. All four of the samples showed similar impedance before salt spray exposure;
15 however, after 2,500 hours of salt spray, considerable differentiation was observed. The
16 coating based on binder “88,” as described in Figure 12 and Appendix 2, was found to
17 possess the highest impedance after 2,500 hours of B117 salt spray exposure. Figure 13
18 displays images of a scribed specimen both before and after 2,500 hours of salt spray. As
19 shown in Figure 13, no corrosion away from the scribed area or blistering in the scribed
20 area was observed after 2,500 hours of salt spray exposure. However, some corrosion
21 product was observed in the scribe. This level of performance obtained after a single
22 iteration of the combinatorial workflow was considered to be a good outcome.
23
24
25
26
27
28
29
30
31
32
33
34
35
36
37
38
39
40
41
42
43
44
45
46
47

48 *Experiments Involving the Development of Mg-rich Primers Based on a Heterogeneous*
49 *HOI Binder System.* In addition to coating binders based on sols derived from a blend of
50 trialkoxysilanes and TEOS, HOI binders derived from colloidal silica nanoparticles were
51 also investigated. These binders can be considered heterogeneous HOI binders since the
52 chemistry utilized, shown schematically in Figure 14, results in silicate nanoparticles
53
54
55
56
57
58
59
60
61
62
63
64
65

1
2
3
4 dispersed in a continuous phase derived from hydrolysis and condensation of a
5 trialkoxysilane.
6
7

8
9 Three different trialkoxysilanes were used for the experiment, namely, PhEtTMS,
10 GpTMS, and CyTMS. The two epoxy-functional trimethoxysilanes were chosen because
11
12 successful functionalization of the silica nanoparticles would enable the investigation of a
13 two-component, epoxy-amine cured binder system in addition to a moisture-cured binder
14 system. Figure 15 provides a schematic representation of the experimental design
15 utilized.
16
17

18 All of the colloidal dispersions were stable after adding the trialkoxysilane and
19 refluxing to drive alkoxy silane hydrolysis and silanol condensation. However, during the
20 solvent exchange process, colloidal stability was lost for all of the materials based on the
21 epoxy-functional trialkoxysilanes. In addition to these materials, four of the materials
22 based on PhEtTMS also formed a precipitate during the solvent exchange process. Thus,
23 as shown in Figure 16, only eight out of the 36 materials originally produced, resulted in
24 stable colloidal dispersions in PMA. These eight materials were used for Mg-rich primer
25 formulation experiments.
26
27

28 Impedance spectroscopy and B117 salt spray exposure were used to evaluate
29 corrosion protection of topcoated specimens. As shown in Figure 17, the difference in
30 low frequency impedance between samples was marginal before salt spray exposure;
31 however, after 1,000 hours salt spray, significant differences were observed (Figure 18).
32 Coatings “119” and “121,” were found to possess the highest impedance after 1,000
33 hours of salt spray. Both of these specimens were based on HOI binders derived from the
34 highest ratio of PhEtTMS to silica.
35
36
37
38
39
40
41
42
43
44
45
46
47
48
49
50
51
52
53
54
55
56
57
58
59
60
61
62
63
64
65

With regard to B117 corrosion testing, all of the specimens based on heterogeneous HOI binders were found to have much less corrosion in the scribed area than specimens based on homogeneous HOI binders. In fact, as shown in Figure 19, sample 121 showed no significant corrosion in the scribe after 3,100 hours of salt spray exposure. The “bump-like” defects shown in Figure 19, which might be mistaken for blisters, were the result of clumps of Mg particles present in the primer layer. The vortex mixing used to produce the Mg-rich primers did not allow for the level of Mg dispersion that could have been achieved with high shear mechanical mixing or ball milling. None-the-less, the Mg-rich primer based on the heterogeneous HOI binder provided excellent cathodic protection in-spite of the poor Mg dispersion. This level of protection is at least as good as the level of protection that can be obtained using conventional chromate-based primers. The much better corrosion protection provided by the heterogeneous HOI binder system as compared to the homogeneous HOI binder system is very interesting and will be the subject of further investigation.

Conclusion

Using the combinatorial/high-throughput workflow, new Mg-rich primers based on a HOI binder system were explored. Approximately 150 unique HOI compositions were rapidly screened based on solution stability, cured film characteristics, and corrosion protection. Based on these screening results, promising HOI compositions were identified for further investigation in Mg-rich primers. Interestingly, it was found that the use of heterogeneous HOI binders based on colloidal silica provided dramatically

1
2
3
4 better corrosion protection than homogeneous HOI binders derived from TEOS. It was
5 found that an Mg-rich primer based on a heterogeneous HOI binder derived from the
6 highest ratio of PhEtTMS to silica gave excellent corrosion protection with essentially no
7 visible evidence of corrosion in the scribe after 3,100 hours of B117 salt spray exposure.
8
9
10
11
12
13
14
15

16 Acknowledgement 17

18
19
20
21 The author's thank the Air Force Research Laboratory for funding through
22 cooperative research agreement, FA8650-04-1-5045.
23
24
25
26
27
28

29 References 30

- 31 1. Loy, DA, "Hybrid Organic-Inorganic Materials" *MRS Bulletin*, **26**, 364-365
32
33 (2001).
- 34 2. Brinker, CJ, Scherer, GW, *Sol-Gel Science*, Academic Press, San Diego, CA,
35 USA (1990).
- 36 3. Webster, DC, Bennet, J, Kuebler, S, Kossuth, MB, Jonasdottir, S, *JCT Coatings*
37
38 *Tech.*, **1**, 34-39 (2004).
- 39 4. Chisholm, BJ, Christianson, DA, Webster, DC, "Combinatorial Materials
40 Research Applied to the Development of New Surface Coatings II: Process
41
42 Capability Analysis of the Coating Formulation Workflow." *Prog. Org. Coat.*, **57**,
43
44 115-122 (2006).

1
2
3
4 5. Chisholm, BJ, Webster, DC, "The Development of Coatings Using
6 Combinatorial/High-Throughput Methods: A Review of the Current Status."
7
8 *JCT Research*, **4**, 1-12 (2007).
9
10 6. Webster, DC, Chisholm, BJ, Stafslien, SJ, "Mini-Review: Combinatorial
11 Approaches for the Design of Novel Coating Systems." *Biofouling*, **23**, 179-192
12
13 (2007).
14
15 7. Nanna ME, Bierwagen, GP, "Mg-rich Coatings: A New Paradigm for Cr-free
16 Corrosion Protection of Al Aerospace Alloys," *JCT Research*, **1**, 69-80 (2004).
17
18 8. Battocchi, D, Simoes, AM, Tallman, DE, Bierwagen, GP, *Corrosion Science*, **48**,
19
20 1292- (2006).
21
22 9. Fawcett, NC, "The Chemistry of Zinc-Rich and Modified Zinc-Rich Primers."
23
24 *Polym. Matr. Sci. Eng.*, **53**, 855-859 (1985).
25
26
27
28
29
30
31
32
33
34
35
36
37
38
39
40
41
42
43
44
45
46
47
48
49
50
51
52
53
54
55
56
57
58
59
60
61
62
63
64
65

Table I. Formulation used for preparing Mg-rich primers.

Order of Addition	Raw Material	Weight percent
1	HOI solution (10% solids)	60
2	AntiTerra 204	0.3
3	Bentone 38	0.7
4	Aerosil R812	0.3
5	Mica 325WG	1.7
6	Mg powder	37

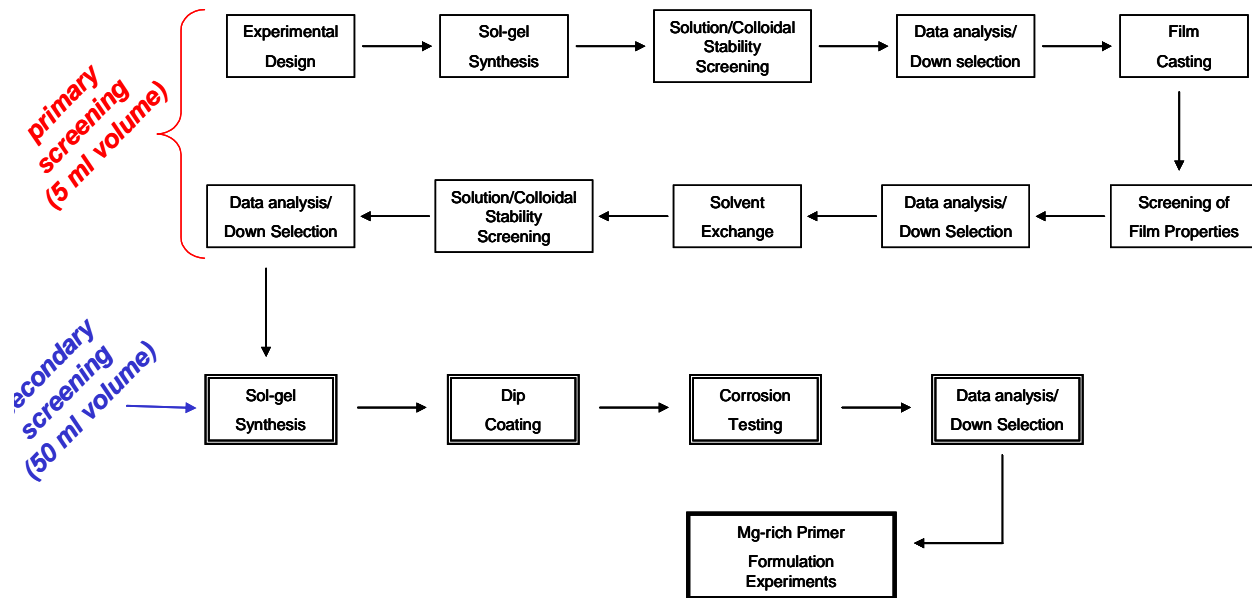


Figure 1. A schematic of the combinatorial workflow used to development new Mg-rich primers based on HOI binder systems.



Figure 2. Photograph of the array template used to prepare coating films with a robotic film casting technique.

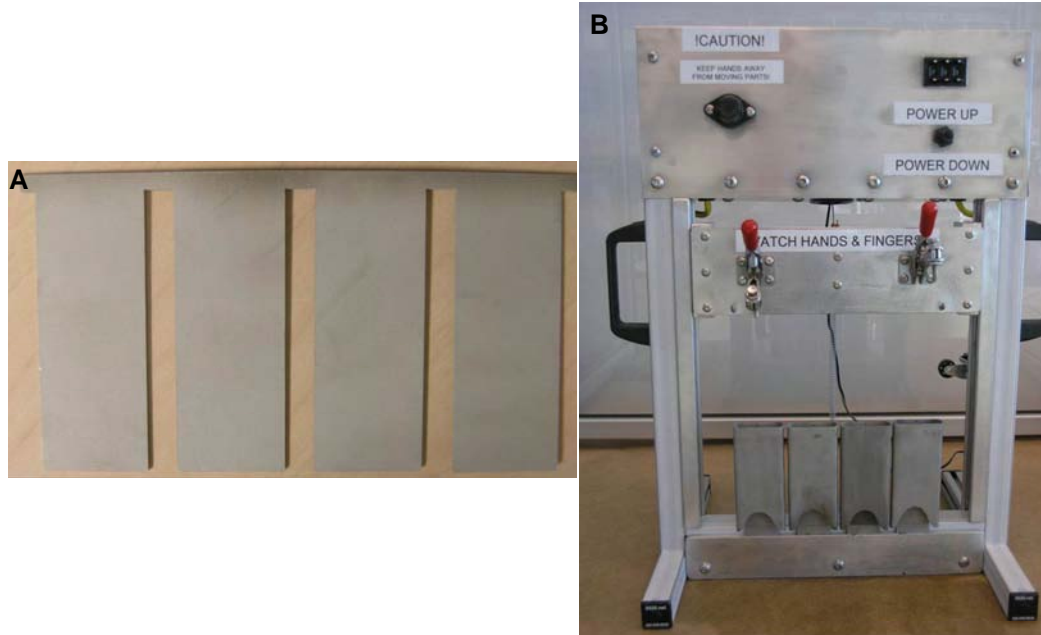


Figure 3. (A) Photograph of substrate used for parallel dip coating. (B) Photograph of the parallel dip coater.

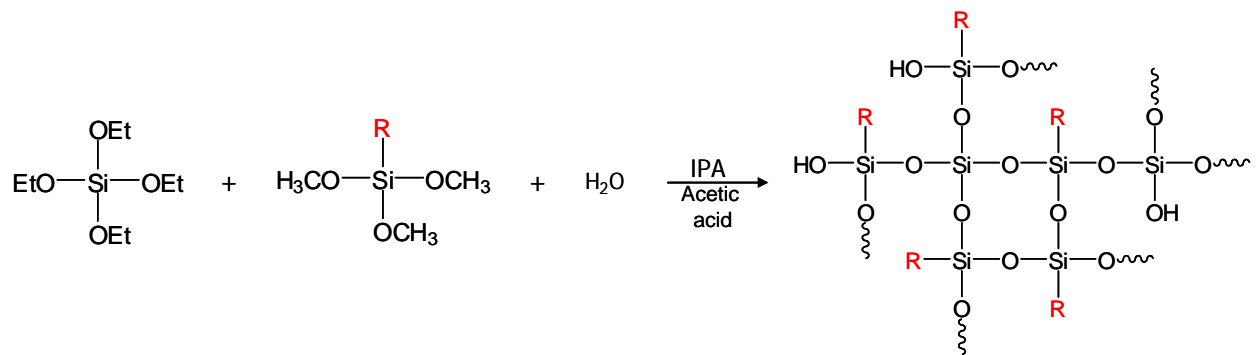


Figure 4. Schematic of the synthesis of homogeneous HOI materials.

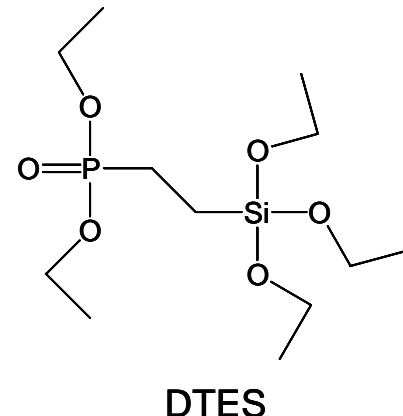
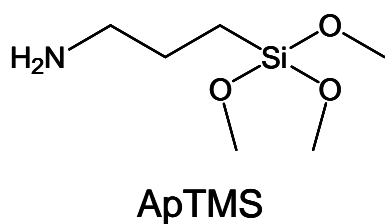
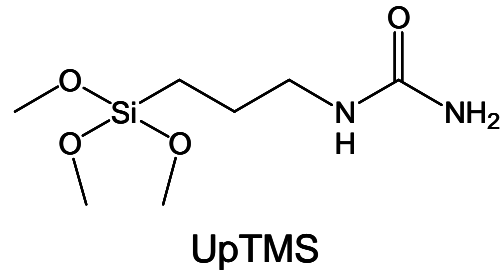
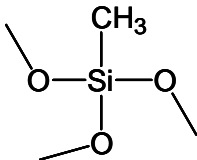


Figure 5. Chemical structure of the trialkoxysilanes investigated for the production of homogeneous HOI binders.

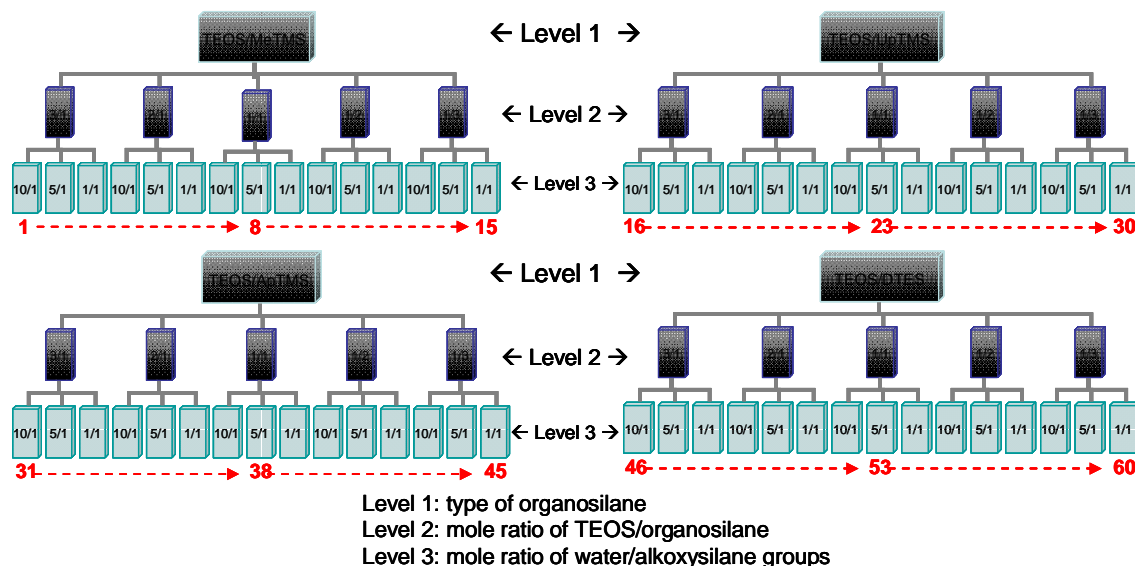


Figure 6. An illustration of the experimental design used to screen homogeneous HOI materials.

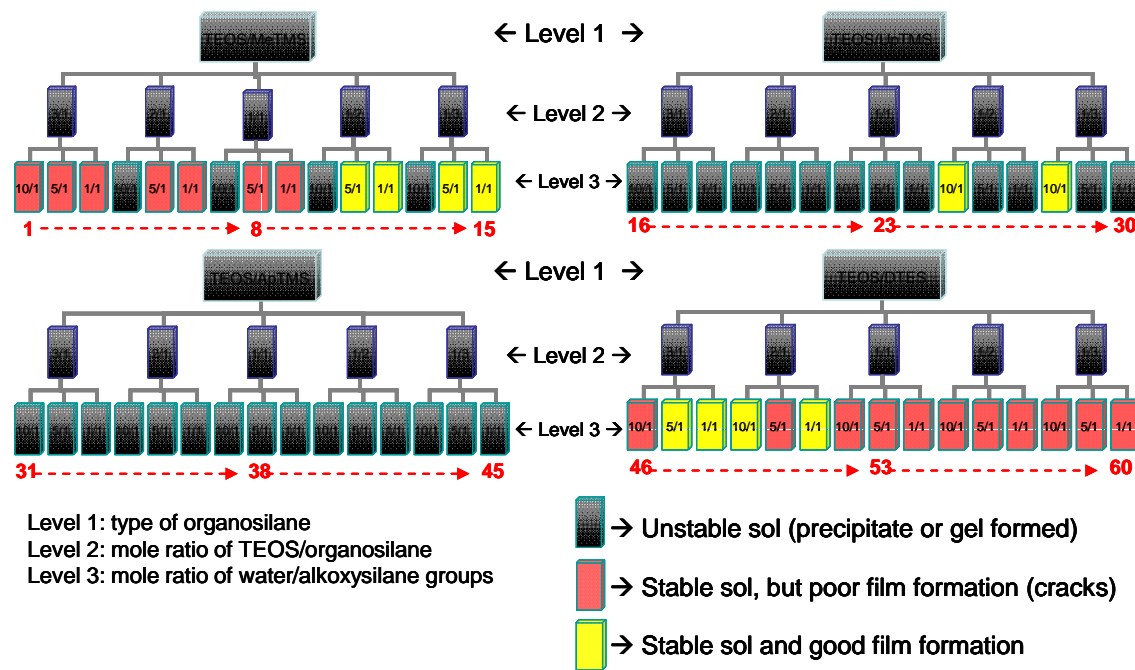


Figure 7. A schematic showing the results of solution stability screening and screening of cured film characteristics.

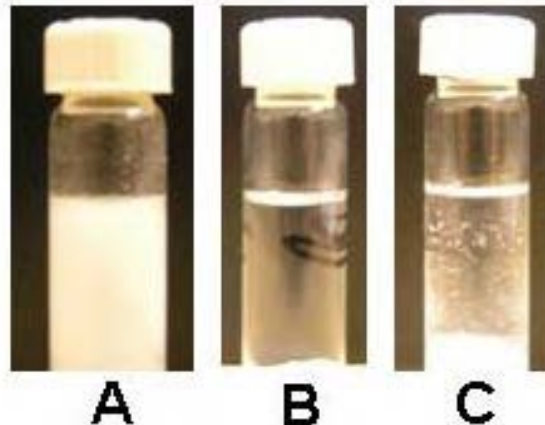


Figure 8. Photographs of representative sols that resulted in the formation of gels (A), homogeneous solutions (B), and precipitates (C).

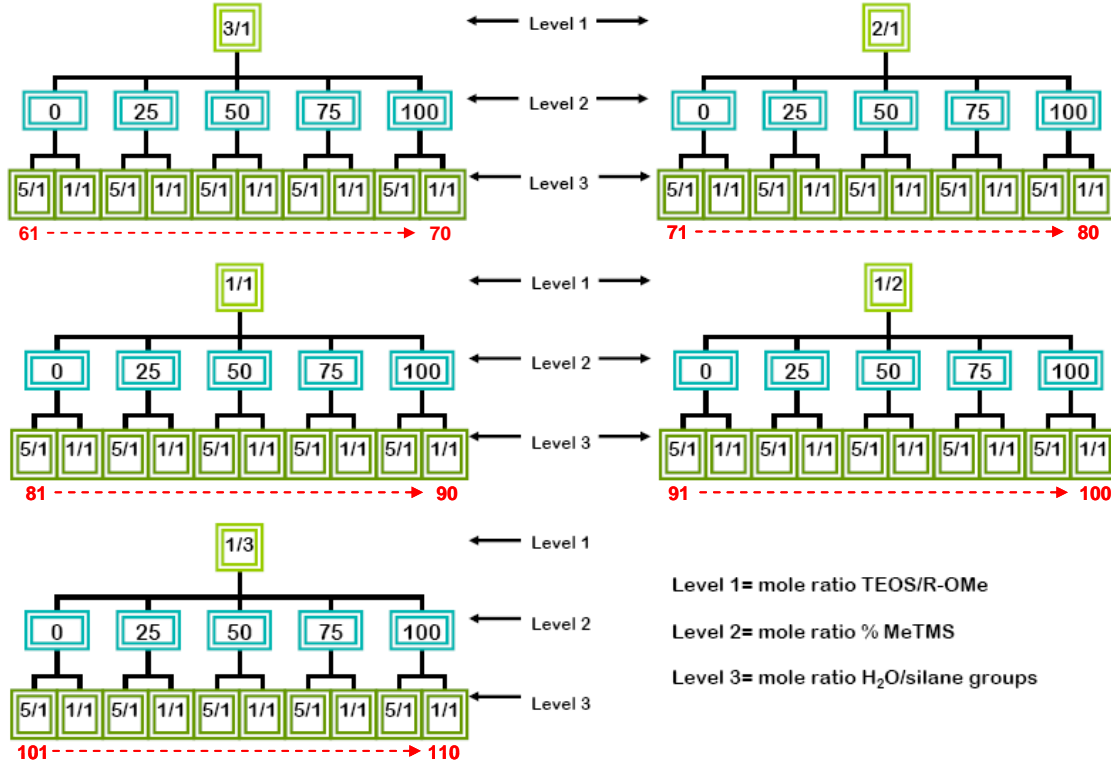


Figure 9. An illustration of the experimental design used to screen HOI materials derived from blends of MeTMS and DTES.

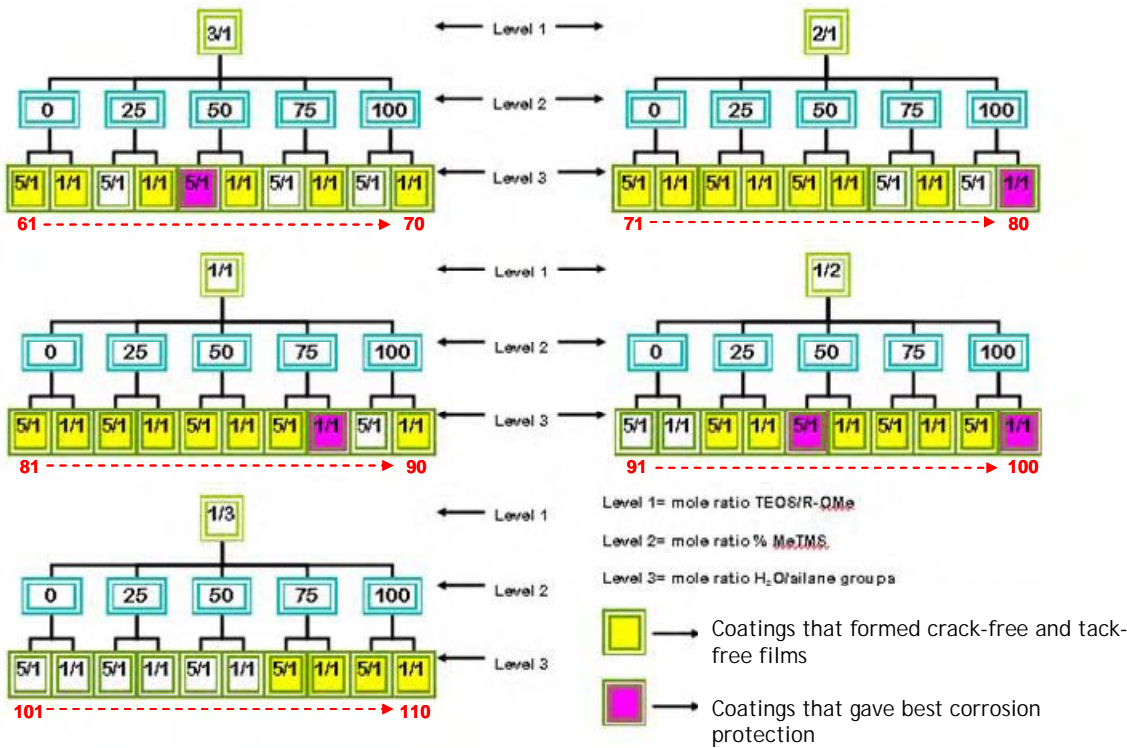


Figure 10. Results obtained for solution stability screening and screening of cured film characteristics.

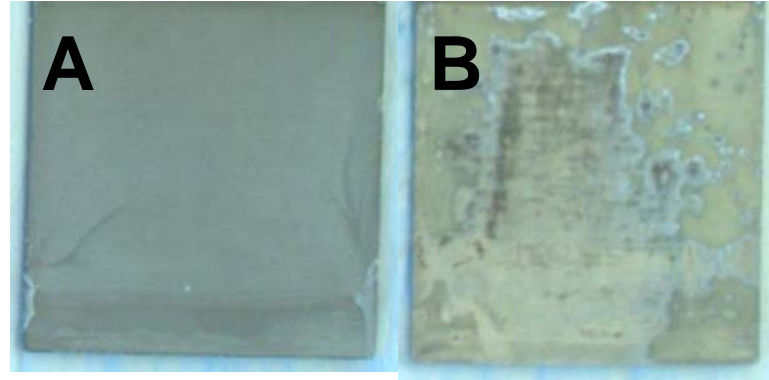


Figure 11. Images of coated aluminum samples displaying relatively good (A) and relatively bad (B) performance with respect to corrosion protection upon salt water immersion.

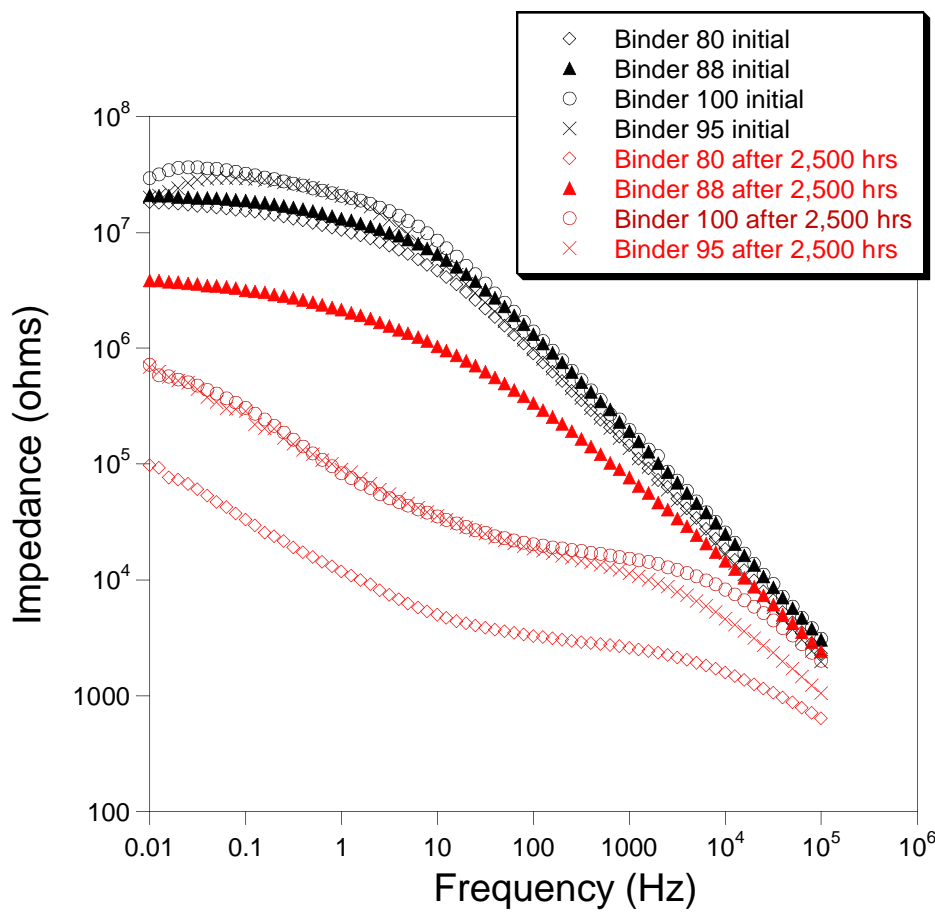


Figure 12. Bode plots of topcoated Mg-rich primers based on the most promising homogeneous HOI binder systems. The data corresponds to materials before and after 2,500 hours of B117 salt spray exposure.



Before salt spray



**After 2,500 hours of
salt spray exposure**

Figure 13. Images illustrating the corrosion protection of a topcoated Mg-rich primer based on HOI binder number 88.

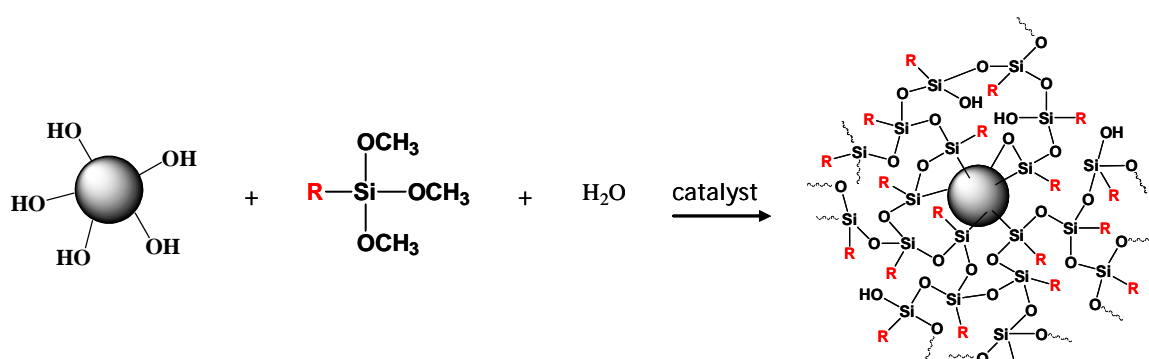


Figure 14. Schematic describing the synthesis of the heterogeneous HOI materials using colloidal silica.

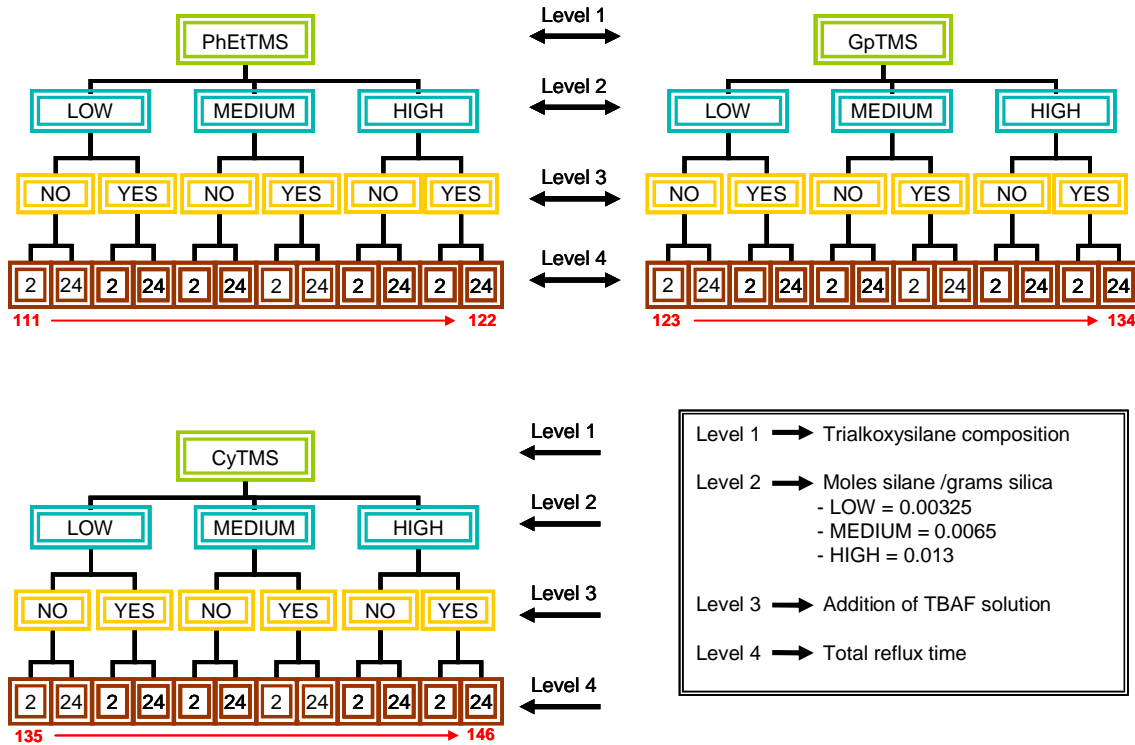


Figure 15. Provides a schematic representation of the experimental design utilized to investigate heterogeneous HOI materials.

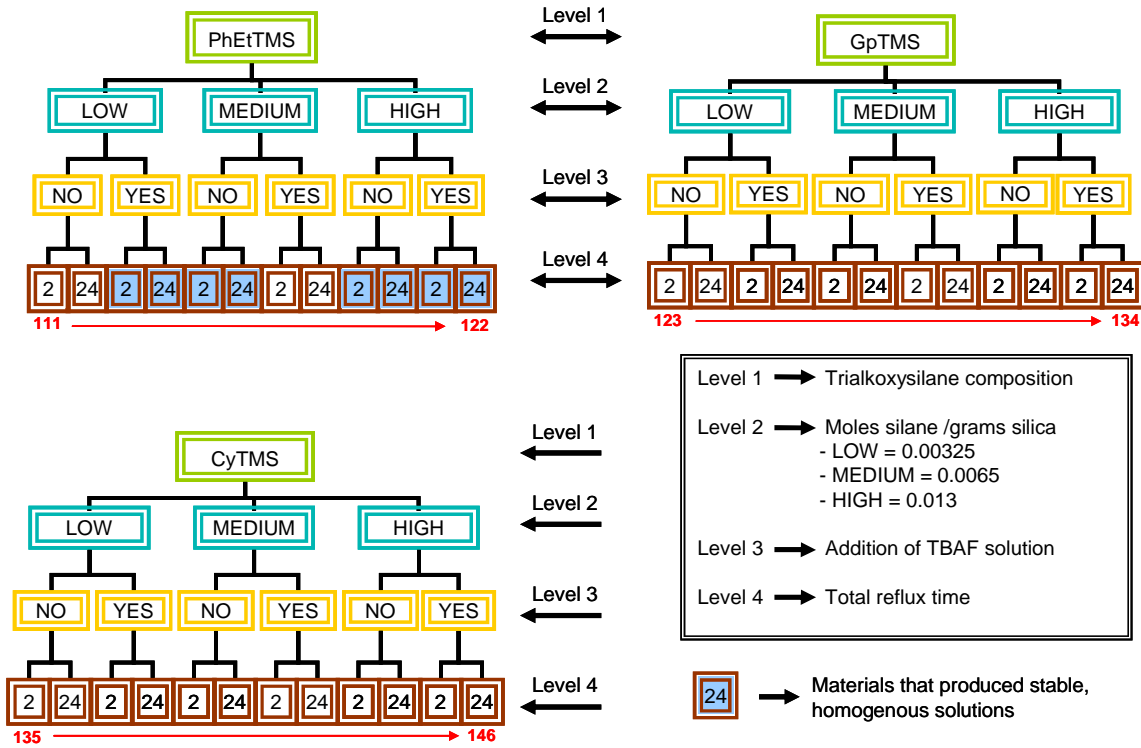


Figure 16. Results of colloidal stability screening for heterogeneous HOI materials.

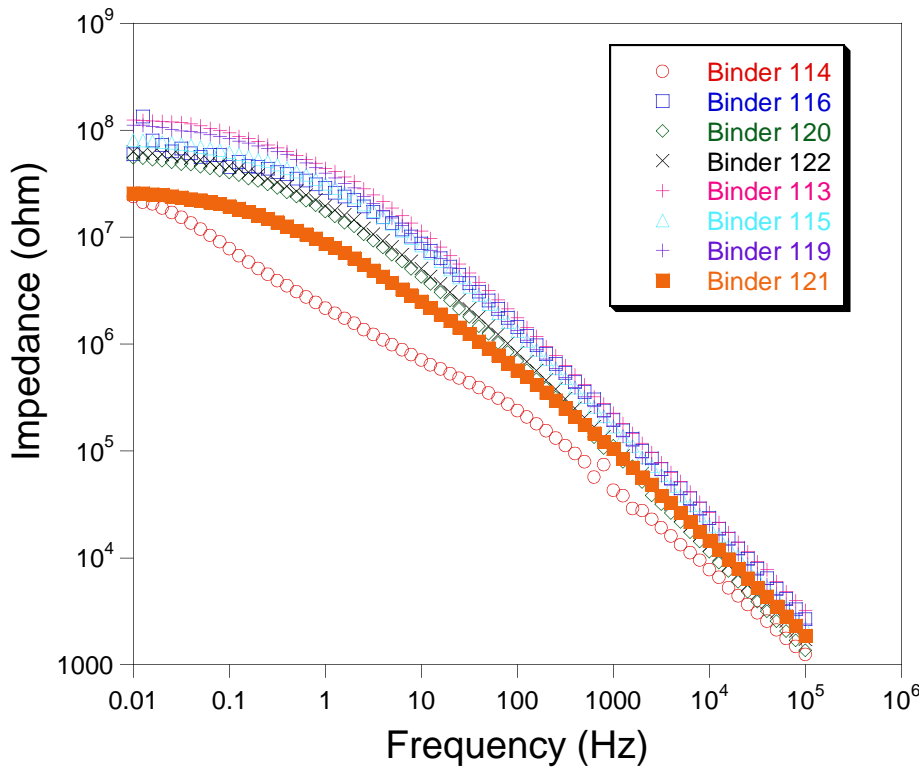


Figure 17. Bode plots of topcoated Mg-rich primers based on heterogeneous HOI binders before salt spray exposure.

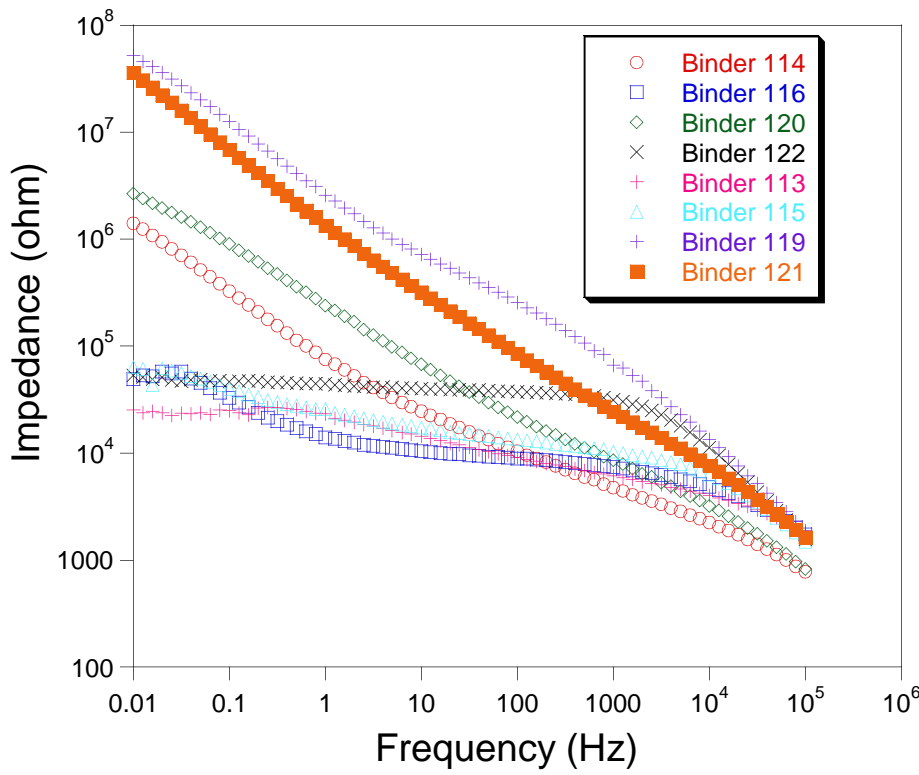


Figure 18. Bode plots of topcoated Mg-rich primers based on heterogeneous HOI binders after 1,000 hours of salt spray exposure.

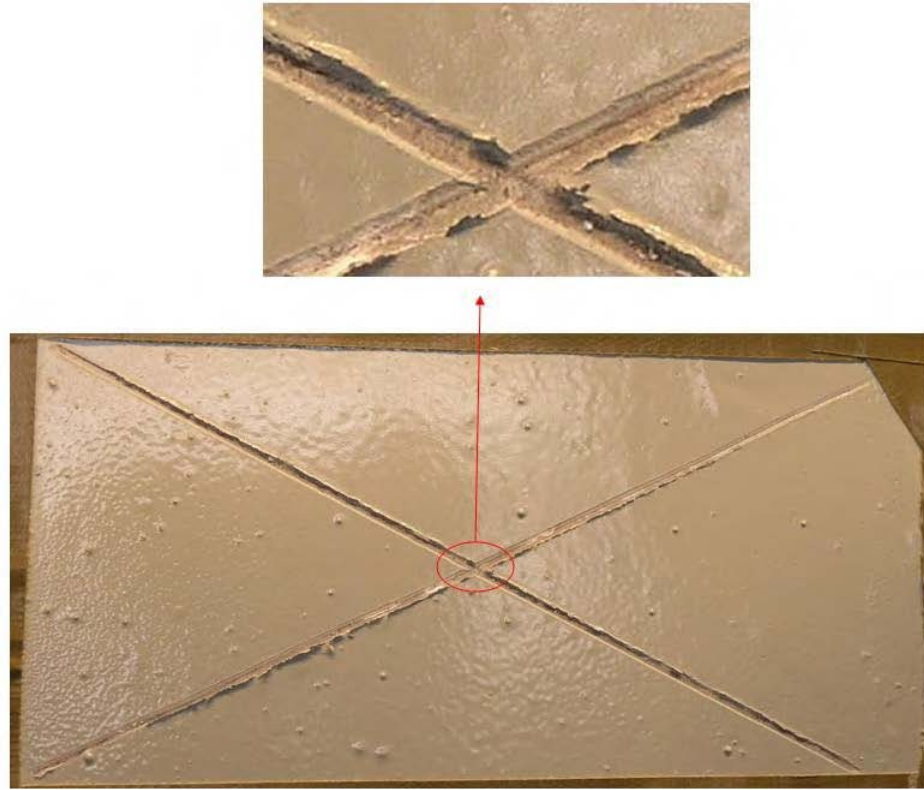


Figure 19. Image of a topcoated specimen derived from HOI binder 121 after 3,100 hours of salt spray exposure.

1
2
3
4 Appendix 1. Coating formulations for the experiment described in Figure 6. All values
5 are in units of microliters.
6

Coating No.	IPA	H2O	Acetic acid	TEOS	MeTMS	UpTMS	ApTMS	DTES
1	240	3900	52	900	204	0	0	0
2	2190	1950	52	900	204	0	0	0
3	3750	390	52	900	204	0	0	0
4	202	3825	51	800	272	0	0	0
5	2114	1912	51	800	272	0	0	0
6	3644	382	51	800	272	0	0	0
7	143	4163	54	680	463	0	0	0
8	2224	2082	54	680	463	0	0	0
9	3890	416	54	680	463	0	0	0
10	63	4403	56	500	680	0	0	0
11	2264	2201	56	500	680	0	0	0
12	4025	440	56	500	680	0	0	0
13	14	4021	51	350	714	0	0	0
14	2025	2011	51	350	714	0	0	0
15	3633	402	51	350	714	0	0	0
16	773	3345	52	800	0	246	0	0
17	2446	1673	52	800	0	246	0	0
18	3784	335	52	800	0	246	0	0
19	911	3187	51	700	0	323	0	0
20	2505	1594	51	700	0	323	0	0
21	3780	319	51	700	0	323	0	0
22	1269	3117	54	550	0	507	0	0
23	2828	1559	54	550	0	507	0	0
24	4075	312	54	550	0	507	0	0
25	1512	2763	53	350	0	645	0	0
26	2894	1382	53	350	0	645	0	0
27	4000	276	53	350	0	645	0	0
28	1584	2531	51	250	0	692	0	0
29	2849	1265	51	250	0	692	0	0
30	3862	253	51	250	0	692	0	0
31	513	3630	52	850	0	0	236	0
32	2328	1815	52	850	0	0	236	0
33	3780	363	52	850	0	0	236	0
34	568	3515	51	750	0	0	312	0
35	2325	1757	51	750	0	0	312	0
36	3731	351	51	750	0	0	312	0
37	695	3382	51	570	0	0	475	0
38	2386	1691	51	570	0	0	475	0
39	3739	338	51	570	0	0	475	0
40	858	3372	53	400	0	0	666	0

41	2544	1686	53	400	0	0	666	0
42	3892	337	53	400	0	0	666	0
43	921	3277	52	300	0	0	749	0
44	2559	1639	52	300	0	0	749	0
45	3870	328	52	300	0	0	749	0
46	1089	2987	51	700	0	0	0	355
47	2582	1494	51	700	0	0	0	355
48	3777	299	51	700	0	0	0	355
49	1311	2809	52	600	0	0	0	456
50	2716	1405	52	600	0	0	0	456
51	3840	281	52	600	0	0	0	456
52	1630	2370	50	400	0	0	0	608
53	2815	1185	50	400	0	0	0	608
54	3763	237	50	400	0	0	0	608
55	1964	2102	51	250	0	0	0	760
56	3016	1051	51	250	0	0	0	760
57	3857	210	51	250	0	0	0	760
58	2328	2179	56	200	0	0	0	912
59	3417	1090	56	200	0	0	0	912
60	4289	218	56	200	0	0	0	912

1
2
3
4 Appendix 2. Coating formulations for the experiment described in Figure 9. All values
5 are in units of milliliters.
6

Coating No.	IPA	H2O	Acetic acid	TEOS	MeTMS	DTES
61	2.535	1.480	0.051	0.700	0.000	0.335
62	3.719	0.296	0.051	0.700	0.000	0.335
63	2.460	1.571	0.051	0.740	0.040	0.266
64	3.717	0.314	0.051	0.740	0.040	0.266
65	2.331	1.640	0.050	0.770	0.083	0.185
66	3.644	0.328	0.050	0.770	0.083	0.185
67	2.239	1.753	0.050	0.820	0.132	0.098
68	3.642	0.351	0.050	0.820	0.132	0.098
69	2.142	1.888	0.051	0.880	0.189	0.000
70	3.652	0.378	0.051	0.880	0.189	0.000
71	2.648	1.387	0.051	0.600	0.000	0.431
72	3.757	0.277	0.051	0.600	0.000	0.431
73	2.540	1.486	0.051	0.640	0.051	0.345
74	3.729	0.297	0.051	0.640	0.051	0.345
75	2.395	1.587	0.050	0.680	0.109	0.244
76	3.665	0.317	0.050	0.680	0.109	0.244
77	2.277	1.736	0.051	0.740	0.179	0.133
78	3.666	0.347	0.051	0.740	0.179	0.133
79	2.105	1.886	0.050	0.800	0.257	0.000
80	3.614	0.377	0.050	0.800	0.257	0.000
81	2.852	1.218	0.051	0.420	0.000	0.604
82	3.826	0.244	0.051	0.420	0.000	0.604
83	2.713	1.345	0.051	0.460	0.074	0.496
84	3.789	0.269	0.051	0.460	0.074	0.496
85	2.504	1.473	0.050	0.500	0.161	0.359
86	3.682	0.295	0.050	0.500	0.161	0.359
87	2.346	1.693	0.051	0.570	0.275	0.205
88	3.701	0.339	0.051	0.570	0.275	0.205
89	2.064	1.916	0.050	0.640	0.412	0.000
90	3.597	0.383	0.050	0.640	0.412	0.000
91	3.001	1.060	0.051	0.260	0.000	0.748
92	3.849	0.212	0.051	0.260	0.000	0.748
93	2.830	1.196	0.050	0.290	0.093	0.625
94	3.787	0.239	0.050	0.290	0.093	0.625
95	2.632	1.376	0.050	0.330	0.212	0.474
96	3.733	0.275	0.050	0.330	0.212	0.474
97	2.354	1.603	0.050	0.380	0.367	0.273
98	3.636	0.321	0.050	0.380	0.367	0.273
99	2.030	1.962	0.050	0.460	0.592	0.000
100	3.599	0.392	0.050	0.460	0.592	0.000

1	101	3.096	0.998	0.051	0.190	0.000	0.820
2	102	3.894	0.200	0.051	0.190	0.000	0.820
3	103	2.860	1.118	0.050	0.210	0.101	0.679
4	104	3.755	0.224	0.050	0.210	0.101	0.679
5	105	2.737	1.349	0.051	0.250	0.241	0.539
6	106	3.816	0.270	0.051	0.250	0.241	0.539
7	107	2.482	1.640	0.052	0.300	0.434	0.323
8	108	3.794	0.328	0.052	0.300	0.434	0.323
9	109	2.016	1.993	0.051	0.360	0.695	0.000
10	110	3.610	0.399	0.051	0.360	0.695	0.000

1
2
3
4 Appendix 3. Coating formulations for the experiment described in Figure 15. All values
5 are in units of milliliters.
6
7
8

Coating No.	IPA	Snowtex-O	PhEtTMS	GpTMS	CyTMS	TBAF	Reflux time
111	2.548	1.770	0.284	0	0	0	2
112	2.548	1.770	0.284	0	0	0	24
113	2.548	1.770	0.284	0	0	0.00354	2
114	2.548	1.770	0.284	0	0	0.00354	24
115	2.548	1.770	0.567	0	0	0	2
116	2.548	1.770	0.567	0	0	0	24
117	2.548	1.770	0.567	0	0	0.00354	2
118	2.548	1.770	0.567	0	0	0.00354	24
119	2.548	1.770	1.135	0	0	0	2
120	2.548	1.770	1.135	0	0	0	24
121	2.548	1.770	1.135	0	0	0.00354	2
122	2.548	1.770	1.135	0	0	0.00354	24
123	2.548	1.770	0	0.287	0	0	2
124	2.548	1.770	0	0.287	0	0	24
125	2.548	1.770	0	0.287	0	0.00354	2
126	2.548	1.770	0	0.287	0	0.00354	24
127	2.548	1.770	0	0.574	0	0	2
128	2.548	1.770	0	0.574	0	0	24
129	2.548	1.770	0	0.574	0	0.00354	2
130	2.548	1.770	0	0.574	0	0.00354	24
131	2.548	1.770	0	1.149	0	0	2
132	2.548	1.770	0	1.149	0	0	24
133	2.548	1.770	0	1.149	0	0.00354	2
134	2.548	1.770	0	1.149	0	0.00354	24
135	2.548	1.770	0	0	0.369	0	2
136	2.548	1.770	0	0	0.369	0	24
137	2.548	1.770	0	0	0.369	0.00354	2
138	2.548	1.770	0	0	0.369	0.00354	24
139	2.548	1.770	0	0	0.739	0	2
140	2.548	1.770	0	0	0.739	0	24
141	2.548	1.770	0	0	0.739	0.00354	2
142	2.548	1.770	0	0	0.739	0.00354	24
143	2.548	1.770	0	0	1.478	0	2
144	2.548	1.770	0	0	1.478	0	24
145	2.548	1.770	0	0	1.478	0.00354	2
146	2.548	1.770	0	0	1.478	0.00354	24

Hybrid Organic/Inorganic Coatings Produced Using a Dual-Cure Mechanism

Jie He,¹ Bret J. Chisholm,^{1,2} Bret A. Mayo,¹ Hanzhen Bao,² Jared Risan,¹ David A. Christianson,¹ and Crystal L. Rafferty¹

¹The Center for Nanoscale Science and Engineering

²Department of Coatings and Polymeric Materials

North Dakota State University

1735 Research Park Drive

Fargo, ND 58102

Abstract

A coating precursor containing both acrylate functionality and trimethoxysilane functionality was produced by reacting bisphenol-A glycerolate diacrylate with 3-isocyanatopropyltrimethoxysilane. With this precursor, two different crosslinked networks can be produced. A polyacrylate network can be produced using a radiation-cure mechanism while a polysiloxane network can be produced by hydrolysis and condensation reactions involving the trimethoxysilane groups. The objective of the study was to determine the utility of this dual-cure system for generating rapid-cure coatings for corrosion protection. Coating properties were determined as a function of cure conditions. The results of the study showed that the formation siloxane crosslinks was significantly hindered by the crosslinked network induced by the UV-curing process. Even though the overall conversion of trimethoxysilane groups to siloxane crosslinks was relatively low, coating barrier properties were significantly enhanced and coating free volume reduced. At ambient conditions, additional crosslinking occurring through siloxane bond formation increased within the first four days after UV-curing. Beyond this period, siloxane bond formation remained unchanged as did coating properties.

Introduction

Historically, chromate salt corrosion inhibitors have been used in corrosion protective aircraft coatings. However, due to health and environmental problems associated with chromates,^{1,2} chromate-containing coatings will most likely be banned. As a result, there exists an urgent need for novel, environmentally-benign aircraft coatings.

In the past two decades, significant advancements have been made toward the development hybrid organic-inorganic (HOI) coatings for corrosion control.³⁻⁶ By combining organic and inorganic components at the atomic or nanometer scale, unique material properties can be achieved that bridge the gap between completely organic and completely inorganic coatings. For example, HOI coatings can possess better fracture toughness than an inorganic coating and better adhesion to metallic substrates than an organic coating. Additionally, HOI coatings are generally more compatible with some inorganic corrosion inhibitors and pigments than traditional organic polymer coatings.^{5, 7-10}

Recently, Bayramoglu et. al¹¹ produced a novel epoxy acrylate containing trimethoxysilane groups. This material enabled the generation of coatings that could be cured using two different mechanisms. Initial curing was accomplished using ultraviolet (UV) cure in which crosslinking involved free radical polymerization of the acrylate functionality, while secondary curing was accomplished by hydrolysis and condensation reactions involving the trimethoxysilane groups. The basic mechanical properties of coatings produced on a plastic substrate were studied as was coating thermal stability.

For military aircraft, rapid curing of the coating layers comprising the aircraft exterior surface is desired in order to minimize the time that the aircraft is out of service due to painting.^{12,13} UV-curing of highly filled coatings such as primers for corrosion protection can be

challenging due to scattering of UV light by corrosion inhibitors resulting in poor through-cure.¹³

The use of a dual-cure mechanism could potentially be used to compensate for inadequate curing achieved during UV-cure. An initial UV-cure could be used to rapidly solidify the coating and put the aircraft into service, while a subsequent ambient temperature cure could be used to fully develop coating properties with time.^{11,14,15}

The authors have been interested in determining the feasibility of using a dual-cure mechanism to produce a rapid-cure, corrosion protective primer for aircraft. This document describes initial work aimed at understanding the influence of cure conditions and extent of cure on the properties of a dual-cure binder system derived from the trimethoxysilane functional epoxy acrylate shown in Figure 1.

Experimental

Materials. Al 2024-T3 was obtained from Q-panel Lab Products (Westlake, OH). The photoinitiator, Irgacure 2022, was obtained from Ciba Specialty Chemicals (Basel, Switzerland). Ethyl-3-ethoxypropionate (EEP), dibutyltindilaurate (DBTL), and bisphenol A glycerolate diacrylate (BAGD) were obtained from Sigma-Aldrich Company. 3-isocyanatopropyltrimethoxysilane (IPTMS) was obtained from GELEST, Inc (Morrisville, PA). All chemicals were used as received from the supplier.

The trimethoxysilane derivative of BAGD (TMS-BAGD) was synthesized as follows: BAGD (53.5g) was dissolved at 70 °C in EEP (98.76g) using a 500 ml three-neck flask equipped with a magnetic stir bar. Upon dissolution, the solution was cooled to room temperature and 20 microliters of DBTL added followed by 45.26 g of IPTMS. The reaction mixture was allowed to stir for 24 hours at room temperature. Fourier transform infrared spectroscopy (FT-IR) was used

to confirm completion of the reaction by monitoring the disappearance of the isocyanate carbonyl band at 2270 cm^{-1} .

Coating Preparation and Processing. Prior to coating application, panels of Al2024-T3 were sandblasted to remove the oxide layer and then degreased with hexane. Coating solutions were 50 weight percent TMS-BAGD in EEP. For coatings to be cured with UV light, 2 weight percent photoinitiator was also added to the coating solution. Coating solutions were cast on to substrate panels and the dry film thickness controlled at $60 \pm 5\text{ }\mu\text{m}$. Several different coating specimens were produced by curing using different curing conditions. Table 1 describes each of the coating specimens prepared.

Instrumentation. UV-curing of coating samples was performed using a Fusion UV system with a F300S/F300SQ mercury arc lamp in air (Gaitehrburg, MD). Light intensity (UV-A, 365 nm) as measured using a traceable EIT UV power Puck II radiometer (EIT, inc. Sterling, VA) was 1326 mW/cm^2 .

Confocal Raman microscopy was conducted using a JOBIN Yvon Horiba Raman Spectrometer model HR800 employing a 47 mW solid state diode laser at 532 nm filtered by a neutral density filter to reduce the laser intensity and a charge-coupled detector (CCD). The Raman spectra were resolved by a 300 line/mm grating giving a resolution of 1.5 cm^{-1} . The laser was focused using a microscope lens at a 100 \times magnification. The diameter of the laser focal point was approximately $2\text{ }\mu\text{m}$. Depth profiling of the coating was conducted by recording Raman spectra at multiple points using an automated 3D sample translation stage. The Raman spectra were collected over the range of 300 cm^{-1} to 4000 cm^{-1} and data processing was achieved using LabSpec 5.2 (JY Horiba) software. The Raman data were used to determine the degree of C=C conversion (DC) by monitoring the intensity change of the C=C stretching band at 1633

cm^{-1} relative to that of the isopropane moiety of the bisphenol-A residue ($\text{C}-\text{CH}_3$) at 1457 cm^{-1} before and after UV processing. The equation used is as follows:

$$DC = 100 \times \left(1 - \frac{\left(\frac{\text{C}=\text{C}}{\text{C}-\text{CH}_3}\right)_{\text{after UV curing}}}{\left(\frac{\text{C}=\text{C}}{\text{C}-\text{CH}_3}\right)_{\text{before UV curing}}}\right)$$

Infrared spectra were obtained using a Bruker FT-IR spectrometer equipped with OPUS software. Spectra were collected in transmission mode over the range of 400 cm^{-1} to 4000 cm^{-1} . The spectral resolution was set at 1 cm^{-1} and a total of 32 scans were obtained. Specimens were prepared by dispensing a few drops of the liquid coating onto a standard KBr pellet to form a layer of thin film. Solvent was allowed to flash off before acquiring data. For some specimens, the coating cast on the KBr was UV-cured prior acquiring data.

Positron lifetime measurements were made using a conventional fast-fast system which has been described elsewhere.¹⁶ The timing resolution of the instrument as measured with a ^{60}Co source, with energy windows set for ^{22}Na , was 240 picoseconds. The source consisted of two pieces of 7.5 microns thick Kapton foil (Lebow Company) between which had been deposited droplets of an aqueous solution of $^{22}\text{NaCl}$ (PerkinElmer Life and Analytical Sciences) to yield a final activity of about 1.5 MBq. The water was evaporated from the droplets and the edges of the foils were sealed with tape. A source correction factor was determined by placing the source between two disks of ultra-high purity copper (American Elements) and was found to be 15%. Each spectrum contained at least 400,000 counts after background subtraction. Each measurement was made in quadruplicate. The multichannel analyzer time constant was 0.01261 ns/channel with a conversion gain of 4096 channels. Samples were provided as coated aluminum panels measuring approximately 4 by 10cm. One sample was placed on either side of the positron source. Since aluminum has an intrinsic bulk positron lifetime of 0.166 nanoseconds,¹⁷ the influence of positrons annihilating in the aluminum could be subtracted from

the spectrum during data analysis, thus accounting for any positrons which passed all the way through the sample. All measurements were made at room temperature. PALSfit software (RISOE National Laboratory, Denmark) was used to analyze the data. The instrument resolution function was found to be the sum of two Gaussian components, one with a FWHM of 190 picoseconds and intensity of 55% and the other with FWHM of 240 picoseconds and intensity of 45%. The 240 picosecond peak was shifted 20 picoseconds from zero time. The spectra were analyzed for three components and no constraints were used. A 15% source correction was applied before analysis of the spectra to account for positrons annihilating in the Kapton foils protecting the positron source. The value for the lifetime of positrons in the Kapton source support was fixed at 0.382 ns. The time zero appeared in channel 477 and did not drift over the course of the measurements. The background averaged less than 8 counts per channel and was subtracted before positron lifetime component analysis.

Electrochemical analysis was conducted using a high-throughput electrochemical system which has been described in detail elsewhere.¹⁸ Spectra from electrochemical impedance spectroscopy (EIS) were acquired over a frequency ranging from 10^5 Hz to 0.01 Hz with an applied 10 mV R.M.S. voltage vs. open circuit potential. 3% NaCl was used as the test electrolyte and also served as a corrosive environment for the constant immersion testing of the coatings. The potentiodynamic polarization measurement was conducted by scanning the samples from -1V to 1V vs. the reference electrode at a scan rate of 10 mV/s. All the reported potentials in this manuscript are relative to a Ag/AgCl (in 3M NaCl) reference electrode (Ref).

Coating hardness was measured with a Hysitron Triboscope (Hysitron Incorporated, Minneapolis, MN) equipped with a Berkovich tip. For tip area calibration, multiple indents on fused silica with a known modulus of 72 GPa were conducted at various contact depths (10-220

nm). The contact area of the indenter tip was then calculated from the slope of the initial unloading curve (stiffness) and the known modulus (72 GPa), followed by fitting a polynomial to the computed area as a function of contact depth to determine the area function. Quasistatic nano-indentation was done in displacement control with the following feedback controlled load function: loading rate of 100 $\mu\text{m}/\text{s}$, hold time of 30 s at the maximum force, and an unloading rate of 100 $\mu\text{m}/\text{s}$. The maximum displacement was \sim 500 nm and 6 indents were performed on each sample. The elastic modulus was obtained using the Oliver and Pharr method.¹⁹

Coating adhesion was evaluated using the pull-off adhesion method according to ASTM D7234-05. The adhesive used was Krazy glue (Krazy glue, Inc. New York) and the tester was a pull-off adhesion gauge from Elcometer instrument, Ltd. Three replicate measurements were made for each sample and the diameter of the dolly was 1 cm.

Results and Discussion

The primary objective of the research described in this document was to understand the effect of curing conditions and extent of cure on the properties of coatings derived from TMS-BAGD. By understanding the relationships between cure conditions, cure rate, extent of cure, and coating properties, the utility of this material as a binder for a rapid-cure coating system for corrosion protection can be better understood.

Confocal Raman microscopy was used to determine the extent of cure achieved as a result of UV irradiation while FTIR was used to characterize crosslinking occurring via the trimethoxysilane functional groups. Figure 2 displays Raman spectra for the coating before and after UV exposure. Before UV exposure (Figure 2A), two strong bands at 1633 cm^{-1} and 1407 cm^{-1} were observed that correspond to C=C stretching and bending, respectively. After UV exposure (Figure 2B), the intensity of the peaks at 1633 cm^{-1} and 1407 cm^{-1} were significantly

reduced indicating extensive polymerization of the acrylate groups. Using the band at 1633 cm^{-1} and the band at 1457 cm^{-1} resulting from the C-CH₃ isopropyl moiety of the bisphenol-A residue, the degree of acrylate conversion was determined as a function of UV dose. As shown in Figure 3, essentially complete conversion of the acrylate groups was achieved even for the lowest UV dose utilized indicating that vitrification of the material does not inhibit complete consumption of the acrylate groups.

An important consideration for a coating designed for a UV-cure process is the uniformity of cure through the thickness of the coating, often referred to as “through-cure”. To determine the extent of cure as a function of coating thickness, the depth-profile feature of the confocal Raman microscope was utilized to collect spectra at 2 um intervals through the coating thickness from the air/coating interface to the coating/substrate interface. As shown in Figure 4, extent of cure varied from 97 percent at the coating/air interface to 93.5 at the coating/substrate interface indicating a high degree cure throughout the thickness of the coating using a UV-A dose of 2230 mJ/cm^2 .

The extent of cure associated with siloxane bond formation was characterized using FTIR by depositing the coating solution on a KBr pellet. To identify bands associated with the formation of siloxane bonds from trimethoxysilane groups, a curing study was conducted in which the coating was cured at different temperatures and changes in the IR spectrum observed. As shown in Figure 5, a band observed at 454 cm^{-1} increased in relative intensity with increasing temperature. This band is attributed to the Si-O-Si symmetric stretching vibration and indicates the formation of additional crosslinks via the trimethoxysilane groups.²⁰

Since this coating system is being investigated for potential use as a binder system for a primer coating for aircraft exteriors, it was of interest to determine the rate of siloxane formation

as a function of time at ambient conditions. In addition, it was of interest to understand the effect of the crosslinked network produced by UV-curing on the rate of siloxane formation. As shown in Figure 6, UV-curing had a dramatic effect on the rate of siloxane bond formation. Casting the coating and allowing the coating to cure exclusively by siloxane bond formation resulted in a continuous increase in siloxane formation for approximately eight days. After eight days, no further siloxane bond formation was observed. UV-curing the coating just after coating application resulted in a major reduction in the rate of siloxane bond formation and the overall content of siloxane bonds was approximately 1/5 of that of the moisture-cured sample. This result suggests that the generation of the crosslinked network derived from UV-curing significantly inhibits diffusion of the trimethoxysilane groups, and possibly also water molecules, resulting in a reduced rate of siloxane bond formation and a reduction in the overall extent of crosslinking that can be achieved by siloxane bond formation.

Considering the spectroscopic results describing the crosslinking reactions involving both the UV-cure mechanism and the moisture-cure mechanism, it was of interest to determine the impact of the secondary moisture-cure process on the barrier properties of the coating. Since the FT-IR results indicated that the relative conversion of trimethoxysilane groups to siloxane crosslinks was relatively low, it was thought that the crosslinked siloxane network may contribute very little to the barrier properties and, thus, the corrosion protection of the coating.

Positron annihilation spectroscopy (PAS) was used to determine the effect of the moisture-cure mechanism on the free volume of the cured film. Figure 7 shows the change in average free volume size of the coating as function of time after being exposed to UV. The results obtained clearly show that the moisture-cure mechanism significantly impacts the free volume of the coating. The average free volume size decreased significantly over the course of

four days after UV curing. Beyond four days at ambient conditions, the free volume size did not change which is very consistent with the FT-IR results shown in Figure 6. Thus, although the extent of conversion of the trimethoxysilane groups to siloxane crosslinks was relatively low, it was high enough to significantly reduce the free volume of the coating.

For corrosion protection, the barrier properties of the coating binder are very important since diffusion of water and electrolyte to the metal substrate is required for corrosion to occur. Electrochemical methods were used to assess the barrier properties and corrosion protection provided by the coating as a function of curing conditions. Figure 8 displays potentiodynamic polarization curves for coatings produced using different curing methods. A comparison of the corrosion currents showed that the corrosion current was much lower for the dual-cure coating (about 100pA) than that for either the UV-cure (20 μ A) or moisture-cure sample (50nA). Interestingly, the corrosion current for the moisture-cure sample was lower than that for the UV-cure sample suggesting that the crosslinked network produced as a result of siloxane bond formation provides better corrosion protection than the crosslinked network produced by polymerization of the acrylate functional groups.

In addition to potentiodynamic polarization measurements, impedance measurements were made to characterize coating barrier properties. Figure 9 (A) displays Bode plots produced after exposing the coatings to the electrolyte solution for 24 hours while Figure 9 (B) displays Bode plots produced after exposing the coating to the electrolyte for two weeks. After one day of electrolyte exposure, the relative ranking of the low frequency impedance of the samples was dual-cure > moisture-cure > UV-cure which was consistent with the results obtained from potentiodynamic polarization measurements. After two weeks of continuous exposure to the electrolyte solution, the low frequency impedance of the dual-cure sample and the moisture-cure

sample dropped approximately 1.5 and 2 orders of magnitude, respectively, while that of the UV-cure sample remained constant. In addition, the relative ranking of low frequency impedance changed to dual-cure > UV-cure > moisture-cure. Furthermore, three time constants were observed in the Bode plot for the moisture-cure sample indicating that electrolyte had permeated through the coating and initiated corrosion. Without further investigation, the impedance behavior observed is difficult to explain. This coating is rather complex because the spectroscopic data clearly show that most of the trimethoxysilane groups remain unreacted even after eight days of aging at ambient conditions. Thus, it is expected that further hydrolysis and condensation of trimethoxysilane groups would occur during electrolyte exposure resulting in in-situ changes in crosslink density and/or coating polarity. The apparent stability of the barrier properties of the UV-cure sample may be due to a higher relative increase in crosslink density during electrolyte exposure compared to the other two samples resulting from the initially higher concentration of unreacted trimethoxysilane groups in the coating.

In addition to barrier properties, adhesion is an important property for protecting the substrate from corrosion. As a result, pull-off adhesion tests were conducted to determine the effect of curing conditions on coating adhesion. As shown in Figure 10, the UV-cure sample showed lower adhesion than either the moisture-cure or dual-cure sample. Essentially no difference in adhesion was observed between the moisture-cure sample and the dual-cure sample. These results suggest that the eight day aging process at ambient conditions used to increase crosslink density via hydrolysis and condensation reactions associated with the trimethoxysilane groups provides improved adhesion of the coating to the substrate. It has been previously shown that Si-O-Al bond formation can occur at a coating/aluminum interface providing enhanced adhesion.²¹ In addition, hydrogen bonding interactions involving silanol

groups present in the coating could provide enhanced adhesion.²² It is also possible that the differences in adhesion may have been the result of differences in the extent of polymer chain stress relaxation with time. The UV-cure sample was adhesion tested within 1 hour of curing which may not have been long enough for the polymer chain segments to relax and form more thermodynamically favored conformations that would maximize intermolecular interactions with the substrate.

To further probe differences in crosslink density as a function of curing conditions, the hardness of the coatings was determined using a nanoindentor. As shown in Figure 11, the relative ranking of hardness was dual-cure > moisture-cure > UV-cure, which is consistent with the electrochemical measurements and the conclusion that the relative ranking of overall crosslink density was dual-cure > moisture-cure > UV-cure. Considering the dramatic difference in barrier properties and hardness between the dual-cure sample and the UV-cure sample, it was of interest to monitor changes in properties as a function of aging time at ambient temperature and humidity. Figure 12 displays hardness as a function of time after UV-curing. As shown in Figure 12, hardness increased rapidly in the first four days after UV-curing and then leveled off. This trend is identical to the trend in siloxane bond formation shown in Figure 6 and illustrates the major impact that the post-UV, moisture-cure mechanism has on coating properties. In addition, it shows that full property development takes about 4 days for this particular coating.

Conclusion

Spectroscopic results clearly showed that the formation siloxane crosslinks through hydrolysis and condensation reactions involving trimethoxysilane groups was significantly hindered by the crosslinked network induced by the UV-curing process. None-the-less, the

formation of even a relatively small percentage of the trimethoxysilane groups to siloxane crosslinks significantly enhanced barrier properties, decreased free volume, and increased coating hardness. At ambient conditions, additional crosslinking occurring through siloxane bond formation increased within the first four days after UV-curing. Beyond this period, siloxane bond formation, free volume, and hardness remained unchanged suggesting that further crosslinking was inhibited. Considering these results, further work involving the preparation of coatings containing corrosion inhibitors is warranted.

Acknowledgement

The authors gratefully acknowledge financial support from the Air Force Research Laboratory under Grant FA8650-04-1-5045.

References

- (1) Stearns, D. M.; Wetterhahn, K. E. *Chem. Res. Toxicology* **1997**, *10*, 271.
- (2) Faisal, M.; Hasnain, S. *J. Pharmacol Toxicol* **2006**, *1*, 248.
- (3) Poznyak, S. K.; Zheludkevich, M. L.; Raps, D.; Gammel, F.; Yasakau, K. A.; Ferreira, M. G. S. *Progress in Organic Coatings* **2008**, *62*, 226-235.
- (4) Moutarlier, V.; Neveu, B.; Gigandet, M. P. *Surface and Coatings Technology* **2008**, *202*, 2052-2058.
- (5) Li, L.; Pi, P.; Wen, X.; Cheng, J.; Yang, Z. *Corrosion Science* **2008**, *50*, 795-803.
- (6) Lamaka, S. V.; Montemor, M. F.; Galio, A. F.; Zheludkevich, M. L.; Trindade, C.; Dick, L. F.; Ferreira, M. G. S. *Electrochimica Acta* **2008**, *53*, 4773-4783.
- (7) Wang, H.; Akid, R. *Corrosion Science* **2008**, *50*, 1142-1148.
- (8) Checmanowski, J. G.; Szczygiel, B. *Journal of Non-Crystalline Solids* **2008**, *354*, 1786-1795.
- (9) Tamar, Y.; Mandler, D. *Electrochimica Acta, In Press, Corrected Proof*, 803.
- (10) Andreatta, F.; Aldighieri, P.; Paussa, L.; Di Maggio, R.; Rossi, S.; Fedrizzi, L. *Electrochimica Acta* **2007**, *52*, 7545-7555.
- (11) Bayramoglu, G.; Kahraman, M. V.; Kayaman-Apohan, N.; Guengoer, A. *Progress in Organic Coatings* **2006**, *57*, 50-55.
- (12) Johnson, J. A.; Bliss, C. Q. In *RadTech Report* July-Aug 2006, pp 21.
- (13) Orbey, N. In *RADTECH Report*, July-Aug 2006, pp 43.
- (14) S. Karataş, C. K., N. Kayaman-Apohan, A. Güngör *Progress in Organic Coatings* **2007**, *60*, 140-147.
- (15) Xu, J.; Pang, W.; Shi, W. *Thin Solid Films* **2006**, *514*, 69-75.

(16) Jean, Y. C.; Schrader, D. M., Eds. *Positron and positronium chemistry*; Elsevier: Amsterdam, 1988.

(17) Djourelov, N.; Misheva, M. *Journal of Physics: Condensed Matter* **1996**, *8*, 2081-2087.

(18) He, J.; Bahr, J.; Chisholm, B. J.; Li, J.; Chen, Z.; Balbyshev, S.; x; va, N.; Bonitz, V.; Bierwagen, G. P. *J. Comb. Chem* **2008**.

(19) Oliver, W. C.; Pharr, G. M. *J. Mater. Res* **1992**, *1564*.

(20) Schrader, B. In *Infrared and Raman Spectroscopy*; VCH: New York, 1995.

(21) Zheludkevich, M. L.; Salvado, I. M.; Ferreira, M. G. S. *Journal of Materials Chemistry* **2005**, *15*, 5099-5111.

(22) Perutz, S.; Wang, J.; Ober, C. K.; Kramer, E. J. *Polymer Preprints (American Chemical Society, Division of Polymer Chemistry)* **1996**, *37*, 45-46.

Table 1. A description of the coating specimens prepared from TMS-BAGD.

Sample ID	Description
UV-cure	After 6 hours of solvent flash, the sample was UV-cured using a UV-A dose of 2230 mJ/cm ² . Properties were tested approximately one hour after UV-curing.
Moisture-cure	Samples were prepared by applying the coating and allowing the coating to age at ambient conditions for eight days prior to testing.
Dual-cure	After UV-curing, samples were allowed to age at ambient conditions for eight days prior to testing.
MC-25°C	Samples were prepared by applying the coating and allowing the coating to age at ambient conditions for one day prior to analyzing.
MC-50°C	Samples were prepared by applying the coating and allowing the coating to age at 50°C for one day prior to analyzing.
MC-85°C	Samples were prepared by applying the coating and allowing the coating to age at 85°C for one day prior to analyzing.
MC-130°C	Samples were prepared by applying the coating and allowing the coating to age at 130°C for one day prior to analyzing.

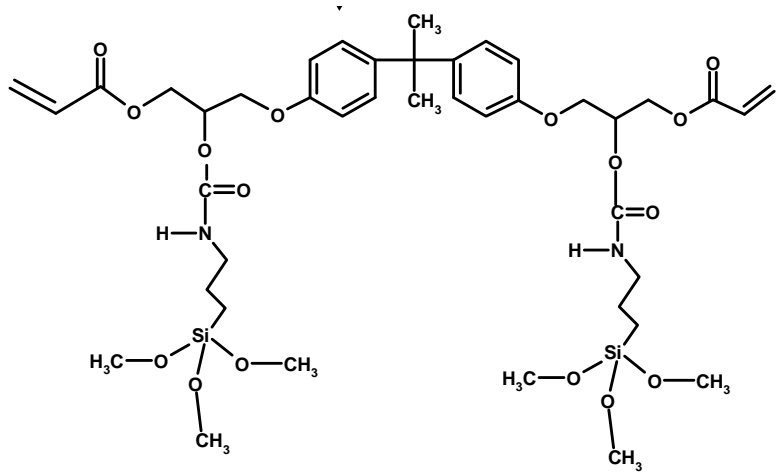


Figure 1. Chemical structure of the trimethoxysilane-functional diacrylate produced (TMS-BAGD).

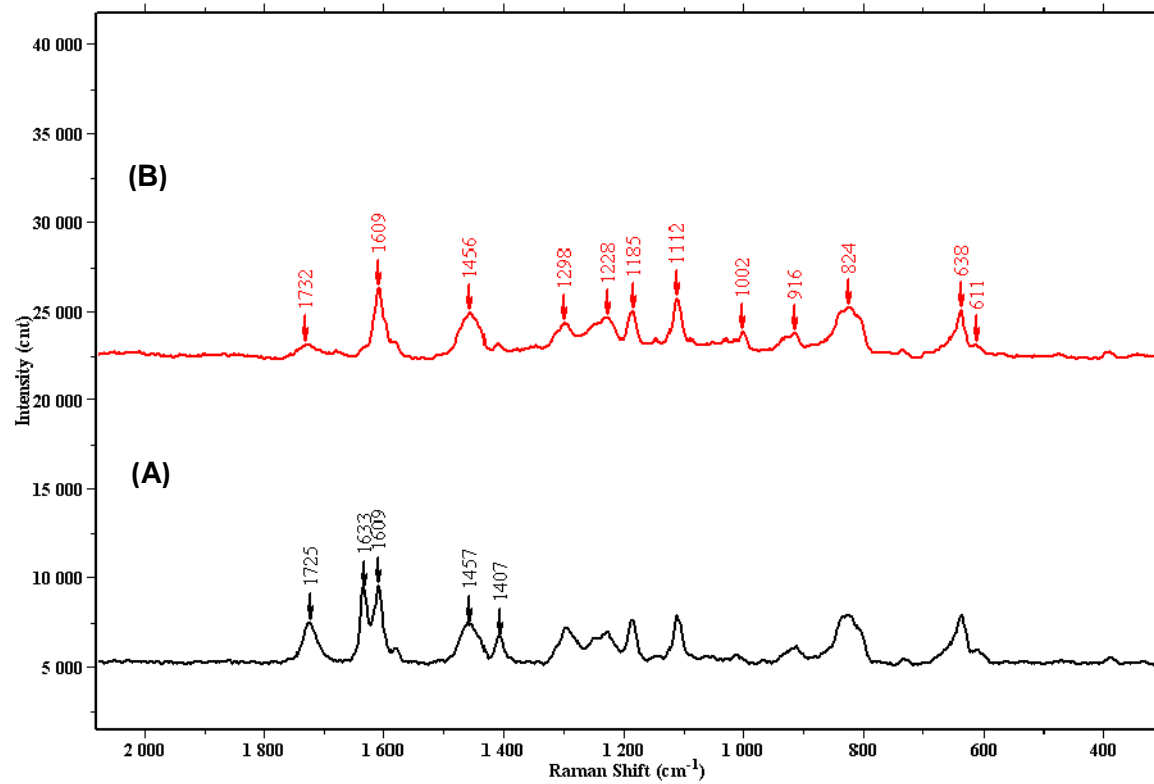


Figure 2. Raman spectra for TMS-BAGD before (A) and just after (B) UV-curing.

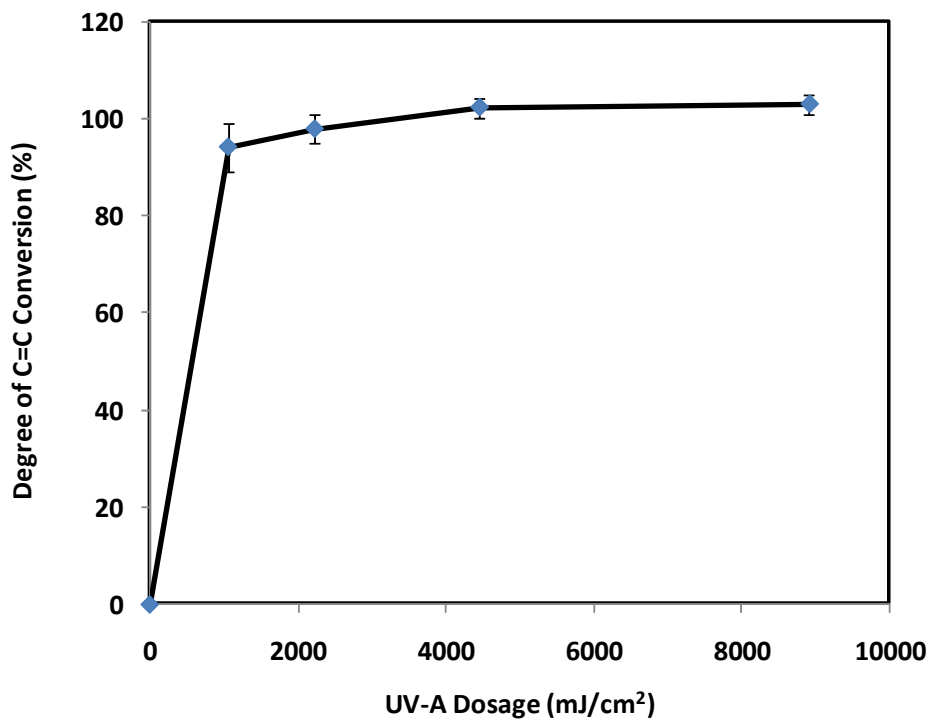


Figure 3. Degree of C=C conversion as a function of UV-A dose for TMS-BAGD.

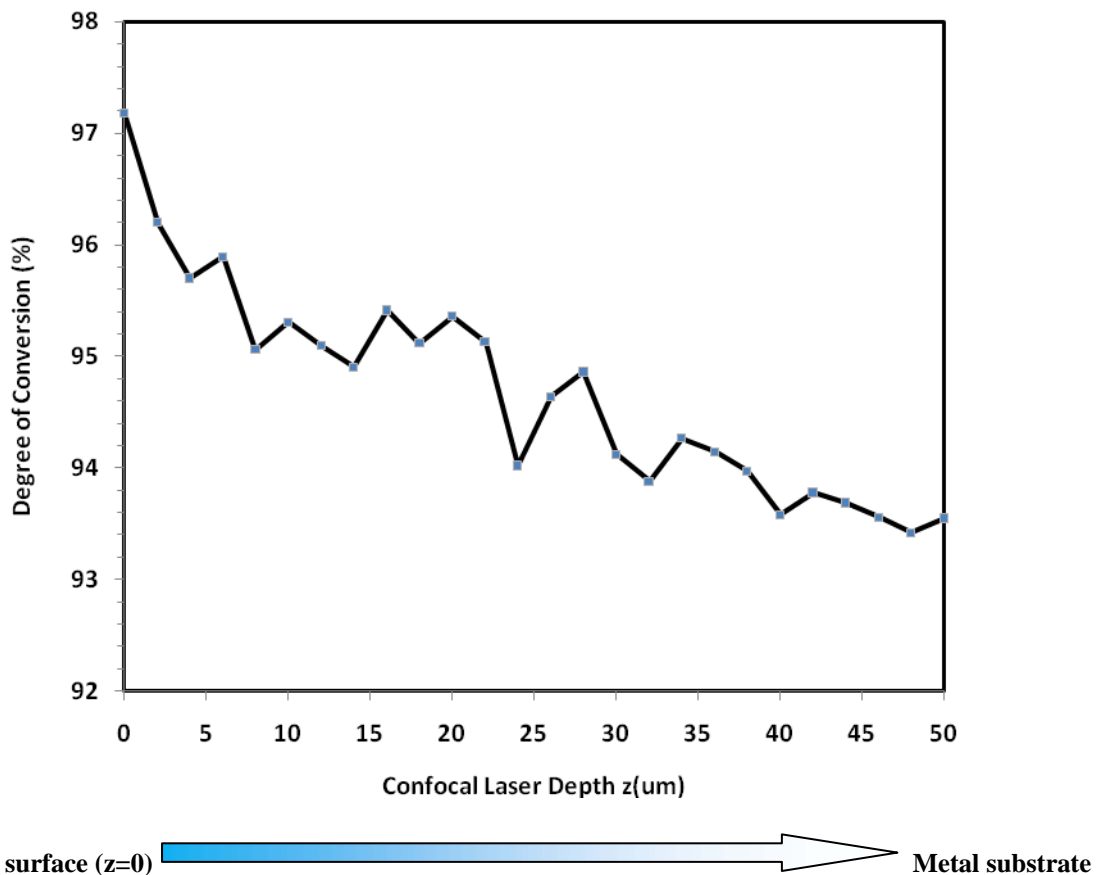


Figure 4. Relative degree of C=C conversion as a function of confocal laser depth for TMS-BAGD cured using a UV-A dose of 2230 mJ/cm^2 .

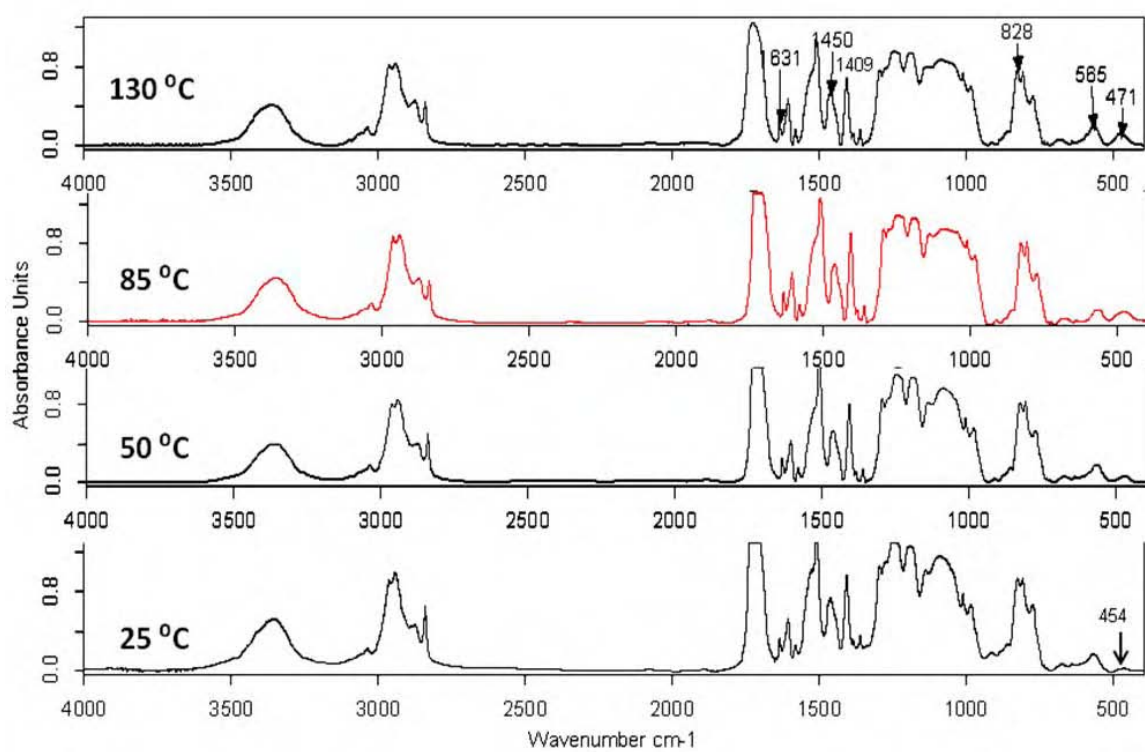


Figure 5. FT-IR spectra of TMS-BADG thermally cured for 1 day at different temperatures.

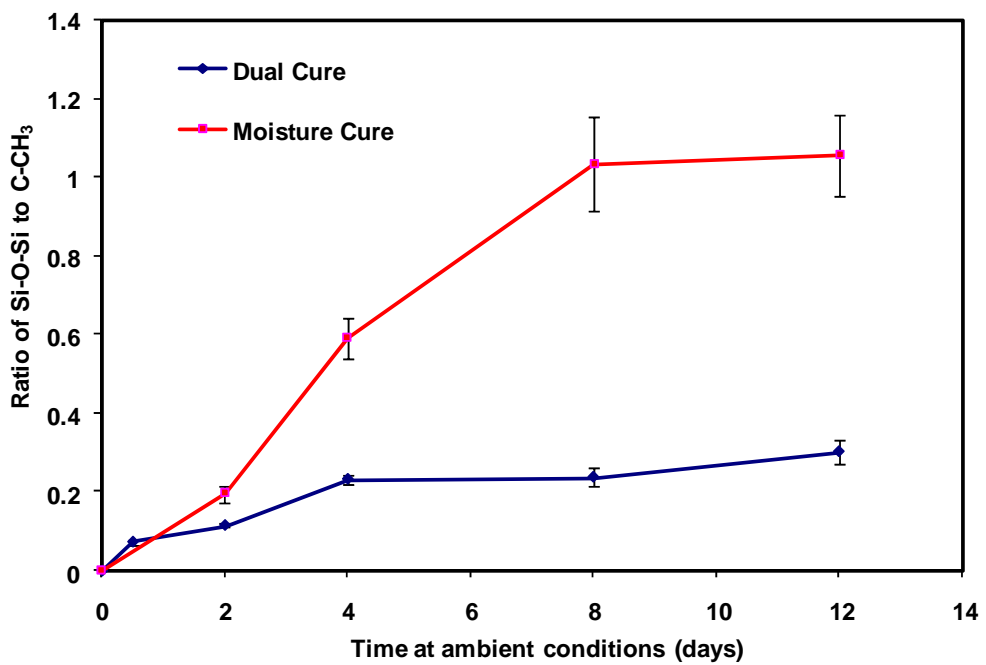


Figure 6. Siloxane network formation as a function of time at ambient conditions.

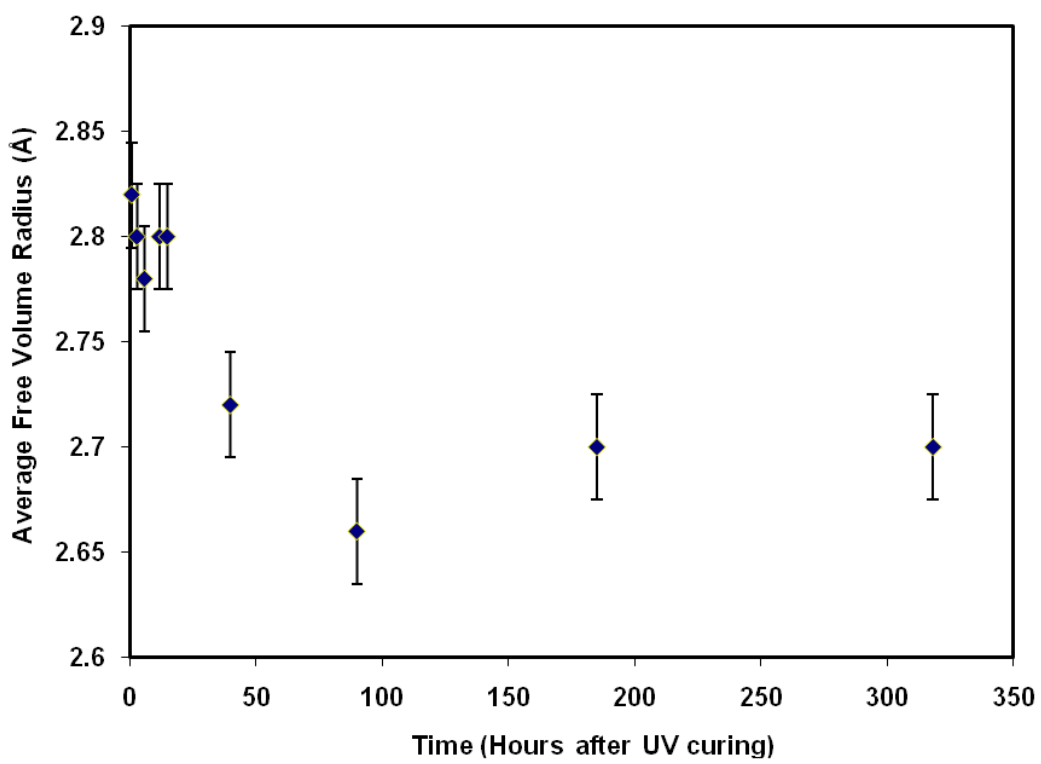


Figure 7. The change in average free volume size as a function of time at ambient conditions after UV curing.

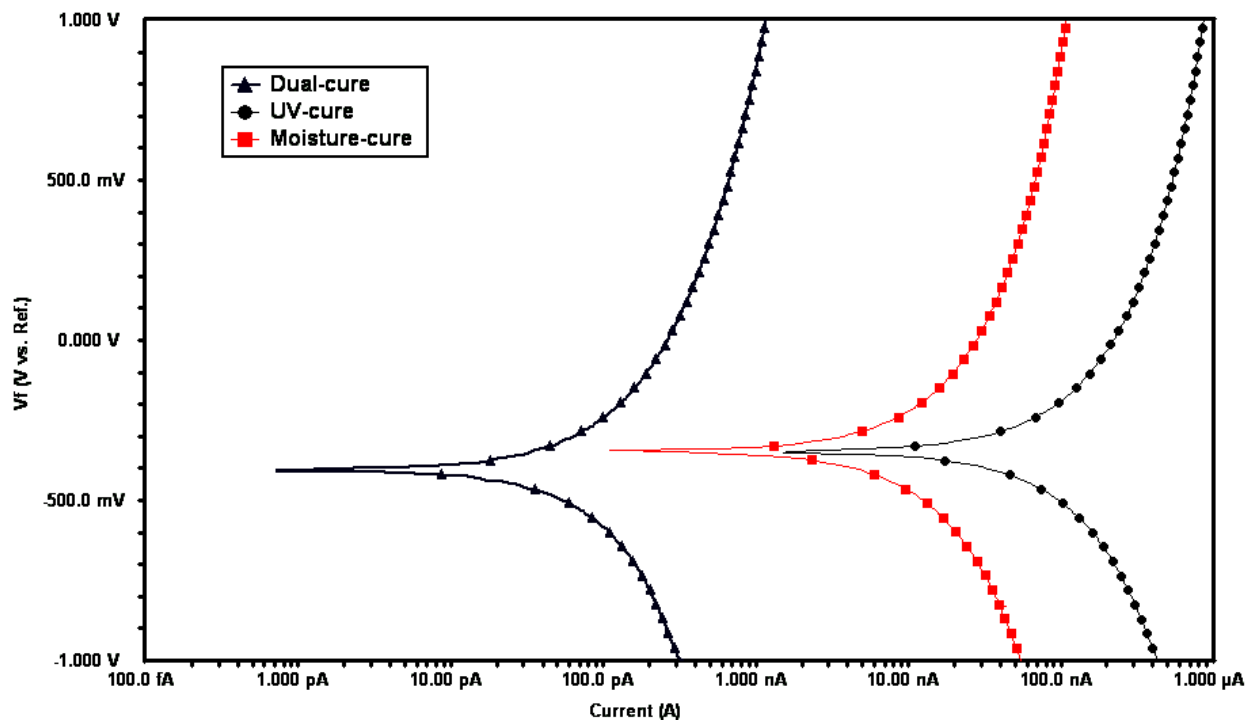


Figure 8. Potentiodynamic polarization data as a function of curing conditions for TMS-BADG coated on Al-2024-T3.

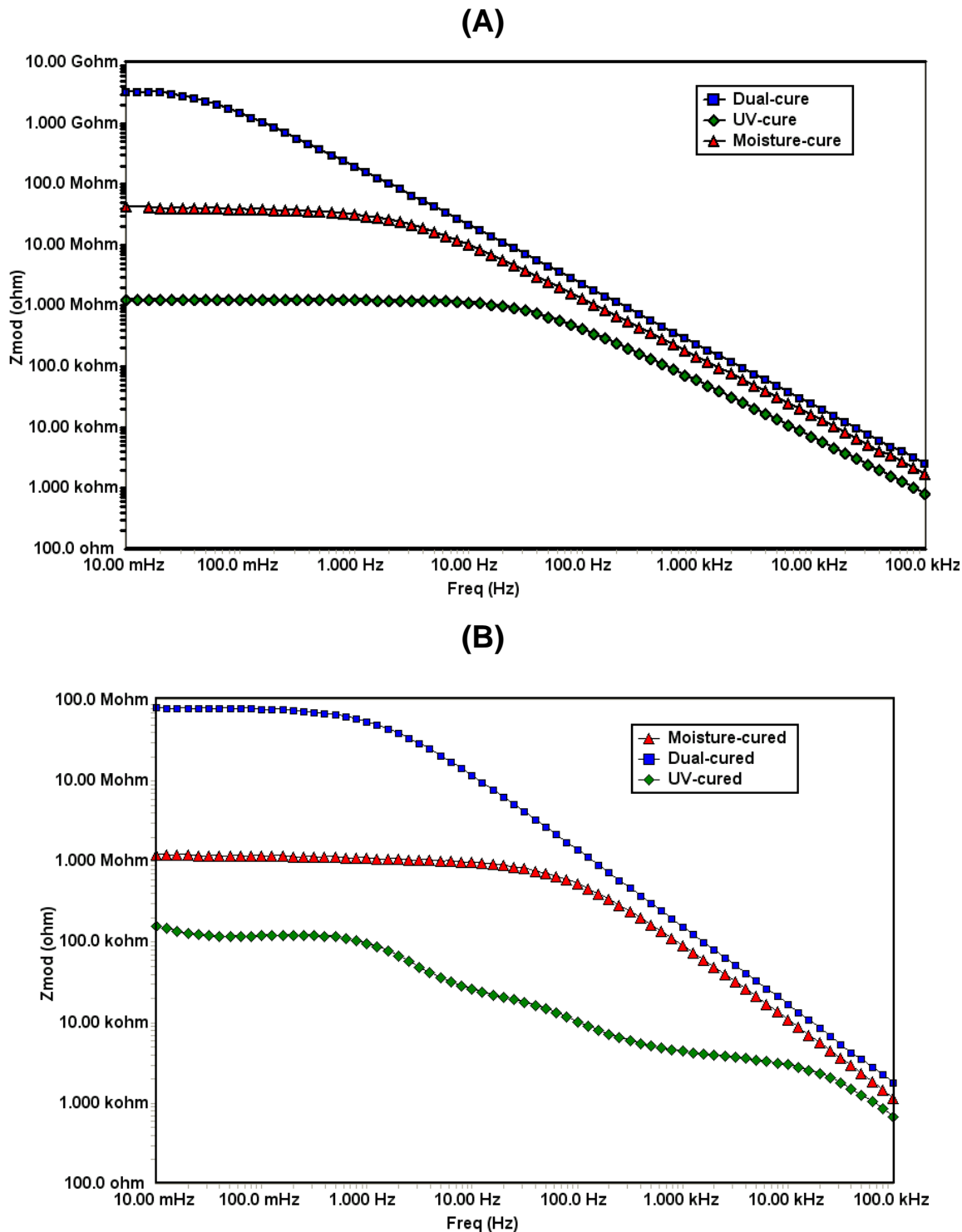


Figure 9. EIS results as a function of curing conditions for TMS-BADG coated on Al-2024-T3 after 1 day immersion (A) and 2 weeks of immersion (B) in 3% aqueous NaCl.

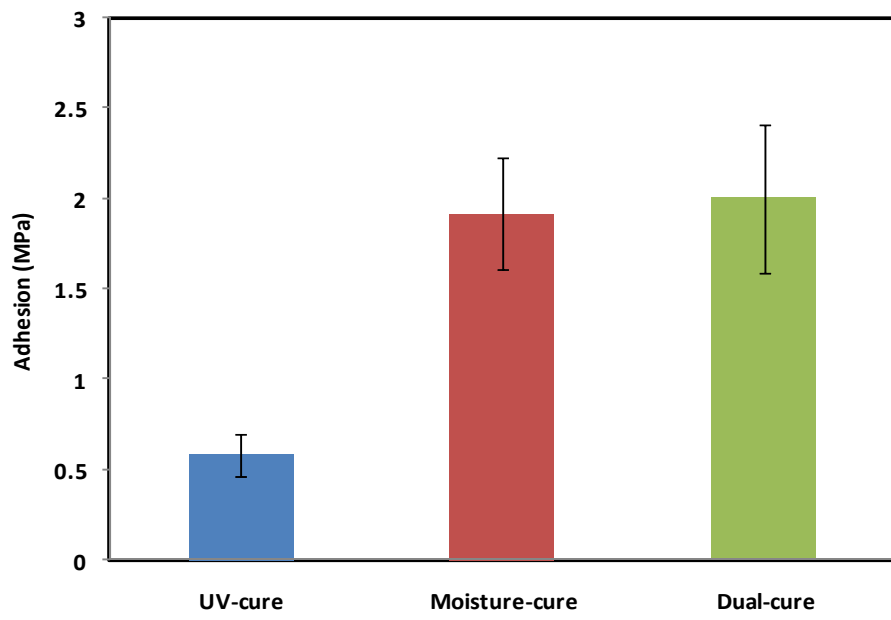


Figure 10. Adhesion as a function of curing conditions for TMS-BADG coated on Al-2024-T3.

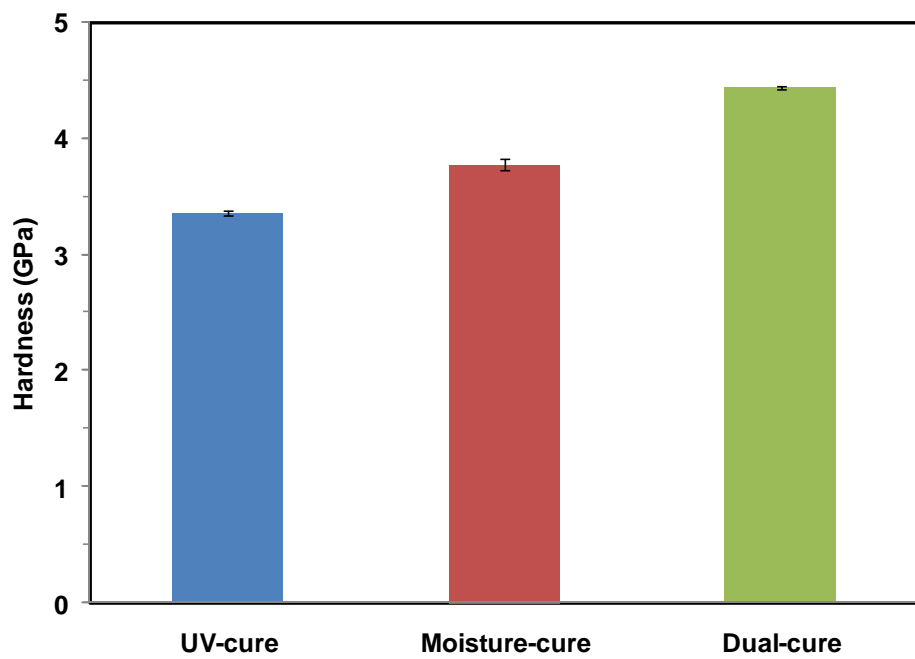


Figure 11. Hardness as a function of curing conditions for TMS-BADG coated on Al-2024-T3.

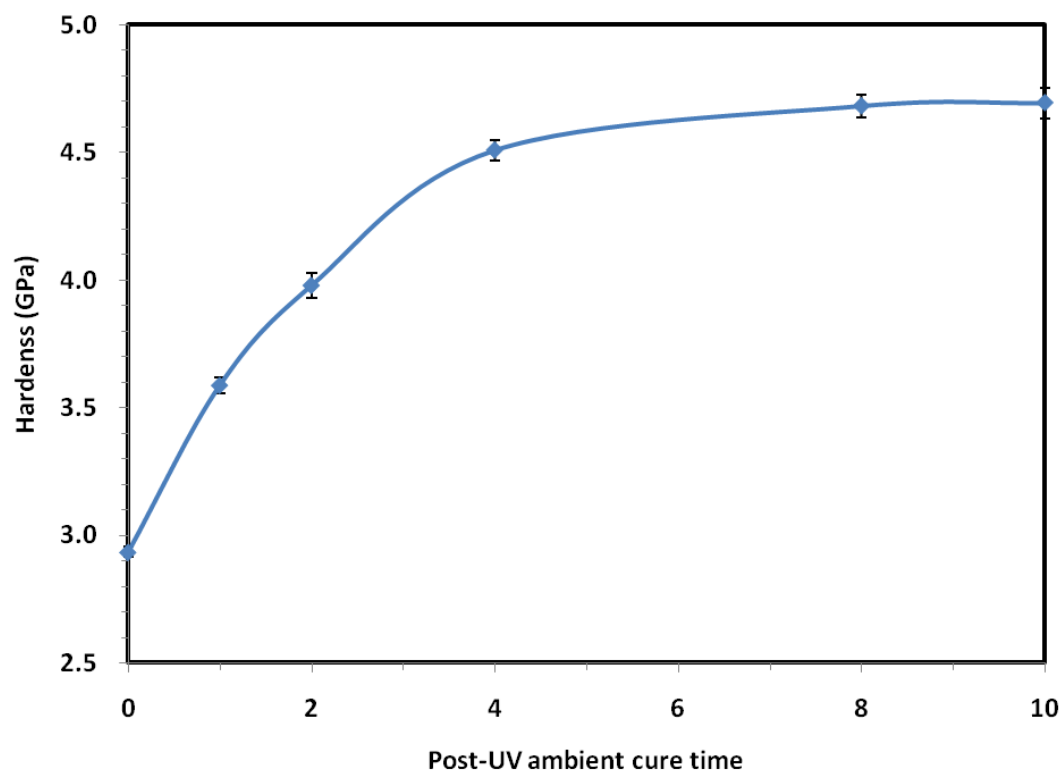


Figure 12. Hardness as a function of time after UV-curing for the TMS-BAGD coating.



Trimethylsilane-based pretreatments in a Mg-rich primer corrosion prevention system

Douglas L. Schulz^{a,b,c,*}, Robert A. Sailer^{a,b,c}, Chris Braun^{a,b}, Andrew Wagner^{a,b}, Natalie Klaverkamp^{a,b}, Kevin Mattson^b, Joseph Sandstrom^b, David Bunzow^b, Scott Payne^d, Jie He^{b,e,f}, Jun Li^{b,e,f}, Bret Chisholm^{b,e,f}

^a Center for Surface Protection, North Dakota State University, Fargo, ND 58102, USA

^b Center for Nanoscale Science and Engineering, North Dakota State University, Fargo, ND 58102, USA

^c Mechanical Engineering and Applied Mechanics Department, North Dakota State University, Fargo, ND 58102, USA

^d Electron Microscopy Center, North Dakota State University, Fargo, ND 58102, USA

^e Combinatorial Materials Research Laboratory, North Dakota State University, Fargo, ND 58102, USA

^f Coatings and Polymeric Materials Department, North Dakota State University, Fargo, ND 58102, USA

ARTICLE INFO

Article history:

Received 25 January 2008

Received in revised form 27 April 2008

Accepted 28 April 2008

Keywords:

Magnesium

Aluminum

Corrosion

Electrochemical impedance spectroscopy

Plasma-enhanced chemical vapor

deposition

ABSTRACT

A trimethylsilane-based coating was investigated as a pretreatment for Al-2024 T3 in a novel Mg-rich primer corrosion prevention system. SiC-based thin films were deposited onto Al substrates by plasma-enhanced chemical vapor deposition (PECVD). A screening study of the pressure (P) dependence of films deposited at 350 °C showed an increase in growth rate from 0.6 to 1.9 Torr. A second screening study where P was fixed at 1.9 Torr and temperature (T) was varied from 125 to 550 °C showed decreasing growth rates with increasing temperature with an apparent transition around 300 °C. Electrochemical impedance spectroscopy (EIS) of the SiC-based films on Al-2024 after exposure to a corrosive environment (i.e., dilute Harrison solution) indicated that samples coated using SiC-based films exhibit higher low frequency impedance (i.e., 100–1000× higher) than bare Al-2024 with open circuit potential remaining 0.1 V higher for the former suggesting the SiC-based films slow the corrosion process. A Mg-rich primer was coated onto the SiC on Al-2024 with the galvanic function of the system determined by EIS. As compared to SiC on Al-2024, a similar behavior for the low frequency impedance was observed for the Mg-rich primer-coated samples with some films exhibiting $1E+8 \Omega$ at 0.1 Hz indicating a strong barrier property. Initial gas jet erosion using acrylic media indicates the Mg-rich primer coatings are removed in preference to the Si-C films—the first step toward demonstrating a permanent pretreatment. When successfully developed and optimized, the value of such a hard, protective coating is the reduction of a three-component coatings system (i.e., pretreatment, primer, and topcoat) to a two-component system (i.e., primer and topcoat).

© 2008 Elsevier B.V. All rights reserved.

1. Introduction

When considered as the structural support for aircraft, aluminum (Al) alloys have several desirable properties including low density (2.7 g/cm³), good fatigue properties (modulus = 91 GPa) and high strength-to-weight ratio. While Al is typically considered quite noble given the formation of a thin native oxide passivation layer, electrochemical corrosion occurs when Al alloys are exposed to the service environment of military and commercial aircraft. Studies indicate that corrosion likely begins in areas where Cu-rich precipitates are exposed to the environment leading to

“pitting” and further failure [1,2]. Corrosion prevention systems based upon chromate continue to be the solution of choice for many end users including the U.S. military. This aircraft coating system typically consists of three components: a chromate-based conversion coating, referred to as “alodine”; an epoxy primer that contains ZnCrO₄ or SrCrO₄ pigment; and, a polyurethane topcoat. While the anticorrosion properties of chromium are a consequence of the multiple valence states available to the metal ion (i.e., Cr²⁺, Cr³⁺, Cr⁴⁺ and Cr⁶⁺), it is now known that hexavalent chromium is a documented human carcinogen [3]/environmental hazard [4] and efforts to provide chromate-free aircraft coatings that provide adequate corrosion protection are ongoing [5,6]. A chromate-replacement primer system that provides galvanic corrosion protection for Al-framed aircraft has recently been developed by Bierwagen and co-workers at North Dakota State University (NDSU) [7,8]. A schematic of the NDSU magnesium-rich primer

* Corresponding author at: North Dakota State University, 1805 NDSU Research Park Drive North, Fargo, ND 58102, USA. Tel.: +1 701 231 5275; fax: +1 701 231 5306.

E-mail address: Doug.Schulz@ndsu.edu (D.L. Schulz).

3-Part Coating System

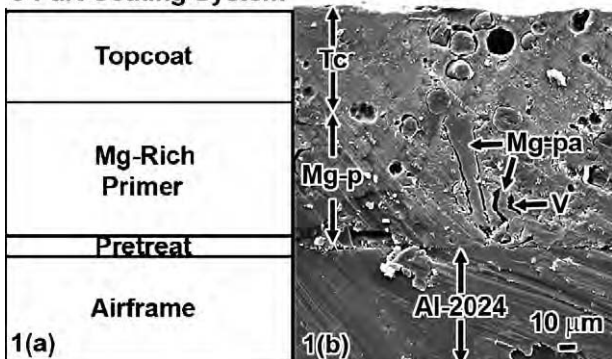


Fig. 1. NDSU Mg-rich primer system shown (a) schematically and (b) photographically where Mg-p=magnesium-rich primer, Mg-pa=magnesium particle, Tc=topcoat and V=void.

and a scanning electron microscopy (SEM) photograph are given in Fig. 1. This technology is now being evaluated for use in both military and commercial applications.

The NDSU “magnesium-rich primer” contains magnesium (Mg) metal flake loaded into an epoxy resin at a level that exceeds the critical pigment volume concentration (CPVC) [9]. Electrical contact to the underlying substrate allows the interconnected Mg network to act as a sacrificial anode for Al alloy—in complete analogy with how zinc anodes protect steel in corrosive environments (e.g., outboard components of marine vessels). This aircraft coating system was initially comprised of three components including a polyurethane topcoat, a Mg-rich epoxy primer and a pretreatment layer with the latter applied to the Al alloy substrate to promote adhesion.

The goal of the research presented in this paper is to develop a permanent pretreatment layer that is (1) compatible with the Mg-rich primer and (2) resistant to the plastic-media blasting employed to strip paint at the depot. Such a thin coating would find value during repainting of aircraft as a nominally three-component system (i.e., pretreatment, primer, and topcoat) could be reduced to two components (i.e., primer and topcoat). A primary requisite for the pretreatment is that the galvanic function of the Mg-rich primer system must not be inhibited and a layer thickness less than 100 nm would be anticipated. In addition, the layer must be durable to withstand media blasting and to accommodate airframe flexure. Finally, to be applied on legacy aircraft, a low deposition temperature is required to preclude ignition of combustibles.

This paper is a preliminary report on the development of Si-C based coatings targeted to be permanent pretreatment layers on Al-2024 alloy. While films in the present study were grown at reduced pressure (i.e., $P < 2$ Torr) via PECVD (a process not amenable to application at the depot), this investigation of feasibility offers valuable initial feedback regarding the utility of gas-phase precursors and a low-temperature process in the production of SiC-based coatings that meet the electrical and durability metrics described above. We show this is the case and look forward to future experiments that might utilize atmospheric-pressure deposition processes such as dielectric glow discharge, atmospheric-pressure plasma jet and plasma spraying.

2. Experimental methodology

2.1. SiC-based film growth by PECVD

Thin SiC-based films were grown via PECVD using 2% $\text{HSi}(\text{CH}_3)_3$ (trimethylsilane or TMS) in argon as the precursor in an Oxford

100 Plus located in a class 100 cleanroom. Al-2024 alloy (Q-panel) 10 cm × 10 cm substrates were rubbed with 0000 steel wool and rinsed with isopropanol immediately prior to film growth. Deposition temperatures (T_{dep}) and pressures (P_{dep}) ranged from 125 to 550 °C and 0.5 to 1.9 Torr, respectively, with deposition time fixed at 20 min. A pulsed plasma was employed to promote film uniformity with the following sequence: 40 W @ 300 kHz for 15 s; 60 W @ 13.56 MHz for 20 s; repeat. Ellipsometric data was collected using a Gaertner L-115S-8 with variable angle Stokes detector and single wavelength laser operating at 632 nm. SEM images were collected using a JEOL JSM-6300 scanning electron microscope operating at 15 kV. SiC and Al-2024 samples were coated with approximately 20 nm of Au using a Technics Hummer II sputter coater to preclude charging during SEM. The XPS measurements were performed on an SSX-100 system (surface science instruments) equipped with a monochromated Al K α X-ray source, a hemispherical sector analyzer (HSA) and a resistive anode detector with curve fittings were realized using ESCA 2005 software.

2.2. Mg-rich primer

A 50% pigment volume concentration primer was applied to SiC/Al-2024 substrates using a high volume low-pressure air spray method [10]. The formulation utilized two forms of Mg powders (Eckagranules™ PK31 and Eckagranules™ PK51 from Ecka GmbH) mixed at a 52/48 (v/v) ratio. The epoxide binder system was comprised of 25 wt.% Epon1001-CX-75 (Resolution Performance Products) dissolved in a 65/35 (v/v) ratio methylisobutylketone/xylene (Sigma-Aldrich). Epicure3140 (Resolution Performance Products) was employed as a polyamide curing agent and Aerosil® R974 (Degussa) was used as a dispersing agent. Fig. 2 shows photographs illustrating how one half of the substrate (i.e., 5 cm × 10 cm) is coated with Mg-rich primer/TMS-derived film while the other half is covered by a TMS-derived thin film only.

2.3. Electrochemical impedance spectroscopy (EIS) testing

Electrochemical impedance spectroscopy (EIS) was conducted using a Gamry MultiEchem 8 Electrochemistry System coupled with EIS300 measurement software. Tubular plastic wells (length ~5 cm; i.d. ~2.54 cm) were glued onto the sample surface using a 2 K epoxy (Marine Goop®). A three-electrode arrangement was used, consisting of a saturated calomel electrode (SCE), a platinum mesh as counter electrode, and a coated sample as the working electrode. The exposed area of the working area was 5 cm². EIS spectra were acquired in the frequency range from 10 kHz to 0.1 Hz with applied 10 mV R.M.S. voltage vs. open circuit potential. Dilute Harrison's solution (0.35% $(\text{NH}_4)_2\text{SO}_4$ and 0.05% NaCl in deionized water) was used as the test electrolyte and also served as a corrosive environment for the constant immersion trials.

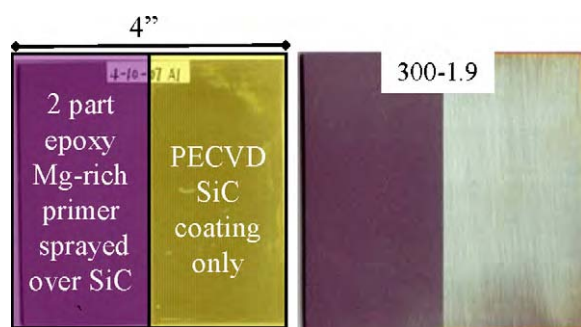


Fig. 2. Photographs of test coupons used in this study.

3. Results and discussion

There are a multitude of reports for PECVD of SiC films and most use higher growth temperatures that are not amenable to application on Al (m.p., 660 °C). While studies of the low-temperature growth (i.e., $T < 400$ °C) using organosilicon precursors have shown silicon carbide-based films to be useful as chemically resistant [11] and protective barrier coatings [12,13], most do not report using Al substrates nor assay the physical properties of the films as they relate to corrosion [14,15]. Loboda et al. [15] reported the PECVD growth of silicon-based films under reaction conditions (i.e., reactor pressure ~1.5 Torr and reactor temperature from 250 to 375 °C) similar to those employed in the current study. In addition, the gas-phase chemistry (i.e., as probed by mass spectrometry using a residual gas analyzer) showed trimethylsilyl radical (i.e., $\cdot\text{Si}(\text{CH}_3)_3$) is a reactive species when using trimethylsilane as a PECVD precursor [15]. Others have reported trimethylsilane gives both silyl and methyl radicals in thermolysis studies [16,17] as well as plasma-assisted deposition of silicon-based films [18]. Given the similarity in growth conditions (i.e., medium-pressure plasma with trimethylsilane as a precursor), it is anticipated that the operative reaction/film growth mechanisms in the present study are comparable to those previously reported [15,18].

Yasuda and co-workers have reported the use of trimethylsilane as a precursor in low-temperature plasma deposition of SiC-based coatings that provide corrosion protection for Al alloys exposed to salt spray testing [19]. van Ooij et al. have been active in the field of corrosion protection of metals and in the past employed hexamethyldisiloxane as a precursor to plasma deposition of SiC-based films on metallic substrates [20]. To the best of our knowledge, however, there are no previous studies whereby the performance of SiC-based films in conjunction with a Mg-primer has been reported.

Fig. 3 shows SEM images of a typical TMS-derived film ($T_{\text{dep}} = 350$ °C, $P_{\text{dep}} = 1.9$ Torr) at low (Fig. 3a) and high magnification (Fig. 3b). Marring of the Al substrate from the steel wool surface preparation step is apparent in Fig. 3a and the surface morphology of the SiC-based coating is illustrated in Fig. 3b. Gas jet erosion testing using acrylic media (ASTM G76) showed the Mg-rich primer coating was removed prior to the TMS-derived films—an essential attribute for a permanent pretreatment. Film adhesion of SiC on Al-2024 as well as Mg-rich primer on SiC on Al-2024 was qualitatively evaluated via the cross-hatch method (ASTM 3359) and all films (except 350-1.2) exhibited excellent adhesion (i.e., 5B rating). van Ooij et al. have previously performed detailed chemical analyses (i.e., XPS, AES and TOF-SIMS) of silicon-containing films on cold-rolled steel deposited by plasma deposition of trimethylsilane and found at least three distinctly different film regions including an interfacial region where the film is intimately mixed with the native metal oxide [21]. While the native oxide layer reported by these authors for cold-rolled steel is likely thicker than for Al substrates, it is possible that the good adhesion in the present study may be due to a similar interfacial region whereby sputtering of the oxide surface leads to the formation of a silicon oxycarbide interlayer that is well-bonded to the substrate.

3.1. Temperature screening study

The experimental conditions and results of the temperature screening study are given in Table 1. In this instance, pressure was fixed at 1.9 Torr and T_{dep} varied from 125 to 550 °C with upper T_{dep} limited by thermal failure of Al substrates. Ellipsometry provides interesting data relative to both refractive index and film thickness. The real portion of the refractive index (n) increases with increasing T_{dep} and varies substantially from 3.13 for films deposited at 550 °C to 1.64 for films grown at 125 °C. By way of

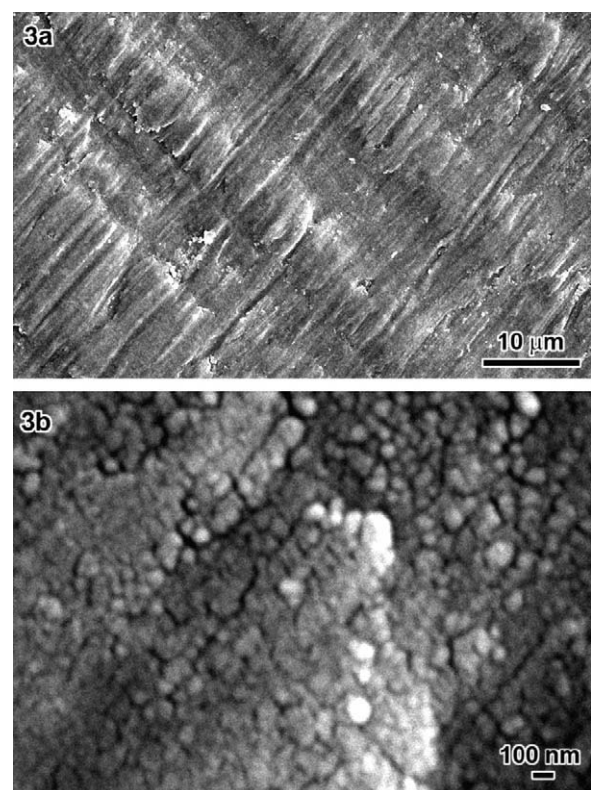


Fig. 3. Scanning electron micrographs of SiC on Al-2024 at (a) 2000 \times and (b) 40,000 \times magnification.

comparison, the following values for n_0 have been reported for pure compounds: amorphous-Si:H = 3.5; amorphous-SiC:H = 3.2; and, $\text{SiO}_2 = 1.46$ [22]. While the refractive index may be a function of properties other than film composition (e.g., crystallinity, density, etc.), it appears that higher T_{dep} favors the formation of a-SiC:H. XPS characterization of films grown at 450 and 550 °C give a film stoichiometry of $\text{Si}_{0.40}\text{C}_{0.41}\text{O}_{0.19}$ and $\text{Si}_{0.20}\text{C}_{0.46}\text{O}_{0.34}$, respectively. As there is no oxygen added to the PECVD chamber during film growth and given a precursor formula of $\text{SiC}_3\text{H}_{10}$ with a carrier gas of UHP Ar, it is apparent that the films oxidize when exposed to air. Propensity toward oxidation was also observed in films grown from trimethylsilane in an atmospheric-pressure glow discharge using a carrier gas of nitrogen [23]. A similar effect was previously noted by van Ooij et al. for plasma polymerized trimethylsilane-based coatings on cold-rolled steel where it was hypothesized that the coatings contain residual long-lived radicals which react with O_2 and/or H_2O after being removed from the reaction chamber and exposed to atmosphere [21].

Also of note is the trend of decreasing growth rates with increasing temperature. Fig. 4 shows a plot of growth rate as a function of T_{dep} . The results of this initial study tend to indicate two growth regimes that transition around 300 °C as illustrated by the two lines intersecting each other in the graph (Fig. 4). While more data is required to generate statistically significant Arrhenius (i.e., $1/T$) relationships, it seems plausible that the lower T_{dep} portion ($T_{\text{dep}} < 300$ °C) of this plot represents a regime where the gas-phase precursors condense to form a partially polymerized structure. By way of comparison, $T_{\text{dep}} > 300$ °C provides enough energy such that the precursors condense and then react on the surface of the substrate to form a film. High-resolution scanning electron microscopy could be used to differentiate these two growth regimes and may be a part of future investigations.

Table 1

Experimental conditions and film characterization for the temperature screening

Sample ID	T_{dep} (°C)	P_{dep} (Torr)	n of SiC ^a	SiC film, t^a (nm)	SiC, 10 min, Z_{mod}^b (Ω)	SiC, 2 day, Z_{mod}^c (Ω)	SiC, 10 min, OCP ^d (V)	SiC, 2 day, OCP ^e (V)	Mg-rich, 10 min, Z_{mod}^f (Ω)	Mg-rich, 2 day, Z_{mod}^g (Ω)	Mg-rich, 10 min, OCP ^h (V)	Mg-rich, 2 day, OCP ⁱ (V)
Al-2024	n.a.	n.a.	n.a.	0	1E+3	3E+3	-0.654	-0.840	4E+3	7E+2	-1.178	-1.055
125-1.9	125	1.9	1.64	247	2E+5	8E+3	-0.670	-0.692	3E+7	2E+5	-1.250	-1.026
200-1.9	200	1.9	1.88	166	1E+5	2E+4	-0.690	-0.685	5E+6	3E+5	-0.910	-1.057
250-1.9	250	1.9	2.33	102	5E+4							
300-1.9	300	1.9	2.46	84	1E+5	9E+4	-0.680	-0.689	2E+7	3E+5	-1.375	-1.067
350-1.9	350	1.9	2.61	76	3E+4	3E+4	-0.660	-0.685	2E+7	3E+5	-1.250	-1.047
450-1.9	450	1.9	2.76	76	7E+3	4E+3	-0.675	-0.695	4E+6	7E+4	-1.360	-1.030
550-1.9	550	1.9	3.13	56	3E+3	1E+3	-0.695	-0.755	3E+4	5E+3	-1.305	-0.995

^a n (real portion of refractive index) and t (film thickness) derived from ellipsometry data.^b 0.1 Hz data for SiC on Al-2024 after 10 min in dilute Harrison solution (DHS).^c 0.1 Hz data for SiC on Al-2024 after 2 days in DHS.^d Open circuit potential (OCP) of SiC on Al-2024 vs. standard calomel electrode (SCE) after 10 min in DHS.^e OCP of SiC on Al-2024 vs. SCE after 2 days in DHS.^f 0.1 Hz data for Mg-rich primer on SiC on Al-2024 after 10 min in DHS.^g 0.1 Hz data for Mg-rich primer on SiC on Al-2024 after 2 days in DHS.^h OCP of Mg-rich primer on SiC on Al-2024 vs. SCE after 10 min in DHS.ⁱ OCP of Mg-rich primer on SiC on Al-2024 vs. SCE after 2 days in DHS.

EIS was used to evaluate the physical barrier properties of the films and the impedance modulus (Z_{mod}) at 0.1 Hz was used as an indicator for the evaluation. As shown in Table 1, the SiC-coated samples prepared at different deposition temperatures exhibit variable impedance initially with the low frequency impedance decreasing with increasing T_{dep} . At the initial point of immersion, the sample prepared at 125 °C showed the highest impedance ($2 \times 10^5 \Omega$) at 0.1 Hz—about two orders of magnitude higher than Al-2024. For T_{dep} from 200 to 350 °C, the low frequency Z_{mod} remains around $10^5 \Omega$ suggesting that the nanometer-scale thin film prepared at these conditions provides an excellent barrier. However, for $T_{dep} > 450$ °C, a significant impedance drop was noted indicating a reduction in barrier properties.

After two days of constant immersion in DHS, a more distinct difference was observed among the samples prepared at variable temperature. For the samples prepared at 450 and 550 °C, the low frequency impedance dropped to the same magnitude as bare Al-2024 ($3 \times 10^3 \Omega$) indicating that the films lose barrier properties during this period of time. In contrast, the samples at lower T_{dep} showed higher impedance though they were about one order of magnitude lower than the measurements made only two days earlier. After immersion in DHS for two days, the SiC coatings prepared at $T_{dep} = 300$ and 350 °C exhibited longer lifetime with respect to corrosion protection of samples prepared at other temperatures. It is interesting to note that the samples prepared in this study appear to possess superior barrier properties than a previous report

by van Ooij et al. who found that direct current plasma polymerized films ($P=80$ W) prepared from trimethylsilane showed 0.1 Hz impedance of 2×10^3 and $\sim 2 \times 10^2 \Omega$ after immersion in 3.5 wt.% NaCl solution for 1 h and 1 day, respectively [18]. The reasons for this may be related to film morphology whereby films grown on a heated substrate using a pulsed plasma are better barriers than those prepared using a dc plasma at ambient temperature. In addition, it is possible the 3.5 wt.% NaCl corrosion solution used by van Ooij et al. is more aggressive than the dilute Harrison's solution (0.35% $(NH_4)_2SO_4$ and 0.05% NaCl in deionized water) used in this study.

In order to study the compatibility of the SiC film with the recently developed Mg-rich coating, a layer of Mg-rich primer with 50% PVC were spray-coated onto the SiC/Al-2024 substrates. The corrosion protection property of the combined coating system was then characterized using EIS. As shown in Table 1, at the initial period of immersion (10 min), most Mg-primer samples exhibited low frequency $Z_{mod} = 10^6$ – $10^7 \Omega$ indicating the coating system was providing a high barrier property to the underlying Al. However, the Mg-rich primer/SiC/Al-2024 sample that utilized a SiC film prepared at $T_{dep} = 550$ °C showed a very low impedance and therefore little protection against corrosion. As mentioned previously, this observation may be due to the poor film morphology of the SiC pretreatment prepared at this temperature, significantly reducing the adhesion of the film to the underlying Al-2024. Poor SiC film quality may also affect the electrochemical interaction of the Mg-rich coating with the metal substrate [24]. After two days of immersion in DHS, the low frequency impedance of all the samples containing Mg-rich coating (i.e., except SiC $T_{dep} = 550$ °C) decreased two orders of magnitude giving $Z_{mod} = 10^4$ – $10^5 \Omega$. The observed decrease in impedance may indicate partial loss of the barrier properties or it may be a consequence of electrolyte penetrating into coating and establishing an electrical or electrochemical interaction between the substrate and the Mg particles in the coating. The latter effect would render the coating more electrically conductive and thereby reduce the low frequency impedance—an observation also supported by open circuit potential measurements. The OCP of Mg-primer/SiC/Al-2024 samples (typically more than -1 V vs. SCE) are much lower than SiC/Al-2024 samples (-0.67 to -0.70 V) suggesting that the SiC treatment does not impede the electron transfer between Mg-rich primer and Al-2024 and the Mg-primer is functional over the course of the 2 day immersion test.

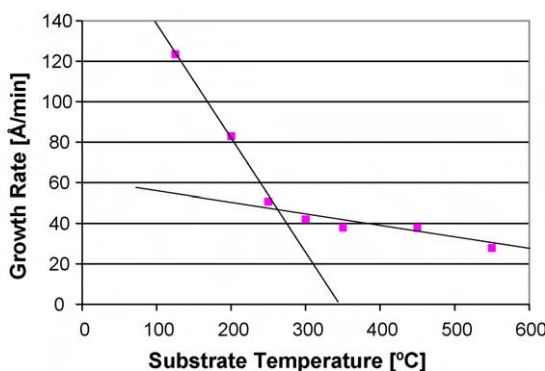
**Fig. 4.** Growth rate as a function of T_{dep} for SiC-based films grown at 1.9 Torr.

Table 2
Experimental conditions and film characterization for the pressure screening

Sample ID	T _{dep} (°C)	P _{dep} (Torr)	n of SiC ^a	SiC film, t ^a (nm)	SiC, 10 min, Z _{mod} ^b (Ω)	SiC, 2 day, Z _{mod} ^c (Ω)	SiC, 10 min, OCP ^d (V)	SiC, 2 day, OCP ^e (V)	Mg-rich, 10 min, Z _{mod} ^f (Ω)	Mg-rich, 2 day, Z _{mod} ^g (Ω)	Mg-rich, 10 min, OCP ^h (V)	Mg-rich, 2 day, OCP ⁱ (V)
Al-2024	n.a.	n.a.	n.a.	0	1E+3	3E+3	-0.654	-0.840	4E+3	7E+2	-1.178	-1.055
350-1.9	350	1.9	2.61	76	3E+4	3E+4	-0.660	-0.685	2E+7	3E+5	-1.250	-1.047
350-1.6	350	1.6	2.64	51	3E+5	1E+4	-0.675	-0.710	5E+7	3E+6	-0.933	-1.028
350-1.2	350	1.2	2.57	45	j	j	j	j	j	j	j	j
350-0.8	350	0.8	2.53	39	7E+5	6E+4	-0.687	-0.705	3E+7	8E+6	-1.253	-1.025
350-0.6	350	0.6	2.56	33	9E+3	8E+3	-0.683	-0.713	2E+6	2E+5	-1.230	-1.001

^a n (real portion of refractive index) and t (film thickness) derived from ellipsometry data.

^b 0.1 Hz data for SiC on Al-2024 after 10 min in dilute Harrison solution (DHS).

^c 0.1 Hz data for SiC on Al-2024 after 2 days in DHS.

^d Open circuit potential (OCP) of SiC on Al-2024 vs. standard calomel electrode (SCE) after 10 min in DHS.

^e OCP of SiC on Al-2024 vs. SCE after 2 days in DHS.

^f 0.1 Hz data for Mg-rich primer on SiC on Al-2024 after 10 min in DHS.

^g 0.1 Hz data for Mg-rich primer on SiC on Al-2024 after 2 days in DHS.

^h OCP of Mg-rich primer on SiC on Al-2024 vs. SCE after 10 min in DHS.

ⁱ OCP of Mg-rich primer on SiC on Al-2024 vs. SCE after 2 days in DHS.

^j Film had poor adhesion.

3.2. Pressure screening study

The experimental conditions employed for the pressure screening study as well as a compilation of the results are given in Table 2. For this study, the temperature was fixed at 350 °C and the pressure was varied from 0.6 to 1.9 Torr the latter being the highest possible given the present plasma controller. One interesting trend is observed from the ellipsometry film thickness measurements where growth rates were significantly increased as a function of increased P_{dep}. Also, the optical constant of the films showed little variance, indicating the P_{dep} only exerted a small effect upon film composition. EIS was also used to study the effect of P_{dep} on the barrier properties of the deposited film. In general, much smaller variations were observed for the samples prepared for the pressure screening (i.e., Table 2) vs. those for the temperature screening (i.e., Table 1). For SiC/Al-2024, most films exhibit low frequency Z_{mod} 10× higher than those for bare Al, however, the Z_{mod} decreases slightly after two days immersion in DHS. The OCP for SiC/Al-2024 films decrease during the two-day immersion but remain at least 100 mV higher than bare Al, suggesting the SiC film slows the corrosion process.

Films consisting of Mg-primer/SiC/Al-2024 show improved barrier properties vs. Mg-primer/Al-2024 with low frequency Z_{mod} at least two orders of magnitude higher for the former at the initial point of immersion. After two days immersion in DHS, the 0.1 Hz Z_{mod} for the Mg-primer with SiC pretreatment decreases by one or two orders of magnitude, indicating the electrolyte to some extent penetrated into the coatings. In contrast to the Mg-rich primer-coated bare Al 2024, the Z_{mod} for the primer with SiC coatings were about three orders of magnitude higher. The OCP of all the coatings remained at -1 V vs. SCE which suggested that the cathodic protection of Mg-rich coating was functional during that period of time.

4. Conclusions

In this paper, a plasma polymerization method was used to grow thin SiC-based films on Al-2024. These initial trimethylsilane-derived films showed good barrier properties and did not negate the galvanic activity of the Mg-based primer anode. Temperature and pressure screening experiments were conducted to optimize the operational condition in the polymerization process. Several points can be concluded from our preliminary results:

1. The deposition temperature used in the process plays an important role in preparing the SiC thin film. At relatively low temperature (T_{dep} < 300 °C), the film formation may have functioned through the condensation of the gas-phase precursors. When T_{dep} > 300 °C, the film may be formed through sequential precursors condensation/crosslinking reaction at the surface of the substrate.
2. The EIS study indicates that the optimal T_{dep} to prepare the SiC film is within the range of 300–350 °C. The films provided better barrier properties than those prepared at higher temperature. They also show good compatibility with the Mg-rich primer in terms of corrosion protection. The combination of SiC pretreatment with Mg-rich coating gives improved barrier properties without sacrificing the galvanic activity of the Mg-rich coating.
3. The pressure screening studies (in the range from 0.6 to 1.9 Torr) showed that increasing deposition pressure significantly increases film growth rate but was not a critical factor in controlling film composition and barrier properties in the plasma polymerization process.

Acknowledgements

This project was funded by the DoD through AFRL Grant FA8650-04-1-5045 Durable Hybrid Coatings. The authors thank Bob Tucker, Steve Szaruga, Joel Johnson and Mike Spicer for helpful discussions. The efforts of Drs. John C. Nelson and Bing Luo at the University of Minnesota who coordinated XPS characterization are kindly acknowledged, as are helpful discussions with NDSU colleagues (Greg McCarthy, Dante Battocchi, Gordon Bierwagen and Dennis Tallman).

References

- [1] J.D. Ramsey, R.L. McCreery, Corros. Sci. 46 (2004) 1729.
- [2] W.J. Clark, J.D. Ramsey, R.L. McCreery, G.S. Frankel, J. Electrochem. Soc. 149 (2002) B179.
- [3] D.M. Stearns, K.E. Wetterhahn, Chem. Res. Toxicol. 10 (1997) 271.
- [4] M. Faisal, S. Hasnain, J. Pharmacol. Toxicol. 1 (2006) 248.
- [5] P.L. Ko, M.F. Robertson, Wear 252 (2002) 880.
- [6] E.D. Daniels, C.J. Brown, T. Strukely, W.D. Scott, Annual Meeting & Exhibition Proceedings CD-ROM—Air & Waste Management Association, 92nd, St. Louis, MO, US, June 20–24 (1999) 3583.
- [7] D. Battocchi, A.M. Simoes, D.E. Tallman, G.P. Bierwagen, Corros. Sci. 48 (2006) 1292.
- [8] D. Battocchi, A.M. Simoes, D.E. Tallman, G.P. Bierwagen, Corros. Sci. 48 (2006) 2226.
- [9] M.E. Nanna, G.P. Bierwagen, JCT Res. 1 (2004) 69.

- [10] <http://www.azdeq.gov/environ/waste/p2/download/hvlp.pdf> (downloaded January 16, 2008).
- [11] A.F. Flannery, N.J. Mourlas, C.W. Storment, S. Tsai, S.H. Tan, J. Heck, D. Monk, T. Kim, B. Gogoi, G.T.A. Kovacs, *Sens. Actuators A* 70 (1998) 48.
- [12] H. Anma, Y. Yoshimoto, M. Warashina, Y. Hatanaka, *Appl. Surf. Sci.* 175–176 (2001) 484.
- [13] C.-C. Chiang, M.-C. Chen, L.-J. Li, Z.-C. Wu, S.-M. Jang, M.-S. Liang, *J. Electrochem. Soc.* 151 (2004) G612.
- [14] M.J. Loboda, J.A. Seifferly, F.C. Dall, *J. Vac. Sci. Technol. A* 12 (1994) 90.
- [15] M.J. Loboda, J.A. Seifferly, C.M. Grove, R.F. Schneider, *Electrochem. Proc.* 97–10 (1997) 443.
- [16] A.C. Baldwin, I.M.T. Davidson, M.D. Reed, *J. Chem. Soc., Faraday Trans.* 74 (1978) 2171.
- [17] M.A. Ring, H.E. O'Neal, S.F. Rickborn, B.A. Sawrey, *Organometallics* 2 (1983) 1891.
- [18] W.J. van Ooij, D. Surman, H.K. Yasuda, *Prog. Org. Coat.* 25 (1995) 319.
- [19] Q. Yu, C.E. Moffitt, D.M. Wieliczka, J. Deffeyes, H. Yasuda, *Prog. Org. Coat.* 44 (2002) 37.
- [20] W.J. van Ooij, S. Eufinger, S. Guo, *Plasma Chem. Plasma Proc.* 17 (1997) 123.
- [21] A. Sabata, W.J. van Ooij, H.K. Yasuda, *Surf. Interface Anal.* 20 (1993) 845.
- [22] <http://ece-www.colorado.edu/~bart/book/ellipstb.htm> (accessed June 13, 2007).
- [23] M. Ray, G. McGuire, R.A. Sailer, D.L. Schulz, unpublished results.
- [24] A.M. Simoes, D. Battocchi, D.E. Tallman, G.P. Bierwagen, *Corros. Sci.* 49 (2007) 3838.

Durable Hybrid Coatings

Final Technical Report 2008

ITC Investigators

Brian D. Schultz and Gary E. McGuire



ITC

International Technology Center

8100-120 Brownleigh Dr.
Raleigh, NC 27617
ph: (919) 881-0500
fax: (919) 881-0440

This report details the work that was undertaken to determine the feasibility of using over-voltage potentials in atmospheric pressure dielectric barrier discharge plasma technology as a means of depositing hard coatings at atmospheric pressure conditions without the use of secondary gases like helium to sustain the glow discharge. The hard coating of interest was a SiC based film from a precursor gas mixture of 2% trimethylsilane ($\text{SiH}(\text{CH}_3)_3$) in a balance of molecular nitrogen (N_2).

Experimental Setup:

Creating an over-voltage potential prior to breakdown at atmospheric pressures enhances the energy of the electrons in the gas phase by providing a large electric field with which to accelerate the particles in the plasma phase. Because an atmospheric pressure plasma is highly conductive, its generation causes any voltage difference applied across the electrodes to quickly equilibrate. A dielectric barrier is used to disperse the charge transfer during the onset of plasma formation and to prevent thermal arcs from forming and shorting the electrodes. The discharge between two electrodes with a dielectric barrier allows current to flow, but the surface of the dielectric quickly begins to charge and eventually the electric field across the plasma region becomes too low to sustain the plasma. As such the charge on the dielectric must be bled off before the cycle is initiated again. In order to achieve a large electric field gradient across the electrodes, a fast voltage rise time is required to establish the desired overvoltage potentials before the onset of ionization occurs in the gas to be broken down. The generation of overvoltage potentials in atmospheric plasmas for the deposition of thin films generally requires the generation of a high voltage (22-25kV) pulse with a rise time on the order of 25ns or less; although the exact rise times vary by a small degree depending on the ease of which the introduced gas ionizes.

Generation of large quantities of energetic electrons and reactive ion species within a relatively high deposition pressure environment was anticipated to produce decent quality films with high growth rates. The frequent gas phase collisions keep the plasma temperature low. The electron energy in the plasma is proportional to their acceleration between collisions and inversely to the rate of collisions. The acceleration is determined by the magnitude of electric field and the electron collision frequency is proportional to the mean free path and ionization cross-sections at a given pressure. One of the problems of an atmospheric plasma that was encountered in this program, is that although the number of excitations created by the plasma produce large numbers of excited species, the large number of neutral molecular species and short mean free path lengths in the gas make multiple collision reaction pathways less probabilistic.

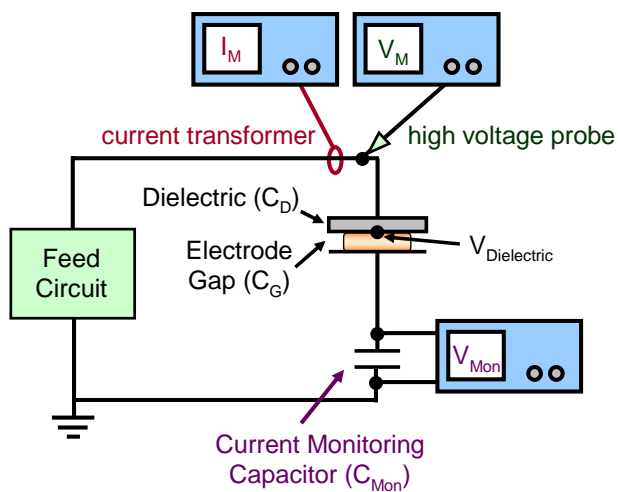


Figure 1 – Schematic drawing of the electrical probes used to monitor the characteristics of each pulse generated from the atmospheric dielectric barrier plasma deposition system.

Monitoring of the applied voltage and charge transfer are critical to providing real time diagnostics of the plasma as well as ensuring reproducibility between multiple runs. The voltage is measured at the top of the chamber with a 1000:1 high voltage probe and the current drawn by the discharge is measured by a 0.1 V/A transformer coil on the input line. Charge transfer is measured using a secondary capacitor on the low voltage electrode to integrate the current passing through the plasma. All of these connections are measured using a series of oscilloscopes. A schematic of the basic electrical monitoring is shown in Fig 1. The custom feed circuit developed by ITC for the generation of fast rise time high voltage pulses is capable of producing pulses at a rate up to 200 Hz with current peaks in excess of a kiloampere.

One of the principle problems identified in the early going of the program was the control of gas phase composition under atmospheric conditions. Oxygen and moisture contamination were considered to pose large problems and a chamber capable of being pumped and purged prior to growth was determined to be a requirement for reproducible growths. However, the large voltages required to achieve the necessary over-voltage condition also required either a significant amount of spacing between the electrode and chamber walls for traditional metal chambers or non conductive deposition chamber. As a first approach, a glass reaction vessel was used to house the electrodes and confine the deposition region while aluminum flanges were machined and sealed to the vessel with viton o-rings to provide the necessary gas and electrical connections. The bottom-most electrode was built with a metal sealed ceramic heater to provide temperature control and the electrode itself had a hole milled into its center to and a thermocouple probe was inserted for good thermal contact and measurements. The chamber is pictured in Figure 2.

The prototype pulser and chamber were built with an open design to allow access to the primary control circuitry and as a result the individual components are not heavily shielded electrically. During the initial deposition testing of the system it was determined that the fast voltage rise time and subsequent current peak produced enough electromagnetic radiation to cause problems with the surrounding electronics including flow meters, thermocouple meters and oscilloscopes. As a result, a large conductive electrical enclosure was built around the pulse and chamber and given a good earth ground to provide the necessary protection to the surrounding equipment. Figure 3 contains a picture of the full system built during the course of this program and a schematic representation showing the gas feed lines, exhaust lines, and valves. An aluminum box was constructed around the pulsing system and chamber, and a copper plate was used as the primary grounding plane. A variac was used to adjust the temperature of the ceramic heater in the reaction vessel. A separate N₂ line was plumbed into the system to enable it to be purged with



Figure 2 – Glass reaction vessel for the dielectric barrier plasma deposition of hard coatings

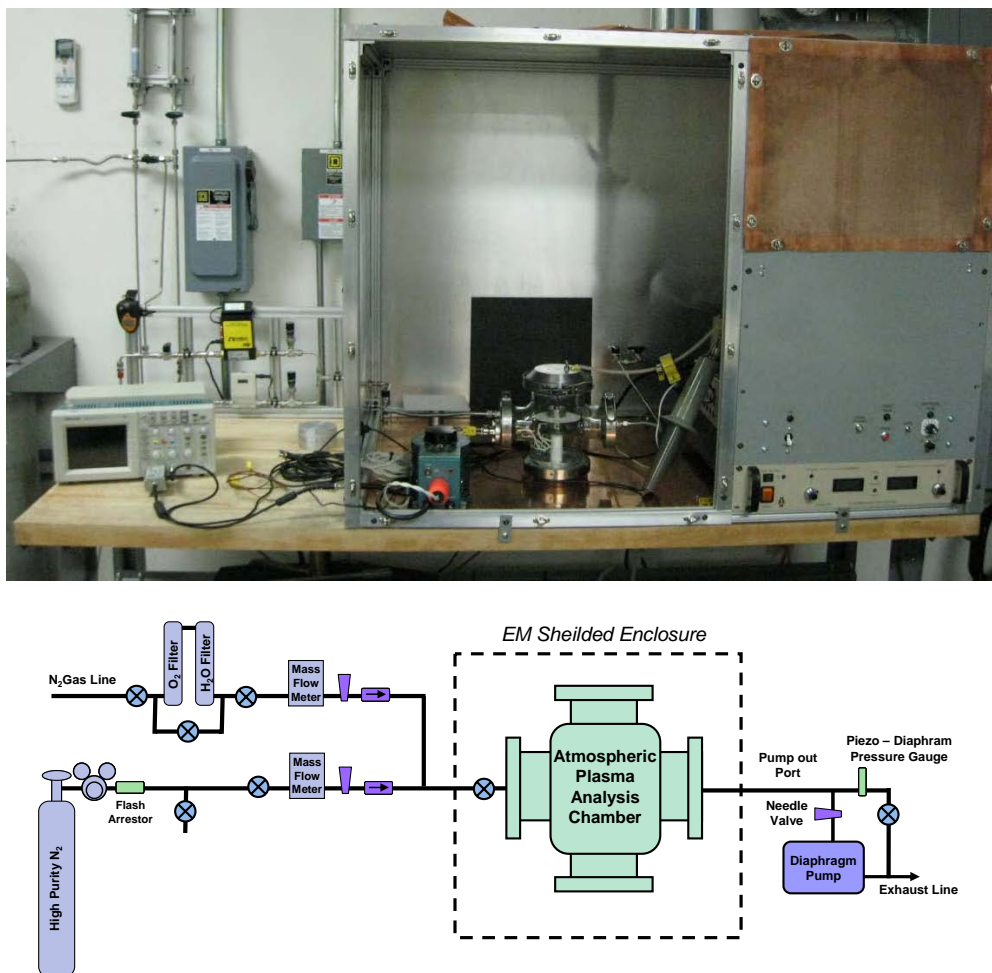


Figure 3: Photo and schematic of the deposition system including the custom pulser electronics, the gas delivery and pumping lines, and the electrical enclosure.

clean gas prior to and following growth. A piezo-diaphragm pressure gauge was used to measure the pressure (1-1000 Torr) and a diaphragm pump was used to purge the chamber of gas before and after growth. Stainless steel lines were used to supply all gases and were run to the pump input on the exhaust end. The internal electrodes were made out of stainless steel, alumina ceramics and insulating beads. The connections to the chamber for power and thermocouple feedthroughs were done with standard KF flanges and o-rings and the gas line connections were 1/8" NPT fittings. The electrode diameters were 1.5" (11.4 cm²), the dielectric ceramic was adhered to the top electrode, and the gap was adjusted to ~2mm for deposition.

Thin Film Growth and Characterization:

As a means of monitoring the plasma emission, optical emission spectroscopy was employed (OES). Although OES is only sensitive to the most common relaxation mechanisms, it provides a means of monitoring the conditions of the plasma. For example, when peaks are detected in

the range of 200nm – 300nm, it is an indication of NO_x emissions and signals the presence of significant quantities of oxygen or moisture in the plasma. The recorded spectrum in Figure 4 was acquired from an N₂ plasma emission. The only emissions recorded by the spectrometer were the second positive emissions of molecular nitrogen. The multiple peaks correspond to the different vibrational modes of the molecule. The first plot is a full linear spectrum recorded from the spectrometer and the second plot is a log plot of a narrower spectral region. The experimentally measured peak positions and the corresponding vibrational transisions are labeled on the second plot.

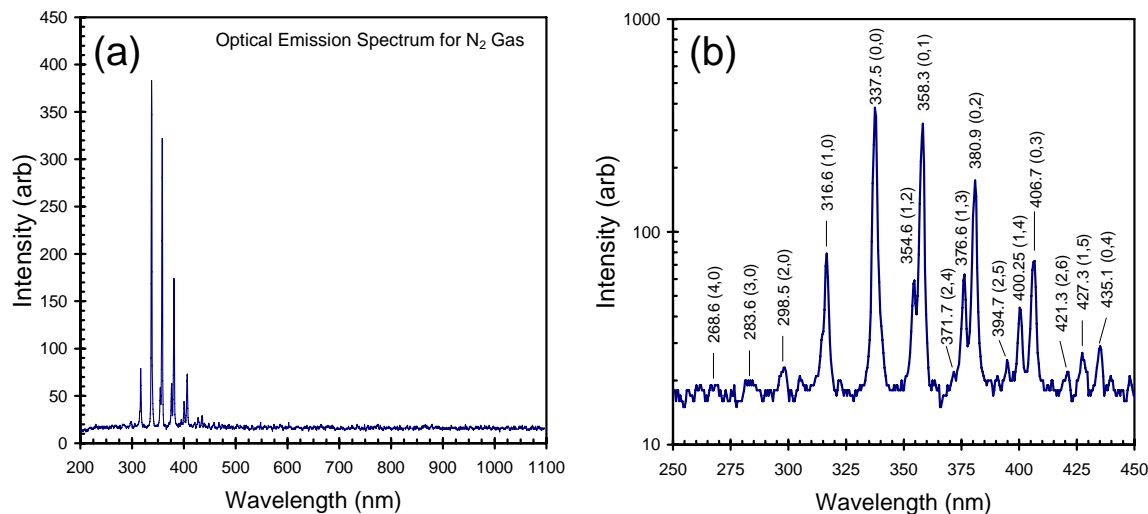


Figure 4: Optical emission spectroscopy of a standard N₂ plasma discharge in the dielectric barrier discharge plasma showing (a) full spectral range and (b) a close up region showing the peaks of the N₂ second positive excitations as measured by the spectrometer.

Originally it was proposed to perform a set of growth experiments covering a wide range of parameters including the growth temperature and the applied voltage and to perform the growths on Aluminum 1”×1” polished substrates. The first few growths were performed on the Al substrates, but the roughness and weight of the substrates made characterization of the deposited films by ellipsometry, XRD, and XPS rather difficult. Consequently, the substrate material was switched to silicon in order to characterize the films and define the optimum growth regime.

The standard growth procedure was followed for all samples. A silicon wafer was diced into a number of small pieces about 2 cm × 2 cm and used as test specimens. Each sample was loaded and secured to the bottom electrode. The chamber was pumped out using a diaphragm pump to a few torr and then vented with nitrogen gas which was filtered for moisture and oxygen. A needle valve was used to throttle the pumping rate to match the feed rate of ~200sccm. The substrate heater was raised to temperature. The nitrogen gas was then closed off and the 2% trimethylsilane was fed into the chamber and the throttle valve was again adjusted to keep the pressure at about 750 torr. The plasma source was then initiated and run for the desired length of time. After growth the trimethylsilane valve was closed and the N₂ feed valve was open. The substrate heater was cooled and the chamber was pumped and purged a couple times to remove any lingering traces of trimethylsilane from the chamber.



The effect of growth temperature was determined to play a significant role in the growth of the films. The system was designed to allow growth up to 250°C, and initial growths showed that growth temperatures in excess of 150°C were needed to produce a “hard film”. Figure 5 shows a film that was deposited at room temperature for 30 minutes using a flow rate of ~200sccm. Visual inspection of the film was sufficient to determine that the desired hard coating had not been deposited, instead it appears that pools of a polymeric solid conglomerated across the surface of the wafer. Growths conducted at 100°C also showed similar behavior over a good fraction of the wafer, although signs of a hard film were seen over parts of the samples. By the time the growth temperature began to approach 200°C, the films began to become uniform and coat the wafers in question. The result of a number of growths was that the temperature of the substrate needed to be 200°C or greater to produce a film of sufficient quality to enable testing.

Besides temperature, the over-voltage conditions also were found to only be favorable in a narrow range. As part of the on-going work at ITC to better understand the physics behind the operation of dielectric barrier plasmas under over-voltage conditions it was determined that there is a minimum voltage threshold that must be passed in order to sustain a uniform plasma discharge. Figure 6 contains a series of current traces for individual pulses measured in N₂ plasmas as function of the applied voltage to a 2mm gap at atmospheric pressure and operating at 100 pulses per second (pps). The first plot shows that the area under the current peak grows as the applied over voltage is increased from 14eV to 22eV and then begins to level off. The second plot is a cumulative integration of the current curves as a function of time and represents

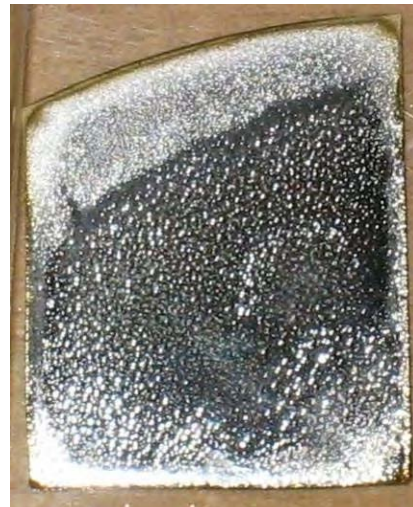


Figure 5: Optical photograph of a coating deposited at 25°C.

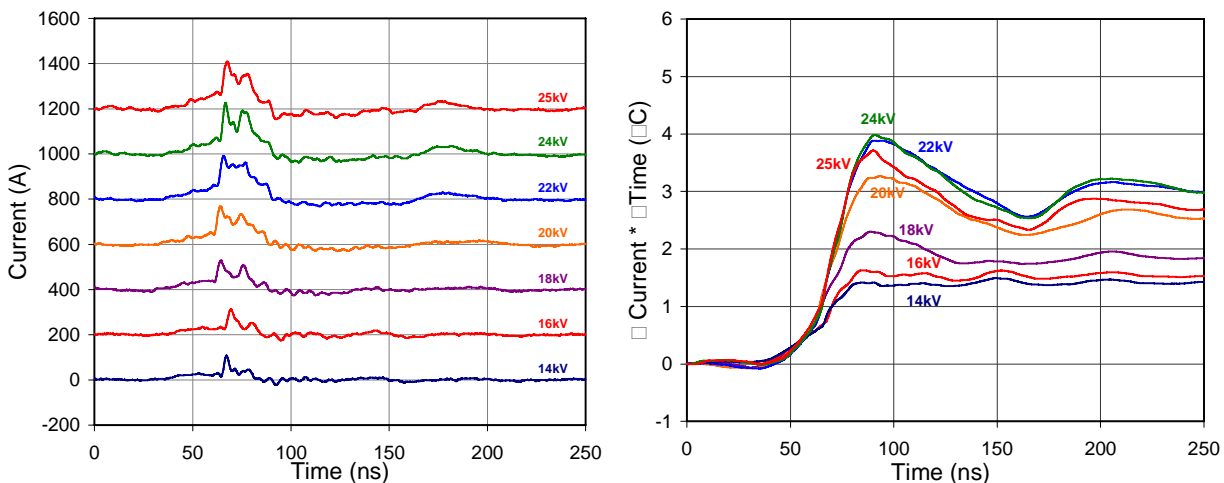


Figure 6: The first figure shows a series of current traces acquired at 100pps, atmospheric pressure, in N₂, with a 2mm gap at a series of applied over-voltages. The second figure shows the cumulative integration curves of the current traces in the first graph and represents the amount of charge transfer as a function of applied over-voltage.

the amount of charge transferred through the plasma. It is expected that the total charge transfer should rise linearly with gap voltage, but the observed dependence does not meet this expectation. The reason for this discrepancy is that it has been determined if the applied over-voltage is not large enough to allow a plasma pulse to reach a pseudo steady-state in size, the plasma does not uniformly cover the full area of the electrodes. Therefore, for a 2mm gap in N₂, an over-voltage of 22kV or greater should be applied. This set a lower limit on the voltages that could be attempted and ultimately the compactness of the glass chamber design limited the upper range of the applied voltages to no more than 24-25kV.

With these limitations in temperature and pressure in place the quality of the films grown within this window were investigated. The current and voltage traces collected from the oscilloscope are plotted in Figure 7 below for a sample grown at 220°C, with a 200sccm flow rate, a 2mm gap, 23kV of applied voltage, and acquired at 750 Torr. The scope traces show a pretty wide current pulse about 185A in magnitude and over 25ns in width. These voltage measurements were acquired at the chamber input. The traces were extremely stable and reproducible during growth. The oscillations in the current peak are due to LCR effects and are believed to be related to the impedance of the plasma gap and the dielectric barrier in the electric circuit.

Figure 8 contains a plot of the same current peak along with a plot of its cumulative integrated area (or time dependent total charge transfer trace). The area under the curve corresponds to approximately 2.6 μC of charge transfer in the plasma with every pulse. The second picture in Figure 8 is an image of the oscilloscope trace taken across the charge monitoring capacitor in the test circuit. The circuit has been designed so that the height of the trace is proportional to the charge transfer of each individual pulse and calibrated such that (1 V = 1 μC). Correspondingly this trace shows 2.6 μC, which is the same result obtained from the integration of the current curve. The advantage of the charge monitor trace is that it allows real time monitoring of the charge transfer with each pulse. Similar to the current and voltage traces, these traces are highly reproducible even at frequencies of 100 Hz and greater.

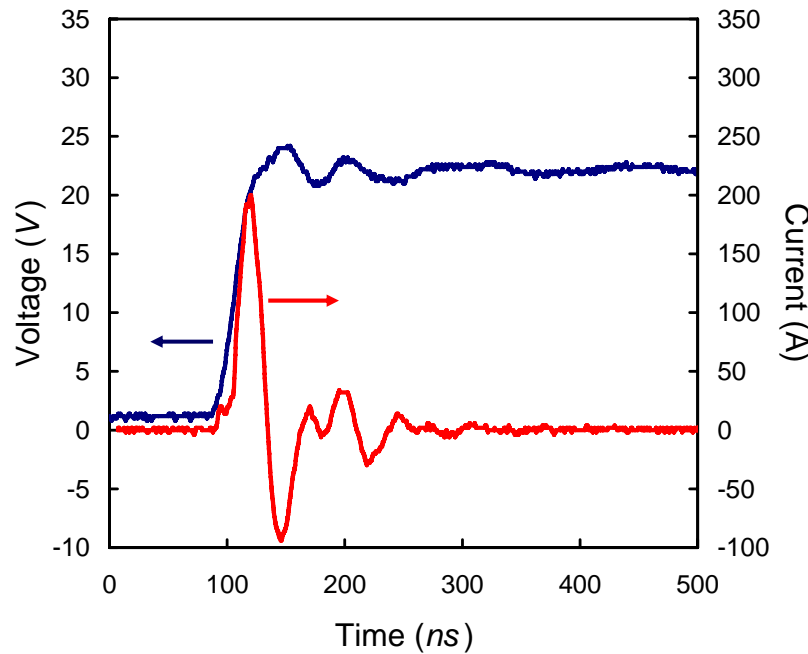


Figure 7: A current and voltage trace for a sample grown at 220°C, with a 200sccm flow rate, a 2mm gap, 23kV of applied voltage, and acquired at 750 Torr.

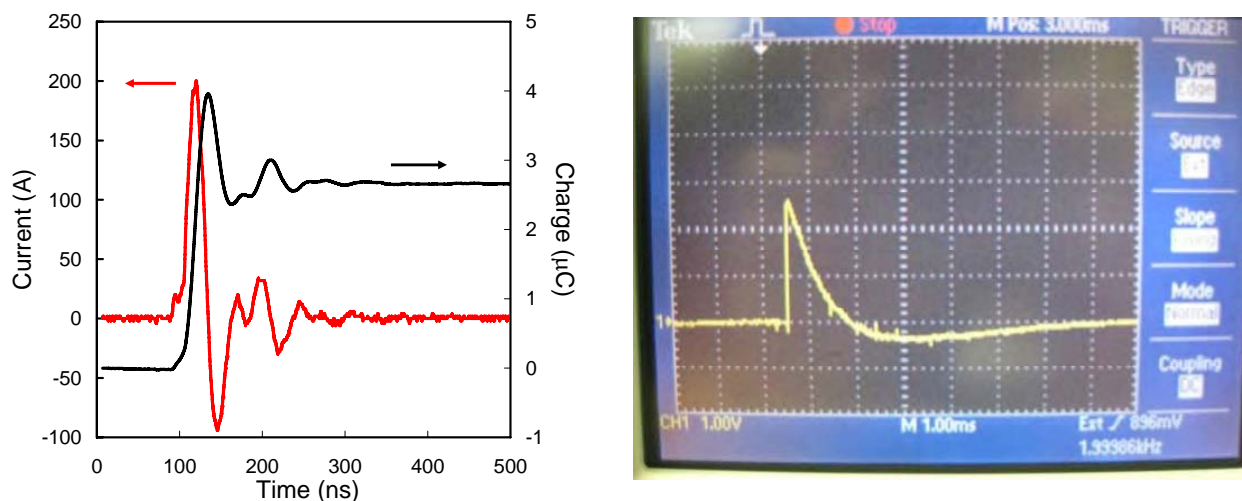


Figure 8: The first plot shows the current peak from Figure 7 along with a plot of its cumulative integrated area (or time dependent total charge transfer trace). The second plot is a real-time trace of the charge transfer circuit whereby the peak of the trace corresponds to the total charge transfer of an individual pulse. (1 V = 1 μ C and 1 V/division)

Following growth a number of tools were used to examine the quality of the films. The first technique that was employed was ellipsometry, which was used primarily to determine the thickness of the films. This technique is the one that benefited the most from having a silicon wafer as the substrate because the flatness of the silicon wafer provided a means of growing flat films and provided an extremely well defined interface for modeling. Figure 9 contains the experimental results from a sample grown at 220°C at three angles of incident (grey lines) and the corresponding fits of the results from a two layer model (colored curves). The experimental data did not fit well with standard SiC material parameters and in fact could be better fit with SiO₂ optical parameters. In the end a generic Cauchy model was used to fit the index of refraction as a function of wavelength and it

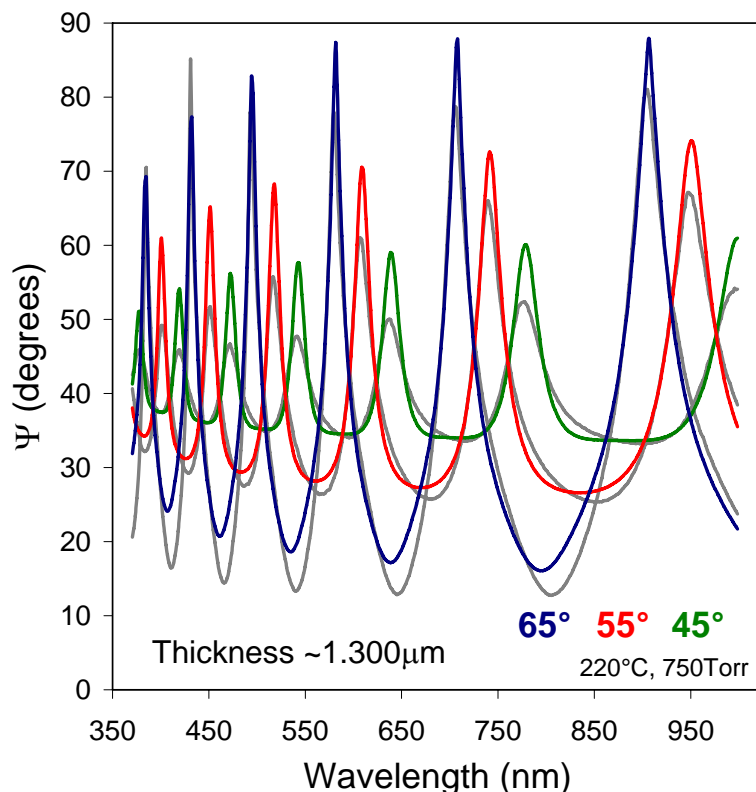


Figure 9: Ellipsometry data taken at three different incident angles from a sample grown at 220°C. The grey curves represent the actual data and the colored curves represent a first order Cauchy fit.

was found the average index of refraction was around 1.55. The estimated thickness of the film was 1300nm or 1.3 μ m which based on 30 minutes of growth indicates a growth rate of 2.6 μ m/hr. The standard Cauchy parameters used to obtain the fit were: $A = 1.51$, $B = 0.0038$, $C = 0.000147$). These results are fairly typical of all films grown above 200°C.

X-ray diffraction was used to look at the out of plane ordering of the higher temperature grown films using theta-2 theta scans but no significant degree of ordering was detected outside of the substrate peaks. The composition of the films was examined using x-ray photoemission spectroscopy (XPS). For all samples, an initial sample was acquired before cleaning and a second spectrum was acquired after Ar sputter cleaning. Figure 10 contains a full scan XPS spectrum for a sample grown at 220°C after sputter annealing. Included on the plot are the core levels and the Auger transitions that produced the individual peaks on the spectrum. Five elemental components were detected from the films: Silicon, Nitrogen, Carbon, Oxygen, and Argon. The Argon was not present in the pre-sputtered films and is clearly an artifact of the cleaning process. The remaining peaks are all contained in the as grown film. The highlighted peaks are the peaks that were used to estimate the composition of the films based on the count rates for each core level and ionization cross section of the core levels in at a 90° detection angle.

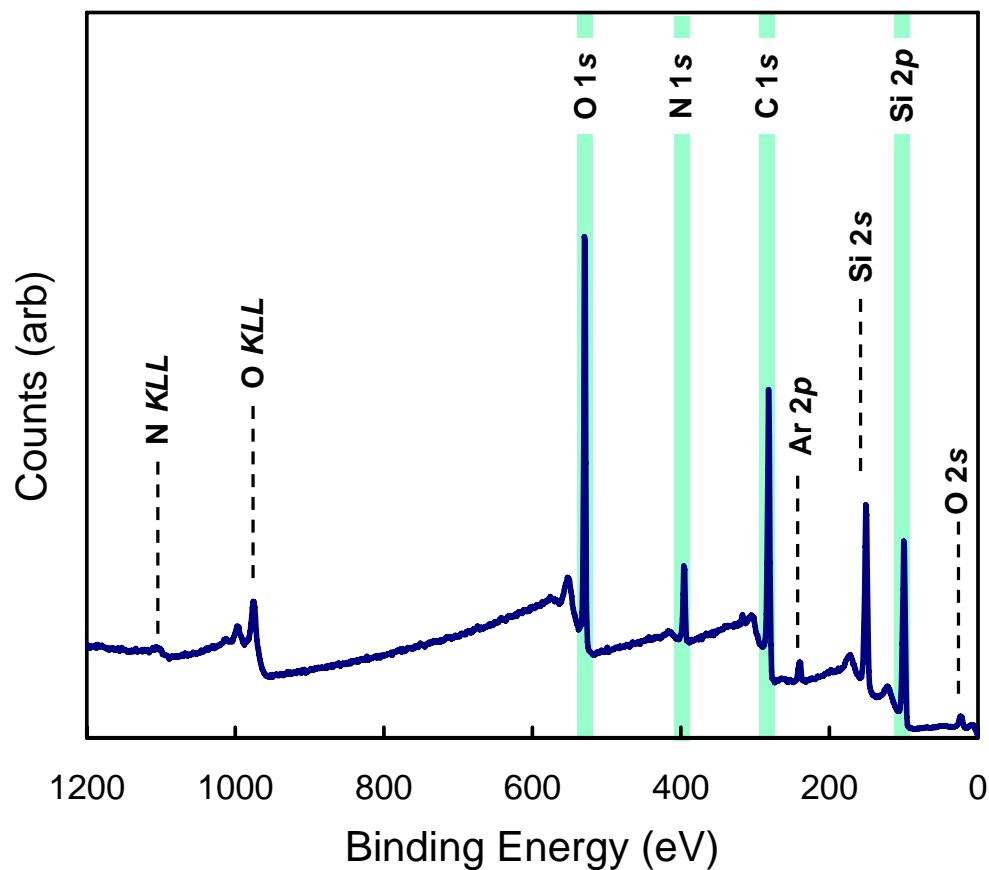


Figure 10: XPS spectrum acquired after an Ar sputter cleaning of the sample surface showing the presence of four elements in the as grown film (Silicon, Carbon, Nitrogen, and Oxygen). The highlighted core levels represent the peaks used to estimate the composition of the film.



Table 1 contains a table of the peak areas and the estimated composition of the film based on these areas and the sensitivity factors of each core level. The table shows that the two most prominent elements in the film are in fact silicon and carbon. However, there is a significant amount of oxygen in the films despite the attempts to minimize the oxygen content. The prominent source of the oxygen is not known at this point.

It is possible that it is from water vapor stuck to the walls of the chamber during venting (although N₂ purges are used to minimize the effect), it is possible the lack of vacuum on the flanges does not provide sufficient compression of the o-ring seals at atmospheric pressure resulting in an easier diffusion pathway for oxygen to diffuse in, or it may even be derived from the dielectric barrier materials used. The fact that the carbon composition is higher than the remaining components also suggests that the film may contain some degree of hydrogen incorporation as well. Unfortunately, XPS has no sensitivity to hydrogen and thus far the incorporation of hydrogen cannot be proved or disproved. Higher resolution scans of the individual components showed no signs of significant peak splitting which made further deconvolution of the peaks difficult and suggests that the bonding within the film is fairly homogeneous. It would be expected that C-H_x and C-Si bonding would produce detectable shifts in the core-level of C, but none were detected. These compositional findings seemed to be repeated nearly identically for films grown at slightly higher temperature (up to 290°C), and at different growth thicknesses. FTIR should be able to provide additional insights into the atomic bonding of the carbon films especially in comparison to films grown under PECVD conditions.

Conclusions and Deliverables:

The program established a means of depositing SiC_x based films via dielectric barrier plasma discharge technologies utilizing an over-voltage potential to create a uniform glow discharge in the deposition region. Films have been deposited on standard Si(001) substrates and on Al substrates provided by NDSU at the most ideal growth conditions using a trimethylsilane precursor in N₂. The limitations in the degree of overvoltage required for a uniform glow discharge and the substrate temperatures required to promote surface desorption and bonding have limited the parameters currently available for tuning the growth and adjusting composition. However, despite the limited parameter space available, films with growth rates on the order of 2.6 μm/h have been repeatedly grown with compositions comprised predominantly of Si and C with moderate levels of oxygen and a few percent nitrogen. Final samples deposited within this regime and included in the characterization above are being sent to NDSU on Al substrates for further testing.

Table 1: XPS core level areas and estimated film composition based on sensitivity factors and assuming a homogeneous film.

Core Level	BE (eV)	Rel Counts	Atomic %
O 1s	528.9	25,000	21.1 %
C 1s	281.9	18,420	43.7 %
N 1s	395.9	5,170	7.1 %
Si 2p	99.9	13,970	28.1 %



Contents lists available at ScienceDirect

Surface & Coatings Technology

journal homepage: www.elsevier.com/locate/surfcoat

Deposition of transparent conductive indium oxide by atmospheric-pressure plasma jet

Robert A. Sailer, Andrew Wagner, Chris Schmit, Natalie Klaverkamp, Douglas L. Schulz*

Center for Nanoscale Science and Engineering at North Dakota State University, 1805 NDSU Research Park Drive, Fargo ND 58102, United States

ARTICLE INFO

Available online xxxx

Keywords:
Indium
Oxide
Atmospheric
Pressure
Plasma
Jet

ABSTRACT

Indium (III) beta-diketonate complexes were employed as the solid precursor sources in the atmospheric-pressure plasma chemical vapor deposition of indium oxide films using He carrier gas, O₂ reactant gas and growth temperatures from 25 to 250 °C. Ellipsometry and X-ray reflectivity showed that the films varied in thicknesses from 40 to 70 nm over the 30 cm² deposition growth area for a 12 min duty cycle. The as-deposited films exhibit transmittance in excess of 90% over the visible spectrum while maintaining resistivity on the order of 10⁻² Ω cm. Improved electrical properties (i.e., ρ<10⁻³ Ω cm) were observed after thermal treatment (T~200 °C) in a controlled gas ambient tube furnace.

© 2008 Elsevier B.V. All rights reserved.

1. Introduction

Transparent conductive oxides (TCO) have found broad application over the past few decades in flat panel displays, photovoltaics and other electronic applications [1]. Traditionally, TCO deposition has been performed at moderate temperature using vacuum-based growth systems although some efforts have been made to grow these films at temperatures compatible with inexpensive polymer substrates (e.g., Lexan and Mylar) [2–4]. The goal of this project has been to demonstrate a system capable of depositing durable conductive transparent oxides at relatively low temperature and atmospheric pressure.

The target application for this study is aircraft canopies where a conductive coating is used to reduce the radar cross section of the aircraft [5]. Aviator line of sight demands this coating must also be transparent. While the as-received canopies exhibit excellent properties, in-field damage (e.g., scratching by flight suit buckles, foreign object impact damage, etc.) significantly alters the utility of the system. The current repair strategy consists of a metal-filled epoxy that gives the appropriate stealth but hinders the aviator's vision. As these airplane canopies are typically replaced when even slightly damaged, this leads to a significant financial and logistical challenge for the US military.

The canopies used by the military are polycarbonate-based laminate structures where the TCO is typically prepared by a sputtering process. The goal of this research project is to define a materials deposition route to transparent conducting oxides that is amenable to in-field repair of aircraft canopies. We envision this repair system to be similar to automobile body work whereby the damaged

area would first be isolated (e.g., with tape), then the surface prepared (e.g., wet sanding) followed by coating the damaged area with the TCO material. While other factors would need to be addressed prior to deployment (e.g., refraction matching of the TCO, the addition of an abrasion-resistance functionality, etc.), the first phase of the project is the development of a process that produces a TCO with a sheet resistance of 10 Ω/□ with 85% transmittance at 450 nm. The application of atmospheric-pressure plasma jet deposition toward these goals is the subject of this paper.

2. Experimental

The metal complexes used in this study exhibited a slight propensity to ligand hydrolysis which leads to oligomerization and a changing vapor pressure during sublimation. As such, beta-diketonates were isolated and handled under an inert nitrogen gas environment using standard Schlenk techniques. Indium (III) acetylacetone (In(acac)₃, 99.99%) was purchased from Sigma-Aldrich and twice sublimed (140–150 °C/20–50 mTorr) giving a colorless solid (mp. 189 °C) that condensed on the cold finger of a Standard Dailey sublimer (ChemGlass).

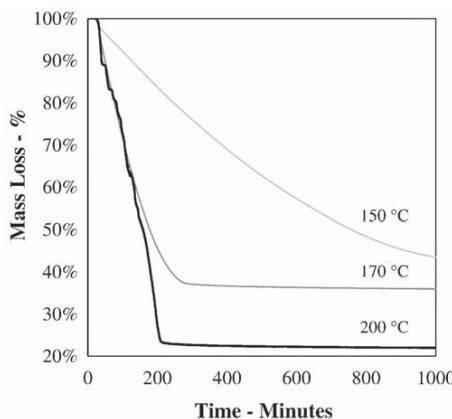
Indium oxide films were deposited using a Surfex Atomflow™ 225D atmospheric plasma system described elsewhere [6,7]. The variables investigated in this work included substrate temperature and the oxygen level in the plasma gas with plasma power fixed at 110 W. The distance of the plasma shower head to the substrate was held constant at 2 mm. Uniform films were produced by rastering the plasma source across the substrate in a serpentine pattern. The use of a solid precursor led to significant equipment modification in the design of a precursor delivery system.

As the precursor is a solid with rather low vapor pressure, a relatively high temperature (i.e., 185 °C) was required to sublime

Q1

* Corresponding author.

E-mail address: doug.schulz@ndsu.edu (D.L. Schulz).

**Fig. 1.** TGA of $\text{In}(\text{acac})_3$ under isothermal conditions and N_2 flow.

sufficient precursor flux to allow practical deposition rates [8]. Numerous challenges were encountered during the initial stages of this research. There was a propensity for the metal complexes to condense at any "cold spot" in the system. This required meticulous attention to ensure that all delivery lines were at or above the temperature of the precursor bubbler. Eventually the precursor bubbler and associated valve components were located inside a small oven which afforded the desired temperature control and minimized condensation in the system. Precursor delivery lines outside the oven were minimized in length and wrapped in resistance heaters to preclude condensation. This arrangement allowed for easy access to the precursor bubbler and excellent control of the overall system with minimum downtime for maintenance.

The Atomflow system requires a 5 slpm precursor flow to ensure proper mixing of the precursor vapor in the plasma afterglow region of the plasma source. In order to accomplish this, two mass flow controllers were used on each precursor delivery line. A bypass flow was designed to allow for up to 5 slpm. A smaller flow, generally on the order of 0.5 slpm, was directed through the bubbler where the precursor was entrained. The precursor gas was then mixed into the bypass flow via a stainless steel tee before passing into the plasma head. The distance between the precursor bubbler and the mixing tee was minimized as the higher gas flow tended to minimize condensation. All lines feeding the precursor bubbler were heated to control the vapor characteristics of the precursor used.

Substrates used in this study consisted of glass microscope slides (38 mm × 76 mm) and small pieces of silicon wafer (~15 mm × ~20 mm). Prior to film growth, substrates were cleaned via a piranha etch and stored in isopropyl alcohol. Immediately prior to use, the substrate was removed from the isopropyl container and blown dry with nitrogen. The substrates were treated with an oxygen plasma equivalent to the deposition conditions but without the precursor flow to clean and condition the surface prior to film deposition.

Prior to the deposition process, the precursor bubbler was first loaded with $\text{In}(\text{acac})_3$ and then connected into the gas/mixed-flow lines. The system was brought up to temperature by preheating the mixed-flow line, gas flow lines, stage, sample bubbler and substrate. The plasma head was preheated by powering on until it reached the steady state. After the precursor delivery system temperature had stabilized, the valves to the precursor bubbler were opened and the gas flow was allowed to enter the plasma head. Deposition was initiated by rastering the plasma head over the surface at a rate of 14 mm/s while indexing the translation stage in 2 mm increments at the end of each pass. During the deposition, the plasma power, temperature, and gas flows were monitored until the process was completed. Upon completion of the X-Y motion, the bypass gas to the precursor bubbler was closed, power to the plasma was turned off and the gas flows ceased.

Film thickness was determined by ellipsometry with a J.A. Woollam WVASE32 M-88 using the full spectrum of the ellipsometer (281.6 nm to 765.4 nm). Film thickness was also determined via X-ray reflectivity using a Bruker Discover D-8 operated in grazing incidence mode. The Bruker D-8 was also used for phase identification but all films were amorphous as deposited. UV-Vis spectroscopy was performed using a Varian Cary 5000 UV-Vis-NIR spectrophotometer in transmittance mode with a scan range from 200 to 800 nm. A scan of a bare microslide was used as a background signal that was subtracted from experimental samples with a scanning rate of 600 nm/min and an interval of 0.1 nm. X-ray photoelectron spectroscopy (XPS) of the indium oxide films was performed using an SSX-100 system (Surface Science Instruments) equipped with a monochromated Al K α X-ray source, a hemispherical sector analyzer and a resistive anode detector spectroscopy at the University of Minnesota IT Characterization Facility. The samples were mounted on sample stages using double-sided carbon tapes and the X-ray power was 200 W with a spot size of about $1 \times 1 \text{ mm}^2$. Scanning electron microscopy was performed using a JEOL JSM6300 at North Dakota State University.

Thermal treatments were realized using a Lindberg Furnace fitted with a fused silica tube. After each set of samples was loaded, the tube was purged with either nitrogen or forming gas (5% H_2 in N_2) until nine tube volumes of gas had passed through the apparatus at which point the gas flow was reduced to a trickle. Prior to thermal treatment, one indium oxide film on glass was scribed and cleaved in half to provide a sample for annealing in nitrogen and a sample for annealing in forming gas. Sheet resistance measurements were recorded after thermal treatment at 200 °C for 2 h in either N_2 or forming gas. The same sample was then treated in either N_2 or forming gas at 300 °C for 2 h and sheet resistance was characterized again. A final electrical characterization was performed after the same sample was treated in either N_2 or forming gas at 400 °C for 2 h.

Sample resistance was determined by using a Cascade Microtech C4S44/S four-point probe (Os tips) with a Keithly 2400 multimeter (4-wire). Multiple measurements were realized by dividing the 38 mm × 76 mm sample into a 25-point grid array consisting of 5 rows and 5 columns spaced 8 mm and 5 mm apart respectively. Resistance readings were then taken upon all of the grid points ensuring stabilization of the reading before moving to the next point.

Two different thermogravimetric analysis (TGA) methods were performed using a Dupont TA-951 TGA. Initially, standard temperature ramps were performed from ambient up to 400 °C at a heating rate of 10 °C/min in flowing nitrogen (10 sccm). Isothermal tests were also performed at several elevated temperatures. A sample size of 2–8 mg was used for all TGA runs with samples transferred from the glove box to the TGA as quickly as possible to avoid air exposure. The chemistry of the volatilization reactions was evaluated by TGA-MS using a TA instruments TGA951 connected to an HP5971 Mass Spectrometer through a heated (300 °C) open slot interface. The thermal profile consisted of room temperature to 600 °C at a heating rate of 10 °C/min and a He purge rate of 120 sccm.

3. Results and discussion

The standard TGA plots were used to determine the onset of volatilization of the precursor. The indium complex required a

Table 1
Electrical properties of indium oxide films deposited at various substrate temperatures

T_{dep} (°C)	R_{sheet} (Ω/\square)	Film thickness (nm)	ρ ($\Omega \text{ cm}$)
50	Out of range	NA	NA
100	Out of range	NA	NA
125	7.4E+09	54	1.8E+05
150	3.6E+08	49	8.0E+03
200	6.6E+03	62	1.9E-01
250	3.7E+03	51	8.6E-02

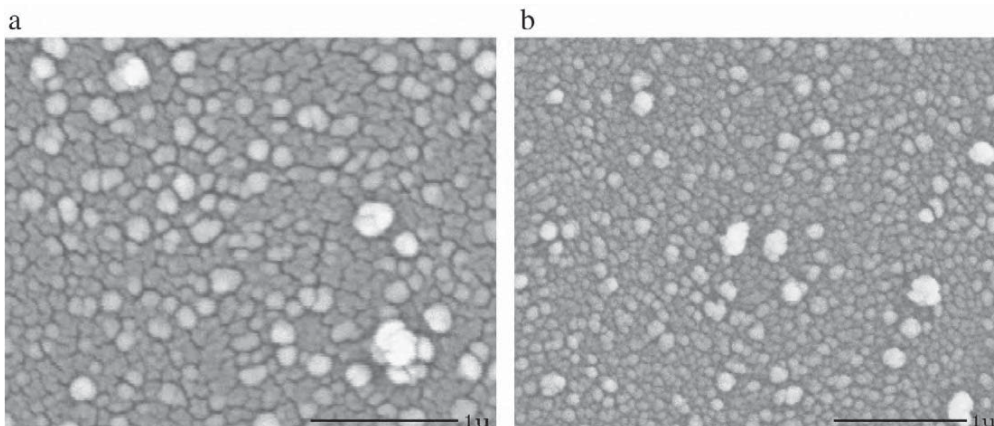


Fig. 2. SEM photos of two different indium oxide films prepared at 250 °C.

temperature of approximately 185 °C to realize appreciable volatilization. Once a sublimation temperature was estimated from the standard TGA runs, isothermal TGA was performed at 20 °C above and below the anticipated vaporization point (Fig. 1). It is interesting to note that the precursor did not volatilize completely at any of the test temperatures. This was, however, consistent with the presence of a residue remaining in the precursor bubbler after it is “emptied” of active precursor. Based on the TGA-MS analysis, little or no free ligand (i.e. acetylacetone, Hacac) is evolved as higher fragments indicative of the metal complexes are always observed with the free ligand fragments.

Indium oxide films were produced using various substrate temperatures (ambient to 250 °C) and oxygen flow rates (200–500 sccm). In general, the most significant factor in attaining reasonably conductive films was the substrate temperature. This is apparent in Table 1 where the sheet resistance begins to drop at a substrate temperature of roughly 125 °C and is minimized around 200 °C. It is interesting to note that transition to lower sheet resistance occurs at a temperature that is consistent with the amorphous to polycrystalline phase transition for indium oxide also around 200 °C [9]. XRD analysis of the films prepared at and above 200 °C showed no peaks which indicates that these films are comprised of nanocrystalline grains.

Film thickness for the indium oxide films was relatively constant between 50 and 65 nm (Table 1). Assuming a 100% dense film and knowing the precursor usage rate, these film thicknesses correlate roughly to a precursor deposition efficiency of 10%. The film thickness values were also used to calculate the resistivity of the samples in the temperature variation experiments (Table 1). The data for higher substrate temperature is encouraging with results reaching the $10^{-2} \Omega \text{ cm}$ range for an unintentionally-doped indium oxide film. Film composition was probed by XPS and a film that was deposited at 250 °C had an O/In ratio of 1.2 ± 0.1 where stoichiometric In_2O_3 would have a ratio of 1.33. A substantial C contamination (i.e., 15.3 at.%) was also observed and this C impurity may also have affected film conductivity in a deleterious manner.

The surface morphology of two different films prepared at 250 °C with 300 sccm O_2 flow and 110 W plasma power was probed by electron microscopy with SEM photographs shown in Fig. 2a and b, respectively. A granular surface is noted in these plan view pictures similar to indium tin oxide (ITO) films prepared by PECVD at 0.53 Torr (see Fig. 3 in Ref. [3]). Such morphology development was observed previously for films prepared at atmospheric pressure using spray deposition [10]. In that study, copper films around 350 nm in thickness were prepared by airbrush spraying liquid $\text{Cu}(\text{hfa})\text{VTMS}$ precursor onto glass and polyimide substrates heated to 230 °C. It is interesting to note that in addition to a similar film morphology (i.e., comparing Fig. 2 below with Fig. 1 from Ref. [10]), a marked change in conductivity was noted as a function of

temperature for both the indium oxide films in this study and the copper films in the cited study. It is reasonable to anticipate that the thermolytic reactions operative in these two studies may apply in general to atmospheric-pressure spray deposition as follows: the deposition temperature must be high enough to render the thermolysis leaving

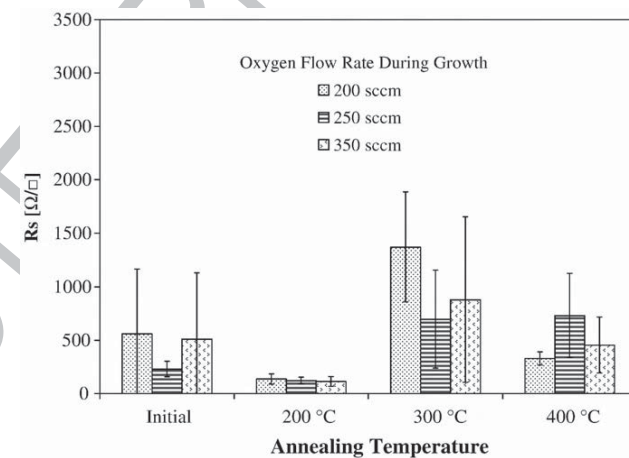


Fig. 3. Resistance of indium oxide films annealed in nitrogen gas.

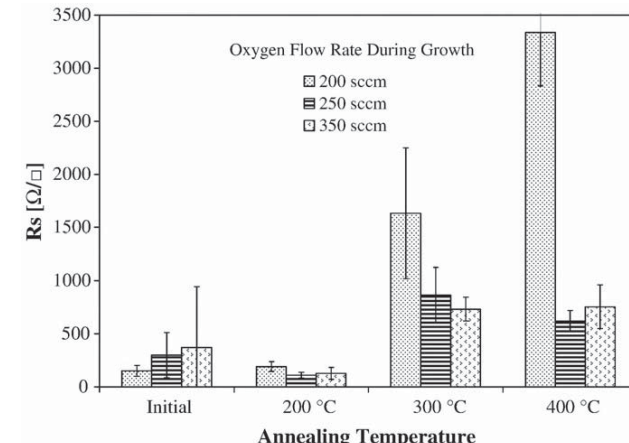


Fig. 4. Resistance of indium oxide films annealed in forming gas.

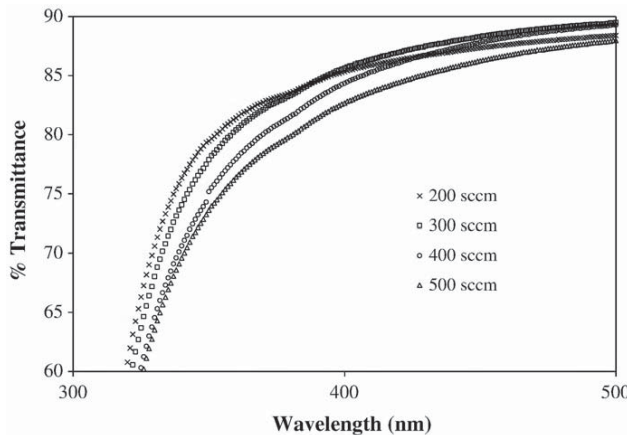


Fig. 5. UV-Vis spectra of indium oxide films deposited at various O_2 flow rates.

groups gaseous in order to observe good morphological development in the film. Therefore, by understanding the chemistry of the thermolytic transformation, a minimum deposition temperature might be estimated *a priori*.

Given the nature of conductivity in TCOs [1], samples were subjected to thermal treatments as a means of introducing oxygen vacancy and/or cation interstitial defects within the forbidden band. Resistance data for samples annealed in both N_2 (Fig. 3) and forming gas (Fig. 4) indicate a reduction in sheet resistance and in the variability observed over the face of the sample at the initial annealing condition of 200 °C. While a slight reduction in the standard deviation of the resistance measurement was noted after the 200 °C treatment, the variance increased for higher annealing temperatures. In addition, higher temperature thermal treatments gave increased resistance as well. This effect may be partially explained by substrate outdiffusion effects whereby chemical species (e.g., metal cations) migrate from the glass substrate into the indium oxide film at higher temperatures thereby quenching the electronic carriers in the forbidden band.

While these films demonstrate reasonable conductivity, they also exhibit excellent optical transparency. UV-Vis spectra for the O_2 variation experiments are given in Fig. 5. Most samples demonstrate greater than 90% transmittance in the visible spectrum from 400–700 nm. Such transparency is a prerequisite for application of these materials as transparent conductors. It is likely that further attempts to improve the conductivity by introducing additional carriers (e.g., by addition of tin oxide) would tend to reduce this transmission. However,

given the metric of 85% transmittance at 450 nm, it is possible that further modifications to the film growth conditions and composition would allow the realization of films with good transparency while maintaining sheet resistance in the 10 Ω/\square range. Further study will be performed to allow the use of UV-Vis spectroscopy in the calculation of band gap and other optical properties.

4. Conclusions

In conclusion, conductive, highly transparent indium oxide films were deposited at moderate temperatures over glass and silicon substrates via atmospheric-pressure plasma jet deposition. Solid source beta-diketonate precursors are shown to be reasonable candidates for APP jet deposition but further modification to the chemical functionality may be required to tailor the thermolysis reactions. Future work will include the addition of a tin oxide precursor to allow the growth of ITO films.

Acknowledgements

This material is based on research sponsored by the Air Force Research Laboratory under agreement number FA8650-04-1-5045. The views and conclusions contained herein are those of the authors and should not be interpreted as necessarily representing the official policies or endorsements, either expressed or implied, of the Air Force Research Laboratory or the U.S. Government. The authors wish to thank Xuliang Dai for assistance with sublimations, Scott Payne for scanning electron microscopy characterization, Bing Luo and John C. Nelson for XPS and Kenny Anderson for arranging the TGA-MS measurements at Edison Analytical Labs.

References

- [1] E. Fortunato, D. Ginley, H. Hosono, D.C. Paine, MRS Bull. 32 (2007) 242.
- [2] J.H. Shin, S.H. Shin, J.I. Park, H.H. Kim, J. Appl. Phys. 89 (2001) 9.
- [3] Y.-S. Kim, Y.-C. Park, S.G. Ansari, B.-S. Lee, H.-K. Shin, Thin Solid Films 426 (2003) 124.
- [4] W.-N. Miao, X.-F. Li, Q. Zhang, L. Huang, Z.-J. Zhang, L. Zhang, X.-J. Yan, Thin Solid Films 500 (2006) 70.
- [5] H.S. Gurev, K. Bickling, Proc. SPIE 2262 (1994) 246.
- [6] M. Moravej, R.F. Hicks, Chem. Vap. Depos. 11 (2005) 469.
- [7] M.D. Barankin, E. Gonzalex, A.M. Ladwig, R.F. Hicks, Sol. Energy Mater. Sol. Cells 91 (2007) 924.
- [8] A. Churpita, Z. Hubicka, M. Cada, D. Chvostova, L. Soukup, L. Jastrabik, P. Ptacek, Surf. Coat. Technol. 174–175 (2003) 1059.
- [9] J.A.A. Williams, D.H. Lee, K.D. Vuong, E. Tenpas, V. Wu, R. Moss, R.A. Condrate, X.W. Wang, Proc. SPIE 2531 (1995) 333.
- [10] D.L. Schulz, C.J. Curtis, D.S. Ginley, Electrochim. Solid-State Lett. 4 (2001) C58.

CATHODIC PROTECTION OF AA 2024-T3 BY A MG-RICH PRIMER

Kerry N. Allahar, Dante Battocchi, Gordon P. Bierwagen
Department of Coatings and Polymeric Materials
North Dakota State University, Fargo, ND, 58105.

Séva Balbyshev
Center for Nanoscale Science & Engineering,
1805 NDSU Research Park Dr., Fargo, ND 58105.

ABSTRACT

Mg-rich primers are an alternate for Cr-rich primers that are currently used by the Air Force for the protection of aluminum structures. The magnesium pigments provide cathodic protection for the less active aluminum substrates and also provide a barrier type protection as the products from the Mg dissolution insulate the substrate from the environment. The cathodic protection is comparable to Zn-rich primers for steel substrates. Electrochemical impedance spectroscopic characterization of a Mg-rich primer and a standard Air Force urethane topcoat/Mg-rich primer system, both on AA 2024-T3 substrates, will be presented. The systems were exposed to constant immersion in dilute Harrison's solution. Embedded electrodes between the topcoat and primer were used to access the behavior of the Mg primer/substrate system while beneath the topcoat. Experimental results demonstrated the cathodic protection of the bare Mg-rich primer and the primer beneath a topcoat. Analysis of the EIS data by a Voigt element model was done to compare the behaviors of the bare primer and the primer beneath the topcoat. Interpretation of the data is intended to highlight the evolution of the electrochemical properties of the primer and topcoat/primer systems as the cathodic protection is reduced during the consumption of the Mg-rich pigments.

Keywords: Mg-rich primer, Cathodic protection, Embedded Sensors

INTRODUCTION

The prototype coating for the protection of aircraft structures made of aluminum alloys has been based on chromate pigments.^{1,2} There are environmental implications as there is leaching of the toxic chromate due to its solubility.³ Ongoing research into alternatives to the chromate based pigments is supported by Federal regulations introduced by the United States government that will curtail the use of chromate-based pigments.⁴ Proposed alternative inhibitors include vanadates, phosphates, molybdates, borates and silicates^{1,5-7}, however the commercial non-chromate inhibitor pigments are less effective in corrosion protection than the industrial standard of SrCrO_4 .⁷

Cathodic protection of coated aluminum alloys has been under investigation. An Al-Co-Ce metallic coating has been shown to provide cathodic protection as its open circuit potential is as much as 750 mV lower than that of AA 2024-T3 depending on the Al-Co-Ce alloy.^{8,9} Release of the Co^{2+} and Ce^{3+} ions from this metallic coating provides additional inhibition of the AA 2024-T3 corrosion. A Mg-rich primer has been shown to provide cathodic protection of aluminum structures.¹⁰⁻¹⁴ These primers provide cathodic protection due to the more active Mg particles compared to the Al substrate. Additionally a barrier-type protection results due to the insulation of the substrate from the environment by products of Mg hydroxide and hydroxy carbonate species that fill pores and voids.^{11,15,16} The applicability of Mg-rich primers has been demonstrated by using open circuit potential monitoring, potentiodynamic polarization, electrochemical impedance spectroscopy (EIS), scanning vibrating

electrode technique (SVET) and scanning electrochemical microscopy (SECM).¹⁰⁻¹⁴ Two and three time-constant equivalent circuit models have been used to interpret EIS data with the results indicating that the reduction of the coating resistance and charge-transfer resistance with immersion time in 0.1% wt. NaCl.¹¹

The cathodic and barrier protective modes of Mg-rich primers are similar to those that have been reported for Zn-rich primers on steel substrates.^{11,12} Electrochemical methods have been used to characterize the cathodic and barrier-type protection provided by Zn-rich primers using a sophisticated transmission-line mode.^{17,18} In this model parameters are attributed to the contact impedance between the particles, the impedance associated with the zinc dissolution, and the percolation resistance of the coating. The applicability of the transmission-line model for characterizing EIS data of Mg rich primers has been previously demonstrated where the model was used to analyze the EIS data associated with a primer on a gold substrate under immersion in dilute Harrison's solution (DHS).^{19,20} The consistency of the EIS data in the 1 mHz-100 kHz frequency with respect to Kramers-Kronig relationships determined by applying the measurement model technique²¹⁻²⁵ has been shown for the gold and aluminum substrates.

Results associated with electrochemical impedance spectroscopic experiments performed periodically on a Mg-rich primer immersed in DHS are presented here. Mg-rich primers would be used together with a topcoat where the topcoat would provide a barrier protection form the environment and the primer the cathodic protection. The EIS data of a topcoat/Mg-primer system (topcoat/primer) is presented here to demonstrate the influence of the topcoat. Embedded sensors were used to monitor the electrochemical behavior of the primer beneath the topcoat. Embedded sensors have been used to monitor in-situ the properties of a primer beneath a topcoat during Prohesion testing using electrochemical noise method experimentation.²⁶ Embedded sensors in two-layer coating systems have been used for coatings subjected to thermal cycling,^{27,28} for the monitoring of water uptake of a topcoat and primer simultaneously, and to determine the effect of moisture/humidity on the interlayer adhesion between a topcoat and a primer.²⁹⁻³¹

EXPERIMENTAL PROCEDURE

The Mg-rich primer was applied onto an AA 2024-T3 substrate that was supplied by Q-Panel, Cleveland, OH. The primer consisted of a 10 μm average-sized Mg particulate in a two-component epoxy of Epon 828 resin and Encamide 3164 crosslinker that was supplied by Resolution Performance Products, Houston TX. The Mg particulate was supplied by Eckagranelles of America, Louisville KY. The coating was formulated at 45% pigment volume concentration that was approximately equal to the critical pigment volume concentration. The primer was applied using a compressed air spray gun to a thickness of approximately 50 μm . A drying period in excess of three days was used. A standard Air Force topcoat was used which comprised of a low gloss polyurethane topcoat (Navy MIL-C-85285B 36473, Type I). The topcoat was also applied using a compressed air spray gun to a thickness of approximately 50 μm .

The embedded electrode was made from platinum leaves that were approximately 130 nm thin. Supported by tissue paper, the platinum leaf was cut into the designed sensor shape with the surface area of the sensor being 2.56 cm^2 and the width of each side 0.4 cm. A schematic diagram of the sensor is shown in Figure 1. The sensor was adhered to the primer with an epoxy adhesive after the primer had been applied and fully cured. A copper core electrical conducting wire was soldered onto the embedded electrode after the adhesive epoxy resin had been cured. An epoxy resin was used to seal the conducting joint with this epoxy given one day at room temperature to harden. The topcoat was applied with the sensor embedded between the layers.

The experimental apparatus included a Perspex cylinder cell that exposed a 7.07 cm² area of the primer. The cell was clamped to the coating with an O-ring between the cell and the coating that prevented leakage. Three-electrode electrochemical measurements were performed with the substrate, a saturated calomel electrode and an approximate 1 cm² Pt mesh as the working, reference, and counter electrodes, respectively. The electrolyte was dilute Harrison's Solution (DHS) which comprised of 0.35 wt.% (NH₄)₂SO₄ and 0.05 wt% NaCl in distilled water. A Gamry FAS2 potentiostat was used in conjunction with EIS300 software to conduct the experiments with both potentiostat and software supplied by Gamry Instruments Inc, Warminster, PA. EIS data were collected for the 100 kHz to 1 mHz frequency range with a 10 mV (rms) amplitude at 10 points per decade. The experimental procedure involved monitoring the systems under constant immersion in DHS by performing EIS experiments daily. A two-electrode configuration, as shown in Figure 2, was used for accessing the behavior of the primer beneath the topcoat where the sensor was the counter/reference electrode and the substrate was the working electrode.

RESULTS

Open Circuit Potential

The time dependence of the open circuit potential (E_{OC}) associated with the primer and topcoat/primer systems are shown in Figure 3. The E_{OC} values, as all the potentials reported here, are relative to a standard calomel reference electrode as well. Values of -1.6 V and -0.6 V have been reported for the E_{OC} for the Mg particulate and the aluminum substrate, respectively.¹² An E_{OC} value between -0.6 V and -1.6 V is interpreted as a mixed potential between the Mg particulate and the substrate. The E_{OC} values for both the primer and topcoat/primer systems increased monotonically with time. Increasing values of the E_{OC} represented a decrease in the cathodic protection provided by the Mg particulate. The E_{OC} value associated with the primer increased from -1.3 V to -1.0 V during the first 5 days and then from -1.0 V to -0.9 V over the next 5 days. The E_{OC} value increased from -0.9 V to -0.4 V over the next 5 days and then remained approximately at -0.4 V for the following 12 days. The E_{OC} associated with the topcoat/primer system increased from an initial value of -1.55 V to a value of -1.1 V over the first 5 days after which it increased to -0.9 V over the following 15 days. The E_{OC} value of the topcoat/primer system increased gradually from -0.9 V to -0.5 V from 20 days through 100 days after which it remained approximately at -0.5 V for the remaining immersion time.

The change in E_{OC} exhibited by the systems demonstrated the influence the topcoat has on the behavior of the Mg primer. The primer lost its cathodic protection over 15 days of immersion whereas the topcoat/primer system retained its protection until 105 days. The changes over the initial 5 days for both systems were similar, except that the E_{OC} for the topcoat/primer system started at a value of -1.5 V while the primer system started at -1.25 V after 1 day of immersion. After 5 days of immersion the E_{OC} of the primer continued to increase at a similar rate as the initial 5 days while the E_{OC} of the topcoat/primer system increased much more gradually. There was some disparity between the E_{OC} values associated with the systems after the loss of cathodic protection with the bare Mg primer having a value of -0.4 V while the topcoat/primer system a value of -0.5 V.

EIS Results

Impedance spectra for the 0.01 Hz to 100 kHz frequency range were measured for the systems daily. Bode representations of the spectra are shown in Figure 4 with immersion time as a parameter for the primer system. The change indicated by the E_{OC} over the initial 5 days for the primer system can also be seen in this figure. The Bode magnitude plot for day 1 included a region at the high frequency end that had a slope less than -1. Positive values for the imaginary component of the impedance at high frequencies are associated with the presence of instrument artifacts. The absence of a positive imaginary

component in the data in the high frequency range supported the assumption that the data at the high frequency end was free of instrument artifacts. The slope (absolute value) decreased as the frequency was reduced in the 10 Hz to 100 Hz region. The slope in the region less than 1 Hz was less than that observed for the high frequency region but there was no plateau region observable at the low frequency end. However, the trend in the data suggested that a low frequency plateau was being approached. The Bode magnitude plot for day 5 included a slope at the high frequency end also less than -1 but did not overlap the plot associated with day 1. The slope decreased as the frequency was reduced with there being an observable increase in the slope over the 1 Hz to 10 Hz region. The slope decreased at the low frequency end suggesting that a low frequency plateau was being approached. The Bode plots for days 10 through 28 overlapped. There was overlap with these days and day 5 in the high frequency end greater than 1000 Hz. In the 10 to 100 Hz region the magnitude of the data for these days was similar to that of day 5, but the trend in the data was different. In the region less than 1 Hz, the slope of the data was close to -1 and there was no observable approach to a low frequency plateau. The Bode phase angle plot for the primer highlighted the change in the EIS data with immersion time. The plot associated with day 5 was different than that of day 1 while it was similar to those associated with days 10 through 28.

Bode representations of the spectra are shown in Figure 5 with immersion time as a parameter for the topcoat/primer system. The Bode magnitude plot for day 1 included a region at the high frequency end that had a slope close to -1. The slope decreased as the frequency was reduced with the slope in the region less than 1 Hz approaching a plateau. The Bode magnitude plot for day 20 included a slope at the high frequency end also close to -1 but did not overlap the plot associated with day 1. The slope decreased as the frequency was reduced but there was no indication of a low frequency plateau being approached. The Bode plots for days 50 through 111 overlapped at the high frequency end for frequencies greater than 1000 Hz where the slope was close to -1. There was no overlap with days 1 and 20. The slopes for these data decreased as the frequency was reduced with there being no overlap in the 0.1 Hz to 200 Hz region. For frequencies less than 0.1 Hz, there was overlap among the data for these three days with there being no approach to a low frequency plateau. The Bode phase angle plot for the topcoat/primer shown in Figure 5 highlighted the change in the EIS data with immersion time. The plot associated with day 1 was different than that of day 20 while the plots associated with days 50, 81 and 111, were similar for frequencies greater than 1000 Hz. The phase angle plot indicated that there were differences in the EIS among days 50, 81, and 111 at the low frequency end while the Bode magnitude plot suggested that the behavior was similar for these plots.

Bode representations of spectra are shown in Figure 6 with immersion time as a parameter for the topcoat/primer system measured using the embedded sensor. The Bode magnitude plot for day 1 included a region at the high frequency end that had a slope close to -1. The slope decreased as the frequency was reduced with the slope approaching a plateau, which was observable for frequencies less than 0.1 Hz. The Bode magnitude plot for days 20, 50, 81 and 111 included a slope at the high frequency end also close to -1 and overlapped. The value of the magnitude for these plots at the high frequency end was less than that for day 1 for a given frequency. The plot associated with day 20 had a slope that decreased as the frequency was reduced and a low frequency plateau was approached for frequencies less than 1 Hz. The data for days 50 and 81 were similar in the frequency range measured with a trend suggesting that a low frequency plateau was being approached. The Bode magnitude increased with lower frequency but there was no overlap with the plots for the other days that are shown. For frequencies less than 1 kHz, a lower value of $|Z|$ was associated with a longer immersion time. The Bode phase angle plot shown in Figure 6 indicated a change in the EIS data with immersion time.

The low frequency modulus value associated with EIS data of organic coatings is a measure of the barrier protection provided by the coating under the reasonable assumption that the resistance of the electrolyte is significantly less than that of the coating. The frequency of 0.01 Hz was used as the low frequency modulus value with the value of $|Z|_{0.01Hz}$ shown as functions of immersion time and E_{OC} in

Figure 7. During the first 5 days the $|Z|_{0.01\text{Hz}}$ value for the primer system increased one order of magnitude after which there was less than a factor of 2 increase over the following 23 days. The increase in one order of magnitude for the primer was associated with a change in E_{OC} from -1.2 V to -0.9 V while the small change in $|Z|_{0.01\text{Hz}}$ over the following 23 days was associated with a change from -0.9 V to -0.4 V . The $|Z|_{0.01\text{Hz}}$ value for the topcoat/primer system decreased by only a factor of 2 over the duration of the immersion time to approximately $10^6 \Omega \text{cm}^2$. This change in $|Z|_{0.01\text{Hz}}$ was associated with a change in E_{OC} from -1.2 V to -0.4 V . The $|Z|_{0.01\text{Hz}}$ value for the topcoat/primer system measured from the embedded sensor increased by a factor of close to 5 to $7 \times 10^6 \Omega \text{cm}^2$ over the first 40 days and remained close to this value for the duration of the immersion. The change over the first 40 days for $|Z|_{0.01\text{Hz}}$ was associated with a change in E_{OC} from -1.2 V to -0.8 V . The approximately constant value of $|Z|_{0.01\text{Hz}}$ after 40 days was associated with an increase in E_{OC} from -0.8 V to -0.4 V .

Equivalent circuit modeling

The measurement model technique involves using a generalized Voigt model to analyze the error associated with replicated EIS data. The model is shown in Figure 8 and consists of a series of Voigt elements comprising of a parallel arrangement of a resistor R_k and capacitor C_k , in series with a resistor R_0 that represents the solution resistance. The characteristic time constant associated with a Voigt element is $\tau_k = R_k C_k$ and the impedance of the model can be expressed as²¹

$$Z = R_0 + \sum_{k=1}^K \frac{R_k}{1 + j\omega\tau_k} \quad (1)$$

The elements of the Voigt measurement model are consistent with Kramers-Kronig relations and the application of the technique can determine the internal consistency of the measured EIS data without need for explicit integration of the Kramers-Kronig relations.²³ The technique involves using a weighting strategy for the complex non-linear least squares regression that is based on the measured error structure associated with replicated EIS data. The technique has been described in detail for the analysis of data associated with a Mg rich primers on gold and aluminum substrates.^{19,20}

A 12 Voigt element model was used to fit the data associated with the primer system using a modulus weighting strategy. The resistance value of an element as a function of the time constant of that element is shown in Figure 9 for immersion times of day 1 and day 28. Included with each data point are error bars of one standard deviation that demonstrate the good fit that was attained between the model and the data. The R values for day 1 and day 28 were similar for time constants less than 0.1 s. The R values for time constants of the three largest values were significantly greater for day 28 as compared with day 1. These time constants would be associated with charge transfer processes that are prevalent at the low frequency end of the spectrum. The R values for these three time constants R_{10} , R_{11} and R_{12} are shown as functions of immersion time for the primer system in Figure 10. During the first 10 days of immersion, there were increases in R_{10} and R_{11} after which the values remained approximately constant up to day 28. The value associated with R_{12} increased during the first 15 days after which there was a small increase up to day 28.

Similar to the primer system, a 12 Voigt element model was used to fit the data associated with the EIS data obtained from the sensor embedded in the topcoat/primer system. Examples of the good fit between the data and the model for the data acquired from the sensor in the topcoat/primer system are shown in Figure 9 for days 1 and 111. The R values are shown as a function of time constant value for days 1 and 111 in Figure 9. There were large differences between the R values for day 1 and day 111 associated with the three largest time constants. The R values for these time constants are shown as functions of immersion

time in Figure 10. The value for R_{10} and R_{11} increased up to day 40 and then remained approximately constant up to day 111. The R_{12} value increased up to day 70 after which it remained approximately constant up to day 111.

The R and τ values associated with the largest time constant were similar for both the primer system and the sensor measured topcoat/primer system. The values of R_{12} for both systems are shown as functions of E_{OC} in Figure 11. The R_{12} value for the primer increased monotonically during the increase in E_{OC} from -1.1 V to -0.85 V after which it was approximately constant until an E_{OC} of -0.55 V. For E_{OC} values from -0.55 V to -0.4 V there was an increase in the R_{12} value. The R_{12} value for the sensor measured EIS data increased monotonically during the change of E_{OC} from -1.2 V to -0.65 V after which the value remained constant up to an E_{OC} value of -0.4 V.

The cathodic protective pigmented coating systems such as Mg-rich primer and Zn-rich primer are monitored by the open circuit potential. This monitoring requires a standard reference electrode and immersion in an aqueous electrolyte and these requirements are not easily attained during field application of these primers. The feasibility of impedance measurement as a measure for the cathodic protection provided by Mg-rich primers was presented. The graphical measure of $|Z|_{0.01Hz}$ associated with the impedance at a low frequency are shown as functions of E_{OC} in Figure 7 for both systems. It can be seen that the value of $|Z|_{0.01Hz}$ increased as E_{OC} increased to -0.8 V but was insensitive to the E_{OC} changing to more positive values. These results indicated that the cathodic protection provided by the Mg-rich primer was not being tracked by the $|Z|_{0.01Hz}$ parameter with the observed constant $|Z|_{0.01Hz}$ not being indicative of the loss of cathodic protection from -0.8 V to -0.4 V.

The use of the R value associated with the largest time constant that was obtained by fitting the 12 element Voigt model tracked the loss of cathodic protection, as shown in Figure 11, better than the $|Z|_{0.01Hz}$ parameter. A Mg-rich primer provides cathodic protection where the Mg particles corrode preferentially rather than the aluminum substrate. An increase in the resistance to the corrosion of the Mg particles would therefore reduce the cathodic protection that is being provided. Increases in the values of R_{12} for both the sensor-measured and primer, that were observed in Figure 11, indicated that the rates of the processes associated with the $R_{12}C_{12}$ element were being reduced in conjunction with the loss of cathodic protection. Therefore, it was assumed that the processes associated with the $R_{12}C_{12}$ element participated in providing cathodic protection. The decrease in the corrosion of the Mg particles as seen by the increase in R_{12} was associated with the loss of cathodic protection as seen by the open circuit potential. This demonstrated the feasibility of using EIS monitoring together with embedded sensors to monitor the protection provided by the Mg-primer beneath a topcoat. The presented results were obtained where the coating systems were under immersion. Further studies are being undertaken to determine the feasibility of sensor measured EIS to track the cathodic protection provided by the primer in non-immersion conditions.

CONCLUSIONS

The time dependent electrochemical behavior of a Mg-rich primer and a topcoat/primer system on AA 2024-T3 was monitored using EIS experimentation. The E_{OC} values monitored over time for both systems indicated the change from a mixed potential value to a value consistent with the substrate. This demonstrated the loss of the cathodic protection. The topcoat extended the time of cathodic protection of the primer. Conventional monitoring of cathodic protection for active pigment coatings is by E_{OC} monitoring, which is not a practical for field monitoring. The feasibility of monitoring the cathodic protection of a primer beneath a topcoat using EIS data acquired with an embedded sensor between the topcoat and primer. EIS data associated with the primer and topcoat/primer systems were analyzed using a 12 element Voigt model. The resistance value associated with the largest time constant tracked the loss of cathodic protection of both systems better than the low frequency modulus parameter. The approach of

using an embedded sensor for tracking cathodic protection presented here is being developed for the field monitoring of Mg-rich primers beneath topcoats.

ACKNOWLEDGMENTS

Financial support from Air Force Research Laboratory under Grant No. FA8650-04-1-5045.

REFERENCES

1. R. Buchheit, H Guan, S. Mahajanam, F. Wong, "Active corrosion protection and corrosion sensing in chromate-free organic coatings," *Progress in Organic Coatings*, 47(2003), p. 174.
2. C. Simpson, *Organic Coatings for Corrosion Control*, G. P. Bierwagen, Editor, ACS Symposium Series, 689(1998), p. 356.
3. P.O. O'Brien, A. Kortenkamp, "The chemistry underlying chromate toxicity," *Transition Metal Chemistry*, 20(1995), p. 636.
4. EPA Federal Register, National Emission Standards for Hazardous Air Pollutants for Source Categories: Aerospace Manufacturing and Rework Facilities, 60(170), p. 45947, Sept. 1, 1995.
5. S. M. Cohen, *Corrosion*, 51(1995), p.71.
6. K.D. Ralston, S. Chrisanti, T.L. Young, R.G. Buchheit, "Corrosion Inhibition of Aluminum Alloy 2024-T3 by aqueous Vanadium Species," *Journal of Electrochemical Society*, 155(2008), p. 350.
7. J. Sinko, "Challenges of chromate inhibitor pigments replacement in organic coatings," *Progress in Organic Coatings*, 42(2001), p. 267.
8. F.J. Presuel-Moreno, M.E. Goldman, R.G. Kelly, J.R. Scully, "Electrochemical Sacrificial Cathodic Prevention Provided by an Al-Co-Ce Metal Coating Coupled to AA2024-T3," *Journal of Electrochemical Society*, 152(2005), p. B302.
9. F.J. Presuel-Moreno, H. Wang, M.A. Jakab, R.G. Kelly, J.R. Scully, "Computational Modeling of Active Corrosion Inhibitor Release from an Al-Co-Ce Metallic Coating," *Journal of Electrochemical Society*, 153(2006), p. B486.
10. M.E. Nanna, G.P. Bierwagen, "Mg-rich coatings: A new paradigm for Cr-free corrosion protection of Al aerospace alloys," *Journal of Coating Technology Research*, 1(2004), p. 69.
11. D. Battocchi, A.M. Simoes, D.E. Tallman, G.P. Bierwagen, "Electrochemical behaviour of a Mg-rich primer in the protection of Al alloys," *Corrosion Science*, 48(2006), p. 1292.
12. D. Battocchi, A.M. Simoes, D.E. Tallman, G.P. Bierwagen, "Comparison of testing solutions on the protection of Al-alloys using a Mg-rich primer," *Corrosion Science*, 48(2006), p. 2226.
13. G. Bierwagen, D. Battocchi, A. Simoes, A. Stamness, D. Tallman, "The use of multiple electrochemical techniques to characterize Mg-rich primers for Al alloys," *Progress in Organic Coatings*, 59(2007), p. 172.
14. A.M. Simoes, D. Battocchi, D.E. Tallman, G.P. Bierwagen, "SVET and SECM imaging of cathodic protection of aluminium by a Mg-rich coating," *Corrosion Science*, 49(2007), p. 3838.
15. N.C. Hosking, M.A. Strom, P.H. Shipway, C.D. Rudd, "Corrosion resistance of zinc-magnesium coated steel," *Corrosion Science*, 49(2007), p. 3669.
16. M. Jonsson, D. Persson, D. Thierry, "Corrosion product formation during NaCl induced atmospheric corrosion of magnesium alloy AZ91D," *Corrosion Science*, 49(2007), p. 1540.
17. C.M. Abreu, M. Izquierdo, M. Keddam, X.R. Novoa, H. Takenouti, "Electrochemical behaviour of zinc-rich epoxy paints in 3% NaCl solution," *Electrochimica Acta*, 41(1996), p. 2405.
18. C.M. Abreu, M. Izquierdo, P. Merino, X.R. Novoa, C. Perez, "A new approach to the determination of the cathodic protection period in zinc-rich paints," *Corrosion*, 55(1999), p. 1173.
19. K. Allahar, Dante Battocchi, Gordon P. Bierwagen, Dennis E. Tallman, "Modeling of electrochemical impedance spectroscopic data of a magnesium rich primer," *Journal of Electrochemical Society*, 155(2008), p. E143.

20. K. Allahar, Dante Battocchi, Gordon P. Bierwagen, Dennis E. Tallman, "Transmission line modeling of the EIS data of a Mg-rich primer on AA 2024-T3," *Transactions of the 213 Meeting of the Electrochemical Society*, May 2008, Phoenix, AZ.
21. M.E. Orazem, "A systematic approach toward error structure identification for impedance spectroscopy," *Journal of Electroanalytical Chemistry*, 572(2004), p. 317.
22. P. Agarwal, M.E. Orazem, L.H. Garcia-Rubio, "Measurement Models for Electrochemical Impedance Spectroscopy," *Journal of Electrochemical Society*, 139(1992), p. 1917.
23. P. Agarwal, O.D. Crisalle, M.E. Orazem, L.H. Garcia-Rubio, "Application of Measurement Models to Impedance Spectroscopy II. Determination of the Stochastic Contribution to the Error structure," *Journal of Electrochemical Society*, 142(1995), p. 4149.
24. P. Agarwal, M.E. Orazem, L.H. Garcia-Rubio, "Application of Measurement Models to Impedance Spectroscopy III. Evaluation of Consistency with the Kramers-Kronig Relations," *Journal of Electrochemical Society*, 142(1995), p. 4159.
25. K.N. Allahar, D.P. Butt, M.E. Orazem, H.A. Chin, G. Danko, W. Ogden, R. Yungk, "Impedance of Steels in New and Degraded Ester Based Lubricating Oil," *Electrochimica Acta*, 51(2006), p. 1497.
26. G.P. Bierwagen, X. Wang, D.E. Tallman, "In situ study of coatings using embedded electrodes for ENM measurements," *Progress in Organic Coatings*, 46(2003), p. 163.
27. G.P. Bierwagen, L. He, J. Li, L. Ellingson, D.E. Tallman, "Studies of a new accelerated evaluation method for coating corrosion resistance-thermal cycling testing," *Progress in Organic Coatings*, 39(2000), p. 67.
28. K. Allahar, Quan Su, G. Bierwagen, D. Battocchi, V. Johnson Gelling, D. Tallman, "Examination of the Feasibility of the use of In-situ Corrosion Sensors in Army Vehicles," Paper # 06T098, Tri-Services Corrosion Conference 2005, Orlando FL.
29. J. Kittel, N. Celati, M. Keddam, H. Takenouti, "New methods for the study of organic coatings by EIS. New insights into attached and free films," *Progress in Organic Coatings*, 41(2001), p. 93.
30. J. Kittel, N. Celati, M. Keddam, H. Takenouti, "Influence of the coating-substrate interactions on the corrosion protection: characterisation by impedance spectroscopy of the inner and outer parts of a coating," *Progress in Organic Coatings*, 46(2003), p. 135.
31. A. Miszczyk, T. Schauer, "Electrochemical approach to evaluate the interlayer adhesion of organic coatings," *Progress in Organic Coatings*, 52(2005), p. 298.

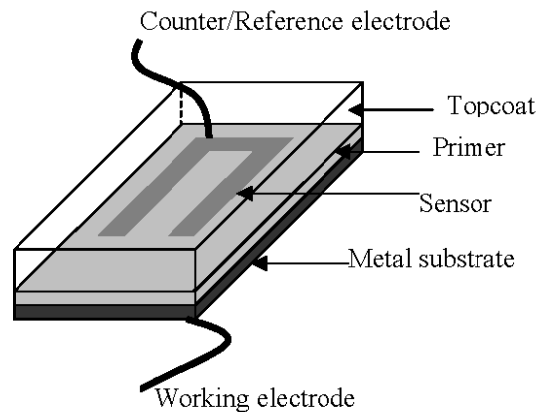


Figure 1. Schematic diagram of embedded sensor between topcoat and primer with electrical connection.

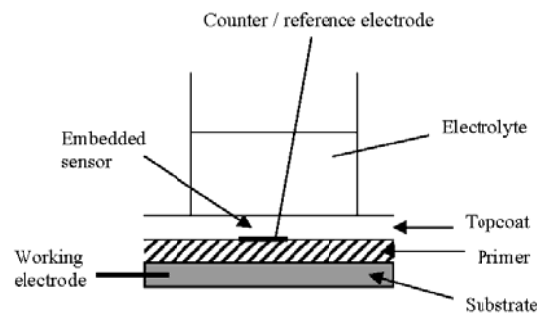


Figure 2. Schematic diagram of the experimental setup for a two-electrode EIS measurement associated with the embedded sensor. The embedded sensor was the counter/ reference electrode and the substrate was the working electrode.

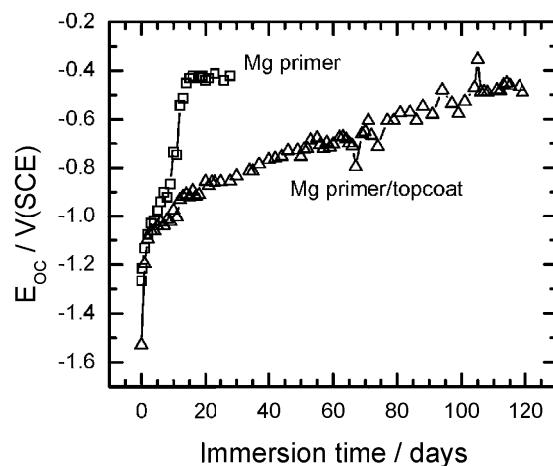


Figure 3. Open circuit potential E_{OC} associated with Mg primer and Mg primer/topcoat systems as functions of immersion time.

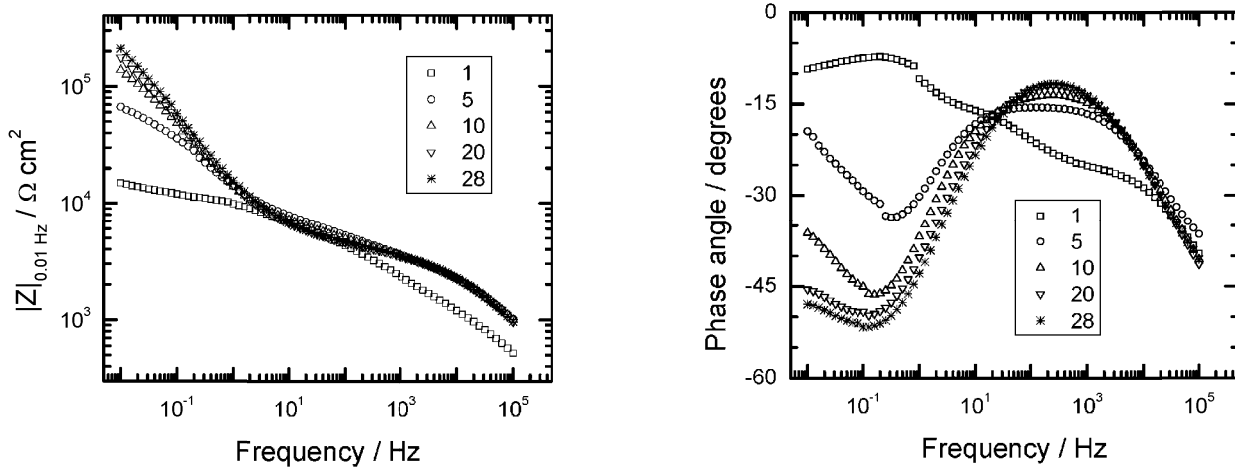


Figure 4. Bode magnitude (left) and phase angle (right) representations of EIS data associated with Mg primer immersed in DHS with immersion time as a parameter.

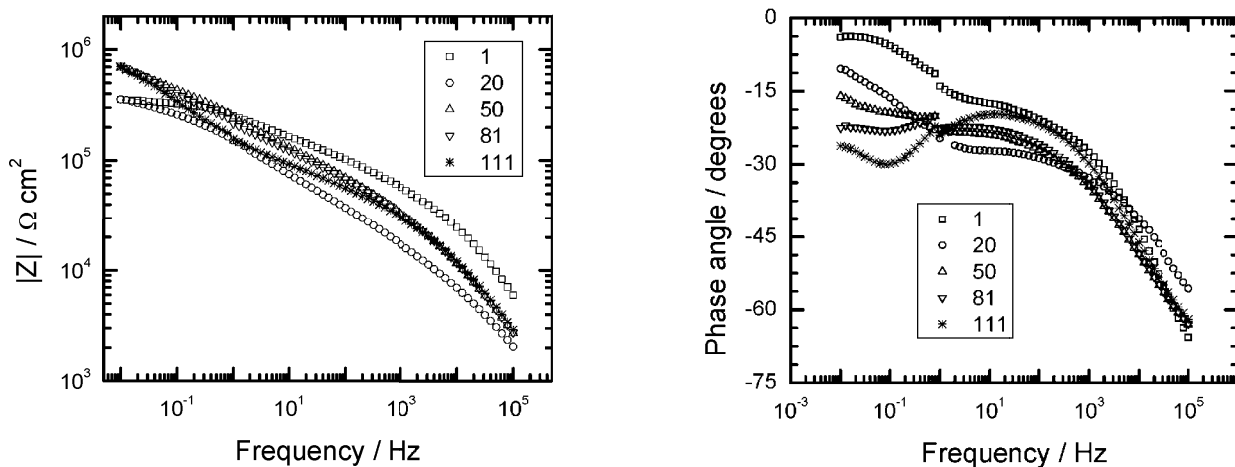


Figure 5. Bode magnitude (left) and phase angle (right) representations of EIS data associated with topcoat/primer system immersed in DHS with immersion time as a parameter.

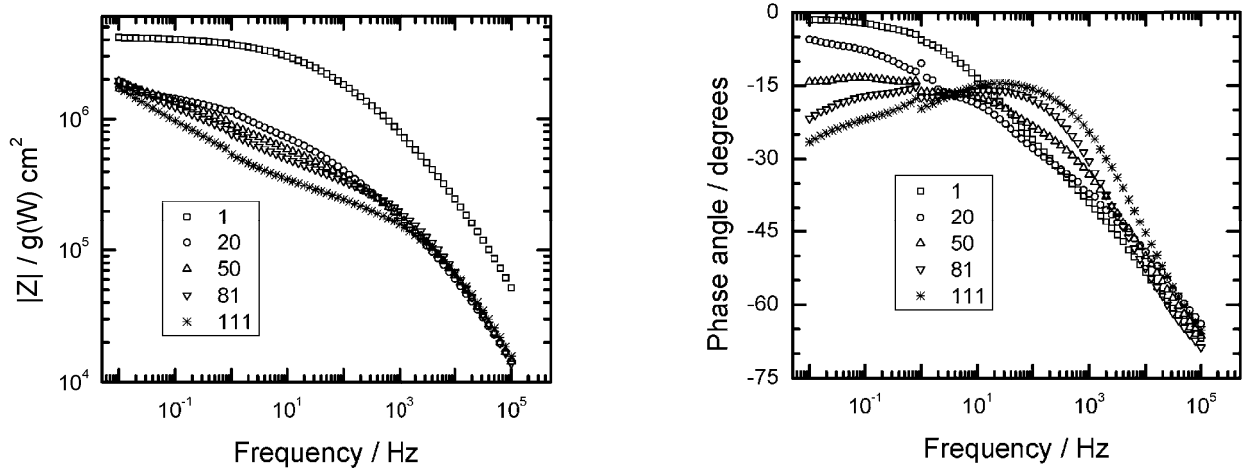


Figure 6. Bode magnitude (left) and phase angle (right) representations of EIS data associated with topcoat/primer system measured using the embedded sensor immersed in DHS with immersion time as a parameter.

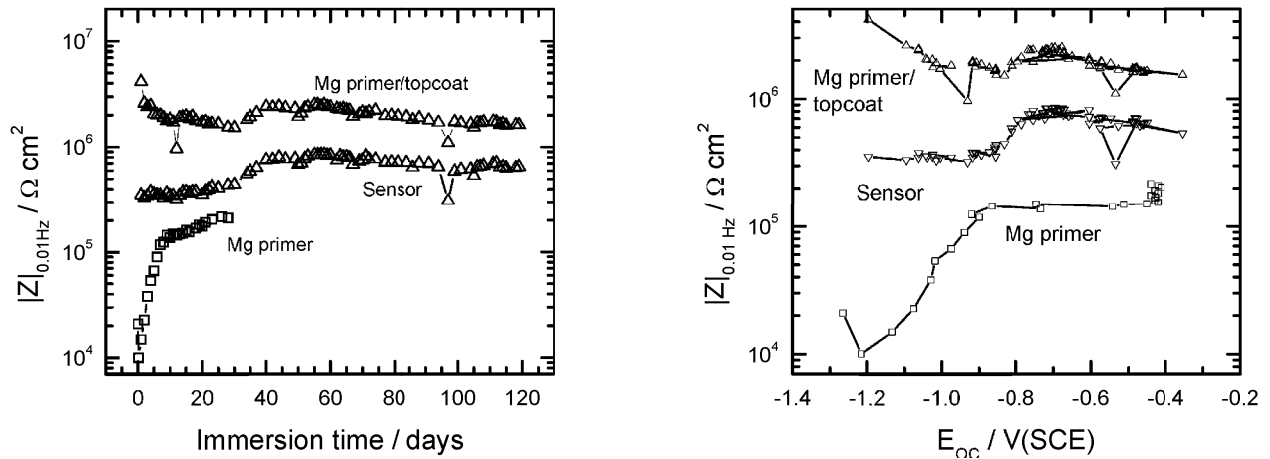


Figure 7. Low frequency modulus value of the EIS data for the Mg-primer and the topcoat/primer systems and the sensor measured topcoat/primer system as functions of immersion time (left) and open circuit potential (right).

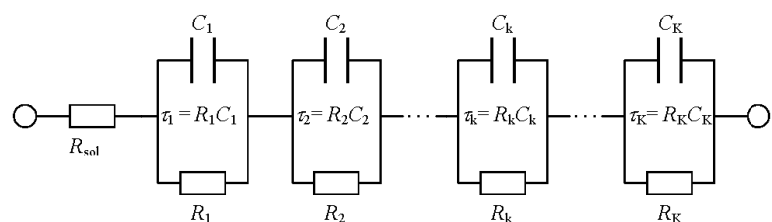


Figure 8. A schematic representation of a Voigt measurement model.

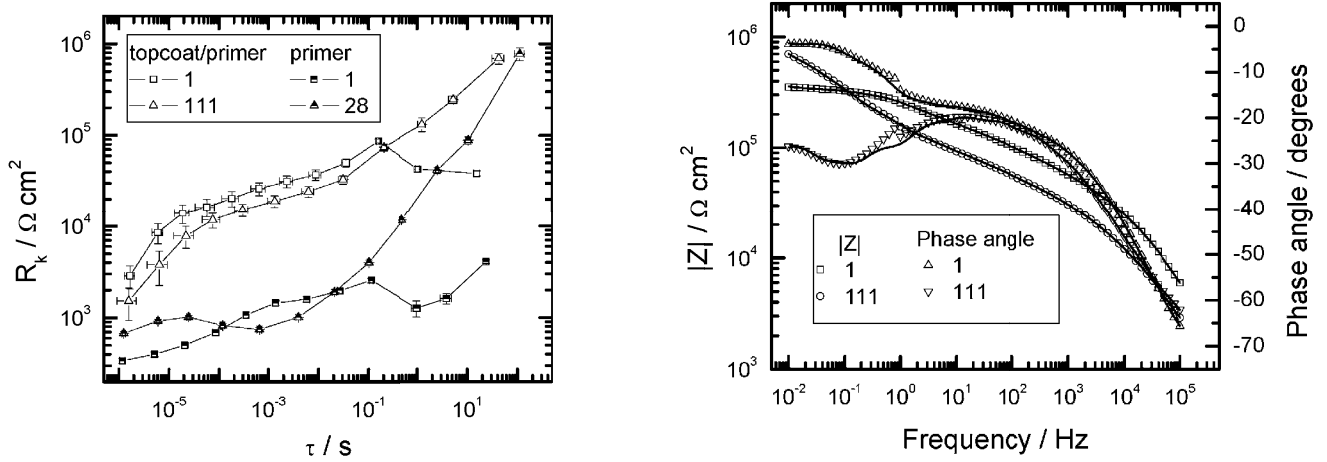


Figure 9. The resistance parameters R_k as a function of time constant for the EIS data of the primer and sensor measured topcoat/primer systems (left). The data for the former system is associated with day 1 and day 28 while the latter is associated with day 1 and day 111. The values were obtained by regressing the EIS data to a 12 element Voigt equivalent circuit. The EIS associated with days 1 and 111 for the sensor measured topcoat/primer system with lines superimposed representing the regression of the model to the data (right).

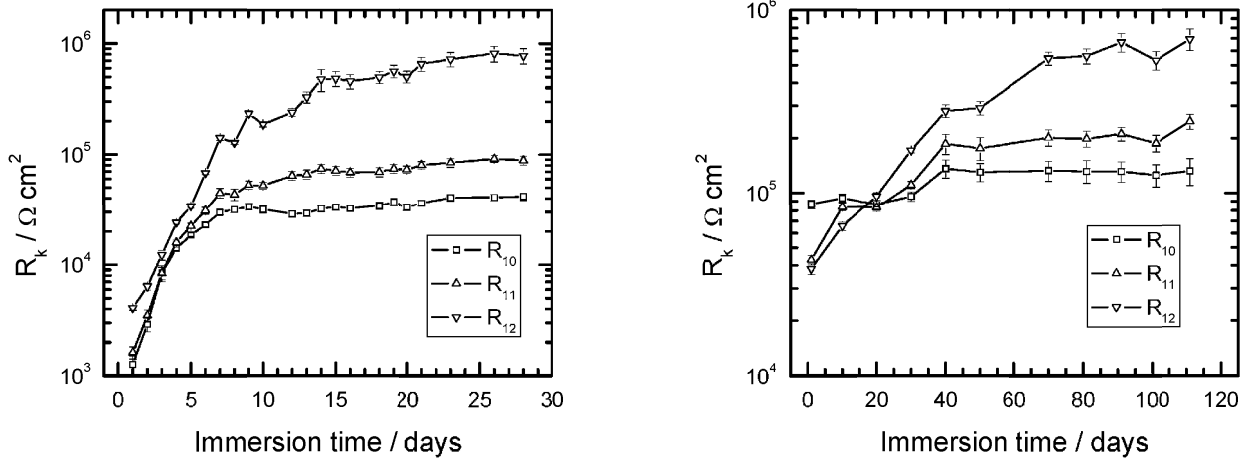


Figure 10. The resistance parameter associated with the largest three time constant R_{10} , R_{11} , and R_{12} as a functions of open circuit potential for the EIS data of the primer (left) and sensor measured topcoat/primer (right) systems. The values were obtained by regressing the EIS data to a 12 element Voigt equivalent circuit.

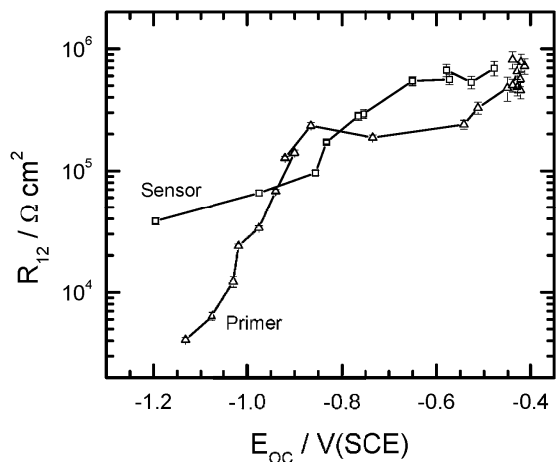


Figure 11. The resistance parameter associated with the largest time constant R_{12} as a function of open circuit potential for the EIS data of the primer and sensor measured topcoat/primer systems. The values were obtained by regressing the EIS data to a 12 element Voigt equivalent circuit.

IN SITU MONITORING OF A MG-RICH PRIMER BENEATH A TOPCOAT EXPOSED TO PROHESION CONDITIONS

Duhua Wang¹, Dante Battocchi^{2*}, Kerry N. Allaha¹, Seva Balbyshev³ and Gordon P. Bierwagen^{1,2}

¹Department of Coatings and Polymeric Materials,

²Center for Surface Protection

³Center for Nanoscale Science And Engineering

1735 NDSU Research Park Drive, Fargo, ND 58105-5376, USA

Ph: 001-701-231-6219

Authors e-mail: Duhua.Wang@ndsu.edu, Dante.Battocchi@ndsu.edu, [Kerry.Allaha@ndsu.edu](mailto>Kerry.Allaha@ndsu.edu),
Gordon.Bierwagen@ndsu.edu, Seva.Balbyshev@ndsu.edu

Abstract:

Mg-rich primers have been proven to be an adequate alternative for Chromium based coatings¹ for the protection of aluminum alloys from corrosion. Its protection behavior was attributed to a combination of cathodic and barrier protection^{2,3}, similar to the protection behavior associate with Zn-rich primers on steel substrates.

The performance of a Mg-rich primer on aluminum 2024-T3 under Prohesion® exposure (ASTM G85) has been monitored using an embedded sensor placed at the surface of the primer and below the topcoat. The accelerated weathering cycle is an alternative of wet and dry cycles to simulate outdoor weather exposure.

Electrochemical impedance spectroscopy (EIS) and noise measurement (ENM) were conducted to monitor the performances and the electrochemical properties of the system beneath the topcoat. The data analysis demonstrates that he sensor is able to detect change in the barrier property of the topcoat in response to the exposure conditions and the activation of the active pigments in the primer in presence of the electrolyte.

1. M. E. Nanna and G. P. Bierwagen, J. Coating technol. Res. 2004, 1, 69.
2. D. Battocchi, A. M. Simoes, D. E. Tallman and G. P. Bierwagen, Corr. Sci. 2006, 48, 1292.
3. D. Battocchi, A. M. Simoes, D. E. Tallman and G. P. Bierwagen, Corr. Sci. 2006, 48, 2226.
4. C. M. Aberu, M. Izquierdo, M. Keddam, X. R. Novoa and H. Takenouti, Electrochim. Acta 1996, 41, 2405.

1. Introduction

Corrosion protection by coatings is mainly based on the combination of binders (polymer resins) and pigments. For epoxy esters, drying oils and phenolic epoxy paints, the corrosion protection is mainly attributed to the barrier properties from binders, which can reduce the transport of water, ions, and oxygen from the environment to the substrate [1-3]. On the other hand, in lead red, zinc chromate yellows and zinc-rich primers, the pigments' inhibition, passivation and cathodic protection are the main causes of reducing corrosion.

Corrosion is a natural process and the accelerated weathering, such as Prohesion® and salt spray exposure, aims to reproduce, in a much shorter time than in the field, natural corrosion and degradation processes of the coating system and the substrate without changing the corrosion/degradation mechanism as occurred in practice. The most often used accelerated test is the salt spray test, which involves continuous spraying of 5% sodium chloride (NaCl) in distilled water at 35°C [2]. It can be performed in accordance with ASTM B117, ISO 7253, ISO 9227, DIN 53167, or BS 3900. Salt spray was first used for corrosion testing about 1914. In 1939, the neutral salt spray test was standardized in ASTM B117. Cyclic

corrosion test results generally correlate better with natural corrosion than salt spray test results do. This is pointed out in many of the references [4-9]. The first cyclic test, the so-called Prohesion® test, was developed in the UK in the 1970s. It is covered since 1994 in an annex of ASTM G85, together with other modifications to the basic salt spray test. Typical Prohesion® test includes a fog/wet step of 1 hour salt spray at 25°C and a dry step of 1 hour hot air at 35°C. Dilute Harrison's solution is used as the salt fog solution in the Prohesion® chamber, which consists of 0.05 percent NaCl and 0.35 percent NH₄SO₄ at a pH of 5.0-5.4. Accelerated weathering can not replica the real natural corrosion process, G. Gardner pointed out that continuous salt spray accentuated blistering and that cyclic salt spray emphasized filiform and undercut corrosion [4]. Because of the problems inherent in exposure testing methods, especially their subjective nature, quantitative electrochemical testing has become quite widely used [10]. The major electrochemical test methods used for examining the coatings systems and metal pretreatments are electrochemical impedance spectroscopy (EIS), electrical noise methods (ENM), and potentiodynamic scanning. [10-15].

A technique for in-situ monitoring of a coating involves an embedded electrode sensor within a coating system. The Coatings and Polymeric Materials Department at NDSU has been at the forefront in the development and application of embedded sensors, which consist of electrodes that act as the counter and reference electrode, but are placed between the layers of a two-layer coating system [16,17]. The major advantage of this sensor application is that the electrochemical measurement of the primer/metal interface can be made without being masked by high resistant topcoat. Till now, the embedded sensors have been applied in characterizing standard Air Force and Army vehicle coatings that use the thermal cycling accelerated testing method [18], and the accelerated ac-dc-ac testing method, [19]. While there have been these limited studies published, there has been no application to metal rich primers, e.g. Mg- or Zn-rich primers. By analogy to the formulation of zinc-rich primers for the protection of steel, magnesium-rich, magnesium pigmented primers are now being formulated for the protection of aluminum alloy. This work has its motivation from the protection of high strength aircraft Al alloys such as 2024 T3 and 7075 T6 without the use of chromate-based pretreatments or chromate pigments. G.P. Bierwagen and the corrosion group at NDSU are leading this Mg-rich primers research and a series of articles have been published [20-22] on their properties. The coupling of embedded sensors and coating systems with Mg-rich primers will be a unique approach that allows in-situ monitoring of the electrochemical behavior a this Mg-rich protective primer beneath a topcoat.

2. Experimental

The protective coating system used in the experimental procedure comprised of a high solids polyurethane clear topcoat (AKZO NOBEL 646-58-7925CLEAR) and a Mg-rich primer developed at NDSU [20]. In this primer, Mg powder with the average particle size of 25 µm (Ecka GmbH) was dispersed in a two-component epoxy-polyamide resin and the pigment volume concentration (PVC) of the primer was 45%. The primer was applied on aluminum alloy 2024-T3 standard panels. After the application of the primer, a platinum sensor was applied on the surface of the primer and followed by the application of the polyurethane topcoat. The embedded sensor was between the primer and the topcoat for each of the final coated panels.

2.1 Sample Preparation

The aluminum alloy 2024-T3 panels were polished by 200 grit followed by 600 grit sanding paper, then washed with hexane and dried with a nitrogen flow. The fresh pretreated metal panels were coated within half an hour after they were polished.

The sensor was made from platinum leaves obtained from Wrights of Lymm Ltd, Manchester, England, that were approximately 130 nm thin. Supported by tissue paper, the platinum leaf was cut into the designed sensor shape with the surface area of the sensor being 2.56 cm² and the width of each side 0.4

cm as shown in figure 1 with the sensor on the surface of the Mg-rich primer and covered by a polyurethane clear topcoat.

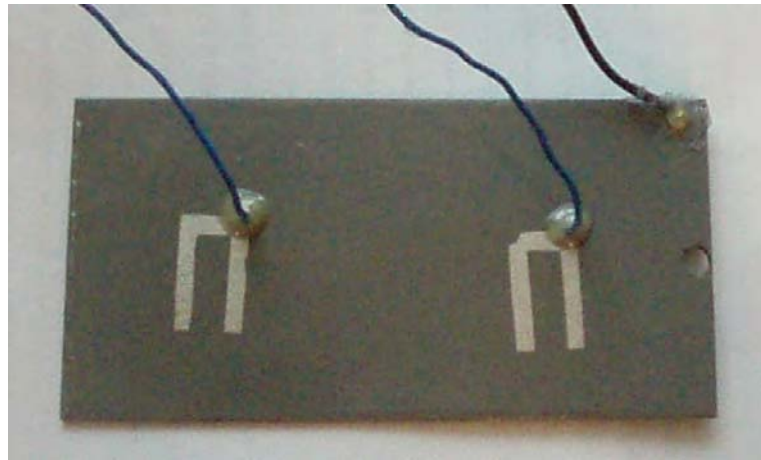


Figure 1. A picture of two platinum sensors embedded onto the Mg-rich primer and topcoated by polyurethane clear coat. The substrate was the Al 2024 T3 panel.

The sensor was adhered to the primer by applying a thin layer of a homemade epoxy resin, D.E.R. 331 epoxy resin/Ancamide 2353/methyl ethyl ketone = 5/3/5 (weight ratio), onto the primer surface in the location for the sensor. The platinum sensor was placed on this epoxy resin and adhered onto the primer after 10 minutes of solvent flash-off and cured. Then a copper core electrical conducting wire was soldered onto the embedded sensor. The same epoxy resin (D.E.R. 331) was used to seal the conducting joint with this epoxy given one day to harden at room temperature before the polyurethane topcoat was applied. The approximate neat dry film thickness of Mg-rich primer was about 50 µm and 40 µm for the topcoat.

The exposure of the panels in the Prohesion® chamber requires that the back of the coated panel be also isolated from the environment. This was done by applying the same coating system, Mg-rich primer and polyurethane clear topcoat, to the back of the panel. The sides of the panels were also dip coated with the same coating system.

2.2 Experimental Configurations

The in-situ monitoring of the Mg-rich primer + polyurethane clear topcoat was carried out under Prohesion® exposure condition. A Gamry PCI4-300 was used for the potentiostatic EIS measurement with a frequency range from 100 kHz to 0.05 Hz and a perturbation potential of 15 mV RMS. A data acquisition rate of 10 points per decade was employed. Two-electrode (2E) EIS method (sensor-substrate) was used to obtain the EIS responses. A 1-panel setup where one coated panel was assembled with two sensors placed approximately 8 cm apart. A schematic diagram is shown in figure 2: the working electrode was connected to the metal substrate and the reference/counter electrode was connected to the embedded sensor.

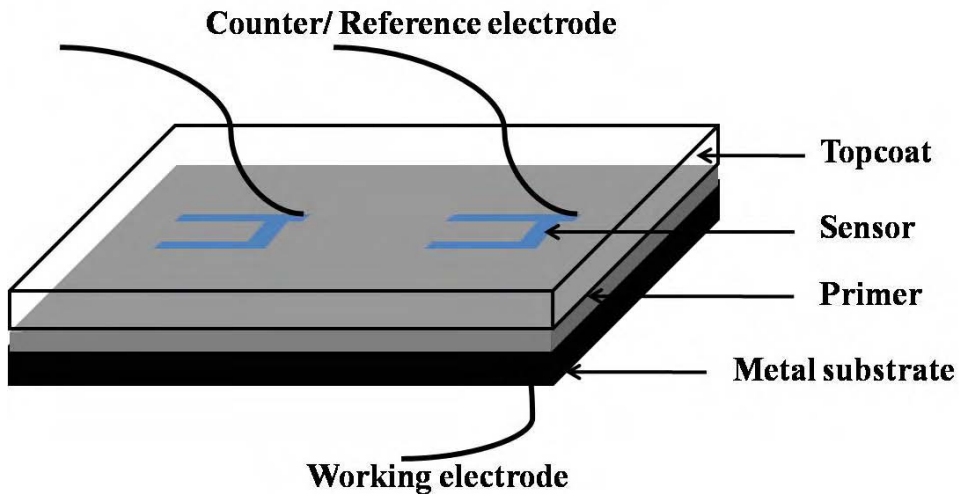


Figure 2. Schematic diagram of the configuration used to perform the EIS experiments, where the embedded sensor was the reference/counter electrode, substrate was the working electrode.

Another 2E EIS setup (sensor-sensor) consisted of one sensor connected to the working electrode and the other sensor connected to the counter/reference electrode (figure 3).

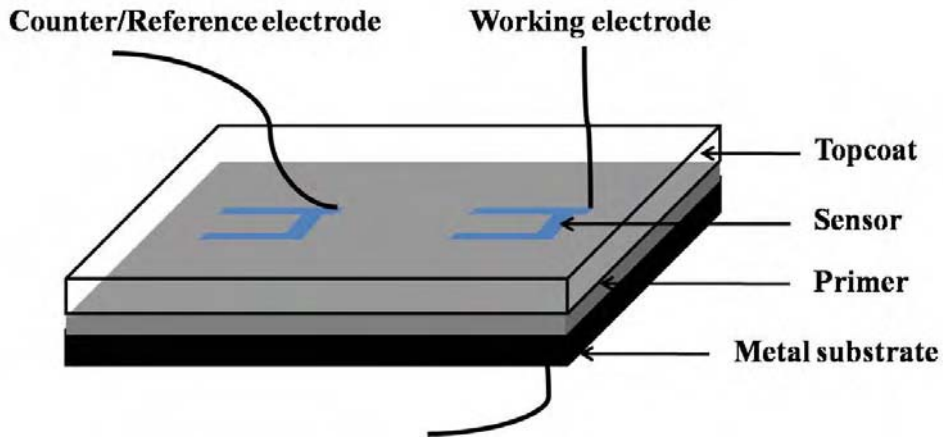


Figure 3. Schematic diagram of the configuration used to perform the EIS experiments, where one embedded sensor was the reference/counter electrode, the other was the working electrode.

The fast mode was used in both two-electrode EIS measurement, and it took about 12-15 minutes for each EIS measurement scanning from 100 kHz to 0.05 Hz. The single frequency impedance measurement was also carried out using the figure 2 EIS configuration at the frequency of 10 kHz.

The configuration for the ENM measurement is shown in figure 4. A 1-panel setup was used where the two sensors were the working electrodes and the substrate was the reference electrode. Experiment was carried out on under zero resistance ammeter (ZRA) mode by using Gamry Framework Version 4.21/ESA400 software and a Gamry PCI4/300 potentiostat supplied by Gamry Instruments, Inc. of Willow Grove, PA. The electrochemical noise data acquisition frequency was 5 Hz in this test. This configuration is theoretically the same as the traditional ENM three-electrode configuration [23], where the panels are the two separate working electrodes with the electrical connection between the electrolytes

above the panels the reference electrode. Similar information were obtained from both the traditional and the present configurations [23,24].

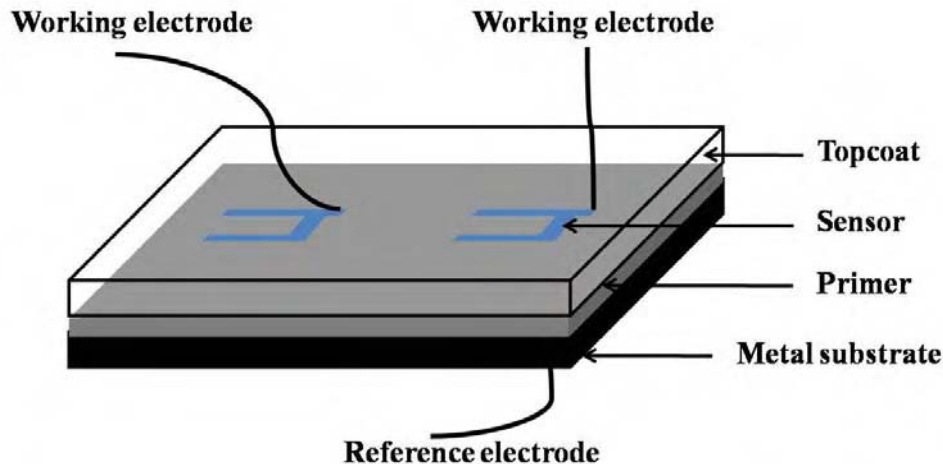


Figure 4. Schematic diagram of the configuration used to perform the ENM experiments. The embedded electrodes were the two working electrodes, and the electrically connected substrate was the reference electrode.

2.3 Testing Procedure

In order for total curing, the tested panels were placed under ambient conditions for at least 10 days before put into the Prohesion® Chamber. The electrical leads for the embedded sensor and the substrate for each panel were long enough to be accessible from outside of the chamber to connect with the potentiostat and computer. After a certain period of time in the Prohesion® chamber, EIS experiments were conducted using the two-electrode configurations during the Prohesion® dry step and wet step respectively, followed by the ENM testing which typical consists of 3 cycles of the dry and wet steps in Prohesion® test.

During the first three weeks in Prohesion® chamber, EIS and ENM testing were carried out everyday. After then, electrochemical measurements were carried out every other day. The total duration for this testing was 60 days.

The EIS experiments were both conducted in the dry step and wet step after 30 minutes when the chamber conditions are more stable and the coating surface are more close to real dry or wet environments. Additional experiments were also conducted to characterize the behavior of the Mg-rich primer during the changing environmental conditions. A single frequency experiment was conducted every other week during Prohesion® exposure to characterize the capacitance behavior of the primer. This experiment involved the measurement of the impedance at an applied frequency of 10 kHz over a period of time, typically 3 cycles. In addition, the temperatures of the coating surface were monitored using thermocouple sensors for several early cycles of Prohesion® exposure.

3. Results and Discussion

3.1 Chamber Temperature and Coating Capacitance Study

Electrochemical impedance measurements require steady state during the measurement process. The environmental conditions in the Prohesion® chamber changed very fast with time. In order to conduct in-situ EIS measurements on the coated panels in the Prohesion® chamber, a relatively stable state should be identified first. The changes of temperature, and the capacitance associated with the measured panel were

investigated and the influence of Prohesion® conditions on coating electrical properties was studied. Based on these studies, a proper time range was identified for the EIS test.

The temperature profile at the coating surface of a coated panel that was measured during an early Prohesion® cycle is shown in figure 5. The 1 hour exposure of a dry step included a temperature increasing from 25°C to 45°C in 20 minutes followed by a drop to 40°C over the next 40 minutes. The 1 hour exposure of the wet (fog) step included a drop from 40°C to 27°C over the first 55 minutes and then a drop to 25°C over the last 5 minutes.

The relative dielectric permittivity of water at room temperature is approximately 80 as compared to that of an epoxy polymer, which is in the range of 3 to 5. The ingress of water into a coating is associated with an increase in the dielectric property of the coating with a consequential increase in coating capacitance [25,26]. The evolution of the impedance of the coating at a high-frequency, 10 kHz, was measured during the dry and wet steps of the Prohesion® cycle. The impedance data was used to calculate the capacitance of the coating, C_c , using:

$$C_c = -1 / (2 \pi f Z'')$$

Where f was the frequency and Z'' was the imaginary component of the impedance.

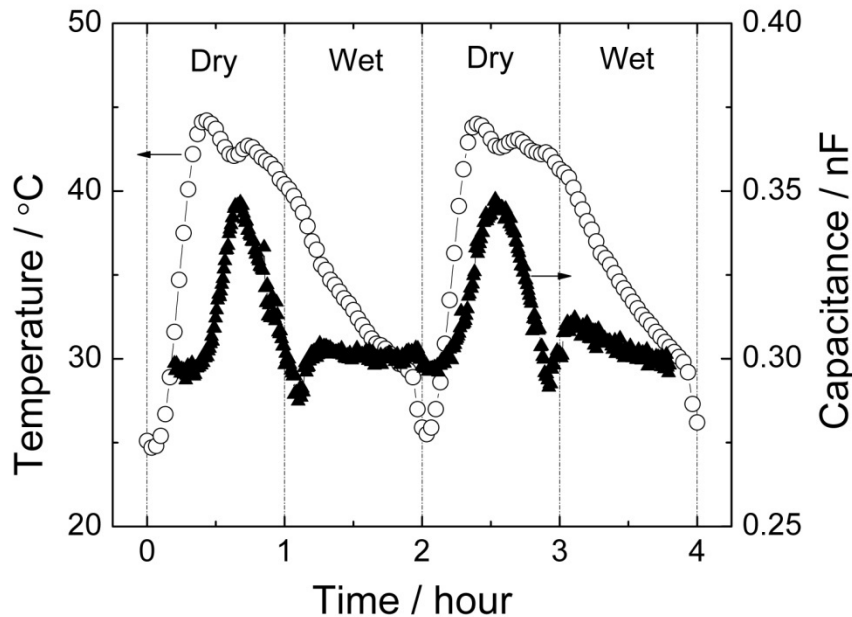


Figure 5. The temperature profile at the surface of the coated panel and the calculated capacitance during the dry and wet steps of Prohesion® conditions. Dashed lines are used to identify the steps.

The evolution of the calculated coating capacitance after 16 days of Prohesion® exposure is also shown in figure 5. In the dry step, the capacitance value clearly had a similar profile as temperature did. The capacitance increased from 0.30 nF to 0.35 nF during the first 35 minutes of the dry step and it decreased to the lowest point of about 0.28 nF at the first several minutes of wet cycle. It seemed that the temperature factor dominated the changes of capacitance in the dry step. With the temperature increasing, the polyurethane topcoat was more porous to water but showed better barrier to moisture when temperature decreased. In the wet step, the capacitance was basically maintained around 0.30 nF probably due to the combination of fog spraying environment and decreasing temperature in the wet step. Overall, the capacitance changes were more attributed to the temperature changes during the dry and wet steps in Prohesion® exposure. It was also found that the environment condition in Prohesion® chamber varied all the time and the electrochemical impedance data also differs during the different periods of chamber

conditions. In order to have an effective analysis and comparison of data, we chose to present and plot the EIS data collected during the 40-50 minutes range in dry and wet steps, respectively.

3.2 EIS Results

3.2.1 Sensor-substrate EIS

Two-electrode EIS method (sensor-substrate) was used to obtain the EIS responses (figure 2). EIS measurements for the frequency range of 100 kHz to 0.05 Hz were performed after 40 minutes of drying and wetting, respectively. Total duration of testing was 60 days when the coatings were found failed both by visual inspection and electrochemical testing results. The EIS Bode plots during the Prohesion® dry and wet steps are shown in figure 6 with the time of exposure days. It was observed that the $|Z|$ data almost superimposed in the 100 Hz to 100 kHz high frequency range before 20 days Prohesion® exposure, which suggested that the capacitance of the coating was approximately the same at the end of 20 days' Prohesion® chamber exposure. Then the high frequency $|Z|$ data decreased with time. The impedance was scatter for about 10 days in the mid-frequency range of 1Hz to 100 Hz, and this scatter became negligible with more time elapsing. The modulus of the low frequency range of 0.05 Hz to 1 Hz was continuously decreased till 43 days' chamber exposure. It was found that the $|Z|$ data of the day 43 and 60 were almost overlapped both for the dry and wet steps. There were plateau regions in the 0.05 Hz to 100 Hz frequency range during the Prohesion® exposure, which suggested the barrier properties provided by the surface coating, here, probably the polyurethane clear topcoat, since the Mg-rich primer usually contributing cathodic protection and shows a lower impedance $< 10^6 \Omega$ [20,21].

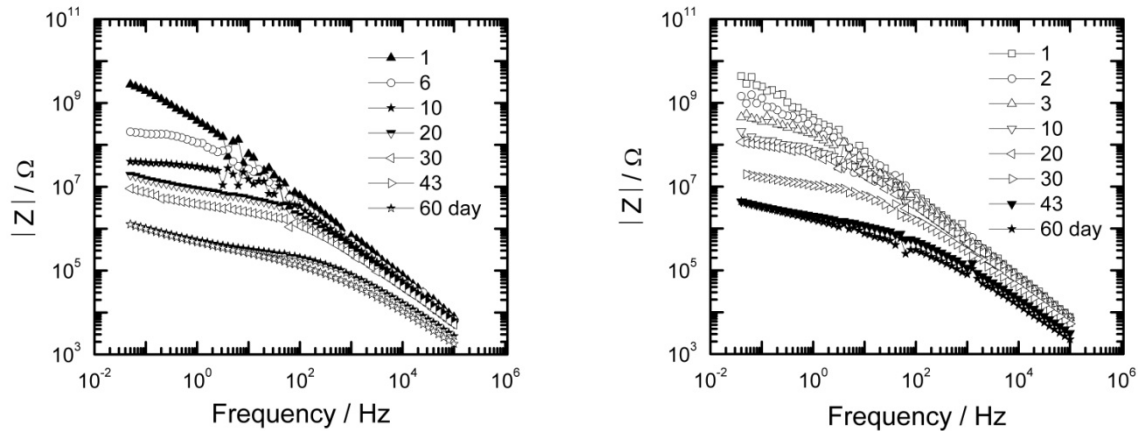


Figure 6. Impedance of sensor-substrate EIS data during the Prohesion dry steps (left) and wet steps (right).

The barrier property is a major method to provide corrosion protection by coatings. The barrier property can be presented as the resistance of the coating to the passage of electric current. For this reason, the low frequency modulus value has been widely used as the estimate of coating resistance and barrier properties [27,28]. In this study, the $|Z|$ value associated with a frequency of 0.05 Hz was used as an estimate of the barrier property of the coating. The $|Z|_{0.05 \text{ Hz}}$ values for both the Prohesion® dry and wet steps are shown in figure 7 as the function of Prohesion® exposure time. It was found that both $|Z|_{0.05 \text{ Hz}}$ values of dry and wet steps had the similar profile, which was decreased rapidly for the first 10 days from about $1 \times 10^9 \Omega$ to $1 \times 10^8 \Omega$. Then the wet $|Z|_{0.05 \text{ Hz}}$ values were kept around $1 \times 10^8 \Omega$, followed by another rapid decreasing to $4 \times 10^6 \Omega$ during 20–40 day period. After about 40 days, the $|Z|_{0.05 \text{ Hz}}$ values were constant around $3 \times 10^6 \Omega$ to the last day of testing. The dry $|Z|_{0.05 \text{ Hz}}$ values showed the similar changes, were about $1 \times 10^7 \Omega$ during 10–20 day period, then rapid drop to $1 \times 10^6 \Omega$ to the day 40, then kept that value for the rest of testing days. It was clearly observed that the barrier properties of the coatings were weakened step by step during the 60 days' Prohesion® chamber exposure. Another found was the wet $|Z|_{0.05 \text{ Hz}}$ values were

relatively higher than the dry ones, that may due to the higher averaging temperature in the dry step (figure 5) and the polyurethane clear topcoat was more sensitive and porous to higher temperature.

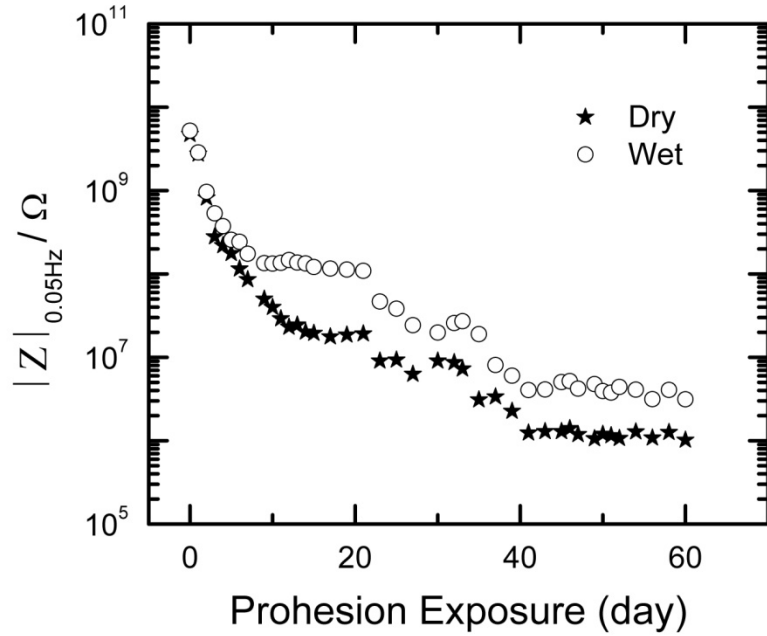


Figure 7. The evolution of the low frequency impedance $|Z|_{0.05 \text{ Hz}}$ values of 2E sensor-substrate EIS measured during the dry and wet steps of different Prohesion® days.

The capacitance values C_c , calculated from the impedance data at the frequency of 9998.2 Hz, were plotted as the function of time in Prohesion® chamber (figure 8). The trends in the C_c values were similar for the dry and wet conditions, increasing from 0.1 to 0.2 nF for the first 20 days, then quicker increasing from 0.2 to 0.7 nF for another 20 days and over 1 nF after the day 50. These results indicated that the barrier property of the coating during the Prohesion® exposure was decreased slowly from the beginning and weakened quickly after 20 days, which were consistent with the Bode plots and $|Z|_{0.05 \text{ Hz}}$ values. All the results showed that the coatings startd to degrade from the beginning of the Prohesion® exposure and failed to provide to provide the barrier properties after about 40 days' Prohesion® exposure.

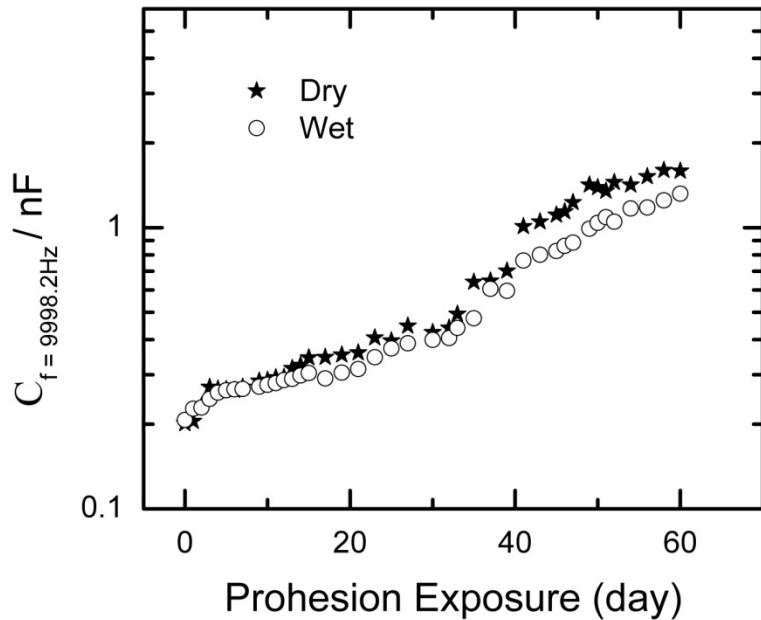


Figure 8. The evolution of the high frequency Capacitance $C_{f=9998.2\text{Hz}}$ values of 2E sensor-substrate EIS measured during the dry and wet steps of different Prohesion® days.

3.2.2. Sensor-sensor EIS

Besides to the two-electrode (2E) sensor-substrate EIS method, sensor-sensor EIS measurement (figure 3) was also used for in-situ monitoring of the coating system changes during the Prohesion exposure. Theoretically, the $|Z|$ data values from the sensor-sensor EIS measurement should be the complex of the two $|Z|$ data values from individual sensor1 and sensor 2, so the EIS data from sensor-sensor configuration should be very similar to the sensor-substrate configuration EIS results.

Sensor-sensor EIS measurements for the frequency range of 100 kHz to 0.05 Hz were also performed after 40 minutes of drying step and wetting step, respectively. The first testing day is day 14, when the testing panel was already under through 14 days of Prohesion® exposure and final day of testing was the day 60, the last day of electrochemical testing. The EIS Bode plots during the Prohesion® dry steps are shown in figure 9 as the function of Prohesion® exposure days. It was observed that the impedance spectroscopy slightly changes from day 14 to day 21 and the low frequency impedance of day 30 was around $1 \times 10^7 \Omega$. The $|Z|$ data spectroscopy of day 43, 52 and day 60 were almost superimposed in all frequency range, and the low frequency modulus were down to about $1 \times 10^6 \Omega$. The phase angles before day 30 were close to -80 degree in the high frequency range, which means coatings performed like a capacitor. Phase angles after day 43 were about -60 degree in the 100 Hz to 100 kHz high frequency range. And all the phase angles were decrease to around -30 degree from the 1 Hz to 0.05 Hz, indicating the failing of the coatings on the substrate and the barrier properties of coatings were losing. The EIS Bode plots during the Prohesion® wet steps had the very similar profiles.

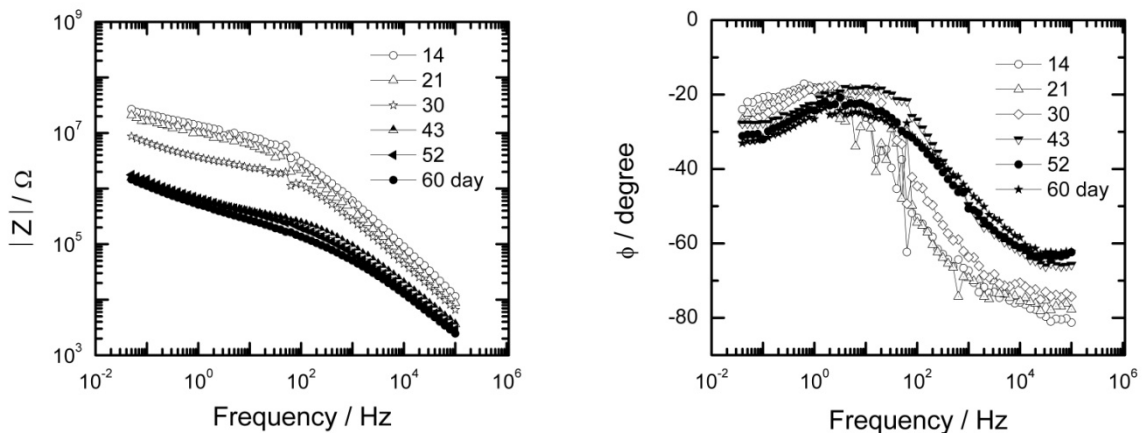


Figure 9. The EIS Bode plots of the coated panel under Prohesion® dry step after 40 minutes of drying: (a) impedance modulus, (b) phase angle.

Figure 10 shows the changes of low frequency modulus $|Z|_{0.05 \text{ Hz}}$ values as the function of Prohesion® exposure time. Both $|Z|_{0.05 \text{ Hz}}$ values of dry and wet steps had the similar profile, which was decreased with time from about 1×10^8 to $8 \times 10^6 \Omega$ for the wet step and from 2×10^7 to $1 \times 10^6 \Omega$ for the dry step during the Prohesion® exposure day 14 to 43 period and kept that values to the end of the testing, which is day 60. Obviously the coatings were failing and losing barrier properties during the Prohesion® exposure. It was also found that the $|Z|_{0.05 \text{ Hz}}$ values of wet steps were higher than the ones of dry steps, which showed the consistent results with the sensor-substrate EIS data.

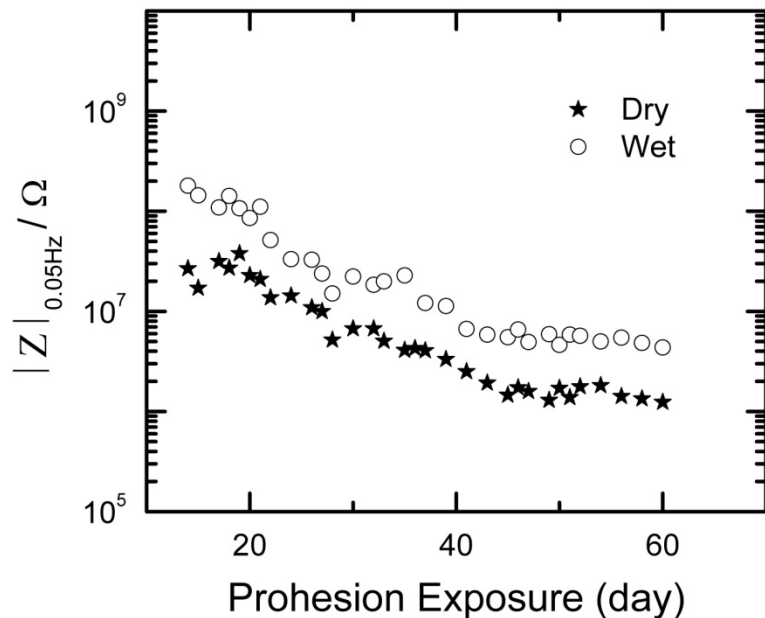


Figure 10. The evolution of the low frequency impedance $|Z|_{0.05 \text{ Hz}}$ values of 2E sensor-sensor EIS measured during the dry and wet steps of different Prohesion® days.

The capacitance values C_c were plotted as the function of Prohesion® exposure time (figure 11). Both the C_c values from dry step and wet step were increasing with time elapsing, from about 0.2 nF to over 1 nF, indicating that the coatings were more accessible to moisture absorbing and losing barrier properties.

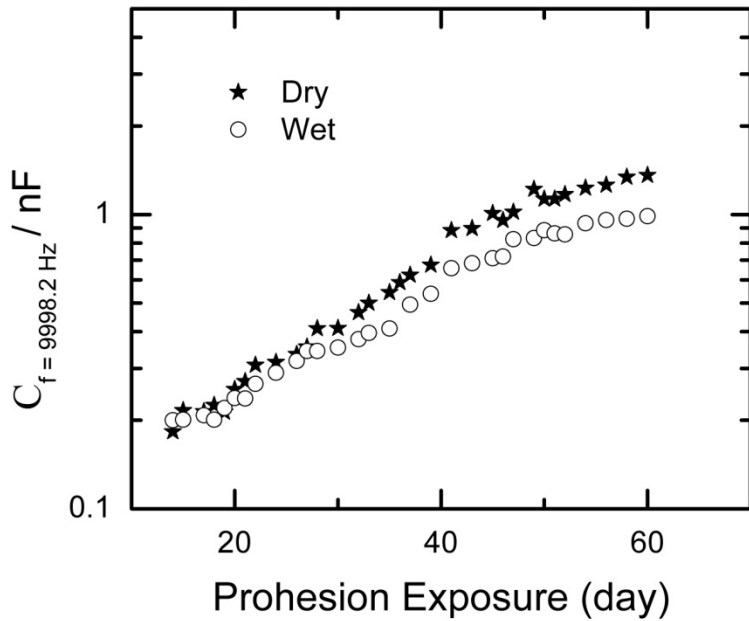


Figure 11. The evolution of the high frequency Capacitance $C_{9998.2\text{Hz}}$ values of 2E sensor-sensor EIS measured during the dry and wet steps of different Prohesion® days.

3.2.3. Single Frequency Capacitance

As mentioned before, the increasing capacitance of a coating means the increasing of the dielectric property and more accessible to water uptaking of a coating. The classic Brasher-Kingsbury equation [29] can even be used to quantitatively calculate the volume percentage of absorbed water (< 5%) in a coating film. And larger coating capacitance value always represents more chance for water to get into the coating film. In this study, the evolution of the impedance of the coating at 9998.2 Hz with different Prohesion® exposure days were measures during 3 dry and wet cycles, totally 6 hour period. And the capacitance $C_{9998.2\text{Hz}}$ were calculated from the impedance data and shown in figure12. Obviously, the $C_{9998.2\text{Hz}}$ changed varied with the Prohesion® Chamber condition: capacitance values fluctuated in dry step and relatively flattened in wet step. This was probably due to the specific polyurethane clear topcoat was very sensitive to the temperature changes in Prohesion® chamber dry step, which increasing from 25°C to 45°C for about 20 minutes, then kept constant and slightly decreased to about 40°C at the end of the dry step. In this dry step, topcoat was soften and more accessible to moisture penetration with temperature increasing and more barrier to electrolyte when temperature decreasing. In the wet step, on one hand, the temperature continues decreasing from 40°C to 25°C, on the other hand, the fog filling in the whole chamber, the combination of the decreasing temperature and wetting atmosphere in chamber kept the capacitance of the coating relatively constant. Another obvious found was that the capacitance levels were increasing with longer time exposure. The $C_{9998.2\text{Hz}}$ values from day 16 were in the 0.25-0.35 nF range, while the $C_{9998.2\text{Hz}}$ values from day 51 were much more fluctuated within the 1.0-1.5 nF range. Clearly, the longer exposed in Prohesion chamber, the higher and more fluctuated $C_{9998.2\text{Hz}}$ values were, showing that the coating barrier property was deteriorated during the Prohesion® exposure.

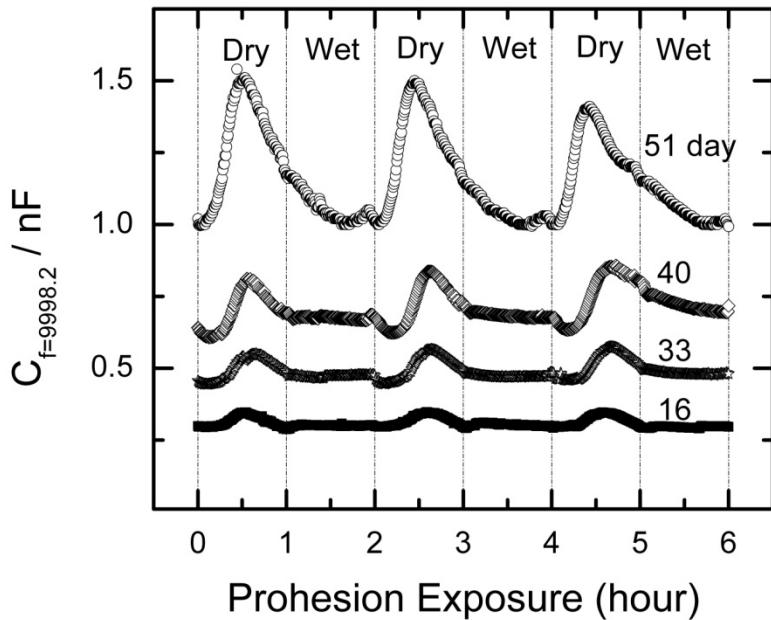


Figure 12. The evolution of high frequency capacitance $C_{9998.2\text{Hz}}$ values during the dry and wet steps of different Prohesion® exposure days.

3.3. ENM Results

Electrochemical noise measurements were also conducted during the coated panels exposed in the Prohesion® chamber. Both the electrochemical potential and current noise could be collected and ENM monitoring was carried out continuously for more than 6 hours, which covered three cycles of drying and wet under Prohesion® conditions.

The ENM original data were not report directly here due to the huge magnitude of the data file. Instead, the noise resistance (R_n) was presented. R_n was obtained by dividing the standard deviation of the potential noise by the standard deviation of the current noise. In fact, the original potential and current noise data were divided into many small blocks with each block having 128 data points, which is 25.6 seconds of test period. Linear detrending was also applied to the original noise data of each block to remove the electrochemical drift and then noise resistance was calculated [30]. So the R_n reported here is the average value over every 128 data points (25.6 seconds).

Previous works found that R_n was close to the coating polarization resistance R_p and the low frequency impedance modulus, which can also provide a good indicator of the barrier properties and life time prediction of coating performance [31-32]. The R_n values during the Prohesion® chamber of three different days' exposure were shown in figure 13. For day 1, the R_n values were very constant in dry step and little scattered in wet step, but all close to $1 \times 10^9 \Omega$ showing that the coating film acted as a good barrier in the early days to Prohesion® exposure. After 10 days' exposure, much more scattered values from 10^7 to $10^9 \Omega$ covered both the dry and wet steps and the averaging R_n value was around $10^8 \Omega$, indicating that coating still provided barrier protection to some extent. But there was no obvious difference in terms of magnitude and the dispersibility of the R_n values in dry and wet steps. It means that coating was start to degrade, and the water and electrolyte absorbed onto the coating surface could not be totally driven out during the dry step or the coating was softened in dry step and more accessible to moistures. The R_n values are only between 10^4 to $10^6 \Omega$ after 60 days' Prohesion® exposure, indicating fairly low barrier property the coating could provide by the end of the testing, the film was easily being wetted and penetrated into the primer and Al substrate surface.

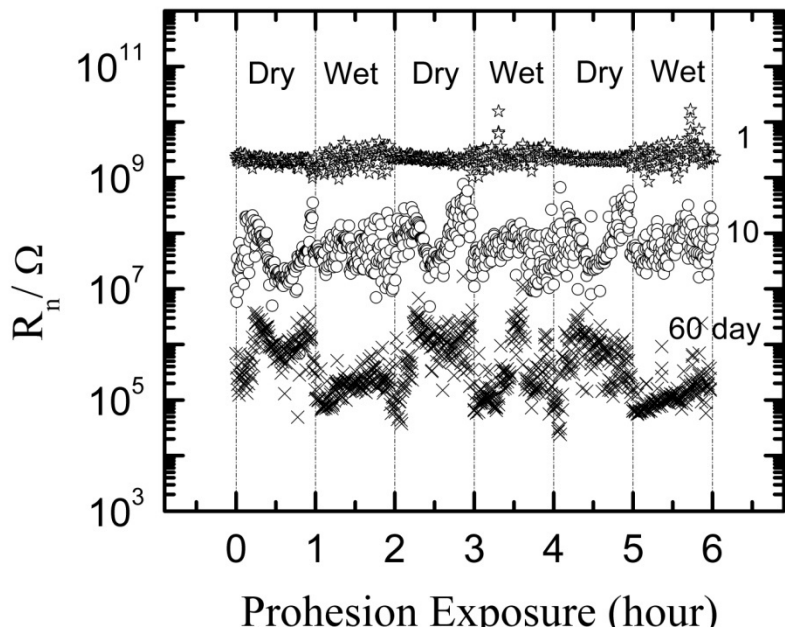


Figure 13. The changes of electrochemical noise R_n values during the Prohesion[®] chamber 3 dry and wet cycles of three different days' exposure.

It was observed from figure 13 that the R_n values changed a lot compared the first day and the last day data. For better showing the evolution of the noise resistance of the coating system, R_n values from both dry and wet steps were plotted as the function of Prohesion[®] exposure time. And here, the R_n value is the average noise resistance value from 30 to 45 minutes in a dry or wet step.

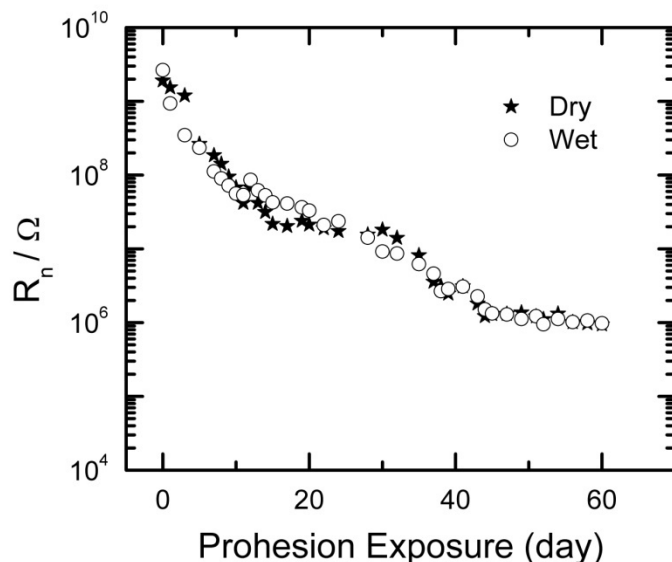


Figure 14. The evolution of the average R_n values obtained at the Prohesion[®] dry and wet steps with the chamber exposure time.

The R_n started from very high values, $1 \times 10^9 \Omega$, then quickly dropped to $1 \times 10^7 \Omega$ after about 10 days and maintained that value for another two weeks, followed by another quick drop to $1 \times 10^6 \Omega$ after about 6 weeks Prohesion® exposure, and leveled off for the rest of the testing days. This R_n value profile was very consistent with the evolution of the low frequency impedance from EIS testing, indicating that both the EIS and ENM combined with sensors can detect the coating changes during the whole Prohesion® exposure and had a good consistence with each other.

4. Conclusions

The Mg-rich primer and polyurethane clear topcoat system were applied onto the Al 2024 T3 substrate and the platinum sensor was embedded between the primer and the topcoat. Then the coated substrate was put into the standardized Prohesion® chamber to simulate weathering conditions in an aggressive manner to induce accelerated coating failure. The acquisition of EIS and ENM data from embedded sensor in-situ monitoring during the Prohesion® dry and wet steps demonstrated the coating behavior evolution. In this study, it was found that both EIS and ENM in-situ monitoring could be conducted under the either Prohesion® dry or wet steps with the embedded sensors. Under the Prohesion dry step, the coatings were sensitive to temperature changing, while in the wet step, the resistance values were more scattered due to the moisture accumulation on the coating surface. Both the temperature and humidity variation related coating property changes in Prohesion® chamber were in-situ monitored by the embedded sensors. It was found that the coating degraded continuously with Prohesion exposure time shown by a continuous decrease both in low frequency impedance $|Z|_{0.05 \text{ Hz}}$ and noise resistance R_n .

Acknowledgments

This work was supported by the Air Force Research Laboratory under Grant No. FA8650-04-1-5045.

References

1. Z. W. Wicks, F. N. Jones and S. P. Pappas. *Organic Coatings Science and Technology*, Second Edition. **1998**, 129-140.
2. G. P. Bierwagen, *Progress in Organic Coatings*, **1996**, 28, 43..
3. Ray Mudd, *Journal of Protective Coatings & Linings*, October **1995**, 51.
4. G. Gardner, "ASTM's New Coating Test Method Addresses Interactive Effects of Weathering and Corrosion," *Journal of Protective Coatings & Linings*, September **1998**, 50.
5. G. Gardner, "Recently Developed ASTM Test Addresses Interactive Effects of Weathering and Corrosion," *Protective Coatings Europe*, February, **1999**, 86.
6. Van Leeuwen, *Protective Coatings Europe*, January, **1996**, 42.
7. C. Simpson and R. C. D. Hicks, "ASTM D5894 and the Development of Corrosion Resistant Coatings," *Paint & Coatings Industry*, May, **1997**, 76.
8. N. D. Cremer, *Polymers Paint Colour Journal*, **1998**, 188, 31.
9. S. L. Chong, *Journal of Protective Coatings & Linings*, March, **1997**, 20.
10. B. S. Skerry and D. A. Eden, *Progress in Organic Coatings*, **1987**, 15, 269.
11. C. H. Tsai and F. Mansfeld, "Determination of Coating Deterioration with EIS. Part II. Development of a Method for Field Testing of Protective Coatings," *Corrosion*, **1993**, 49, 726.
12. F. M. Greenen, J. H. W. DeWit and E. P. M. Van Westing, *Progress in Organic Coatings*, **1990**, 18, 299.
13. D. Loveday, P. Peterson and B. Rogers-Gamry Instruments "Evaluation of organic coatings with Electrochemical Impedance Spectroscopy, part 2: Applications of EIS to coatings" *J. Coat. Technol.*, October, **2004**, 88.

14. D. A. Eden, M. Hoffman and B. S. Skerry, Application of electrochemical noise measurements to coated systems, in: R.A. Dicke, F.L. Floyd (Eds.), *Polymeric Materials for Corrosion Control*, ACS Symposium Series 322, American Chemical Society, Washington, DC **1986**.
15. M. Selvaraj and S. Guruviah, *Progress in Organic Coatings*, **1996**, 28, 271.
16. G. P. Bierwagen, X. Wang and D. E. Tallman, "In-situ Study of Coatings Using Embedded Electrodes for ENM Measurements", *Progress in Organic Coatings*, **2003**, 46, 163.
17. K. Allahar, Quan, Su, G. P. Bierwagen, D. Battocchi, V. J. Gelling and D. Tallman, "Future Studies of Embedded Electrodes for In-situ Measurement of Corrosion Protective Properties of Organic Coatings," NACE Corrosion/2006 Conference, March **2006**, San Diego CA.
18. K. Allahar, Quan, Su, G. P. Bierwagen, D. Battocchi, V. J. Gelling and D. Tallman, "Examination of the Feasibility of the Use of In-situ Corrosion Sensors in Army Vehicles", **2005** Tri-service Corrosion Conference, Orlando, FL.
19. K. Allahar, Quan, Su, G. P. Bierwagen, "Monitoring of the AC-DC-AC Degradation of Organic Coatings by Embedded Sensors", NACE Corrosion **2007** Conference, Nashville, TN.
20. M. Nanna and G. P. Bierwagen. *Journal of Coatings Technology*, April, **2004**, 1, 52.
21. D. Battocchi and G. P. Bierwagen. *Corrosion Science*, **2006**, 48, 1292.
22. D. Battocchi and G. P. Bierwagen. *Corrosion Science*, **2006**, 48, 2226.
23. X. Wang, "Study on novel electrode configurations for in situ corrosion monitoring on coated metal systems", Ph.D. Thesis, Chapter 3, Faculty of Science and Mathematics, North Dakota State University, **2002**.
24. S. Mabbutt, D.J. Mills, *Surf. Coat. Int. Part B: Coat. Trans.*, **2001**, 84, 277
25. R. A. Cottis, *Corrosion*, **2001**, 57, 265
26. H. A. Al-Mazeedi and R. A. Cottis, *Electrochim. Acta*, **2004**, 49, 2787
27. H. K. Yasuda, C. M. Reddy, Q. S. Yu, J. E. Deffeyes, G. P. Bierwagen and L. He, *Corrosion*, **2001**, 57, 29
28. J. N. Murray, *Progress in Organic Coatings*, **1997**, 31, 375
29. D. M. Brasher and A. H. Kingsbury, *Journal of Applied Chemistry*, **1954**, 4, 62.
30. R. A. Cottis, *Corrosion*, **2001**, 57, 265.
31. D. J. Mills and S. Mabbutt, *Progress in Organic Coatings*, **2000**, 39, 41.
32. G. P. Bierwagen, C. S. Jeffcoate, J. Li, S. Balbyshev, D. E. Tallman and D.J. Mills, *Progress in Organic Coatings*, **1996**, 29, 21.